GeoForschungsZentrum Potsdam
STIFTUNG DES ÖFFENTLICHEN RECHTS

Scientific Technical Report

Analysis of deformation and tectonic history of the Southern Altiplano Plateau (Bolivia) and their importance for plateau formation

Kirsten Elger

Dissertation zur Erlangung des Doktorgrades
im Fachbereich Geowissenschaften
an der
Freien Universität Berlin

14th March 2003

Abstract

The Altiplano represents a key region of the Central Andes, where the interplay between faults and syn-tectonic sediments allow the reconstruction of the kinematic evolution of the Central Andean high plateau. This study aims, by the use of incrementally-balanced cross-sections, interpretation of reflection-seismic profiles, 3D strain analysis, gravity data interpretation, isotopic-age dating, and surface observations, to reconstruct the geological and tectonic history of the Southern Altiplano at 21° S between the Eastern and the Western Cordillera.

The Southern Altiplano is a complex intramontane basin with 6–8 km Cenozoic fill. It can be structurally divided in three domains; the Eastern, Central, and Western Altiplano. 2D balanced cross-sections based on seismic-reflector analysis and field observations show that the Eastern Altiplano is the buried, thin-skinned deformation front of the western part of the Eastern Cordillera's bivergent thrust system. The 20–40° dipping, blind faults merge into a shallow, eastward-dipping detachment at 7–9 km depth that continues into the Eastern Cordillera. The Central Altiplano forms a bivergent system with 30–90° dipping, basement-involving thrusts in the east, and fault-propagation folds in the west. The shallow, westward-dipping detachment lies at 9–10 km depth and possibly continues into the Western Altiplano, which forms a separate bivergent thrust-system.

The computer-aided (GeoSec and 2DMove), incremental restoration of the balanced cross-sections of the Eastern and Central Altiplano, and preliminary line-length balancing of the Western Altiplano, yields 38 km shortening due to folding and thrusting. 3D strain analysis of sandstone grain shapes (R_f/ϕ' and centre-to-centre techniques on three perpendicular sections) reveals that an additional 7.7% of shortening was accumulated as ductile, micro-scale strain. This increases the total shortening in the entire cross-section of the Southern Altiplano at 21° S to 60 km or 21%. In addition, I suggest that the contribution of outcrop-scale structures possibly accounts for another 20 km. 3D strain analysis further shows that the 7.7% of micro-scale strain were accompanied by 13% orogen-parallel extension. These shortening estimates more than double the published shortening values from the Altiplano.

Crustal thickening and plateau uplift in the arc-backarc domain of the South American convergent margin took place during the Cenozoic. K-Ar and Ar-Ar age-dating on syn-tectonic sediments, together with seismic-sequence analysis, demonstrates that the Southern Altiplano structure formed during two independent compressional increments (Early Oligocene [≥27 Ma] and Middle/Late Miocene [17–8 Ma]), which were preceded by an Eocene/Oligocene extensional event that led to the formation of a half graben in the Central, and possibly a second in the Eastern Altiplano. Horizontal contraction of the Altiplano ended between 11–8 Ma, as indicated by the age of undeformed volcanic rocks.

Detailed seismic analysis of single syn-tectonic basins combined with isotopic ages of syn-tectonic sediments, reveal a complex deformation history characterised by spatially and temporally irregular fault activation, which excludes the existence of large-scale eastward or westward propagating deformation during plateau formation. This diffuse pattern of deformation was characteristic for the entire plateau domain, i.e. from the western flank to the eastern edge of the Eastern Cordillera, during a first stage of plateau formation between 30 and 10 Ma. This

possibly indicates that the plateau has remained flat since its formation and did not evolve from an initially doubly-vergent orogen.

The syn-tectonic stratigraphic units of the Southern Altiplano domain overlie shallow marine, Late Cretaceous sediments that still form a sub-horizontal regional near sea level. This indicates that plateau surface-uplift in this part of the plateau was mainly achieved by sedimentary infill of tectonically-controlled, internally-drained basins, and not by tectonic uplift.

The tectonic evolution of the Southern Altiplano was largely accompanied by magmatic activity. An episode of strong volcanic activity affected the entire width of the Altiplano and adjacent parts of the Eastern Cordillera between 25–8 Ma. However, a causal relationship between magmatism and deformation could not be shown for the Southern Altiplano. Strong Oligocene/Miocene volcanic activity, together with the diffuse pattern of deformation, suggests that the formation of the Altiplano Plateau was initiated by magmatically-controlled thermal weakening of the crust, possibly as the result of the removal of the mantle lithosphere. At present, the Altiplano has a flat topography, high heat-flow, and is spatially related to a variety of geophysical anomalies that are interpreted as partial melting of the middle crust (20–40 km depth). From this evidence, I propose that the process of plateau formation is still active.

Zusammenfassung

Für die zentralen Anden stellt der Altiplano eine Schlüsselregion dar, in der das Zusammenspiel zwischen tektonischen Störungen und syntektonischen Sedimenten es ermöglicht, die Bildung des zentralandinen Altiplano-Puna Plateaus zu rekonstruieren. Ziel der vorliegenden Arbeit ist es, die geologische und tektonische Geschichte des südlichen Altiplano bei 21° südlicher Breite mit Hilfe inkrementell bilanzierter Profile zu rekonstruieren. Dieses Rekonstruktion stützt sich auf die Interpretation reflektionsseismischer Profile, dreidimensionale Strainanalyse, isotopische Altersdatierungen, die Interpretation von Schwereanomalien und auf Felduntersuchungen.

Der südliche Altiplano ist ein komplexes intramontanes Becken, welches mit 6-8 km mächtigen, überwiegend syn- und posttektonischen Sedimenten gefüllt ist. Die vorliegende Untersuchung gliedert den südlichen Altiplano in drei Strukturdomänen: den östlichen, zentralen und westlichen Altiplano. Die im Rahmen dieser Arbeit erstellten zweidimensionalen bilanzierten Profile basieren vor allem auf der Interpretation seismischer Daten, welche durch Karteninterpretation und Feldbeobachtungen ergänzt werden. Diese Profile zeigen, dass der östliche Altiplano die Deformationsfront des westlichen Teils des bivergenten Überschiebungssystems der bolivianischen Ostkordillere repräsentiert. Die westvergenten Überschiebungen fallen mit 20–40° ein und münden in 7–9 km Tiefe in einen flach nach Osten einfallenden basalen Abscherhorizont, der sich unter der Ostkordillere fortsetzt. Der zentrale Altiplano bildet ein bivergentes Störungssystem, dessen östlicher Teil die Khenayani-Uyuni Störungszone bildet. Deren 30–90° steilen, ostvergenten Überschiebungen sind durch starke Horizontal- und Vertikalversätze gekennzeichnet. Im Hangenden wird zum Teil paläozoisches Grundgebirge (silurische Quarzite) bis an die Erdoberfläche gebracht. Der westvergente Teil des zentralen Altiplano ist durch Störungswachstumsfalten mit nach Westen abnehmender Verkürzung gekennzeichnet. Der basale Abscherhorizont des bivergenten Störungssystems des zentralen

Altiplanos liegt in 9–10 km Tiefe und fällt sehr flach nach Westen ein. Der westliche Altiplano stellt ein weiteres bivergentes Störungssystem dar, welches vermutlich durch einen gemeinsamen Abscherhorizont kinematisch mit dem zentralen Altiplano gekoppelt ist.

Die computergestützte (GeoSec und 2DMove) Abwicklung der bilanzierten Profile des östlichen und zentralen Altiplano sowie eine vorläufige Abschätzung der Linienlängenverkürzung des westlichen Altiplano ergeben für den südbolivianischen Altiplano einen Verkürzungsbetrag von 38 km aufgrund von Faltung und Überschiebung. Zusätzlich wurden dreidimensionale Strainanalysen an orientierten Sandsteinen durchgeführt. Diese basieren auf R_f/ϕ' und Fry-Analysen an jeweils drei zueinander senkrechten Schnittlagen. Das Ergebnis der Analyse zeigt, dass weitere 7,7% horizontale Verkürzung auf Korngrößenebene akkumuliert wurden. Die Gesamtverkürzung des südlichen Altiplano liegt damit bei 60 km oder 21%. Darüber hinaus verbergen sich möglicherweise bis zu 20 km Verkürzung in Kleinstrukturen, die bei der Bilanzierung nicht berücksichtigt werden konnten, da ihre Größe sowohl unter dem Auflösungsbereich der seismischen Daten als auch unter dem Maßstab des für diese Arbeit verfügbaren Kartenmaterials liegt. Die Strainanalyse zeigt darüber hinaus, dass die 7,7% horizontale Verkürzung in der Profilebene durch 13% gebirgsparallele Längung kompensiert wurden. Die im Rahmen dieser Studie ermittelten Verkürzungsbeträge sind mehr als doppelt so groß wie die aus früheren Arbeiten bekannten Werte.

Das Altiplano-Puna Plateau entstand während der letzten 30–40 Ma. Radiometrische Altersbestimmungen (K-Ar und Ar-Ar) an vulkanischen Einschaltungen in syntektonischen Becken zeigen in Kombination mit mit detaillierter seismischer Sequenzanalyse und sedimentologischen und strukturgeologischen Feldbeobachtungen, dass die Strukturen des südliches Altiplano das Resultat zweier unabhängiger kompressiver Deformationsinkremente im oberen Unteroligozän ($\geq$27 Ma) und im Mittel- bis Obermiozän (17–8 Ma) sind. Diesen einengenden Bewegungen ging eine eozän-oligozäne Dehnungsphase voraus, welche zur Bildung eines Halbgrabens im zentralen, und möglicherweise eines zweiten im östlichen Altiplano führte. Undeformierte vulkanische Gesteine belegen, dass der gesamte südliche Altiplano seit 11–8 Ma nicht mehr deformiert wurde.

Die Füllung der syntektonischen Becken reflektiert die Deformationsgeschichte der assoziierten Strukturen. Diese Becken sind besonders gut in den oberflächennahen Bereichen der seismischen Profile, welche für den zentralen Altiplano zur Verfügung standen, aufgelöst. Die Analyse mehrerer solcher syntektonischer Becken, die sich auch auf Ar-Ar Altersdatierungen stützen kann, zeigt für den Altiplano eine sehr komplexe Deformationsgeschichte auf, die durch unregelmäßige, sehr stark räumlich variierende Störungsaktivierung gekennzeichnet ist. Die räumlich-zeitliche Verteilung der Deformation schließt die Existenz einer ostwärts oder westwärts wandernden Deformationsfront für den Zeitraum der ersten Phase der Plateauentwicklung (zwischen 30–10 Ma) für den gesamten Plateaubereich — also für den Bereich von der Altiplano Westflanke bis zum Ostrand der Ostkordillere — aus. Diese Beobachtung könnte möglicherweise ein Hinweis darauf sein, dass die Oberfläche des Altiplano immer flach gewesen ist, dass sich also die Hochebene nicht aus einem klassischen Kollisionsorogen entwickelt hat, sondern schon immer ein Plateau war.

Die synorogenen tertiären Sedimente des südlichen Altiplano überlagern konkordant oberkretazische flachmarine Kalke, die auf Meeresspiegelniveau abgelagert wurden. Die Beobachtung, dass diese heute immer noch subhorizontal auf Meeresspiegelhöhe liegen ('regional'), weist darauf hin, dass die Höhe der heutigen Plateauoberfläche vor allem das Ergebnis von Sedi-

IV

mentation in tektonisch kontrollierte Becken mit interner Drainage und nicht auf tektonische Hebung zurückzuführen ist.

Die Entstehung des südlichen Altiplano war vor allem zwischen 25–8 Ma von starker vulkanischer Aktivität begleitet, die den gesamten südlichen Altiplano und auch angrenzende Bereiche der Ostkordillere erfaßte. Ein kausaler Zusammenhang zwischen Magmatismus und Tektonik konnte im Rahmen dieser Arbeit nicht nachgewiesen werden. Der oligozän-miozäne Vulkanismus und das durchgehend diffuse Deformationsmuster könnten jedoch darauf hindeuten, dass eine thermale Aufweichung der Kruste — evtl. im Zusammenhang mit dem Verlust von Mantellithosphäre — die Plateaubildung ausgelöst hat.

Auch der heutige Altiplano ist durch eine flache Topographie charakterisiert. Er zeigt einen erhöhten geothermischen Gradienten und ist durch eine Vielzahl geophysikalischer Anomalien gekennzeichnet, die eine parziell geschmolzene mittlere Kruste (in 20–40 km Tiefe) andeuten. Diese Beobachtungen weisen darauf hin, dass der Prozess der Plateaubildung heute noch anhält.

Resumen

El Altiplano representa una región clave de los Andes Centrales, donde la interacción entre fallas y sedimentos sintectónicos permite la reconstrucción de la evolución cinemática de la planicie elevada de los Andes Centrales. El objetivo del presente estudio, por medio del uso de secciones incrementalmente balanceadas, interpretación de perfiles sísmicos, análisis 3D de la deformación, interpretación de datos gravimétricos, dataciones radiométricas, y observaciones de terreno, de reconstruir la historia geológica y tectónica de la parte sur del Altiplano a los 21° S, entre la Cordillera Occidental y la Oriental.

La parte sur del Altiplano es una compleja cuenca intramontana con un relleno Cenozoico de 6-8 km. Se puede dividir en tres dominios; el Altiplano Oriental, Central y Occidental. Secciones balanceadas 2D, basadas en el análisis de reflectores sísmicos y observaciones de terreno, muestran que el Altiplano Oriental es el frente enterrado de deformación tipo piel delgada de la parte occidental del sistema bivergente de corrimientos de la Cordillera Oriental. Las fallas ciegas, que inclinan 20-40°, se convierten en un despegue somero, inclinado hacia el este, a 7-9 km de profundidad, que continua hacia la Cordillera Oriental. El Altiplano Central forma un sistema bivergente, con inclinaciones de 30-90° corrimientos que involucran al basamento, y pliegues por propagación de fallas en el oeste. El despegue somero, inclinado hacia el oeste, se encuentra a 9-10 km de profundidad y posiblemente continua en el Altiplano Occidental, el cual forma un sistema bivergente separado de corrimientos.

La restauración incremental de las secciones balanceadas, realizada con computadora (GeoSec y 2DMove), del Altiplano Oriental y Central, y el balanceo preliminar de largo de línea del Altiplano Occidental, entregaron valores de 38 km de acortamiento debido a plegamiento y fallamiento. El análisis 3D de la deformación, realizado en granos de areniscas (R_f/ϕ' y técnicas centro a centro en tres secciones perpendiculares) muestra que un 7,7% de acortamiento adicional fue acumulado en forma de microdeformación dúctil. Esto aumenta el acortamiento total en la sección completa del Altiplano Sur, a los 21° S, a 60 km o 21%. Además, sugiero que

la contribución de estructuras a escala de afloramiento, posiblemente contribuyan con otros 20 km. El análisis 3D de la deformación muestra que el 7,7% de esta, a microescala, estuvo acompañada de 13% de extensión paralela al orógeno. Estas estimaciones de acortamiento muestran valores dos veces mayores que los publicados para el Altiplano.

El engrosamiento cortical y alzamiento de la planicie Altiplánica, en el dominio de arco y tras-arco del margen convergente sudamericano, tuvo lugar durante el Cenozoico. Dataciones K-Ar y Ar-Ar de sedimentos sintectónicos, en conjunto con el análisis de secuencias sísmicas, demuestran que la estructura del Altiplano Sur fue formada durante dos incrementos compresivos independientes (Oligoceno Temprano ≥27 Ma y Mioceno Medio-Tardío 17–8 Ma), a los cuales precedió un evento extensional Eoceno-Oligoceno que llevó a la formación de un hemigraben en el Central y, posiblemente un segundo en el Altiplano Oriental. La contracción horizontal del Altiplano finalizó hace 11–8 Ma, como lo indican las edades de rocas volcánicas no deformadas.

El análisis detallado de cuencas individuales sintectónicas, combinado con dataciones radiométricas de sedimentos sintectónicos, reveló una historia de deformación compleja, caracterizada por la activación irregular, espacial y temporal, de fallas, lo que excluye la existencia de propagación lateral a gran escala durante la formación de la planicie. Este patrón difuso de deformación, fue característico para todo el dominio de la planicie, i.e. desde el flanco occidental hasta el borde oriental de la Cordillera homónima, durante un primer estadío en la formación de la planicie entre 30 y 10 Ma. Esto indica posiblemente que la planicie se ha mantenido plana desde su formación y que no evolucionó desde un orógeno inicialmente de doble vergencia.

Las unidades estratigráficas sintectónicas del dominio del Altiplano Sur cubren a sedimentos marinos someros del Cretácico Superior, que aún forman un nivel regional subhorizontal cercana al nivel del mar. Esto indica que el alzamiento de superficie en esta parte de la planicie fue principalmente realizada por el relleno sedimentario de cuencas con control tectónico y drenaje interno, y no por alzamiento tectónico.

La evolución tectónica del Altiplano Sur fue ampliamente acompañada por actividad magmática. Un episodio de fuerte actividad volcánica afectó el total del ancho del Altiplano y sectores adyacentes en la Cordillera Oriental entre 25–8 Ma. Sin embargo, una relación casual entre el magmatismo y la deformación no puede ser establecida para el Altiplano Sur. La fuerte actividad volcánica Oligo-Miocena, junto con un patrón difuso de deformación, sugiere que la formación de la planicie Altiplánica tuvo inicialmente un debilitamiento termal de la corteza, controlado por el magmatismo, posiblemente como resultado de la substracción de material del manto litosférico. Actualmente, el Altiplano tiene una topografía plana, elevado flujo calórico, y se encuentra espacialmente relacionado con una variedad de anomalías geofísicas que han sido interpretadas como fusión parcial de la corteza media (20–40 km de profundidad). Con estas evidencias, propongo que el proceso de formación de planicie se encuentra aún activo.

VI

Contents

Chapter 1

Introduction

1.1 The Andean 'plate-tectonic paradox'

The Altiplano-Puna Plateau is located in the Central Andes between 15 and 27° S. With an average elevation of 4000 m, it forms the world's second-largest high plateau. Typically, high surface elevation on Earth is considered to be caused by processes related to continental collision. The Altiplano-Puna Plateau, however, is located at the plate boundary between the continental South American Plate and the oceanic Nazca Plate and therefore has been described as a 'plate-tectonic paradox' (Riller and Oncken, 2003).

To investigate the processes controlling orogen formation at this ocean-continent collision zone, the Central Andes have been the subject of intense geological and geophysical investigations during the past decades. Large-scale seismic and seismological studies provided detailed information about the velocity and the attenuation of seismic waves of the Andean crust and mantle (e.g. ANCORP-Working Group, 1999; ANCORP-Working Group, 2003; Beck et al., 1996; Dorbath and Granet, 1996; Gräber and Asch, 1999; Haberland and Rietbrock, 2001; Masson et al., 2000; Schurr et al., 1999; Swenson et al., 2000; Wigger et al., 1994; Yuan et al., 2000). Furthermore, the Bolivian Altiplano was the subject of several reflection-seismic research campaigns of the Bolivian oil industry (YPFB). Gravimetric surveys generate high-quality models of the of the density of the crust (e.g. Götze and Kirchner, 1997; Götze et al., 1994) and magnetotelluric studies provide a picture of the electrical conductivity beneath the Central Andes (Brasse et al., 2002; Echternacht et al., 1997; Schwarz and Krüger, 1997). Balanced cross-sections exist for the forearc (Günther, 2001; Victor et al., 2003) and backarc region (e.g. Baby et al., 1990; 1997; Dunn et al., 1995; Kley, 1993; 1996; Kley et al., 1997; Lamb et al., 1997; Leturmy et al., 2000; McQuarrie, 1999; 2002; Müller, 2000; Müller et al., 2002).

The most important results of the geophysical investigations with respect to the Central Andean Plateau are that its high topographic elevation is isostatically compensated by a 60–75 km thick, predominantly felsic crust (Beck et al., 1996; Götze and Kirchner, 1997; James, 1971; Swenson et al., 2000; Wigger et al., 1994; Zandt et al., 1994). In contrast to the 'doubled' crust, the Altiplano is only underlain by a 'single', 100 km thick lithosphere. Lithospheric thinning of a few tens of kilometres occurs only beneath the Puna (Yuan et al., 2002). The absence of an expected increase in lithospheric thickness in regions with doubled crust was interpreted as indication of the partial removal of the mantle lithosphere beneath the entire plateau area
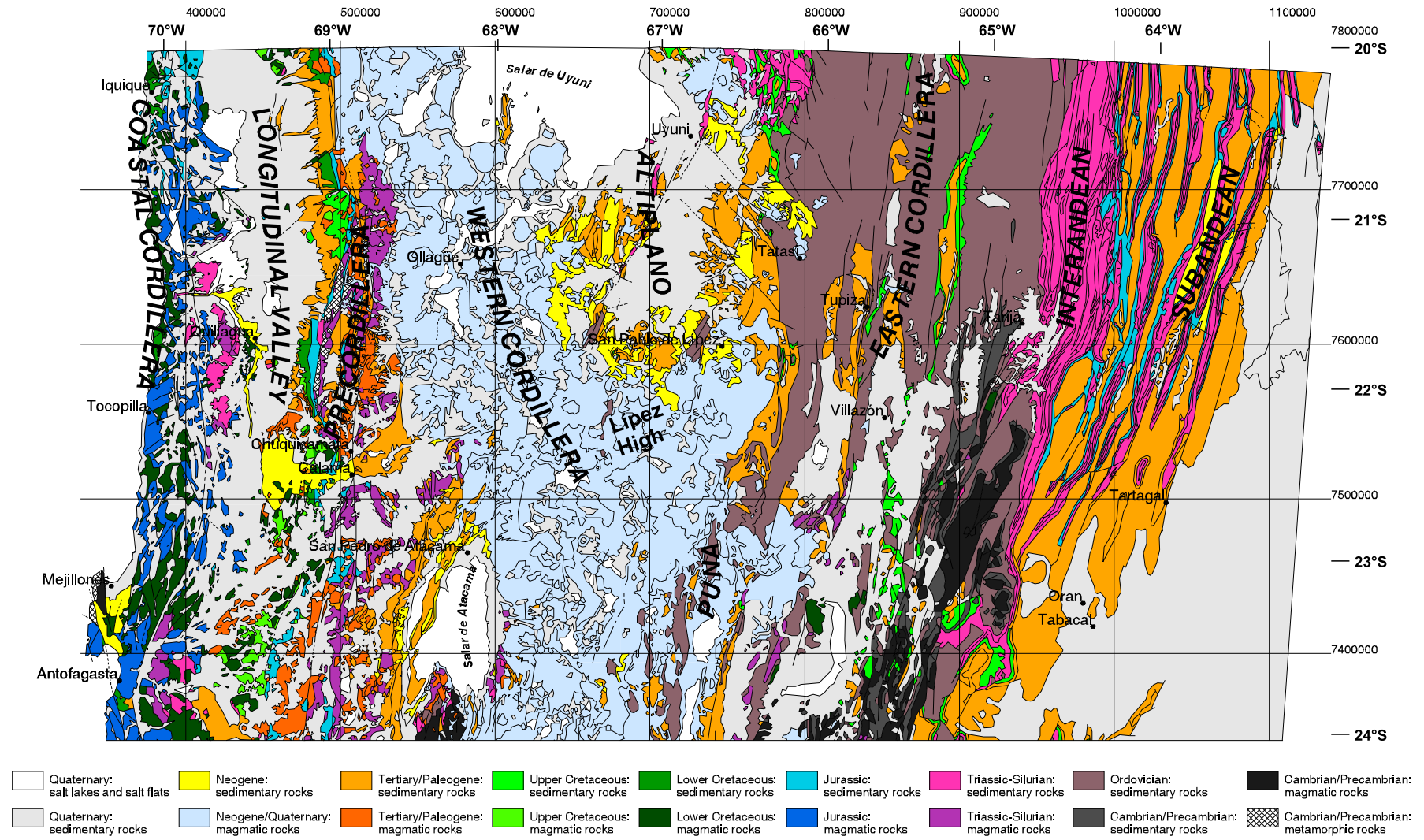
Figure 1.1: Geological map of the southern Central Andes between 20 and 24° S, modified after Reutter (1994).
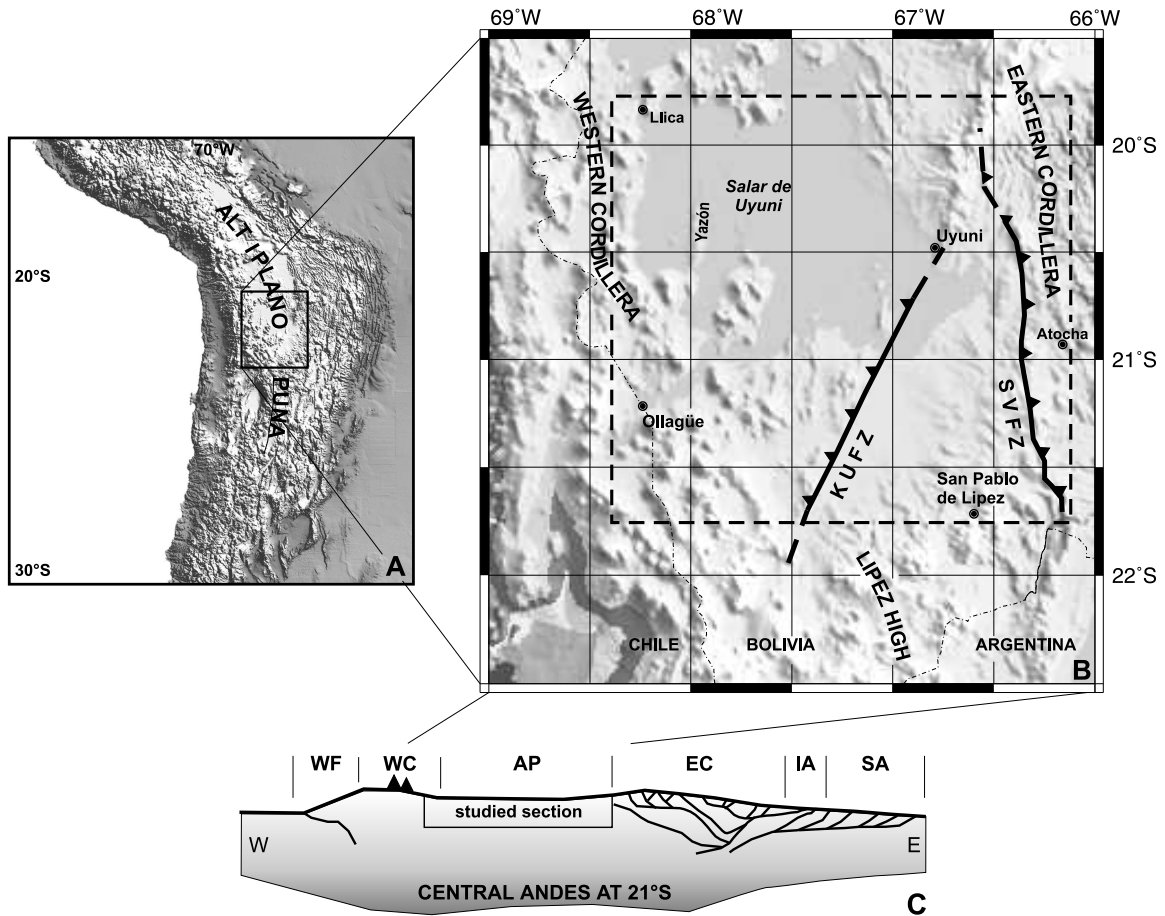
Figure 1.2: Shaded relief of the topography of the Central Andes (**A**) and a close-up of the Southern Altiplano in Bolivia (**B**). Major structural elements on the Southern Altiplano are the Khenayani-Uyuni Fault Zone (KUFZ) and the San Vicente Fault Zone (SVFZ), the working area is marked by a dashed box. (**C**) Schematic cross-section of the Central Andean Plateau at ∼21° S. WF = Western Flank and Precordillera, WC = Western Cordillera, AP = Altiplano, EC = Eastern Cordillera, IA = Interandean, SA = Subandean.

(Yuan et al., 2002). Furthermore, the Andean Plateau is characterised by a mid-crustal, seismic low-velocity zone as detected by receiver functions (Yuan et al., 2000), whose upper limit correlates with an extremely high conductivity anomaly (Brasse et al., 2002) and bright seismic reflectors from the ANCORP'96 profile (ANCORP-Working Group, 1999). This first-order geophysical anomaly was interpreted as a partial-melt zone decoupling upper-crustal imbrication from lower-crustal thickening (Brasse et al., 2002; Schilling and Partzsch, 2001; Yuan et al., 2000).

1.2 Geological setting

The Altiplano-Puna plateau forms the central part of the Southern Central Andes. Under the modern Andes, the oceanic Nazca Plate has been subducted for the last ∼200 Ma. Long-term tectonic erosion of the upper plate led to continuous eastward migration of the magmatic arc since the Jurassic. The Chilean forearc at 21–22° S can be differentiated from W to E into the

Coastal Cordillera: the Jurassic magmatic arc, the Longitudinal Valley: the 'western foreland' of the Andean Plateau with an average elevation of 1600 m, and the Chilean Precordillera. The latter consists of predominantly Paleozoic and Mesozoic rocks which form a crustal-scale anticline above the west-vergent, thick-skinned thrust system of the western plateau flank (Günther, 2001; Muñoz and Charrier, 1996; Victor et al., 2003). The 4200 m high Western Cordillera is the site of the Neogene to Recent magmatic arc with peak elevations of up to 6000 m, formed by Pliocene/Quaternary volcanoes. The Altiplano Plateau, the Eastern Cordillera, the Interandean, the Subandean, and the Chaco foreland basin are the main structural domains of the Bolivian backarc (Figs. 1.1 and 1.2C). The Altiplano, a complex intramontane basin, is characterised by 4–10 km thick, Cenozoic, syn-orogenic, continental sediment fill and a flat topography (e.g. Baby et al., 1997; Rochat et al., 1999; Welsink et al., 1995, see Fig. 1.2A). Peak elevations of up to 6000 m are also reached in the bivergent, thick-skinned thrust-system of the Eastern Cordillera, which involves the Precambrian to Ordovician basement (Kley et al., 1996; Müller et al., 2002, see also Figs. 1.1 and 1.2C). East of the Eastern Cordillera the mean elevation drops by ~1000 m to the Interandean Zone, a 2000-3000 m high, east-vergent, thin-skinned thrust belt entirely raised by underlying basement structures (Kley, 1996). The thin-skinned Subandean Ranges form a 'classical', east-vergent, foreland fold-thrust belt (Figs. 1.1 and 1.2C). East of the Subandean deformation front is the down-flexed, but otherwise undeformed Chaco Foreland Basin, a 200 km wide, sedimentary basin with a Neogene clastic fill of up to 5 km. The Central Andean Plateau extends from the Western Flank to the eastern border of the Eastern Cordillera (Figs. 1.1 and 1.2C).

The Southern Altiplano has an average altitude of ~3800 m. Most of the area is covered by Quaternary fluvial and lacustrine sediments, including several large salt pans (e.g. Salar de Uyuni, Fig. 1.2B). Local exposure of Paleozoic, Cretaceous, and Tertiary strata is fault-controlled and related to the Cenozoic uplift of the Altiplano-Puna plateau. The Lípez High forms the southern limit of the Altiplano and the transition to the Argentine Puna (Fig. 1.2B). The main structural element of the Southern Altiplano is the NNE–SSW trending Khenayani-Uyuni Fault Zone (KUFZ), where Paleozoic sediments were thrust over Oligocene-Miocene strata (Fig. 1.2B). The KUFZ is a major tectonic element that appears to have largely controlled both Phanerozoic sedimentation and Cenozoic deformation in Southern Bolivia (Sempere, 1994). The kinematics of the KUFZ include reverse faulting (Baby et al., 1990; 1997, 1990; Martínez et al., 1994) and/or strike-slip faulting (e.g. Sempere et al., 1997). The second major structural element is the steeply eastward-dipping thrust system of the San Vicente Fault Zone (SVFZ), which forms the dominant feature delimiting the Eastern Cordillera in the east and the sediment-covered Altiplano in the west (Fig. 1.2B).

1.3 Crustal shortening and models of plateau formation

The contribution of different processes such as crustal shortening, magmatic addition, mantle delamination and hydration to plateau formation have been a matter of controversial discussion for many years (e.g. Allmendinger et al., 1997; Isacks, 1988; James, 1971; Wdowinski and Bock, 1994a). Today it is widely believed that orogen-normal crustal shortening was the main mechanism of plateau formation (Allmendinger et al., 1997; Isacks, 1988; Kley and Monaldi, 1998; Roeder, 1988; Sheffels, 1990). Magmatic addition apparently contributes less than 5% to the crustal volume (Allmendinger et al., 1997). The respective tectonic models are gener-

ally based on the assertion of plane-strain deformation, i.e. horizontal shortening is only compensated by vertical thickening (Allmendinger and Gubbels, 1996; Allmendinger et al., 1997; Isacks, 1988; Kley and Monaldi, 1998; McQuarrie, 2002).

The central Altiplano region began its principal phase of uplift about 25–28 Ma ago (Baby et al., 1990; Isacks, 1988; Sempere et al., 1990; Victor, 2000), although some uplift may have occurred as early as the Eocene (53–34 Ma) (e.g. Allmendinger et al., 1997; Kennan et al., 1995; Lamb and Hoke, 1997; Sempere et al., 1997). Isacks (1988) and Gubbels et al. (1993) proposed a two-stage model for the uplift of the Andean Plateau by horizontal shortening and vertical thickening. Early plateau formation occurred in response to distributed contraction of the plateau domain with a possible earlier start at the margins, which form the present-day Eastern and Western Cordilleras. Crustal shortening is thought to be homogeneously distributed in the upper and lower crust by a pure shear mechanism (Allmendinger and Gubbels, 1996). Some authors suggested that the plateau reached an elevation of only ∼1500–2500 m at the end of the first stage around 10 Ma ago (Gregory-Wodzicki, 2000; Gubbels et al., 1993). After this critical period of elevation the zone of active deformation migrated eastwards into the Subandean Ranges while the plateau north of 23° S deformed in a simple shear mode (Allmendinger and Gubbels, 1996). Deformation in the Altiplano ended with the end of the first stage ∼10 Ma ago (Allmendinger et al., 1997; Gregory-Wodzicki, 2000; Isacks, 1988).

All presented models for plateau formation caused by tectonic shortening mainly focus on the eastern margin of the plateau. Crustal shortening estimated from balanced cross-sections in the bivergent thrust system of the Eastern Cordillera and the thin-skinned foreland fold-and-thrust belt of the Interandean and Subandean Ranges (see Fig. 1.2C) explains approximately 60–70% of present-day crustal thickness (i.e. 180–235 km, Dunn et al., 1995; Kley, 1996; Kley et al., 1997; Müller, 2000; Müller et al., 2002; Schmitz, 1994). Estimates of shortening for the plateau domain (Baby et al., 1997; Lamb et al., 1997; Rochat et al., 1996) are not well constrained and tend to be very low, probably due to the widespread coverage by syn- and post-tectonic sediments, and the lack of information at deeper crustal level. McQuarrie and DeCelles (2001) and McQuarrie et al. (2002) indicate substantially higher values of shortening after re-evaluating structures. Recent studies of the western margin of the plateau show the existence of a west-vergent thrust system (Victor, 2000). Geometric modelling detected a transcrustal ramp (ramp-flat-ramp geometry) extending down to a depth of 30–35 km, which generated a surface uplift of 2640 m only by minor amounts of horizontal shortening (∼2.5 km; Victor, 2000). Total horizontal shortening accumulated at the western margin, including the Precordillera, is as little as ∼15–20 km since the Eocene (Günther, 2001; Victor et al., 2003).

1.4 Aims

The Altiplano represents a key region of the Central Andes, where the interplay between faults and syn-tectonic sediments allow the reconstruction of the kinematic evolution of the plateau. The section at 20–21° S is characterised by the highest density of geophysical and geological data in the Central Andes (see section 1.1). In addition, high resolution, industrial, reflection-seismic sections (YPFB) were made available to this project; they are fundamental in imaging the structure beneath the largely sediment-covered plateau down to 4 s two-way travel-time (TWT).

This study aims, by the use of incrementally-balanced cross-sections based on reflection-seismic profiles, 3D strain analysis, gravity data, isotopic-age dating, and surface observations, to answer the following questions:

- What is the structural style and evolution associated with plateau formation and uplift?

- What is the time frame of deformation in the Southern Altiplano?

- How far does tectonic shortening of the Southern Altiplano contribute to the observed crustal thickness?

- Which amount of tectonic shortening occurs at micro-scale?

- Can the amount of out-of-plane material flow during horizontal shortening be quantified?

- How did deformation propagate over time during plateau formation?

- Is there a relationship between the timing of deformation and the regional distribution of magmatism?

Chapter 2

Database

Table 2.1 shows the available data. Their spatial distribution is shown in Figs. 2.1, 4.1, 4.4, 5.1, and App. F.1. I organised data storage and visualisation by GIS functionality (ARC/INFO, ESRI) to be able to work in an overall geo-referenced system.

The identification of seismic facies, their geometry, and seismic sequence analysis, in combination with the stratigraphic information from the Vilque Well and field observations, yielded the general stratigraphy that was used to correlate the seismic sections, identify tectonic increments, their relative ages, and the sequence of fault activation. Detailed structural analysis of field observations, as well as structural interpretation from geological maps, aerial photographs, and satellite images supported and complemented the seismic interpretation.

Database	Source
16 Reflection-seismic profiles, paper prints of migrated or stacked TWT sections (see Table B.1)	YPFB, Santa Cruz, Bolivia
Geological maps of different scales from 1:50000 to 1:1000000 with reports (see Table B.2)	YPFB, Santa Cruz, Bolivia; SERGEOMIN, La Paz, Bolivia
Topographic maps 1:250000	IGM La Paz, Bolivia
Well reports and logs (Vilque and Colchani wells)	YPFB, Santa Cruz, Bolivia
Gravity and aeromagnetic maps	SFB-267 data, YPFB, Santa Cruz, Bolivia
Aerial photography	IGM, La Paz, Bolivia
Satellite images (Landsat 5 TM scenes, Landsat 7 [ETM+] panchromatic merge)	SFB-267 data, Free University of Berlin, Germany (processing)
Field structural data regarding fault kinematics, maps, etc.	Own data
Strain data derived from sandstones and tuffs	Own data
Radiometric ages of key stratigraphic and structural units	Own data and data from the parallel SFB-267 subproject (FU Berlin)
ANCORP reflection-seismic profile (below 10–15 km)	DEKORP, GFZ Potsdam, Germany

Table 2.1: Database for this study. SFB-267 refers to the German 'Collaborative Research Centre 267 — Deformation Processes in the Andes' (Berlin and Potsdam, Germany), which was the frame of the present study.
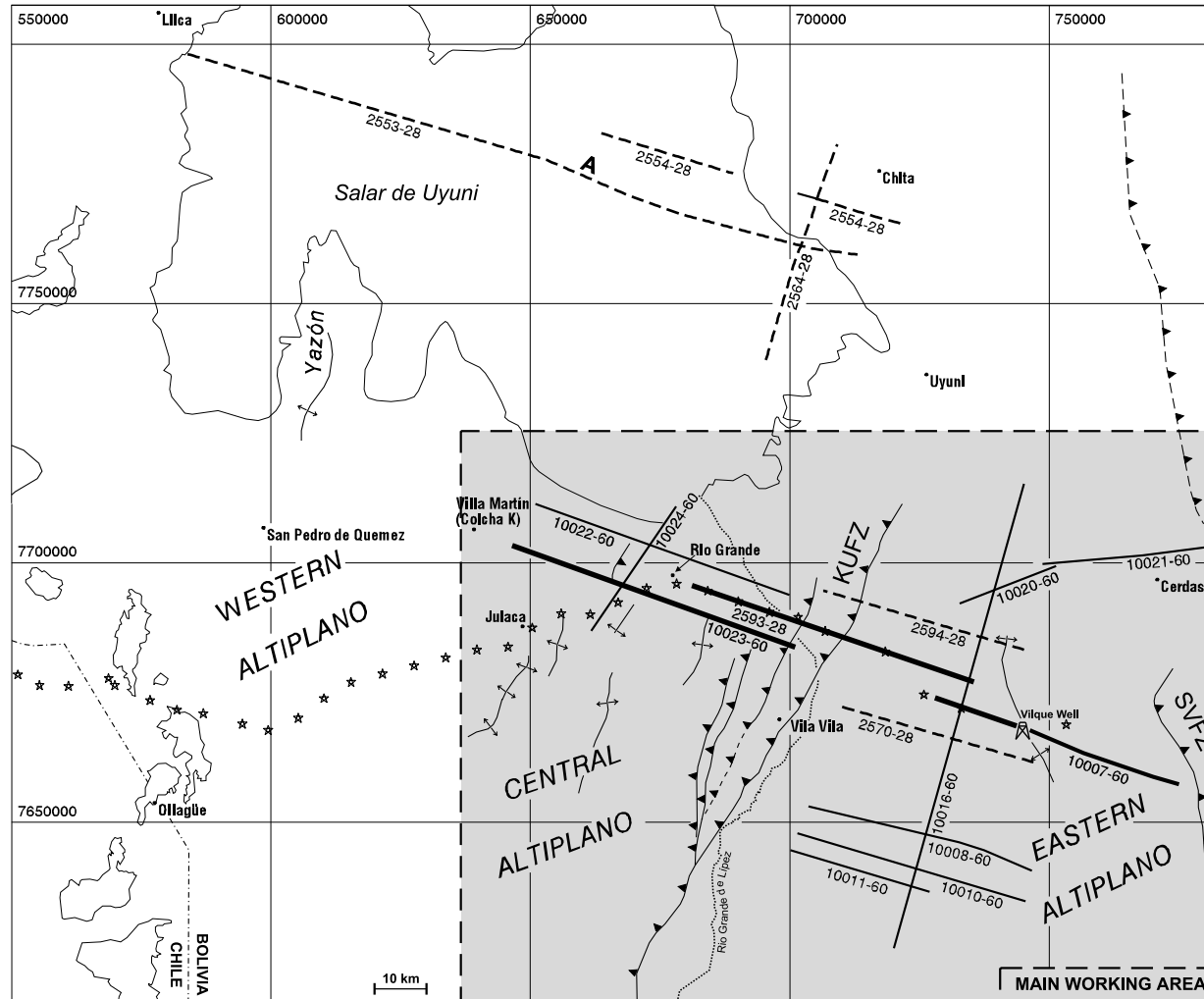
Figure 2.1: Overview of the working area on the Southern Altiplano in Bolivia showing industrial reflection-seismic lines used (YPFB, Santa Cruz, Bolivia). Seismic lines with suffix -28 are from the first exploration campaign (1974–1975), those with suffix -60 from the second (1993–1994, see section 2.5 for details). Solid lines mark seismic profiles which exist as migrated time-sections. Dashed profiles exist only as stacked sections. Bold solid lines delineate the Main Cross-Section which is the base for the balanced cross-section. The line-drawing of the section west of point A (line 2553) is shown in chapter 7. Stars show the shot points of the ANCORP'96 profile (ANCORP-Working Group, 1999). The main working area, which correlates with the extent of the geological map (App. F.1), is shaded grey.

The working area, i.e. the Southern Altiplano, was divided into three domains, the Eastern, Central and Western Altiplano (see Fig. 2.1) on the basis of structural style, outcrop availability, and the quality of seismic data. The three criteria also determined which combination of seismic and map interpretation, and surface observations were employed in each respective domain. The balanced cross-section of the Eastern Altiplano is mainly based on seismic interpretation. Here the weakly-folded strata yielded very continuous reflectors; significant outcrops are restricted to the eastern part of the section, near the edge of the Eastern Cordillera. In the Central Altiplano, strongly folded and faulted strata led to repeated gaps in the seismic image. In this domain, without surface bedding data, the position of major faults and stratigraphic boundaries, the construction of the balanced cross-section would have been impossible. In the Western Altiplano the database is rather poor, as large areas are covered by Neogene volcanic and sedimentary rocks. Nevertheless, a preliminary structural interpretation of the Western Altiplano, based on the interpretation of seismic and gravity data, was possible (see sections 7.4 and 7.1.3). Limited exposure of Tertiary strata at the Yazón Peninsula (Fig. 2.1) enabled me to correlate the geophysical data locally with stratigraphy. However, due to the very limited database, it was not possible to construct a balanced cross-section of the Western Altiplano.

The first objective of the seismic and structural analysis was to generate boundary conditions for the construction of the balanced cross-section (kinematic analysis, determination of deformation mechanisms, etc.) and its incremental restoration, i.e. the determination of target horizons. I also incorporated the accumulated micro-scale strain, determined on oriented samples, to take into account its contribution to the horizontal shortening in cross-section plane and the third component of the deformation tensor.

2.1   Maps and projections

YPFB provided a detailed geological map at the scale of 1:50000 that formed the main database for surface geology, after its conversion into a digital format (ARC/INFO, ESRI) during this project (see App. F.1). It covers the area of the southern seismic profiles, i.e. the main working area (see Fig. 2.1), and allowed a very detailed structural analysis. Supplementary information was derived from published geological maps of the Bolivian Geological Survey (SERGEOMIN), and from the Geological Map of the Central Andes (Reutter et al., 1994). The latter covers the entire Central Andean forearc and backarc between 20 and 26° S. This map is partly shown in Fig. 1.1. A full list of available maps is given in Table B.2.

The standard projection for the Bolivian maps is Universal Transversal Mercator (UTM) with the datum 'Provisorial South American 1956'. This is also the projection I used for all the maps presented here, except of those which have geographical, i.e. longitude/latitude co-ordinates.

2.2   Field data

The main focus of the field work was to verify the available geological maps and to correlate the seismic profiles with surface geology. During field work I also collected fifteen oriented samples for strain analysis. Thirteen volcanic rock samples from key structural positions and
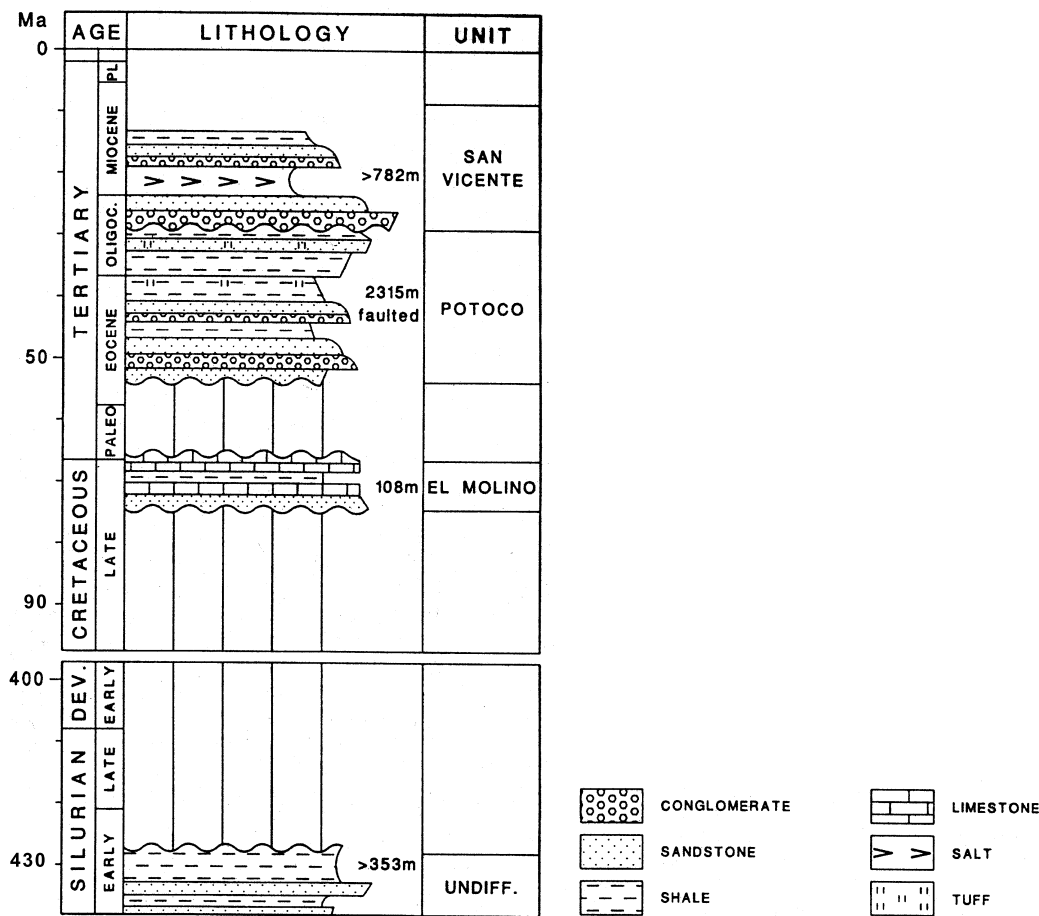
Figure 2.2: Lithological column of the Vilque Well (modified after Welsink et al., 1995).

stratigraphic units were collected for Ar-Ar and K-Ar isotopic age determinations (see chapter 6). As a part of a parallel project at the Free University of Berlin, another thirty-three volcanic and plutonic rock samples were collected for isotopic age determination (see App. F.1 and Silva-González, in prep.). Fault kinematics were determined, especially along the seismic profiles, to constrain the kinematic evolution, the direction of tectonic transport, and the deformation mechanism. These are essential elements of information to constrain the incremental cross-section balancing strategy (see chapter 4 and Tables B.3 and B.4).

2.3   Well data

The Vilque Well is the only well in the main working area. It was drilled in 1972–1973 as part of the first exploration survey of YPFB on the Southern Altiplano. The well reached a final depth of 3559 m in Lower Paleozoic sediments. It is situated in the core of the Vilque Anticline, in the seismic profile 10007 (Eastern Altiplano, see Fig. 2.1). Units encountered include the Tertiary San Vicente and Potoco Fms., the Cretaceous El Molino Fm., and undifferentiated Silurian (Fig. 2.2). A remarkable feature of the Vilque Well is a 600 m thick salt layer within the San Vicente Fm. This was interpreted as a local phenomenon, e.g. a salt cushion, with only limited lateral extent (Oscar Aranibar, Santa Cruz, Bolivia, pers. comm.). The correlation

of seismic reflectors with stratigraphic horizons in the Eastern Altiplano was based on stratigraphic boundaries mapped at the surface and the information of the Vilque Well.

2.4 Satellite data and aerial photography

In addition to 'classical' field work and map analysis, satellite images and air photos were essential tools for the regional structural interpretation, the detection of key structural outcrops, and for orientation during field work. The available satellite data included subsets from a mosaic of Landsat 5 Thematic Mapper (TM) scenes of the Southern Central Andes (with

Figure 2.3: Example of the Landsat 7 (ETM+) satellite image of the Serranía Corregidores with the geological map, modified from YPFB (excerpt from App. F.1, legend is same). The satellite data was processed and kindly provided by P. Gôni and K. Munier (Free University of Berlin, Germany).

a modified resolution of 50 m/pixel) as well as two Landsat 7 (ETM+) scenes with an IHS-to-panchromatic merge (SFB 267 data, processed from the Remote-Sensing Group of the Free University of Berlin, Germany). The IHS-to-panchromatic merge (Munier and Gôni, 2000) combined the very high resolution (15 m/pixel) from the panchromatic channel with the common RGB-741 colour information. This allowed enhanced satellite images to be printed at a scale of 1:50000, making them preferable to to topographic maps and aerial photography.

2.5   2D reflection-seismic profiles

844 profile kilometres in 16 seismic sections with lengths between 20 and 135 km (Fig. 2.1) were made available as paper copies by YPFB, Santa Cruz, Bolivia.

YPFB started the first large exploration campaign on the Southern Altiplano in 1970. In 1974–1975, YPFB acquired 1200 km of 48-channel vibroseis data in the Salar de Uyuni area and another 705 km in the Vilque area. The data were processed to a 24-fold final stack and have a shot point distance of 100 m. Six of the available lines are from this older campaign (lines with suffix -28, Fig. 2.1 and Table B.1). These are mainly those that cross the Salar de Uyuni (northern lines) and three of the southern lines which close the gap between the Central and Eastern Altiplano (see Fig. 2.1). The quality of these lines is poorer than of those from the second exploration campaign, between 1993 and 1994. During this period, YPFB gathered another 820 km of vibroseis data on the Southern Altiplano (50 m shot point distance). These lines are DMO-corrected, migrated time sections (all lines with suffix -60, see Fig. 2.1 and Table B.1). Detailed information about acquisition and processing parameters is given in Appendix B. The migrated seismic profiles have variable data quality. The quality is very good in the Eastern Altiplano. Data quality in the Central Altiplano, where some lines were shot above the Salar de Uyuni, is rather poor. The only section with interpretable quality is line 10023-60, the western part of the Main Cross-Section.

The Main Cross-Section is an WNW–ESE section that extends for ∼140 km across the Eastern and Central Altiplano (Fig. 2.1). It covers the entire eastern half of the inner plateau area and forms the base for the balanced cross-section (cf. chapter 9). Stratigraphic information from the Vilque Well (see Fig. 2.2 and Fig. 2.1 for location), in combination with surface mapping, was used to correlate stratigraphy with seismic facies (see section 7.2.1). Lines 10023-60 and 10007-60 are situated along one WNW–ESE trending line and are both part of the younger seismic campaign. The middle profile (2593-28) was shot during the first exploration campaign, but re-processed and migrated in 1994 (wave-equation migration). The Western Altiplano is only imaged by one seismic profile from 1972 (stacked section). It lies in the northern part of the Salar de Uyuni. For reasons of simplicity, I will not use the suffices of the seismic lines (e.g. 10007 instead of 10007-60).

Chapter 3

Stratigraphy

The Southern Altiplano has an average altitude of 3800 m and is bounded by the Eastern Cordillera to the east and the Western Cordillera to the west. The latter is also part of the Andean high plateau. Most of the Southern Altiplano is covered by Quaternary alluvial, fluvial, and lacustrine sediments including several large salt pans (e.g. Salar de Uyuni). Local exposures of Paleozoic, Cretaceous, and Tertiary strata occur mainly in the eastern and central part of the Southern Altiplano. They are fault-related and due to the Cenozoic uplift of the Altiplano-Puna Plateau. The western part of the Southern Altiplano is almost entirely covered with post-tectonic volcanic rocks from the active magmatic arc of the Western Cordillera. The Lípez High forms the southern limit of the Altiplano and the transition to the Argentine Puna (Figs. 1.1 and 1.2B).

Rocks that outcrop below undeformed Quaternary sediments and volcanic rocks in the Southern Altiplano are Ordovician, Silurian, Devonian, Cretaceous, and Tertiary in age. A detailed stratigraphic analysis of the Tertiary is subject of a Ph.D. thesis in progress (2003) at the FU Berlin (Silva-González). Therefore, I will here only summarise lithologies and rock facies cropping out in the Southern Altiplano to create a basis for further discussion about potential detachment horizons, erosional unconformities, etc., and their significance for plateau formation and cross-section balancing (i.e. tectonic history, age of deformation).

3.1 Paleozoic

Ordovician rocks make up the bulk of the fold-and-thrust belt of the Eastern Cordillera. Silurian and Devonian sediments are abundant in the Interandean Ranges, situated between the Eastern Cordillera and the Subandean (Fig. 1.1). Further south, in the northern Puna, Ordovician rocks frequently crop-out below Neogene volcanics of the Recent magmatic arc. The Eastern Cordillera of Argentina is composed of Ordovician and older sediments and magmatites (see Fig. 1.1).

Outcrops of marine Paleozoic rocks (Upper Ordovician, Silurian, Devonian) on the Southern Altiplano are sparse and always occur in hanging walls of thrusts. They mainly form small elongated hills that parallel the NNE–SSW trending Khenayani-Uyuni Fault Zone (KUFZ). Further south, two larger outcrops of Ordovician are present in the Southern Altiplano ('Soniquera'
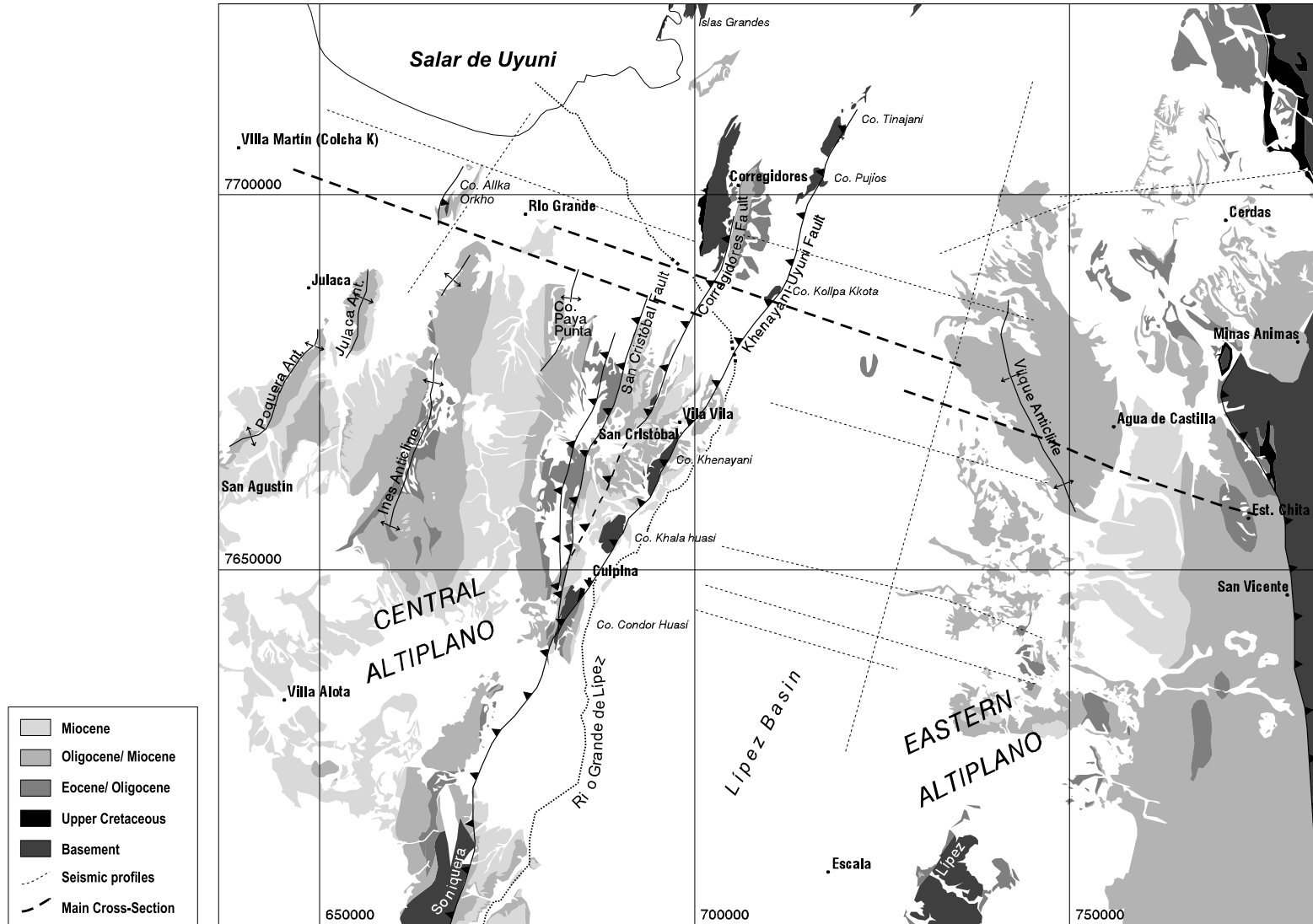
Figure 3.1: Overview of the geological units of the working area with locality names. Dottet lines represent traces of seismic profiles, dashed lines delineate the Main Cross-Section.

at the KUFZ and 'Lípez' in the Eastern Altiplano, SE of Escala, W of San Pablo de Lípez, see Fig. 3.1 and 1.1) (Egenhoff, 2000). Late Silurian-Devonian strata crop out on the Islas Grandes, at the eastern edge of the Salar de Uyuni, and in the Serranía Corregidores (Fig. 3.1).

Lower Ordovician rocks form roughly the eastern part of the south Bolivian Eastern Cordillera and continue in NW Argentina. During the Lower Ordovician the present Eastern Cordillera of NW Argentina and S Bolivia was part of the same depositional system, a broad shelf at South America's western margin that was filled mainly during the Arenig (Egenhoff, 2000). In Middle Arenig times, sedimentation continued in a deep-marine foreland basin west of the former shelf area. Similar to the Lower Ordovician, a parallel development in NW Argentina and S Bolivia is assumed for the Middle Ordovician as well. This was supported by a paleocurrent analysis in the Puna and the Eastern Cordillera of NW Argentina (e.g. Bahlburg, 1990) which showed continuous sediment transport towards the north, the Southern Altiplano. Accordingly, even where no outcrop of Middle Ordovician strata in the Southern Altiplano exist, the whole Middle Ordovician succession has to be assumed to subcrop in the plateau area. The observation that the oldest outcropping strata on the Southern Altiplano has Caradocian age, indicates that the basal detachment is just below or within Caradocian sediments.

The Late Ordovician (Caradocian, Egenhoff, 2000) sandstones and conglomerates, interbedded with pelites, were deposited by marine turbidity currents. The westward increase in grain-size indicates a more proximal environment in the Central Altiplano (Soniquera) than the finer-grained part in the Eastern Altiplano (Lípez) and the adjacent Eastern Cordillera (Fig. 3.1). This can be interpreted as indication that today's Central Altiplano was closer to the western edge of the Late Ordovician basin than the Eastern Altiplano and the Eastern Cordillera (Egenhoff, 2000). Therefore it is possible that Late Ordovician strata do not underlie the entire Altiplano, but wedge out in its western part.

The lowermost Silurian deposits are represented by the Cancañiri Fm., a sequence of diamictites and reworked marine sediments deposited during the glaciation at the Ordovician-Silurian transition. According to Suárez-Soruco (1995), the Cancañiri Fm. has a depocentre near Tica Tica, at the western edge of the Eastern Cordillera at about $20°$ S, where the thickness amounts to $\sim$1400 m. In the Southern Altiplano, the Cancañiri Fm. outcrops in small areas, which are below map-scale, along a line starting 8 km east of Uyuni and ending at the confluence of the Rio Alota and Rio Grande de Lípez, south of Culpina in the hanging wall of the KUFZ. All outcrops are thrust bound, so there is little information about distribution and thickness of this unit in the Southern Altiplano. In the Eastern Cordillera, a southward decrease in thickness can be observed (from $\sim$1400 m near $20°$ S to $\sim$200 m near $22°$ S, Suárez-Soruco, 1995). This could be valid for the Southern Altiplano too. The Cancañiri Fm. is interpreted as syn-tectonic because it contains reworked clasts of Ordovician units (Suárez-Soruco, 1995).

The Late Ordovician–Early Silurian deformation increment was responsible for the formation of the slaty cleavage that penetrates the Ordovician, but not the Silurian and the Cenozoic cover. Ordovician sediments have been deformed under anchizone-metamorphic conditions ($\sim$250–300$°$ C, Kley and Reinhard, 1994), corresponding to an overburden of at least 7 km (Kley and Reinhard, 1994). This deformation also led to the formation of the observed low-angle angular unconformity between Ordovician and younger strata ($\sim$10-20$°$, Jacobshagen et al., 2002; Müller et al., 2002).

The Silurian-Devonian sediments, unconformably overlying the Cancañiri Fm., are coarse to medium-sand turbidites and subordinate siltstone of the Llallagua Fm., which grade transitionally into the Uncía Fm. With this unit, the Llallagua Fm. forms a thinning- and fining-

upward succession that was deposited in a proximal shallow-marine environment. Gagnier et al. (1996) interpreted the entire Silurian-Devonian succession (from Llandovery to Famenne) to have been deposited in a large marine 'foreland' basin related to sinistral transpression along Gondwana's western margin (Sempere, 1995). In contrast to the Ordovician, no slaty cleavage exists within the Silurian sediments of the Southern Altiplano.

3.2   Mesozoic

Cretaceous rocks in South Bolivia unconformably overlie the Paleozoic. The thickness of each of the Cretaceous beds, as well as the age of the lowest Cretaceous sediments, decreases southward. Lower Cretaceous rocks are only present in the Potosí area (Miraflores, Eastern Cordillera). There, up to ∼2000 m of Cretaceous red beds were observed (Fiedler, 2001; Ressetar and Alfonso, 1990). Further south, northeast of the Salar de Uyuni (Tambo Tambillo, Chita areas), the Late Cretaceous Aroifilla Fm. (Coniacian-Campanian) marks the basal Cretaceous transgression.

Several marine ingressions were described from the Cretaceous of the Eastern Cordillera in South Bolivia (Fiedler, 2001). The shallow marine, lacustrine, and fluvial sediments of the El Molino Fm. (Maastrichtian/Paleocene) are the only Cretaceous rocks that were deposited in the Southern Altiplano. The El Molino Fm. consists of a thin (1.5–2 m), crossbedded sandstone at the base, overlain by interbedded dark-grey calcareous shale and limestone. The marine limestone of the El Molino Fm. represents a significant marker horizon deposited in a shallow subtidal or intertidal environment, as shown by oolites and stromatolites. This indicates an elevation at around sea level for its entire area of deposition, i.e. the Southern Altiplano and the Eastern Cordillera, at the Cretaceaous/Tertiary transition. The El Molino limestone marks the final marine conditions for the entire plateau area, prior to uplift. All younger sediments are continental (see following sections). In the Southern Altiplano, the thickness of the El Molino Fm. decreases southward from 370 m as drilled in the Colchani well (∼20 km north of Uyuni) down to ∼30 m in Soniquera and Culpina (KUFZ, Ressetar and Alfonso, 1990).

Surface outcrops of El Molino sedimentary rocks in the Southern Altiplano are restricted to the eastern edge of the Altiplano, where they are exposed in several anticlinal cores directly west of the San Vicente Fault Zone, and to one or two small outcrops in the Khenayani-Uyuni Fault Zone, i.e. at the western flank of the Serranía Corregidores and near Culpina, northeast of Cerro Condor Huasi (see Fig. 3.1 and App. F.1).

3.3   Cenozoic

Cenozoic rocks, especially Tertiary sediments and volcanic rocks, record the uplift history of the Altiplano-Puna Plateau. This includes the Eocene/Oligocene transformation of the former foreland basin into a basin with internal drainage, a Middle Miocene episode of very strong magmatic arc activity in the entire Altiplano and the adjacent western parts of the Eastern Cordillera, and widely-distributed syn-tectonic sediments of the Middle/Late Miocene. Subsequently (post 8 Ma ago) the Altiplano was covered by post-tectonic volcanic and volcano-clastic rocks from the Recent magmatic arc of the Western Cordillera (Western Altiplano) or by Quaternary fluvial and lacustrine sediments (Eastern Altiplano).

3.3.1 Paleocene

The Paleocene Santa Lucía Fm. overlies the El Molino Fm. conformably and probably gradually. It consists of monotonous red mudstone with thin beds of sandstone and limestone that were deposited in a distal fluvial environment (Horton et al., 2001). Its thickness in the Southern Altiplano varies between 50 and 90 m (Ressetar and Alfonso, 1990; Welsink et al., 1995). The age of the Santa Lucía Fm. is best defined by magnetostratigraphy and Paleocene mammal fossils in the Eastern Cordillera of Bolivia (Gayet et al., 1991; Marshall et al., 1997; Sempere et al., 1997). The top of the Santa Lucía Fm. is assigned an age of ∼58 Ma (Horton et al., 2001).

The upper part of the Santa Lucía Fm. is a white to yellow, fluvial sandstone. This unit was considered an individual formation in South Bolivia (Cayara Fm.), due to an angular unconformity observed in the Eastern Cordillera (Fiedler, 2001; Marocco et al., 1987). In the Eastern Altiplano, only ∼5 m of Cayara sandstone crop out at the easternmost margin of the Southern Altiplano. In the Central Altiplano, a few metres of Cayara sandstone were observed in the southern part of the KUFZ (Soniquera), but further north, in the San Cristóbal area, this unit is completely missing. There the Santa Lucía Fm. grades into the Potoco Fm. (Silva-González, in prep.).

3.3.2 Eocene/ Oligocene

The Santa Lucía Fm. is overlain conformably by the Potoco Fm., a reddish, mainly pelitic succession with interbedded sandstone and limited evaporites that crops out nearly continuously in the entire Altiplano (from Lake Titicaca in the north to the Southern Altiplano). In the northern and central part of the Altiplano Horton et al. (2001) divide the Potoco Fm. in a lower part with a 20–100 m thick zone of paleosols followed by the 'main body' of the Potoco Fm., which consists of laterally continuous, sheet-like sandstones with interbedded mudstones. Palynological examinations of the upper unit revealed ages between Late Eocene and Oligocene for the fluvial-lacustrine facies association (Horton et al., 2001). Dating of the lowermost paleosol zone was impossible due to the lack of specimens. However, its age can be estimated as between post-mid Paleocene (youngest Santa Lucía age, see section 3.3.1) and pre-Late Eocene (oldest age of the Potoco 'main body', Horton et al., 2001).

In the Central Altiplano the Potoco Fm. is represented mainly by red, thin-bedded to laminated pelites that were deposited in a playa-plain environment (Mertmann et al., 2001). This very fine-grained facies was only observed in the hanging wall of the San Cristóbal Fault and in the core of the Ines Anticline, (Mertmann et al., 2001). In the Eastern Altiplano, near the border to the Eastern Cordillera, the Potoco Fm. forms a thickening- and coarsening-upward succession of pelites interbedded with an upward increasing amount of sandstone (up to 50% sandstone, Mertmann et al., 2001) and partly fine-grained conglomerates in the higher parts of the section. Coarser-grained varieties of the Potoco Fm. are also reported from the western part of the Central Altiplano (near San Agustín) and from the southwestern Altiplano near the Argentine border, where sandstones up to 1000 m thick have been reported (Mertmann et al., 2001). These observations suggest that the southern Central Altiplano was a basin centre in which sediments were shed from three directions (E, W, and S). Furthermore, it seems as if the Southern Altiplano was an almost closed basin already during Eocene/Oligocene times. This interpretation stands in conflict with observations from the northern and central parts of the

Altiplano, where paleocurrent data of the Potoco Fm. show sediment transport consistently towards the east (Horton et al., 2001). The thickness of the Potoco Fm. in the Southern Altiplano amounts to 3000–4000 m. A wind-blown tuff within strongly-dissected Potoco pelites in the footwall of the Corregidores Fault provided an age of 40.4 ± 1.1 Ma (K-Ar, sr99-03, see App. F.1 and Silva-González, in prep.).

The highest parts of the Potoco Fm. in the Southern Altiplano have a Lower Oligocene age as determined by the oldest volcanics of the overlying San Vicente Fm. (29.3 ± 2 Ma, Ar-Ar, ke41-00, see Tables 6.2 and C.1). This contrasts with observations from the northern and central parts of the Altiplano, where the Potoco Fm. was deposited continuously throughout the entire Oligocene, as shown by palynological data by Horton et al. (2001).

3.3.3   Late Oligocene/Miocene

Overlying the Potoco Fm. is an up to 4000 m thick succession of Oligocene to Middle Miocene sedimentary and volcanic rocks of the San Vicente Fm. It conformably overlies the Potoco Fm. or unconformably overlies Paleozoic, Cretaceous and Eocene/Oligocene rocks and is characterised by large lateral variations in thickness and facies (Martínez et al., 1994). This is due to (i) its partial syn-tectonic sedimentation (see section 3.3.3.1) and (ii) the interfingering of volcanic rocks from the magmatic arc with the sediments, which affects especially the western half of the Southern Altiplano. The largest variations in thickness occur between the hanging walls and the footwalls of major thrusts, especially in the KUFZ. In cross-section, the bulk thickness of the San Vicente Fm. in the hanging walls is quite continuous (2050 m the Ines Anticline, 1600 m in the Vilque Well, Welsink et al., 1992). The highest part of the San Vicente Fm. is the up to 1500 m thick Pilkhaua Subsequence which will be described separately in section 3.3.3.1. In the following, I will use name 'San Vicente Fm.' only for the main part of the San Vicente, and not for the overlying Pilkhaua Subsequence.

In the Eastern Altiplano, the San Vicente Fm. can be subdivided into a basal conglomeratic (OMsv1) and an upper volcano-sedimentary part (OMsv2). The thicknesses of both facies are similar. The basal San Vicente Fm. (OMsv1) overlies the Potoco Fm both conformably and unconformably. It consists of basal conglomerates, coarse sandstone, and conglomerates that were deposited in alluvial fan and fluvial systems. The fluvio-lacustrine sandy, and pelitic higher part of the San Vicente Fm. (OMsv2) shows an increasing volcanic influence upsection with interbedded tuffs and volcanoclastites. In the Eastern Altiplano, evaporites are locally interbedded with OMsv2 strata (e.g. Vilque Well, see Fig. 2.2).

In the Central Altiplano the basal conglomeratic facies is missing except for a basal conglomerate of a few decametres (Silva-González, in prep.). Here two different facies can be distinguished: a sedimentary facies (OMs) that is interbedded with a volcanic facies (OMv). These facies are interpreted as lateral equivalents of the OMsv1 and OMsv2 facies of the Eastern Altiplano. According to Welsink et al. (1995), the facies of the Eastern Altiplano interfinger with those of the Central Altiplano. The volume of interbedded volcanics (OMv) increases westward.

The sedimentary OMs is a coarse-grained alluvial fan and fluvial facies above a basal conglomerate. The volcanic part of the San Vicente Fm. of the Central Altiplano (OMv) was termed Julaca Fm. by several authors (west of Río Grande, e.g. Fornani et al., 1993; Martínez et al.,

1994). According to Mertmann et al. (2001), the Julaca Fm. should be considered to be a variation on the San Vicente Fm. and should not be regarded as an independent formation. This mainly volcanic unit consists of ignimbrites, basaltic or andesitic lavas interbedded with conglomerates, sandstones, and pyroclastites. It forms the flanks of the Ines Anticline, the cores of Julaca, Poquera, and San Agustín Anticlines, and also the anticline of the Yazón Peninsula (see Fig. 3.1 and 4.1).

The lower San Vicente conglomerates mainly contain clasts from the neighbouring basement highs (i.e. Silurian rocks in the hanging walls of thrusts [KUFZ; especially in the hanging wall of the San Cristóbal Fault], Ordovician clasts near the Eastern Cordillera), and some 'Potoco' and 'El Molino' clasts.

In some areas, mostly at the western flanks of Paleozoic ridges of the KUFZ, higher OMsv2/OMs strata directly overlie Silurian sediments above an erosional unconformity (see Fig. A.2D). The erosional character of this unconformity is clearly shown by a basal zone (20–50 cm) of in-situ brecciation of the Silurian quartzite, which grades upwards into the 'normal' facies of OMsv2/Oms.

The age of the San Vicente Fm. is well defined by the interbedded volcanic rocks. The oldest intrastratified tuff was found ∼350 m above the onset of the basal conglomerate SE of Cerro (Co.) Paya Punta in the Central Altiplano (Fig. 3.1), and yielded a maximum age of 27.4 ± 0.7 Ma (K-Ar on biotite) (Mertmann et al., 2001). Only an Ar-Ar analysis of amphiboles of a volcanic clast within syn-tectonic sediments of the Pilkhaua Subsequence, described below, gave a slightly older age of 29.3 ± 2 Ma (Central Altiplano, Ar-Ar, ke41-00, see Table C.1 and App. F.1).

The Julaca Lavas of the Central Altiplano are interpreted to be the western equivalent of the Rondal Lavas east of San Pablo de Lípez (22.9 ± 0.9 Ma and 23.5 Ma [K-Ar, Kussmaul et al., 1975] ; 21 ± 0.6 and 18 ± 0.5 Ma [K-Ar, Bonhomme in Fornani et al., 1989; 1993]) and also equivalent to the basalts of Tambillo (K-Ar 22 Ma [Evernden et al., 1966; 1977]; 23.1 and 25.2 Ma [Hoke et al., 1993], and 27.4 Ma [Soler et al., 1993]. The Rondal and Julaca Lavas mark an episode of very strong magmatic activity, which affected the entire southern and southwestern Altiplano at the end of the OMsv2 Subsequence (Fornani et al., 1989). In the Eastern Altiplano, the 'Toba 22' in the Vilque area is the base of the OMsv2 and is regarded as a distal part of this Oligocene-Miocene magmatic event. The oldest syn-tectonic sediments, overlying the OMs and OMv Subsequences, have ages between 17.1 ± 0.6 Ma (Ar-Ar, ke24-00, Table C.1) in the Western Altiplano (Yazón Peninsula) to 15.8 ± 1.2 Ma (Ar-Ar, ke01-00, Table C.1) in the bivergent thrust-system of the Central Altiplano.

In the Eastern Altiplano, near the border to the Eastern Cordillera, the oldest age of the San Vicente Fm. is slightly younger than of that in the Central Altiplano (25.3 ± 1 Ma, K-Ar, an14-2000, see App. F.1 and Silva-González, in prep.). The 'Toba 22' (∼22 Ma) marks the onset of the OMsv2 Subsequence (Martínez et al., 1994). The youngest available ages of the San Vicente Fm. in the Eastern Altiplano are from the middle part of the OMsv2 Subsequence (18.2 ± 0.5 and 17.8 ± 0.5 Ma, K-Ar maximum age, ke10-99 and ke06-99, see Table C.1 and App. F.2). The oldest ages of the overlying units near the edge of the Eastern Cordillera are between 16.8 ± 0.3 Ma and 17.2 ± 0.3 Ma (K-Ar, biotite, Grant et al., 1979). Consequently, I estimate the deposition of the youngest part of the OMsv2 Subsequence not to be younger than 17–16 Ma.

Magmatic arc activity of the Western Cordillera started roughly with the beginning of the Miocene. Wörner et al. (2000b) described several volcanic intervals. The oldest stratovolcanoes, east of the Western Cordillera, which directly overlie Lower Miocene ignimbrites, have

Miocene ages (20.3–9 Ma, see Wörner et al., 2000a). These are overlain by the Miocene to Pleistocene arc system of the Western Cordillera. Volcanic rocks in the Central Altiplano, which were deposited synchronously with compressional tectonics (see section 3.3.3.1), mainly have ages between 9 and 18 Ma (own data and Baker and Francis, 1978; Castaños and Saavedra, 1979; Fornani et al., 1993; Grant et al., 1979; Kussmaul et al., 1975).

3.3.3.1   Miocene syn-tectonic sediments

The highest part of the San Vicente Fm., here named Pilkhaua Subsequence, was deposited in small piggy-back or thrust-front basins that are syn-tectonic with respect to the youngest deformation increment. Such basins are common throughout the entire Altiplano. Nearly every syncline has Pilkhaua sediments in its core, while older strata crop out in the anticlines. In some parts, especially in the footwalls of the Khenayani-Uyuni Fault Zone, the facies of the syn-tectonic sediments does not differ significantly from that of the 'pre-tectonic' facies of the OMs (i.e. well-stratified, medium- to coarse-grained sandstones, e.g. Fig. A.1A). In most parts of the Western and Central Altiplano however, the syn-tectonic sediments have a different facies, which led me to split the Pilkhaua Subsequence from the San Vicente Fm. *sensu stricto*. The Pilkhaua Subsequence is not equivalent to a stratigraphic unit because it is the result of a tectonic and not a depositional period (see Figs. A.1D and A.4B–C).

I first recognised the Pilkhaua Subsequence at the Yazón Peninsula where is forms the western syncline (details about the structural style will be discussed in section 4.3 and Fig. 4.3). Lithologically the syn-tectonic sediments are texturally and mineralogically immature, poorly lithified sandstones that experienced very little compaction. Their thickness varies across the Southern Altiplano. I interpreted them as a very proximal facies. The stratification is weak in the lower parts and almost absent in the upper parts (see Figs. A.1D and A.4E). The syn-tectonic character is shown by a strong increase of bank thickness with increasing distance from the source area and by wedge-shaped sediment bodies (see Figs. 7.12 and A.1D). The poor cementation and weak to absent stratification makes the Pilkhaua Subsequence clearly distinguishable from the underlying well-stratified, well-lithified, 'pre-tectonic' part of the upper San Vicente Fm. (Fig. A.1A).

The age of deformation can be dated by small tuffs and ignimbrites within the basal parts of most of the syn-tectonic, thrust-front or piggy-back basins. Although volcanic layers were not found in the upper parts of the basin fill, volcanically-derived minerals, i.e. biotite, are abundant within the sediments. This may indicate short transport distances of eroded volcanics and unconsolidated sediments and their rapid re-deposition during the compressional tectonics that led to the formation of the basin.

Lahars locally occur in the Pilkhaua Subsequence in the Eastern Altiplano (east of the Vilque Anticline). They consist of poorly stratified, unconsolidated sediments with pumice fragments up to 20 cm in diametre (Fig. A.1C). The provenance of these volcanics are presumably volcanic centres near the border between the Southern Altiplano and the Eastern Cordillera (e.g. Chocaya, Minas Animas, etc.) which have ages between 17.2 ± 0.3 Ma and 12.5 ± 0.2 Ma (Grant et al., 1979).

In the Central and Western Altiplano, the ages of the Pilkhaua Subsequence range between 17.1 ± 1.1 Ma and 7.6 ± 0.9 Ma (Ar-Ar, samples ke24-00 and ke39-00 respectively, see Table C.1 and App. F.2).

3.3.4 Pliocene to Recent

In the western part of the Southern Altiplano, syn-tectonic sediments are conformably and unconformably overlain by volcanic rocks (lavas and ignimbrites) from the Miocene to Pliocene arc system with ages between 10.5 and ~3 Ma (Wörner et al., 2000b), and also from some volcanic centres in the Southern Altiplano (e.g. San Cristóbal Volcano with a K-Ar age of 11 ± 0.5 Ma of the basal lavas, sr99-10, see App. F.1). Volcanic rocks from the active chain of stratovolcanoes are mainly younger than 0.9 Ma (Wörner et al., 2000b).

With exception of the Pleistocene lacustrine deposits, post-tectonic sediments are not well developed on the Southern Altiplano. This may be related to the end of deformation of the Altiplano about ~11–8 Ma ago and also with the desertification of the Central Andes that started ~15 Ma ago (Alpers and Brimhall, 1988; Gregory-Wodzicki, 2000). The latter resulted in a strong decrease in erosion rates and could explain the very thin cover of post-tectonic sediments.

The Pleistocene was characterised by wetter climate, which led to repeated coverage of the Altiplano by several extensive paleolakes (e.g. Tauca and Minchin Lakes, see Argollo and Mourguiart, 2000; Bills et al., 1994; Fornari et al., 2001). Climatic changes from humid tropical conditions with short dry events during the Interglacials to cooler drier conditions during the Glacials are marked by several lake-level high-stands and drying-out periods in the higher Paleocene (Argollo and Mourguiart, 2000). The large salars of the Southern Altiplano (Salars de Uyuni and Coipasa) and also Lake Popóo further north are the remnants of Pocuyo Paleolake that covered almost the entire Southern Altiplano, extending southward to the Lípez High. In the Southern Altiplano, the alternation of lacustrine episodes and dry periods is expressed in several mud-beds interbedded with salt crusts. New results from a 121 m long sediment core of the Salar de Uyuni show that the mud consists mainly of calcium carbonate, gypsum, and volcanic detritus. The salt crusts are mainly halite with minor amounts of gypsum (Fornari et al., 2001). In the Salar de Uyuni, the thickness of the mud layers increases up-section, indicating an increase of duration and extension of lacustrine events during the Pleistocene (Fornari et al., 2001). This is in contrast to the northern part of the Altiplano where paleolake levels consistently decrease from oldest known. This was interpreted as indication that the formation of paleolakes in the Southern Altiplano was at least partly controlled by the overflow of the northern Titicaca Basin, and not only by the local paleoclimatic evolution (Fornari et al., 2001). The former highstands of the lake are still marked by horizontal 'bands' of algal bioherms at different altitudes throughout the working area (Fig. A.1B).

Today the Altiplano is an internally-drained basin, characterised by extremely low relief. The central part of the Southern Altiplano is covered by two giant salt pans, the Salars de Uyuni (10000 km^2) and Coipasa (2500 km^2), that are located at an altitude of ~3650 m and 3700 m, respectively. Quaternary siliciclastic sediments include interfingering alluvial and fluvial deposits, which correlate with topographic relief. Fluvial sediments are strongly related to seasonal rainfall.

Chapter 4

Structures

The main structural elements are folds that are always associated with thrusts. Folds range in type and size from regional open folds with up to 30 kilometre wavelength to small, outcrop-scale, open to tight folds (below 1 m wavelength) in or around major thrust zones. Thrusts are shallowly to steeply inclined, east- or west-verging and merge into sub-horizontal detachments within Paleozoic sediments (Silurian to Upper Ordovician, see section 3.1).

Regional folds are upright, nearly cylindrical, with fold axes plunging less than 5° N or S (see Fig. 4.1). Only the fold axis of the north-eastern part of the working area plunges 7° towards the south (upper-right stereonet in Fig. 4.1). Surface and map observations as well as N–S directed seismic profiles show gentle culminations of fold axes along trend. The sub-horizontal fold axes, shown in the stereonets of Fig. 4.1, are therefore regarded as average values of several N and S-plunging fold axes.

Sedimentary-thickness changes in the limbs of folds are due to syn-tectonic sedimentation. Smaller-scale folds are mostly symmetrical and show neither forelimb nor backlimb thickening or thinning (i.e. parallel folds, see Fig. A.3). This is also the case for those folds, imaged in the seismic data, where this could be determined (e.g. the Vilque Anticline, App. F.2). The formation of parallel folds, in combination with the abundant presence of well-developed slickensides on the bedding planes, indicates that these folds are flexural-slip folds ("parallel folds produced by slip of layers over each other", McClay, 2000, p. 55). Furthermore, the observation that most of these slickensides are oriented perpendicular to horizontal fold axes shows that the displacement vector was mostly dip-slip, i.e. perpendicular to the trend of the fold axes. These observations are relevant for selecting the adequate restoration algorithm for the cross-section balancing (cf. chapter 9).

Apart from folding, most of the deformation is recorded by NNE–SSW trending reverse faults. Strike-slip faults are of minor importance. Important extensional structures are not observed on the Southern Altiplano, except for small-scale structures, as striated faults, which usually show displacements of a few decimetres to a few meters (e.g. Fig. A.2A).

Analysis of seismic sections, large-scale structures (folds and thrust faults), and stratigraphy led to the division of the main working area (see Fig. 2.1 for location) into two tectono-stratigraphic domains: the Eastern and the Central Altiplano. They are divided by the Tertiary/Quaternary Lípez Basin, which itself is also part of the Eastern Altiplano (Fig. 4.1). The Eastern Altiplano is interpreted as the westernmost part of the Eastern Cordillera's west-vergent, thin-skinned
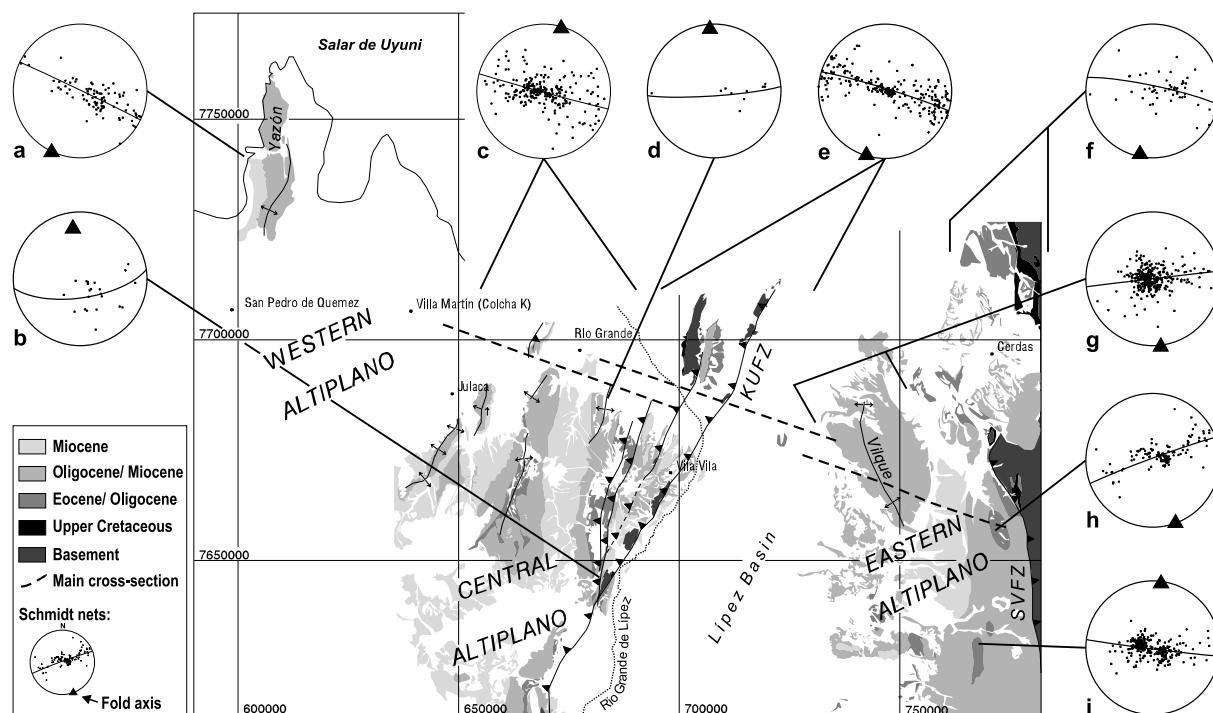
Figure 4.1: Regional fold axes (lower-hemisphere, equal-area stereonet projection) of the main working area. Generalised geological map (modified after YPFB) of pre-Quaternary units of the working area as background. KUFZ = Khenayani-Uyuni Fault Zone, SVFZ = San Vicente Fault Zone. See text for explanation.

part of the bivergent thrust system. The Central Altiplano forms a bivergent thrust system independent of the Eastern Cordillera. Its east-vergent part comprises the N–S to NNE–SSW trending Khenayani-Uyuni Fault Zone, the most important thrust system of the Southern Altiplano. The structural grain of the Central Altiplano domain is characterised by NNE–SSW trending structures, whereas the easternmost Altiplano shows the 'typical' N–S trend of the Eastern Cordillera (Fig. 4.1).

The Western Altiplano lies to the west of the main working area, i.e. west of the area covered by the geological map (App. F.1). Late Miocene to Pliocene sediments and volcanic rocks are exposed over the entire Western Altiplano except for the Yazón Peninsula in the Salar de Uyuni (~68° W), where folded strata of the San Vicente Fm. crop out (Fig. 4.1).

4.1   Eastern Altiplano

The morphological border between the Southern Altiplano and the Eastern Cordillera is marked by the transition from the Cenozoic and Cretaceous fill of the Lípez Basin to Paleozoic rocks of the Eastern Cordillera, and by a rapid increase in altitude, from ~3800 m on the Southern Altiplano to more than 5000 m in the Eastern Cordillera, within a horizontal distance of ~20 km.

The Eastern Altiplano is the westernmost part of the bivergent thrust system of the Eastern Cordillera. It is characterised by west-vergent, thin-skinned structures and gently-dipping or flat-lying sediments. Faults are shallow to moderately-dipping, resulting in widely-spaced ramp anticlines with blind thrusts (Fig. 4.1 and App. F.1).

The San Vicente Fault is the westernmost emergent thrust of the west-vergent thrust system. Folded Ordovician metasediments were thrust upon mostly Cenozoic sediments of the Lípez Basin. The footwall is characterised either by west-vergent thrust-front synclines with steep eastern limb, exposing Cretaceous to Eocene strata, or by footwall anticlines. Locally, hanging-wall anticlines are developed (e.g. NNE of Cerdas, see App. F.1).

The surface expression of several west-vergent blind thrusts in the Eastern Altiplano are widely-spaced ramp-detachment folds or hanging-wall folds with interlimb-angles of 140–160° and an average wavelength of 20–30 km. The spacing of anticlines and the age of the strata involved in the folding decreases westward: Paleozoic and Cretaceous rocks crop out in the core of some anticlines near the border between the Southern Altiplano and the Eastern Cordillera. In the core of the Vilque Anticline, only higher San Vicente strata (OMsv2) are present. The buried deformation front of the Eastern Cordillera's west-vergent thrust system, as interpreted in seismic profile 10007 (see section 2.1 for location), lies ∼50 km east of the San Vicente Fault Zone in the Eastern Altiplano (see App. F.1 and F.2). West of this, the fill of the Lípez Basin is undeformed.

Fold axes trend parallel to the contact between the Ordovician and the Cenozoic, i.e. lie parallel to the San Vicente Fault. They have a N–S to NNW–SSE trend, and slightly plunge ($< 4°$) in both directions (see Fig. 4.1).

The balanced profile crosses two anticlines in the Eastern Altiplano: the Eastern Anticline, cored by Eocene/Oligocene sediments (Potoco Fm.), and the Vilque Anticline further west (see Fig. 4.1 and App. F.1). The open syncline between these anticlines developed as a piggy-back basin on top of the west-vergent Vilque Ramp Fault and also forms the thrust-front basin of the Eastern Anticline. The basin is filled with Miocene syn-tectonic sediments of the Pilkhaua Subsequence (see section 3.3.3.1). Post-Miocene salt movements were responsible for the formation of subordinate N–S directed normal faults that have been detected in field and in the seismic lines (App. F.2).

In the Eastern Altiplano, seismic interpretation was the main tool for the structural interpretation because of the gently-dipping strata that is continuously imaged in the seismic data. Line-to-line correlation was possible. The Vilque Well provides stratigraphic control (Fig. 2.2). The analysis of reflection-seismic sections is subject of chapter 7.

4.2   Central Altiplano

The Central Altiplano structure is formed by a bivergent thrust system. The east-vergent part is represented by the Khenayani-Uyuni Fault Zone, the most important structural element of the Southern Altiplano. It is characterised by a splay of four major, N–S to NNE–SSW trending, emergent thrusts along which Paleozoic to Oligocene sediments were displaced eastward over the Cenozoic fill of the Lípez Basin. Surface observations show that there is folded, faulted, and uplifted Ordovician and Silurian/Devonian basement with a few Mesozoic relics, and a

reduced and incomplete Cenozoic cover in the hanging wall. The footwall is characterised by open to close thrust-front synclines with steep, partly overturned western limbs and up to 2 km long, gently-dipping eastern limbs (e.g. Fig. 2.3 and A.3A). Thrust displacement is difficult to assess because of complete erosion of hanging-wall cutoffs.

Four major faults can be distinguished. The age of the basal units in the hanging walls decreases westward. The NNE–SSW trending Khenayani-Uyuni Fault *sensu stricto* is the easternmost thrust of the KUFZ and the western border of the Lípez Basin. The thrust is mostly buried beneath Quaternary sediments, but crops out on the north-eastern flank of Cerro Khala Huasi, SSE of San Cristóbal, where it consists of a 20–30° westward-dipping cataclasite zone of several metres width. In the hanging wall is a folded Silurian quartzite. The steep to overturned eastern limb of the thrust-front basin consists of volcano-sedimentary series of the higher OMsv2/OMs Subsequences at the base, overlain by Middle/Late Miocene Pilkhaua sediments (see Fig. A.3A and App. F.1). At the surface, the Silurian to Ordovician strata of the Cerro Khala Huasi form a fault-dissected hanging-wall anticline that is possibly connected to a west-vergent back thrust of the Khenayani-Uyuni Fault (cf. App. F.1). Neither the back thrust nor the hanging-wall anticline could be resolved from the seismic data. This may indicate that the west-vergent back-thrust is only a small-scale phenomenon and not a major structural feature.

The next thrust towards the west is the NNE–SSW trending Corregidores Fault. It is best preserved in the Serranía Corregidores where it dips 30–40° westward. Similar to the Khenayani-Uyuni Fault, it has folded Silurian strata in the hanging wall. The footwall east of the Serranía Corregidores consists of intensely-folded pelites of the Potoco Fm., which are unconformably overlain by weakly eastward-dipping upper San Vicente sediments (OMs, see Fig. 2.3 and App. F.1).

The San Cristóbal Fault lies west of the Corregidores Fault. The centre of the San Cristóbal volcanic complex lies close to the fault (see Fig. A.3B). The base of the Eocene/Oligocene Potoco Fm., with few metres of underlying pre-Potoco strata (Silva-González, in prep.), forms the vertically-dipping strata of the hanging wall. The footwall is formed by a syn-tectonic basin of higher San Vicente sediments (OMs). Its diverging strata are vertically inclined near the thrust but lie nearly horizontal 1000–1500 m east (see Fig. A.3C). The almost N–S trending, vertically-inclined thrust itself is characterised by a 1–2 m wide fault gouge and strongly-folded pelites of the Potoco Fm. (see Fig. A.3D, E). Most of these subordinate folds have sub-horizontal fold axes that plunge $< 20°$ NNE/SSW or NNW/SSE, i.e. parallel to sub-parallel to the strike of the thrust plane (cf. Fig. 4.2). Fold types range from close kink folds to open folds (see Fig. A.3D, E) and have an amplitude of several decimetres to few metres, depending on lithology (sandstone-, siltstone-, or pelite-dominated). The angle between the flat-lying fold axes and the trend of the thrust are within the 'normal' distribution assuming dip-slip movement. Higher strain would probably rotate all fold axes into parallelism to the fault direction.

In the hanging wall of the San Cristóbal Fault is an up to 3500 m thick succession of westward younging, vertically inclined, in places overturned pelites with interbedded sand- and siltstones of the Potoco Fm. (Fig. A.3B). This is followed by a steep (~85° eastward-dipping), slightly overturned, east-vergent Intra-Potoco Thrust. It is characterised by the ~100 m wide zone of east-vergent folds with weakly northward-plunging fold axes ($< 20°$), within the still vertically-inclined Potoco strata younging towards the west. The concordant transition of Potoco pelites to the basal conglomerate of the San Vicente Fm. lies ~1.5 km further west (see App. F.1 and F.2).
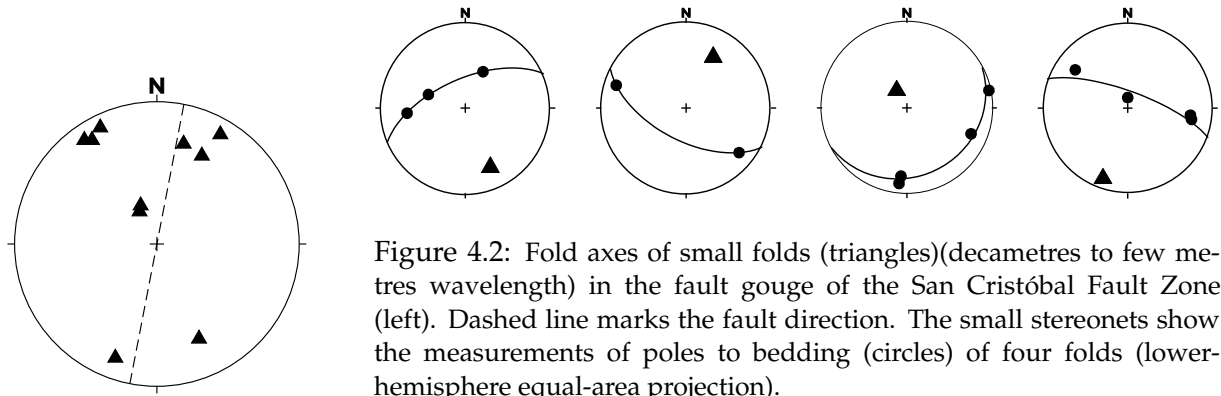
Figure 4.2: Fold axes of small folds (triangles)(decametres to few metres wavelength) in the fault gouge of the San Cristóbal Fault Zone (left). Dashed line marks the fault direction. The small stereonets show the measurements of poles to bedding (circles) of four folds (lower-hemisphere equal-area projection).

West of a narrow syncline of San Vicente strata is an upright, symmetrical detachment-fold with horizontal fold axis (Cerro Paya Punta, see Schmidt net d in Fig. 4.1 and Fig. 3.1 for location). The anticline of Co. Paya Punta, i.e. the Central Anticline, is the centre of the bivergent thrust system of the Central Altiplano and the transition between the east-vergent and the west-vergent structures (see App. F.2).

In the western part of the Central Altiplano's bivergent thrust system, west-vergent fault-propagation folds with 6–10 km wavelength and blind thrusts are the dominant structures. The asymmetrical folds have associated, small thrust-front basins. Fold vergence increases westward, as indicated by westward decrease in dip of the axial planes (Ines Anticline 26°, Yazón Anticline 38°, see Fig. 4.3 and App. F.2). The westward decrease of age in the anticlinal-core strata indicates westward decreasing deformation. The synclines are filled with syn-tectonic growth strata of the Pilkhaua Subsequence. The hanging-wall cutoffs permit the quantification of thrust displacement and detachment depth, which is essential for the construction of the balanced cross-section that will be discussed in chapter 9.

An exception to the observation of westward-decreasing age of strata involved in the structures is the Cerro Allka Orkho (see Fig. 3.1). It is formed by two parallel, elongated ridges that form an island in the Salar de Uyuni. The structural trend varies from N–S in the southern part to NNE–SSW in the north. This is the only place on the Southern Altiplano west of the Serranía Corregidores, where Paleozoic basement crops out at surface, (see Fig. 3.1 for location). Weakly-metamorphic Paleozoic basement, on the western ridge of the island, was thrust westward upon Neogene sediments. The eastern ridge is built up of shallow eastward-dipping upper San Vicente sediments that contain volcanic clasts up to 1 m in size and unconformably overlie the basement (see App. F.1).

The Salar de Uyuni is not only a large salt pan, but also a structural depression. Fold axes, faults, etc. of the Central Altiplano plunge weakly northward underneath the Salar. South of the Salar, geological outcrops allow insight into southward-progressively deeper structural levels.

4.3 Western Altiplano (Yazón Peninsula)

West of the Poquera Anticline, no Tertiary strata crop-out with the exception of the Yazón Peninsula, ca. 60–70 km NW of Julaca (see Figs. 3.1 and 4.1 for location). The lack of outcrop in the Western Altiplano is due to the widespread coverage by lava flows and ignimbrites related to the Miocene to Recent magmatic arc activity of the Western Cordillera.
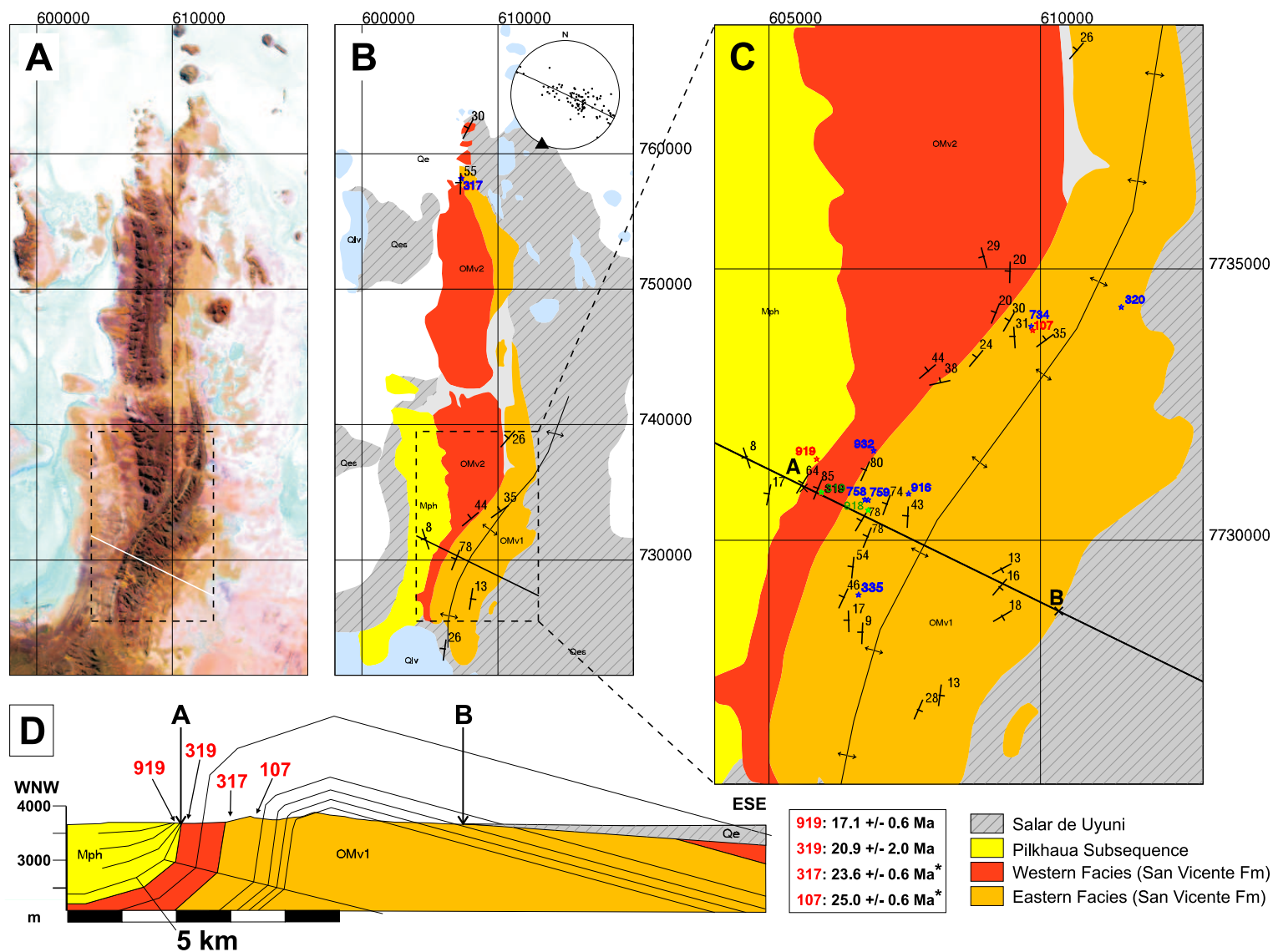
Figure 4.3: Geological map of the Yazón Peninsula with different colours for the 'Eastern' and 'Western' facies. **A:** Satellite image, **B:** Geological overview with stereonet of poles to bedding and fold axis (triangle). **C:** close-up of the southern part with profile-line and database. D: Cross-section of the southern part with isotopic ages and legend. *: K-Ar age = maximum age. See App. F.1 for detailed legend.

Morphologically, the Yazón Peninsula is characterised by two parallel, N–S trending ridges of San Vicente strata that form a peninsula into the Salar de Uyuni. The structure of the Yazón Peninsula is a west vergent, fault-propagation fold with a long back-limb, and a short, vertically-dipping to overturned forelimb in the southern part of the peninsula. The sub-horizontal fold axis has a NNE–SSW trend (Fig. 4.3B). The blind thrust is probably located beneath the syn-tectonic basin to the west. The structurally most interesting feature of the Yazón Peninsula is a structural bend in the southern part of the peninsula that leads to an east-ward displacement of the eastern ridge by ∼6 km. There the N–S strike of the structure changes for about 10 km to strike NNE–SSW, parallel to the fold axis (see Fig. 4.3A and B).

The lithology of the San Vicente Fm. of the Yazón Peninsula (dated at maximal 25–21 Ma, see Fig. 4.3D) is composed of sedimentary rocks of predominantly volcanic provenance and vol-canic rocks (lavas and tuffs, see section 3.3.3). Two facies could be distinguished. The 'Eastern Facies' (Fig. A.4A) consists of red, green or white tuffs and tuffaceous sandstones or conglom-erates, and is overlain by the 'Western Facies' which consists of lava flows, conglomerates with mainly volcanic clasts, and some tuffs in the higher parts.

The 'Eastern Facies' is dominant in the southern part of the peninsula where it forms the core of the west-vergent, fault-propagation fold (Fig. 4.3D). North of the structural bend it continues in the eastern ridge that is part of the westward-dipping forelimb. North of the bend, the eastern fold limb is buried beneath the Salar de Uyuni (see Figs. 4.3A and B).

The northern part of the peninsula is dominated by the 'Western Facies'. In contrast to the vertically-dipping strata of the forelimb in the south, the beds of the northern part dip shal-lowly westward (∼30° average dip angle, see Fig. 4.3B). In addition to the smaller dip angle north of the bend, a southward decrease of stratigraphic thickness accounts for the narrowing of the 'Western Facies' in map view close to the structural bend and south of it. In the south, the highly-condensed strata of the 'Western Facies' are mostly buried beneath Recent alluvial sediments, but crop out in dry river channels.

The fault-propagation fold is associated with a thrust-front basin filled with unconsolidated syn-tectonic sediments of the Pilkhaua Subsequence with growth strata. In the lower parts of the syn-tectonic sediments, weak stratification is developed that is nearly absent in the upper parts (Fig. A.4).

4.4 Kinematic analysis

Small-scale structures are mainly formed together with regional structures (Wilson and Cos-grove, 1982, p. 18ff). The kinematic analysis of the former allows the reconstruction of the kinematic regime of a region.

The kinematic analysis was carried out with the software programme 'StereoNett' of Duyster (2000). Fault planes and lineations were plotted after the convention of Hoeppener (1955). The arrows point away from the extension axis and to the compression axis. The principal kinematic axes were determined from the pattern of arrows in the Schmidt net. StereoNett calculates the main kinematic axes ($\sigma_1, \sigma_2, \sigma_3$) using the P/T-method of Turner (1953). This simple method is based on the assumption that fractures are always oriented parallel to σ_2 and form an angle of 30° to σ_1. This assumption is only valid in homogeneous, unfractured rocks,

but can also be used to approximate the principal kinematic axes in anisotropic rocks — such as from the Southern Altiplano.

Small, striated faults with slickensides or slickenfibres are rare on the Southern Altiplano because of the poor consolidation of sediments. This is the reason for the rather small database in a large region (47 data points in an area of ∼200 km width). Striated faults were measured in Silurian quartzites (3 values), El Molino and Chaunaca sediments (14 values), Potoco pelites (4 values), San Vicente sediments (including Pilkhaua Subsequence, 24 values) and post-tectonic sediments (2 values). Fig. 4.4 shows the spatial distribution of measured striated faults and Hoeppener diagrams of the data from each outcrop. The measured data, their UTM co-ordinates and descriptions are given in Appendix B (Tables B.3 and B.4). The aim of the kinematic analysis was not the precise determination of the regional paleostress field, but to assess the main kinematic axes of the particle displacement field, which is necessary to estimate out-of-section mass transfer of the balanced cross-section.

The kinematic data of a region with a two-stage deformation system (I will discuss this in chapter 8), such as the Southern Altiplano, should then show the following: Subordinate faults within sediments that are older than or syn-tectonic to the first deformation increment could have formed during both deformation increments and also after. Younger sediments that were deposited between the first and the second tectonic increment and sediments syn-tectonic to the younger increment would only be affected by the younger tectonic event. Fault striation data within post-tectonic sediments should image only the post-tectonic kinematic conditions. Following this hypothesis for the Southern Altiplano, I would expect the following: Paleozoic, El Molino, and Potoco sediments were deposited prior to the first, Oligocene, compressional increment. The San Vicente Fm. was deposited between the first and the second deformation increment (OMsv1, OMsv2, OMs, OMv) or was syn-tectonic to the second, Miocene deformation (Pilkhaua Subsequence). Pliocene to Recent sediments and volcanics are post-tectonic. The derivation of deformation ages on the Southern Altiplano will be discussed in chapter 8 and section 7.3.

Fig. 4.5A shows a synopsis of all data points. Values from the Eastern (right) and the Central Altiplano (left) were interpreted separately because they belong to different structural domains (see introduction of this chapter). For both structural domains the distribution of Hoeppener arrows suggests the data separation in three different populations (see Fig. 4.5B). The comparison of Hoeppener-Diagrams from the Central and Eastern Altiplano shows that the calculated principal kinematic axes for the three populations do not differ between the Eastern and the Central Altiplano. Consequently, the division of the Southern Altiplano in two different structural domains is not required for the kinematic data.

Furthermore, one major observation of the fault-striation data (Fig. 4.5) is that in each of the three population none of the principal kinematic axes is parallel to the major structural trend of the Eastern (N–S, see section 4.1) or the Central Altiplano (NNE-SSW, see section 4.2). Population 1 shows NW–SE directed extension with a vertical σ_1 and horizontal σ_2 and σ_3 axes. Population 2 is characterised by NW–SE compression with steep or vertical σ_3 and horizontal σ_1 and σ_2. Population 3 represents a strike-slip system with horizontal σ_1 in NE- and σ_3 in NW direction, and a steep σ_2 (Fig. 4.5B).

Note that Population 3 consists only of faults in pre-San Vicente strata, while Populations 1 and 2 have data points from all ages. Following the hypothesis mentioned above, the complete absence of young values, i.e. post-Potoco Fm., in Population 3 suggests that they represent an
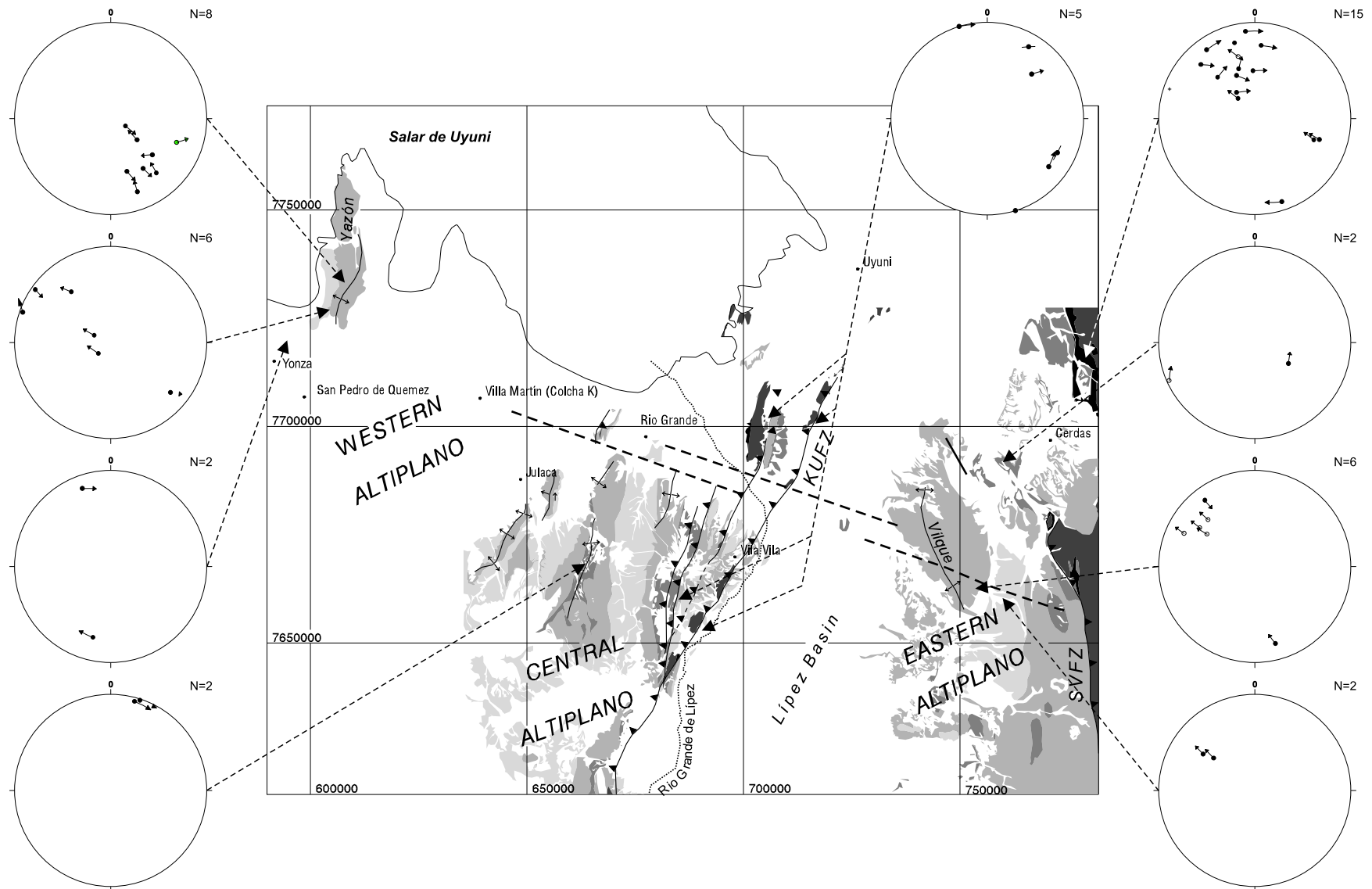
Figure 4.4: Fault planes and lineations of the Southern Altiplano plotted after the convention of Hoeppener (1955). These are lower hemisphere, equal area, stereonet projections. The common great circle between the pole of the fault plane and the slip linear is drawn in the area around the pole point of the fault plane. The arrow indicates the slip of the hanging wall. Where no slip direction could be determined, no arrow is drawn. See Fig. 4.1 for legend of geological units.
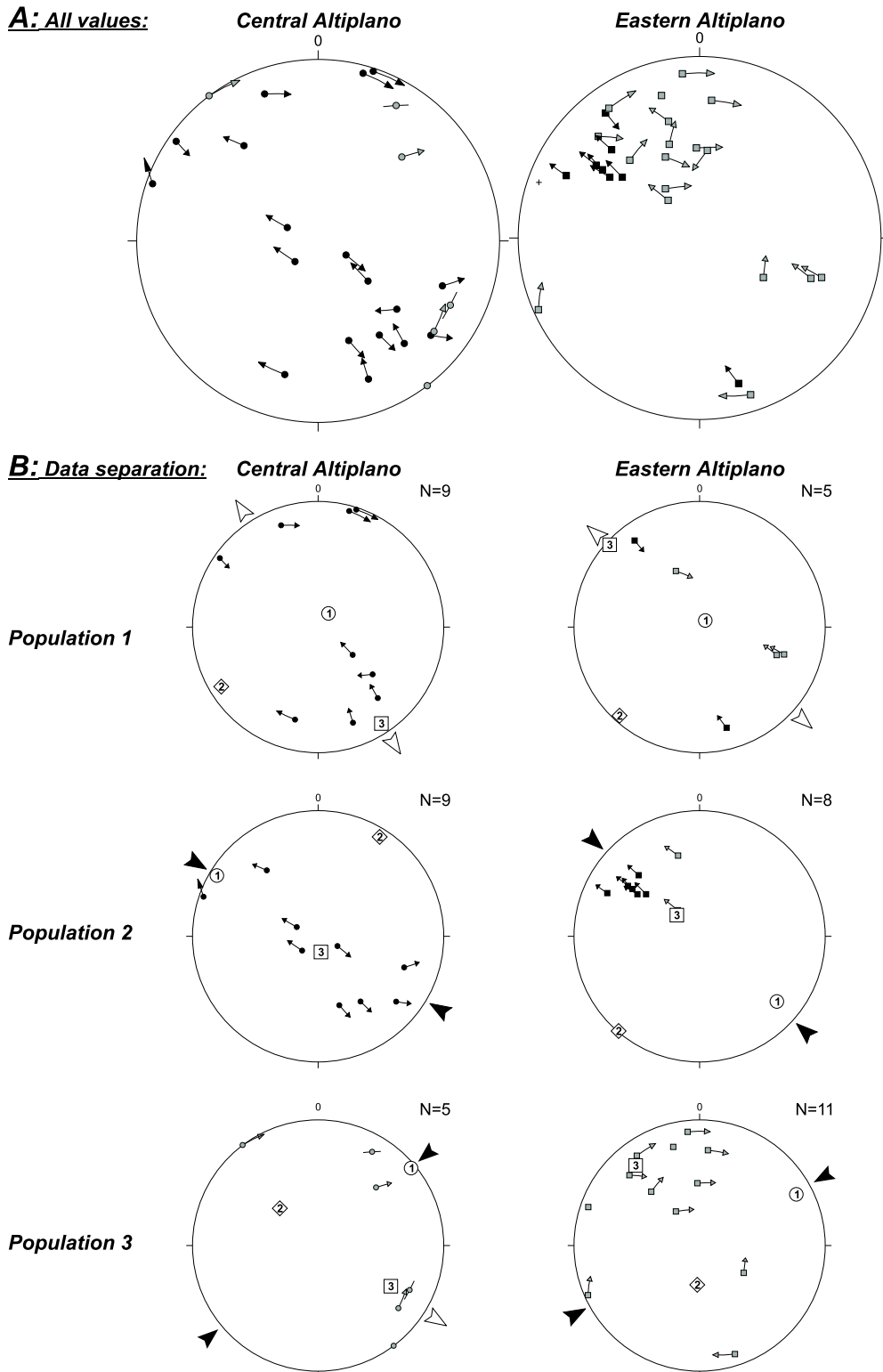
Figure 4.5: **A:** Slip-movement directions of the Southern Altiplano (all values) after Hoeppener (1955). Circles represent faults from the Central Altiplano (left), squares from the Eastern Altiplano (right). Black data points represent San Vicente and post-San Vicente strata (Middle Oligocene to Recent), light-grey points indicate pre-San Vicente strata (Silurian to Eocene). 1, 2, and 3 are the principal kinematic axes (σ_1, σ_2, σ_3) after Turner (1953). **B:** Separation of the data into three populations. See text for explanation.

older deformation increment (Oligocene deformation). This is consistent with the observation that Populations 1 and 2 have data points from all stratigraphic units (pre and post-San Vicente Fm.).

Populations 1 and 2 were both collected from higher San Vicente and younger, post-tectonic, sediments. They represent two contrasting populations, i.e. NW–SE directed extension and NW–SE directed compression. There is no difference between the two post-tectonic samples and the others (see second-lower left Hoeppener Diagram of Fig. 4.4). Both populations usually occur within the same outcrop, i.e. they were formed coevally (e.g. Hoeppener Diagrams from the Yazón Peninsula [upper left and below], Fig. 4.4). To explain this, several scenarios are possible: In some cases, the rotation of the strata back into the horizontal could transform a normal into a reverse fault (i.e. passive rotation of faults during a later deformation increment) — but this is not the case here. A second possible explanation for the co-existence of these two populations could be the structural position: If all normal faults were located in anticlinal hinges and the reverse faults at the flanks of folds, they could have been formed synchronously. This is also not the case. The structural position is not related to the formation of normal or reverse faults. Furthermore, the exchange of σ_1 and σ_3 could be explained by compression and relaxation during a seismic cycle (Wang, 2000) or by strain partitioning during orogen-parallel extension (Riller and Oncken, 2003; Riller et al., 1999).

The compressional axes σ_1 of the Population 3 (strike-slip regime) is sub-parallel to the convergence vector of the Nazca plate until $\sim$28 Ma ago (38-39° dextral oblique to the normal of the trench; Somoza, 1998). An early strike-slip component could possibly explain the apparent paradox of the tectonic map of the Central Altiplano: It resembles a positive flower structure which was commonly attributed to transpressional regimes, but no strike-slip faults have been mapped. It may be possible that a strike-slip component was more important during the first, Oligocene, deformation increment and less so during the Miocene.

Even though this interpretation may be plausible, it should be kept in mind that it is based on only 47 measurements. This number is far to small to be a 'hard' database or representative, especially regarding the large working area. Hence, there is a high potential for errors due to irregular sampling (availability of outcrops) or aliasing effects. On the other hand, the data separation in three populations is independent of the data source. The populations are similar in the entire area — from the Yazón Peninsula in the west to the eastern edge of the Southern Altiplano. Especially Population 2 is composed of fault measurements from the Yazón Peninsula (all black values, except two), the westernmost Tertiary outcrop of the Southern Altiplano, and folded Late Cretaceous (El Molino) sediments from the easternmost edge of the Southern Altiplano (grey values). Population 1 consists of the broadest range of sample points (Yazón, Yonza, Ines Anticline, Eastern Altiplano, see Fig. 4.4), and Population 3 is partly from the Khenayani-Uyuni Fault Zone (five values, left diagram, Fig. 4.5) and partly from the region near the border to the Eastern Cordillera (eleven values, right diagram, Fig. 4.5). The determination of the principal stress axes is very consistent throughout these three populations. Adding or removing different groups of values, e.g. from different outcrops, did not change the position of the principal axes significantly.

4.5   Strike-slip movements

Many authors assigned a major strike-slip component to the Khenayani-Uyuni Fault Zone (e.g.
Mertmann et al., 2001; Müller et al., 2002; Sempere, 1994; Sempere et al., 1997; Welsink et
al., 1995). Map analysis also suggests the interpretation of the bivergent thrust system of the
Central Altiplano to be a positive flower structure, i.e. the result of a transpressional tectonic
regime. Indications of major strike-slip displacements, however, were not found on the South-
ern Altiplano. The larger thrusts of the Khenayani-Uyuni Fault Zone in particular show mostly
dip-slip movements (e.g. horizontal fold axes of subordinate folds [Fig. 4.2] or slickensides indi-
cating dip-slip).

Nevertheless, some indications for strike-slip movements were found on the Southern Alti-
plano: In the southern part of the Central Altiplano (N of Soniquera, see Fig. A.2C and Fig. 3.1
for location) the southern branch of the Khenayani-Uyuni Fault is characterised by a vertical,
several decametres wide, NE–SW trending (40°) fault gouge at the contact between Ordovician
sediments in the west and San Vicente strata in the east. Within the cataclastic zone, many dex-
tral strike-slip indicators were found (e.g. drag-folds with vertical fold axes) besides indicators
of thrusts. This shows that the southern branch of the Khenayani-Uyuni Fault Zone was at
least partially transpressive. In the northern part of the Central Altiplano, indications of strike-
slip displacement are sparse and mainly restricted to the extensive pelitic series of the Potoco
Fm. in the hanging wall of the San Cristóbal Fault. Nevertheless, in the working area of the
Southern Altiplano not a single strike-slip or transpressive fault was mapped.

Chapter 5

Strain analysis

The construction techniques of balanced cross-sections generally require that the section plane is closely parallel to the particle displacement vector field. This requirement relates to the principal rule of 2D area balancing (Dahlstrom, 1969), which assumes plane strain in the section plane. To correct for out-of-section movements at small scale, strain measurements of rock samples can be used. Furthermore, strain analysis can quantify the amount and geometry of ductile strain that was accumulated in the section plane. It can also be used in conjunction with kinematic data to constrain the appropriate restoration algorithm (i.e. 'inclined shear', 'flexural slip', fault-bend folding, etc.). In addition, a complete restoration requires that the relative age of various deformation structures and increments are known, since these constrain the sequence of restoration steps (see chapter 8).

Although the role of ductile strain in unmetamorphosed, weakly-consolidated sediments is usually neglected in section-balancing studies, various studies have indicated that this assumption may not be valid. Significant amounts of ductile strain (up to 30%) were reported from comparable foreland fold belts in poorly-consolidated sediments such as the Alpine Molasse Basin (Schrader, 1988) and the German Rhenohercynian Thrust Belt (Plessmann, 1966a; 1966b).

In low-strained rocks, in particular, identification of all the components that contribute to the finite strain is paramount. The finite-strain ellipsoid may be the result of all strain increments that occurred since deposition (see Ramsay and Huber, 1983a).

5.1 Samples

The Western Altiplano is almost entirely covered by post-tectonic sediments and volcanic rocks. Deformed Tertiary strata only crop out at the anticline of the Yazón Peninsula (see Fig. 4.1 and section 4.3). In the eastern part of the Southern Altiplano, outcrops of deformed units are common and mainly located south of the Main Cross-Section (Fig. 5.1). This regional inbalance of outcrops is also reflected in the distribution of samples for strain analysis (see Fig. 5.1).

Because I expected very low strain, a first test series (Series A) of 5 samples from different stratigraphic units and structural position (5°–85° dip angle) was run to establish the order of magnitude and an appropriate methodology. New sample sites (Series B) were chosen, based on the results from the first series.
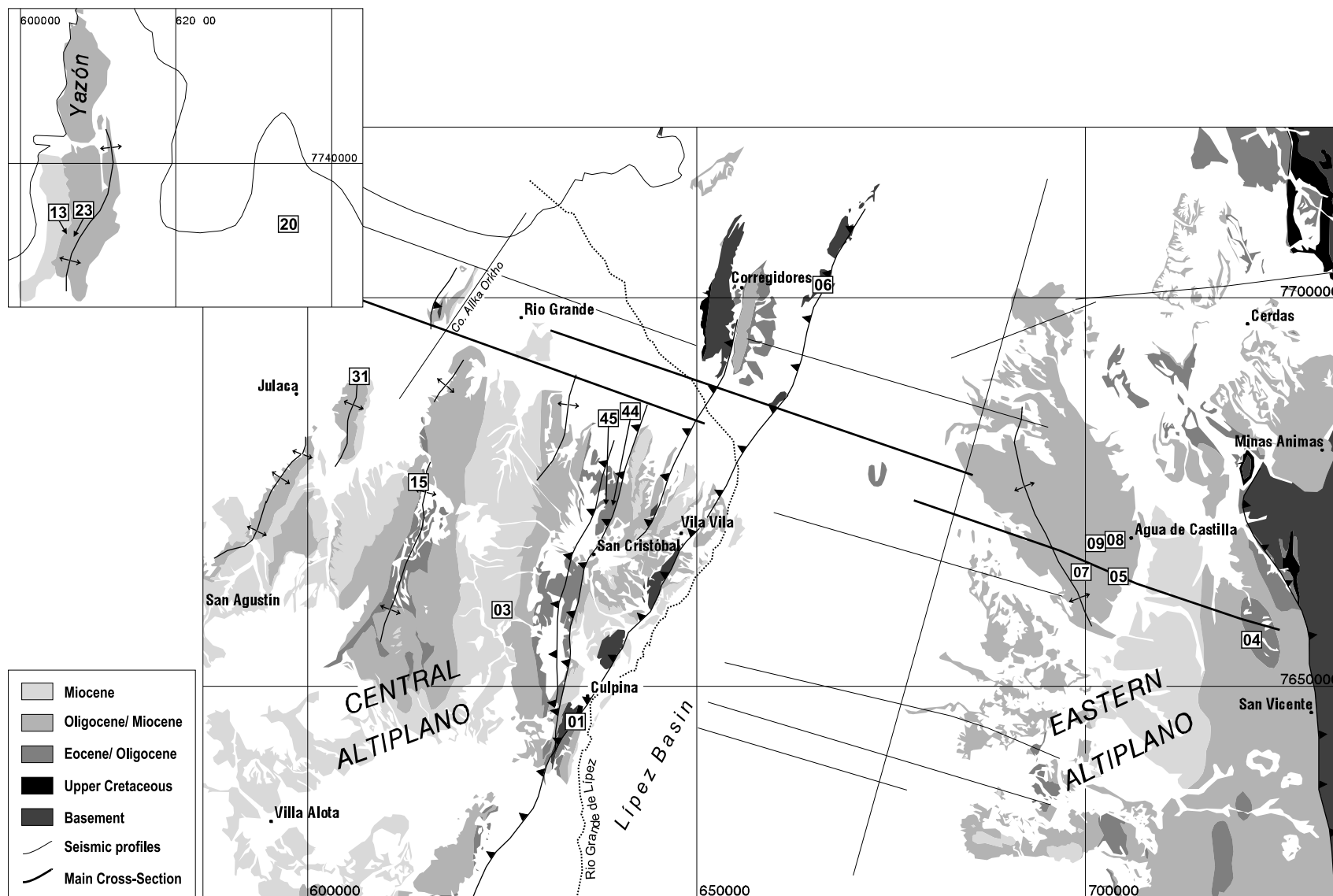
Figure 5.1: Generalised geological map of the working area with sample locations for strain analysis (No. 20 = sample ke20). The small map in the upper left shows strain sample locations from the Western Altiplano (Yazón Peninsula in the west). Lines delineate the seismic database.

In total I analysed 15 oriented rock samples from all available stratigraphic units in the cross-section area (Silurian to Miocene), including some post-tectonic rocks to calibrate the unde-formed strain ellipsoid (see Tables D.1 and D.2). The samples consisted of a Silurian quartzite (sample ke06), an Late Cretaceous oolite (ke01), three Eocene/Oligocene (ke04, ke44, ke45), six Late Oligocene/Miocene (ke05, ke07, ke08, ke13, ke15, ke23), one Late Miocene sand-stone (ke03), two Late Oligocene/Miocene tuffs (ke09, ke31), and one Late Miocene tuff (ke20). The Tertiary sandstones are compositionally immature, mostly unsorted, poorly consolidated, and have grain- or matrix-supported fabric. One Oligocene/Miocene crystal tuff is grain-supported. The other Oligocene/Miocene and the Late Miocene tuffs are porphyroblastic (= matrix-supported). The two Miocene samples are late syn-tectonic (ke03) or post-tectonic (ke20) to the Miocene deformation increment, i.e. they are undeformed.

None of the rock samples showed any tectonic fabric (stretching lineation, foliation or cleav-age), in macroscopic or microscopic view. Microscopic analysis revealed only weak evidence of pressure solution, which occurs only at grain boundaries between different minerals (i.e. quartz/feldspar, quartz/calcite or feldspar/calcite). Some feldspar crystals developed small pressure shadows of quartz and the beginning of an oriented growth of phyllosilicates along the grain boundaries, but these features do not produce a foliation (sample ke05, cf. Table D.1). The Cretaceous limestone had slightly deformed oolites. All other samples seem to be com-pletely undeformed on macroscopic and microscopic scale. Additional information about UTM co-ordinates, bedding, structural position and microscopic observations of each sample are given in Tables D.1 and D.2.

5.2 Methods

For 2D strain analysis, three mutually-orthogonal thin sections were examined from each rock sample, using the centre-to-centre technique after Fry (1979, see section 5.2.1.1) and the R_f/ϕ' Method after Ramsay and Huber (1983a) and Peach and Lisle (1979) (see section 5.2.1.2). Three sections are a minimum requirement to reconstruct the orientation of the finite-strain ellipsoid where fabric is absent.

In the first series of five samples one horizontal and two vertical thin sections were made (Se-ries A: ke01, ke04, ke05, ke13, and ke15). One of the vertical sections was oriented parallel to the fold axis, the other was parallel to the profile plane of the fold, i.e. closely parallel to the cross-section plane. For the remaining samples (Series B: ke03, ke06, ke07, ke08, ke09, ke20, ke31, ke44, ke45) one section was parallel to the bedding plane and the fold axis, the second perpendicular to the bedding and parallel to the fold axis, and the third was orthogonal to the previous two (in profile plane of the fold) and nearly in cross-section plane.

It has been shown (Ramsay, 1967; Siddans, 1980) that the section planes for strain analysis need not to be parallel to the principal planes of the strain ellipsoid. I ignored the orientation of bedding planes in Series A to avoid the effects of preferred grain orientation that are highest in the plane perpendicular to the bedding plane (Holst, 1982; Paterson and Hao, 1994, see also section 5.2.1.3).

Furthermore, every section was tested for the existence of a pre-tectonic sedimentary orienta-tion using the R_f/ϕ'-based hyperbolic net of De Paor (1988) and the 'unstrained plot' of Unzog (1990, 1992), an additional function of the program used to calculate the R_f/ϕ' Method after Peach and Lisle (1979)(see section 5.2.1.3).

FRY PLOTS   NORMALIZED FRY PLOTS

SF=1.10
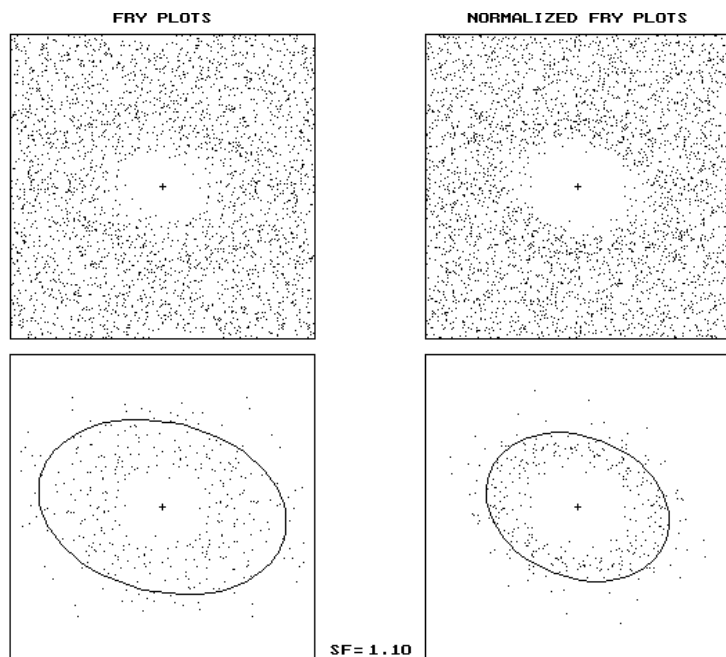
Figure 5.2: Example of the 2D strain analysis after Fry (1979); vertical section of sample ke05 parallel to the fold axis. Above, the conventional and the normalised Fry-plot. Below, the least-squares ellipse calculated with a selection factor of 1.10 (Enhanced Fry Plots). The ellipse is best determined by the Enhanced Normalised Fry Plot (lower right) with $X/Y = 1.334$, $\phi = -21.75°$, and an average error of 18.88%. Enhanced Conventional Fry Plot (lower left) : $X/Y = 1.477$, $\phi = -13.4°$, average error 28.61%.

To calculate the geometry and orientation of the strain ellipsoid from any three, mutually-orthogonal, thin-sections (see section 5.2.3), I used the TRISEC program of Milton (1980) which is part of the strain programs of Ratschbacher et al. (1994). In the last part of this chapter (5.4), the compaction component, approximated from published porosity-depth-graphs, was removed from the finite-strain ellipsoid to obtain the 'pure' tectonic strain.

5.2.1   2D methods

In this section, a short overview of the methods used in the 2D strain analysis is given. The intention is not to describe every method in detail, but to present the pathway of the data and interpret the results. An extensive overview of most of the methods for strain analysis is given by Lisle (1994).

5.2.1.1   Centre-to-centre technique

By assuming the particles were initially homogeneously distributed, Ramsay (1967) designed a method to find the strain ratio from the ratio of the maximum and minimum neighbour distances. Fry (1979) proposed a graphical solution to perform the centre-to-centre technique by producing the so-called 'all-object separations' plot which shows centre-to-centre distances for all permutations of markers with each other as a function of direction. This simple method involves placing a plot over the image of the deformed markers and, with the origin centered on each grain in turn, marking the position of all the other grain centres on an overlay. This results in a plot that normally possesses a region around the first point devoid of plotted centres. The shape and orientation of this central void is equal to the two-dimensional strain ellipse.

One of the main areas of subjectivity is to decide on the shape of the ellipse, because this is usually done by the visually contouring the ellipse. To avoid this, Erslev and Ge (1990) numerically determined the best-fit ellipse using a least-squares fit to the innermost points. This method from Erslev and Ge (1990) is available within the INSTRAIN program. The numerically selected, best-fit ellipses yielded good results with the Bolivian samples.

The degree to which the ellipse is constrained depends mainly on the initial degree of 'anticlustering'. Strongly varying grain sizes in a sample can also decrease the sharpness of the ellipse. To deal with small amounts of clustering or highly-unsorted samples the grain-size normalised Fry Method is applied (Erslev and Ge, 1990). This involves normalisation of the inter-marker distance to the radii of the markers. The intention of this 'Enhanced Normalised Fry Plot' of INSTRAIN (Erslev and Ge, 1990) is to increase the accuracy of the ellipse by applying a minimum object-pair selection factor to select touching pairs. INSTRAIN uses two different selection factors (1.05 and 1.10) and calculates the least-squares ellipses with both selection factors for the conventional and the normalised technique. All Bolivian samples showed better results, i.e. better-defined ellipses, after applying the 'Enhanced Normalised Fry Method'.

The advantage of the centre-to-centre technique is that it offers the possibility to determine the whole-rock strain (matrix-strain), which may not be the same as the strain accumulated by the markers themselves. It is therefore an adequate method for matrix-supported samples. In grain-supported samples the results from the Fry and the R_f/ϕ' Methods should be similar.

5.2.1.2 R_f/ϕ' **Method**

In contrast to the Fry Method, the R_f/ϕ' technique uses the outline of marker grains to determine the strain ellipse. During deformation, variations of the grain shapes (e.g. elongation of the ellipses) and rotations of the principal axes of the ellipses occur. The changes correlate with the intensity of deformation.

The R_f/ϕ' Method (Peach and Lisle, 1979; Ramsay and Huber, 1983a) is a technique for strain analysis of initially-elliptical objects. The aspect ratio (R_f) and orientation (ϕ') of a deformed elliptical marker depend not only on the strain ratio (R_s), but also on the initial orientation of the marker (θ) and its original axial ratio (R_i). It is based on the concept that a group of deformed elliptical markers that share the same initial eccentricity will give a characteristic curve when plotted on a graph of R_f vs. ϕ' (Ramsay, 1967). The shape of this curve is diagnostic of the strain ratio and the R_i values of the markers. The variables are solved by comparison with theoretical curves developed by Dunnet (1969) and Lisle (1985a). Most computer-based strain programs have implemented this comparison of the curves and give values for R_i, θ, and R_s; e.g. INSTRAIN (Erslev and Ge, 1990) or THETA (Unzog, 1990, 1992).

Peach and Lisle (1979) proposed a statistical approach for the interpretation of R_f/ϕ' graphs. They calculated the harmonic mean ($R_{f\ (\text{harm})}$) of all measured ellipticities (R_f) and the corresponding orientations (ϕ') and used the χ^2 test to determine the shape and orientation of the strain ellipse ($R_{s\ (\text{from }\chi^2)}$ and $\chi^2 = \phi$). The subtraction of the strain ellipse (R_s) from the finite ellipse (R_f) determines the initial ellipse ($R_{i\ (\text{harm})}, \theta$). This method is implemented in the THETA program (Unzog, 1990, 1992) which additionally gives an R_i/θ diagram of the initial ellipses prior to deformation (see Fig. 5.3). This so-called 'unstrained plot' allows visual control of the initial marker orientation: If a maximum occurs in the 'unstrained plot', this suggests the grains possessed a preferred orientation prior to deformation; contrary to the example in Fig. 5.3 (see also section 5.2.1.3).
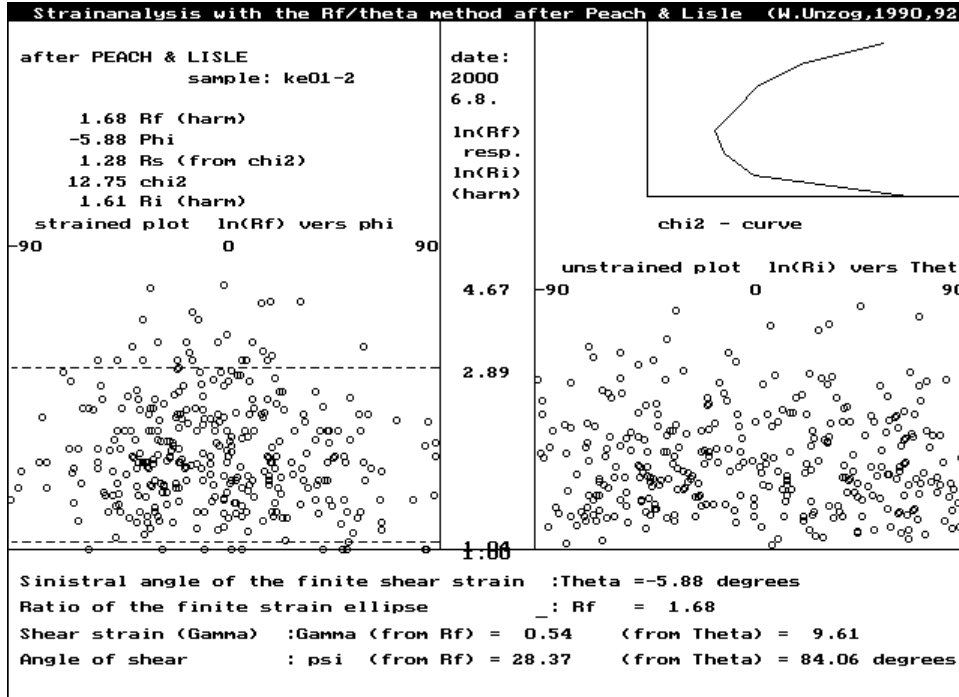
Figure 5.3: Example of 2D strain analysis after Peach and Lisle (1979)(section vertical and parallel to the fold axis of sample ke01). The left side shows the R_f/ϕ' diagram of the measured section. The enveloping curve of data points is almost symmetrical and has a maximum at $-5.88°$ ($= \phi'$). In the 'unstrained' plot ($ln(R_i)$ versus θ) (to the right) all data points are homogeneously distributed. The orientations of the long axes of the markers spread from $-90°$ to $+90°$ without clustering in a preferred direction. This suggests that a pre-tectonic fabric that has a different orientation than the finite-strain ellipse did not exist for this sample. The χ^2 versus R_s graph in the upper right shows the results of a symmetry test performed for different strain intensities (R_s). The smallest χ^2 value is on the left.

In addition to the analysis with THETA, I interpreted the R_f/ϕ' graphs from INSTRAIN (Erslev and Ge, 1990). INSTRAIN calculates the harmonic mean from the R_f/ϕ' diagram. In many cases, the harmonic mean of the R_f/ϕ' diagram is close to the tectonic strain R_s (Ramsay and Huber, 1983a). To check this, I manually interpreted the R_f/ϕ' diagram of the first series and determined $R_{i \ (max)}$ and R_s using the equations of Ramsay and Huber (1983a, pp. 75–86):

$$\sqrt{R_{f \ (max)} \cdot R_{f \ (min)}} = R_{i \ (max)} \tag{5.1}$$

$$\sqrt{\frac{R_{f \ (max)}}{R_{f \ (min)}}} = R_s \tag{5.2}$$

for $R_{i \ (max)} > R_s$. This corresponds to a near $180°$ fluctuation of R_f over ϕ which was always the case for the very low-strained samples of the Southern Altiplano. In addition, the least-squares best-fit ellipse from the shape of objects was calculated within the so-called Mean Object Ellipse Method (Erslev and Ge, 1990).

5.2.1.3 Pre-tectonic fabric

One of the pre-conditions for the Fry- and the R_f/ϕ' Methods is that the grains do not possess an initial fabric, i.e. do not show a preferred orientation prior to deformation (Lisle, 1994). This requirement is often not fulfilled. Especially sediments show a preferred orientation of grains acquired during deposition. It is commonly assumed that the primary fabric of a two-dimensional section is parallel to the bedding trace and will produce an asymmetry of data points in the R_f/ϕ' graph. Practical applications, however, showed that this is often not the case. Thus, in theory, but not practice, pre-tectonic fabric can be detected from an asymmetry in the R_f/ϕ' plot (Lisle, 1985b).

Many authors investigated the influence of non-random sedimentary fabric on the strain measurements (e.g. Dunnet and Siddans, 1971; Holst, 1982; Paterson and Hao, 1994; Paterson et al., 1995; Wheeler, 1986). Their main conclusion was that the effect of pre-tectonic fabric for the strain determination is higher the less the rocks were strained, and that the influence of sedimentary fabric is highest in the sections perpendicular to the bedding. To investigate the magnitude and orientation of pre-tectonic fabric, Paterson and Yu (1994) determined the strain in undeformed sandstones. Their results showed that undeformed sandstones have non-spherical fabric ellipsoids with small axial ratios ($X < 1.5$), but a wide range of shapes. They suggested that all strain measurements of deformed sandstones should be corrected for primary fabric. This correction is particulary important for low-strained sandstones, with $R_f < 1.5$, where the ellipticities of the primary fabric and the strain increment have the same order of magnitude.

De Paor (1988) proposed a hyperbolic net to detect pre-tectonic fabrics. Braun (1999) implemented this analysis into a computer program (HYPOPAOR). This program produces various types of isogon plots and calculates a homogeneous and an optimised tectonic strain. It uses standard deviation of R_i to quantify the magnitude of the determined preferred orientations. In general, the effect of pre-tectonic fabric can be neglected if the variations lie within one order of standard deviation.

For the analysis I used HYPOPAOR (Braun, 1999), and also the unstrained plot from THETA (Unzog, 1990, 1992) for visual control of a possible asymmetry of the initial, i.e. unstrained, markers in the R_f/ϕ' diagram (see section 5.2.1.2).

5.2.2 Work flow of the 2D strain analysis

The required input format for 2D strain analysis varies from method to method. While the centre-to-centre technique requires x,y co-ordinates of grain centres, the R_f/ϕ' Methods require the x/y co-ordinates of the beginning and the end points of the two perpendicular-oriented main axes of an inscribed ellipse for each grain.

The number of measured ellipses to reach an adequate accuracy also varies between the Fry and the R_f/ϕ' Method. According to Dittmar (1994), the INSTRAIN program (Erslev and Ge, 1990) yields the best-defined ellipse using 300–400 grain centres for the Fry analysis. Erslev (1990) gave a 'mean radial error' of $13 \pm 2\%$ or $13 \pm 1.25\%$ for sandstone with the 'Enhanced Normalised Fry Method', using 300 and 400 grains, respectively. For the R_f/ϕ' Methods the measurement of 80–150 grains is sufficient (see Dittmar et al., 1994).

In this work, my aim was to apply the largest variety of methods with the minimum digitising effort. I analysed 300–400 grains in each thin section. For all grains, the beginning and the end points of the two main axes of the inscribed ellipse in each grain were digitised. The intersection of the two axes marked the grain centre for the Fry analysis in INSTRAIN.

The work flow was fully computerised: A digital photography of each section was imported into ARC/INFO (ESRI). The main axes of the inscribed ellipse of each grain were were visually determined and digitised as *'arcs'* (one arc per grain). The co-ordinates of the vertices of the *'arcs'* correspond to the beginning and the end of the ellipse's long and short axes. They were exported into ascii format using the *'ungenerate'* command. The ascii file was then transformed into the required format and imported in the strain analysis programs. The input format for 'HYPOPAOR' (see section 5.2.1.3) was the lowest-denominating format, so all files were transformed into this format to avoid numerous transformations between the different programs. The largest advantage to use ARC/INFO (ESRI) (or Autocad) for the digitisation is that this procedure allows a good control of digitising errors and also the possibility to correct the original data if necessary. This procedure saves time because there is no need to re-digitise the whole sample in case of errors. Instead, the error in the ARC/INFO (ESRI) coverage was simply corrected and the ascii file re-formatted. The largest potential for errors consisted in overlooked or supplementary points during digitisation of a grain.

5.2.3   3D methods

5.2.3.1   Calculation of the strain ellipsoid

The determination of the strain ellipsoid from 2D strain measurements on any three randomly-oriented sections was achieved with TRISEC (Milton, 1980). In theory, the strain ellipsoid may be reconstructed from any three differently-oriented sections. In practice, the calculation of the strain ellipsoid from three sections is complicated by local strain inhomogeneity and experimental error inherent in the 2D methods. Milton (1980) proposed a two-stage method; firstly, to adjust the three ellipses to make them compatible, and secondly, to calculate the strain ellipsoid. The principal axes are derived from the ellipsoid by eigenvector analysis. According to Milton (1980), the optimum geometry for the determination of the strain ellipsoid occurs when the measured sections are the three principal sections of the ellipsoid. If this is impossible, e.g. in case of absent fabric, orthogonal sections are preferred (Milton, 1980).

The result of TRISEC is a third-order matrix representing the strain ellipsoid, the $X/Y/Z$ ratios (main axes of the ellipsoid: $X \geq Y \geq Z$), the strain intensity factor (ε_s), Lode's parameter (ν), the length and orientation (dip direction and dip angle) of the principal axes X, Y, Z, the XY plane, and the adjustment factors of each ellipse. See Ramsay and Huber (1983a, page 201ff) for definitions of ε_s and ν.

A problem of TRISEC is that it apparently does not assume a constant volume for each ellipsoid, i.e. the product of the principal axes is $\neq 1$ and differs for each sample. This makes a direct comparison of the axial length between different ellipsoids impossible. Normalisation is therefore required. Since in an ellipsoid without volume change $X \cdot Y \cdot Z = 1$, each axes produced by TRISEC can be multiplied by the correction factor CF, given as:

$$CF = \sqrt[3]{\frac{1}{X \cdot Y \cdot Z}} \qquad (5.3)$$
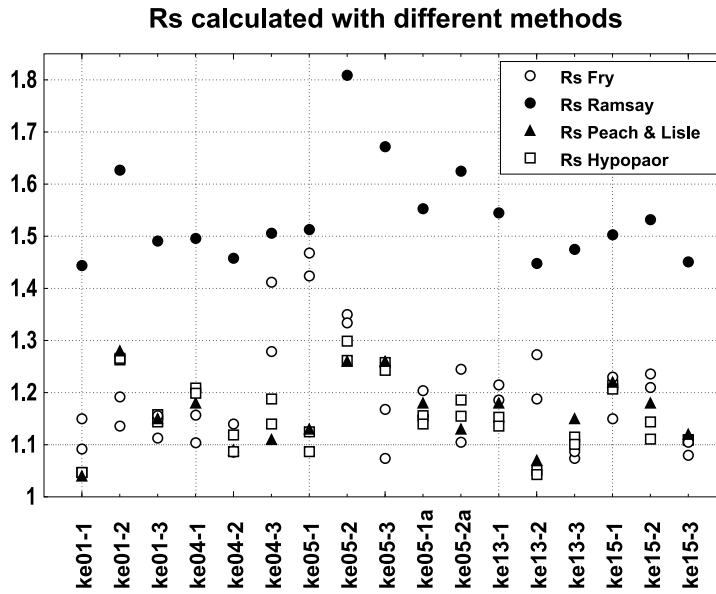
Figure 5.4: 2D strain derived from different methods: R_f/ϕ' after Ramsay and Huber (1983a), R_f/ϕ' after Peach and Lisle (1979), centre-to-centre after Fry (1979), and HYPOPAOR (De Paor, 1988). For the first series of samples (ke01, ke04, ke05, ke13, and ke15) the results from the three perpendicular sections are plotted, plus two additional results from sample ke05 because two domains with different grain size existed. See text for explanation.

where X, Y, Z are the lengths of the principal ellipsoid axes given from TRISEC. Table D.7 gives both the 'original' (X_{length}, Y_{length}, and Z_{length}) and the normalised length (X_{norm}, Y_{norm}, and Z_{norm}) of the principal axes. For further interpretation, I used the normalised axes lengths (e.g. Fig. 5.5, 5.6). This normalisation is based on the assumption of isovolumetric strain, a general supposition which can only be measured independently of the strain analysis method.

The Flinn Graph (Flinn, 1979) is used to classify the shape of the ellipsoids. It is based on a comparison of the ellipticities of the two principal planes of the strain ellipses and is essentially a description of the ellipsoids' shape irrespective of volumetric dilatation. The Flinn Graph (Fig. 5.5) plots the value of R_{yz} as abscissa and R_{xy} as ordinate. The origin represents a sphere. Every ellipsoid is represented by a single point in the positive sector of the graph. The positive diagonal through the origin separates oblate ellipsoids (e.g. compaction ellipsoid) below the diagonal from prolate ellipsoids above it. The diagonal itself represents plane-strain ellipsoids.

5.3 Strain results

5.3.1 2D results

In all samples, the initial ellipticity of the sediment grains was higher than the ellipticity of the finite-strain ellipse. All strain ellipses have axial ratios < 1.5, i.e. very low strain.

Ten samples have a grain-supported fabric and are compositionally immature sandstones. In grain-supported sandstones, the results from the Fry- and the R_f/ϕ' Methods should be theoretically the same, because the grain itself accumulates the deformation and is not only a passive marker in a deformable matrix.

The results of the two-dimensional strain analysis show that the latter is only partly true. Fig. 5.4 shows the axial ratios of R_s measured with different methods. It is interesting to note that in grain-supported samples (ke01, ke04, ke15) the R_s values derived from the Peach and Lisle method (Peach and Lisle, 1979) are very close to the R_s from the Fry analysis. In most

cases, however, the values of R_s from the manually-interpreted R_f/ϕ' diagrams after Ramsay and Huber (1983a) are significantly higher (Fig. 5.4). A reason for this could be the subjectivity of manual interpretation of the INSTRAIN-R_f/ϕ' diagram (e.g. the interpretation of outliers). On the other hand, observations made on synthetic data (ellipses being strained with a known strain ellipse) also consistently show excessive R_s values after applying the Ramsay and Huber (1983a) method (Günther, 1994). I therefore neglect the Ramsay and Huber (1983a) results.

The test of a pre-tectonic, i.e. sedimentary, fabric (open squares in Fig. 5.4) results in only small variations of the strain ellipse (R_s) compared to the R_f/ϕ' result from Peach and Lisle (1979). The analysis with the hyperbolic net revealed that the magnitude of any preferred orientation did not exceed one standard deviation. In addition, the 'unstrained plot' (Unzog, 1990, 1992) always shows a 180$^{\text{o}}$ fluctuation of the data points. This precludes the existence of any pre-tectonic fabric with a different orientation than the measured finite-strain ellipse. A superposition of two ellipses with the same orientation would result in a higher axial ratio. In this case the separation of pre-tectonic and tectonic strain is impossible. The 180$^{\text{o}}$ fluctuation of data points in the 'unstrained plots' of every sample shows that (within the limit mentioned above) the effect of sedimentary fabric is negligible.

For further analysis and calculations (2D strain measurement of the new samples of Series B, 3D strain analysis) I only used the R_f/ϕ' Method after Peach and Lisle (1979) for all grain-supported samples (see Table D.4 for detailed results).

In matrix-supported samples, best results were obtained with the 'Enhanced Normalised Fry Method' and a selection factor of 1.10. 'Best results' included both the visually-verified fit of the calculated ellipse, and the statistically-acquired average error from the least-squares method. For all samples the error is highest in the enhanced conventional Fry plots (30–50%), median in the conventional diagram (20–30%), but always lowest ($< 20\%$) in the enhanced normalised plots. The results from the Fry-analysis are shown in Table D.3.

5.3.2   3D finite strain results

The Flinn Graph (Fig. 5.5) shows a wide variation of ellipsoid shapes for the Southern Altiplano sandstones, which range from apparent flattening to apparent constrictional. The axial ratios of the principal strain axes are very small (< 1.5) and indicate very low strain.

The highest-strained samples, even though the absolute strain values are very low, come from the Eastern Altiplano (triangles, Fig. 5.5, see also Table D.7). They include prolate and oblate ellipsoids. The samples from the Central and Western Altiplano can be separated in two groups: all samples from hanging walls of thrusts or steep fold limbs plot near or below the positive diagonal, indicating plane strain, or show a weak oblate shape (diamonds, Fig. 5.5). Stratigraphically young samples that experienced only minor deformation or post-tectonic samples cluster near the origin of the graph or plot along the positive diagonal (circles, Fig. 5.5). In the following discussion, this grouping will be maintained.

Fig. 5.6 shows the orientation of the main axes of the strain ellipsoid and the bedding plane for each sample in stereonet projection and the length of each axis with regard to a unit sphere below (bar plot, see Fig. 5.6). In many samples, only one of the principal axes can be clearly distinguished from the others with respect to length (X or Z). The other two axes are very similar. In this case (e.g. Y and Z in sample ke04, Fig. 5.6) the significance of the orientation of
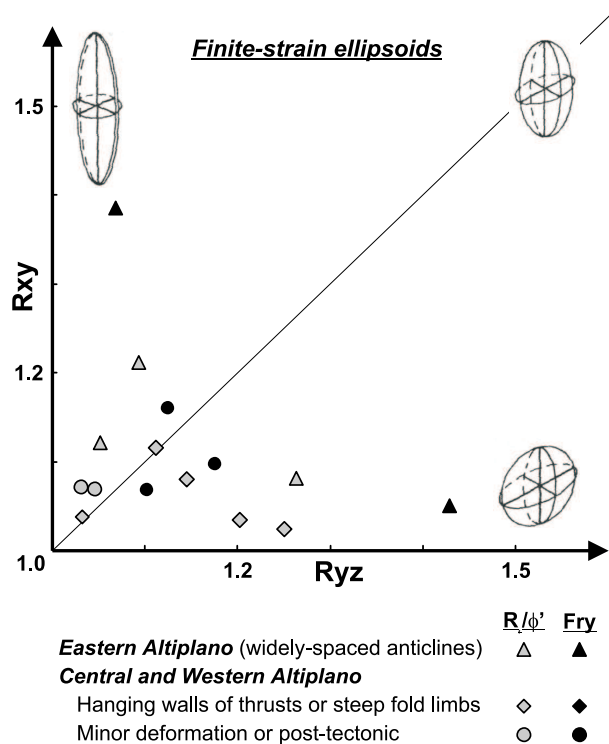
Figure 5.5: Flinn Graph showing the calculated finite-strain ellipsoids (R_s) from all 15 samples. Grey data points are grain-supported samples (R_f/ϕ'-results), black data points matrix-supported (Fry-results). Different symbols represent different groups of samples (see text for explanation).

the two similar axes for geological interpretation is small and the axes are exchangeable. In the two post-tectonic samples (ke03, ke20, see Fig. 5.6 and section 5.1) the length of all axes is very close to 1, and the differences between the three principal axes are very small (see Fig. 5.6 and Table D.7).

The most striking observation is that in most samples, except for the post-tectonic or minor deformed samples, the compression axis (Z) has a steep to nearly-vertical orientation and the extension axis (X) is horizontal to very-gently dipping. This orientation is independent of the dip of the strata. This points to a polyphase deformation history of the samples from the Southern Altiplano.

One of the principal axes (mostly X or Y) is parallel or sub-parallel to the general structural trend i.e. they have a N–S trend in the Eastern Altiplano and a NNE–SSW trend in the Central Altiplano.

5.4 Removal of compaction

The finite-strain ellipsoids represent the bulk strain a sample accumulated. The first strain increment sediments accumulate after deposition is compaction. Later on, the compaction ellipsoid may be overprinted by one or more tectonic strain increments prior to, or during folding and thrusting. If the compaction ellipsoid for a sample is known, it can be subtracted from the finite-strain ellipsoid to reveal the 'true' tectonic-strain ellipsoid that will be used to calculate line length and thickness changes of the balanced profile (see section 5.6).

Published porosity-depth graphs offer the possibility to approximate the compaction for each sample without laboratory measurements. The decompaction was performed for the three 2D sections for each sample. The results of the 2D decompaction were combined to calculate the 3D tectonic-strain ellipsoid.

FINITE-STRAIN ELLIPSOIDS
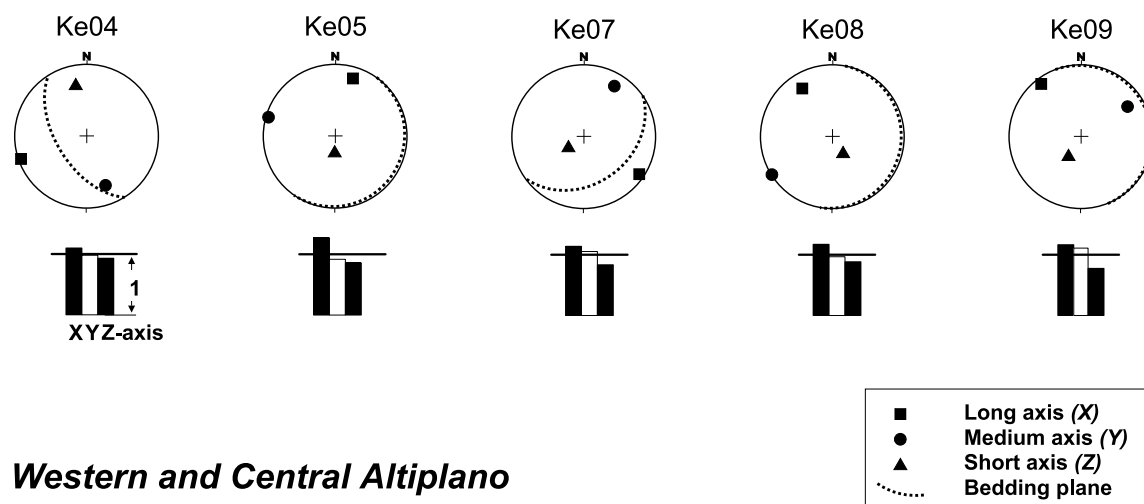
Eastern Altiplano
Widely-spaced anticlines

Ke04   Ke05   Ke07   Ke08   Ke09

X Y Z-axis

Western and Central Altiplano
Hanging walls of thrusts or steep fold-limbs

■ Long axis *(X)*
● Medium axis *(Y)*
▲ Short axis *(Z)*
⋯⋯ Bedding plane

Ke01   Ke06   Ke15   Ke44   Ke45

Minor deformation or post-tectonic

Ke03   Ke13   Ke20   Ke23   Ke31
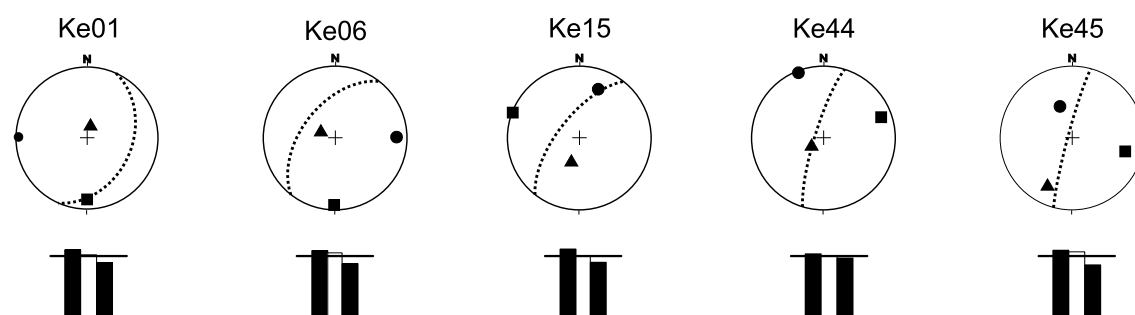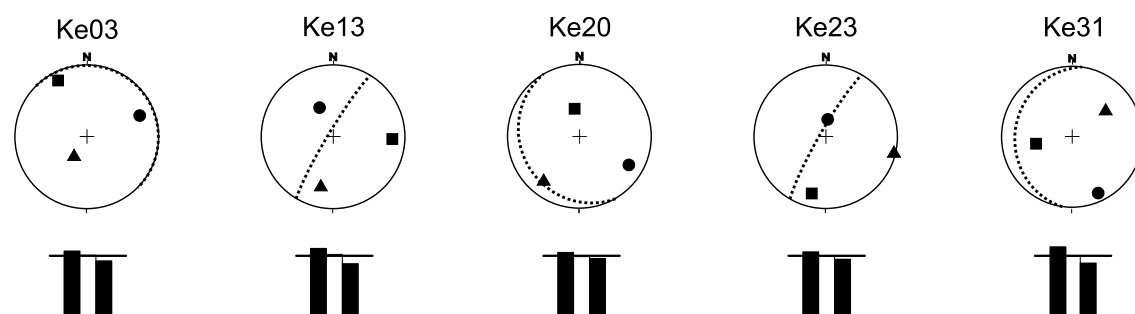
Figure 5.6: Schmidt-net projections (lower hemisphere, equal area) of the principal axes (X, Y, Z) of the finite-strain ellipsoids and the bedding plane of each sample. The diagram below each Schmidt net shows the length of X, Y, and Z normalised to a constant volume of 1 (cf. section 5.2.3.1). The black, horizontal line marks unity.

5.4.1 Calculation of the inverse compaction ellipsoid

The compaction ellipsoid can be described as uniaxial strain ellipsoid with its short axis normal to the bedding plane. During 'pure' compaction, only the axis normal to the bedding plane is shortened while the remaining principal axes remain constant ($X = Y = 1$, $Z < 1$).

In low-strained rocks, the importance of compaction is higher than in high-strained rocks, i.e. tectonic strain and compaction have the same order of magnitude. The amount of compaction depends mainly on the initial porosity, which in turn is dependent on the lithology and the thickness of overlying sediments (maximum burial depth, see Fig. 5.17). The magnitude of compaction thus increases with depth. The porosity at depth (ϕ_{depth}) was approximated with the following equation:

$$\phi_{\text{depth}} = \phi_0 \cdot e^{\frac{-\sigma_{\text{m}}}{k}} \tag{5.4}$$

where ϕ_0 is the initial depositional porosity, k the compaction modulus, and σ_{m} the maximum vertical effective stress reached during the burial history (Giles, 1995). σ_{m} is defined as the difference between the lithostatic pressure ($\sigma_{\text{v}} = \rho \cdot g \cdot h$) and the pore fluid pressure (P_f), or:

$$\sigma_{\text{m}} = \sigma_{\text{v}} - P_{\text{f}} \tag{5.5}$$

Neglecting pore fluid pressure ($P_{\text{f}} = 0$) simplifies Equation 5.5 to

$$\sigma_{\text{m}} = \sigma_{\text{v}} \tag{5.6}$$

The consequence of this simplification is that the maximum porosity loss is calculated, because pore fluid pressure would always reduce σ_{m} (see Equation 5.5). Thus the calculated compaction ellipsoid is a maximum approximation. For the initial porosity ϕ_0 and the compaction modulus k, average values from published data for sandstone and siltstone were used (Table 5.1). The range of the values is discussed in section 5.8.

Apart from the compaction modulus (see discussion in 5.8), the most sensitive parameter for the shape of the compaction ellipsoid is the burial depth h. Because of the strong lateral variation in the thickness of the stratigraphic units, h was determined directly from the balanced cross-section and not from a stratigraphic column (h values in Table D.5). This minimised the error in depth determination.

The porosity loss between the surface and the burial depth ($\delta\phi_{\text{depth}}$ in %) is given by

$$\delta\phi_{\text{depth}} = \phi_0 - \phi_{\text{depth}} \tag{5.7}$$

To 'decompact' the finite-strain ellipse, the inverse compaction ellipsoid was used. The length of the long axis of the inverse compaction ellipse (corresponding to the inverse of the short axis in the compaction ellipse) was calculated using

$$X_{\text{depth}} = \frac{1}{1 - (\frac{\delta\phi_{\text{depth}}}{100})} \tag{5.8}$$

where X_{depth} is always > 1 and oriented normal to the bedding plane. The remaining axes did not change their length ($Y = Z = 1$) and are both in the bedding plane and orthogonal to the other principal axes.

Porosity loss coefficients

Lithology	k	k Range	ϕ_0	ϕ_0 Range
Sandstones	31 MPa	19.28–51.5 MPa	48%	52–40%
Siltstones	25 MPa	?	38%	?

Table 5.1: Porosity-loss coefficients used for the calculation of the inverse compaction ellipsoid. The values are typical values from various sources (e.g. Hindle, pers. comm., Angenheister, 1982; Sclater and Christie, 1980). For the calculation of the tectonic-strain ellipsoids the average values of the compaction modulus k and the initial porosity ϕ_0 were used. The effect of the maximum and minimum k and ϕ_0 values on the strain ellipsoids will be discussed in section 5.8.

5.4.2 Decompaction of 2D sections — methods

The decompaction was realised separately for each of the three sections of every sample. Afterwards the (decompacted =) tectonic-strain ellipsoids were calculated from the three decompacted sections from each sample with TRISEC (see section 5.2.3.1).

The projection of three planes through the inverse compaction ellipsoid (parallel to each section) yields the corresponding inverse compaction ellipses for the examined sections. The projection procedure is described in Appendix D.1; the results are given in Table D.6.

The sections of the Series B samples parallel the principal axes of the inverse compaction ellipsoid (see section 5.2 for definition of Series A and B). Generally, samples with the suffix -1 (e.g. ke01-**1**) parallel the XY plane, those with the suffix -2 (e.g. ke01-**2**) parallel the YZ plane, and those with the suffix -3 (e.g. ke01-**3**) represent the XZ plane of the compaction ellipsoid.

Series A samples have two sections which cut obliquely through the compaction ellipsoid and one section parallel to the XZ plane of the compaction ellipsoid (suffix -3). The oblique sections are horizontally (suffix -1) or vertically (suffix -2) oriented. In this case the length of the two principal axes of the compaction ellipsoid change because the section plane is not parallel to a principal plane of the compaction ellipsoid (see Appendix D.1 for a description of the length correction). The corrected lengths of the principal axes of the inverse compaction ellipsoid are given in Table D.5.

The inverse compaction ellipse was superimposed on the corresponding measured finite-strain ellipse. This superposition was achieved with the program 'Shear 3.0' (Klügel, 1993, see Fig. 5.7). From the resulting 2D tectonic-strain ellipses the three dimensional tectonic-strain ellipsoids were calculated with TRISEC (see section 5.2.3.1).

5.4.3 Decompaction results

Fig. 5.8 shows the results of the 2D decompaction for all samples in the cross-section plane, parallel to the XZ plane of the inverse compaction ellipsoid. The dark-grey ellipses to the left of each example are the finite-strain ellipses from the R_f/ϕ' or Fry Method (Tables D.3 and D.4). The light-grey ellipses in the middle represent the inverse compaction ellipse with the long axis perpendicular to the bedding. The black ellipses to the right are the 'decompacted' tectonic-strain ellipses. The black line is the trace of the bedding plane.
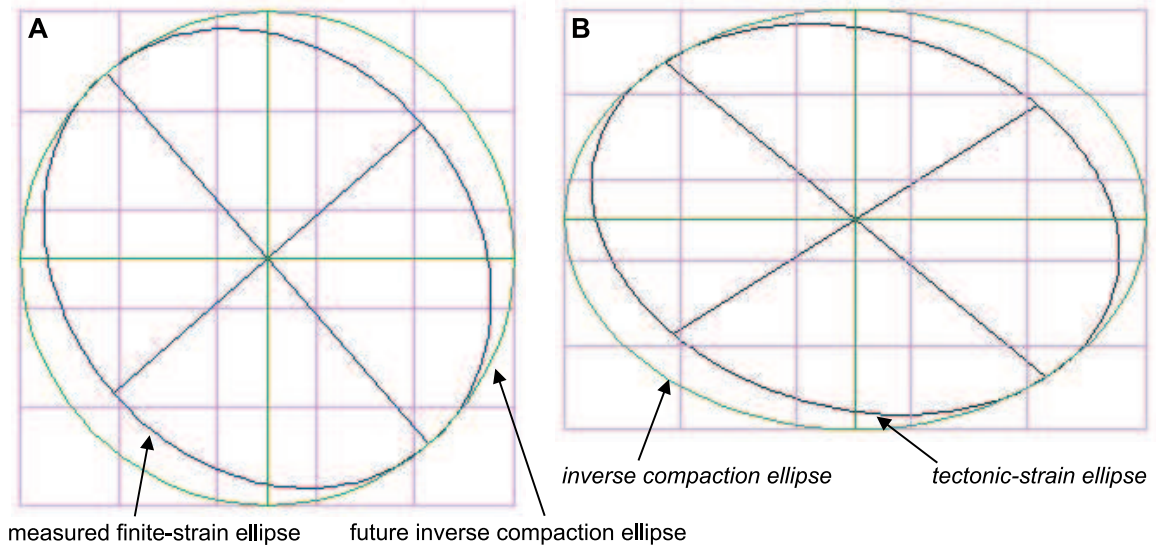
Figure 5.7: Example of the decompaction of a 2D section with 'Shear 3.0': **A:** State prior to the decompaction. A measured finite-strain ellipse was rotated until the bedding was vertical ($R_f = 1.2$, $\phi_f = -49°$). The outer circle represents the future inverse compaction ellipse. **B:** Retro-deformed state of the finite-strain ellipse (= tectonic-strain ellipse) after the superposition of a plane-strain inverse compaction ellipse with $R_s = 1.39$ and $\phi_s = 0$ (perpendicular to the bedding). The reference for ϕ is horizontal, angles are anticlockwise positive. The resulting tectonic-strain ellipse has an axial ratio of $R_{ts} = 1.42$ and $\phi_{ts} = -15.6°$.

After decompaction most of the strain ellipses are oriented with their long axis perpendicular to the bedding (i.e. ke04 and ke07 in the left column, the entire middle, and ke13 and ke23 from the right column, Fig. 5.8). In these cases, the inverse compaction ellipse has a noticeable higher axial ratio than the finite-strain ellipse. Therefore, the form of the tectonic-strain ellipse strongly resembles the inverse compaction ellipse (i.e. long axis orthogonal to bedding). Only three samples (ke08, ke09, ke31) have their long axis oblique to the bedding, and in the remaining three samples (ke03, ke05, ke31) the short axis is perpendicular to the bedding. All samples in which the long axis of the tectonic-strain ellipsoid is not normal to bedding, show that the ellipticity of the inverse compaction ellipse is close to unity (e.g. samples ke05, ke08, ke31, see Fig. 5.8). Therefore, the orientation of these tectonic-strain ellipses was not significantly modified by compaction and, hence, is similar to the finite-strain ellipse.

In the Flinn diagram (Fig. 5.9) the axial ratios of principal strains (R_{xy}/R_{yz}) of the tectonic-strain ellipsoids are generally higher (> 1.2) than those of the finite-strain ellipsoids (< 1.2, Fig. 5.5). All tectonic-strain ellipsoids, except for two, cluster in the plane strain or prolate field, independent of the structural position of the samples. Two of the very low-strained samples are post-tectonic (ke03, ke20). In the highest-strained sample (ke04, the grey triangle plotting near 1.8 in the prolate field) the long axis of the finite-strain ellipsoid and the inverse compaction ellipsoid have a similar orientation, i.e. both long axes are oblique to bedding (see Fig. 5.6). The superposition of these two ellipsoids during decompaction resulted in the extraordinary high prolate strain compared to the rest of the samples.

The Schmidt-net projections of the orientation of the principal axes of the tectonic-strain ellipsoids (Fig. 5.10) show three major preferred orientations. With few exceptions, one of the principal planes of the tectonic-strain ellipsoids is nearly parallel to the bedding. Most samples

De-compaction of finite-strain ellipses in cross-section plane

Eastern Altiplano
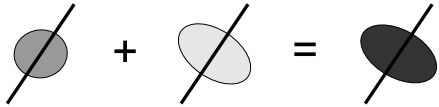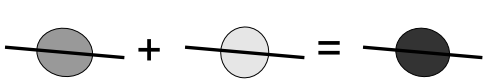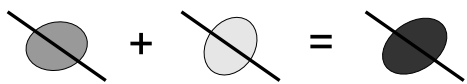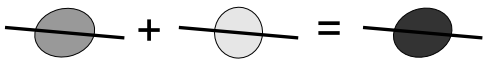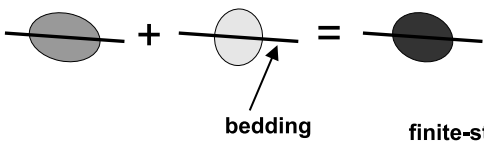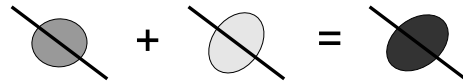
Central and Western Altiplano
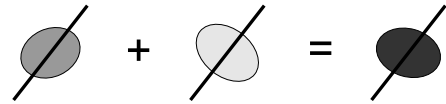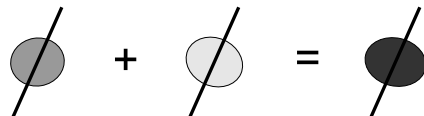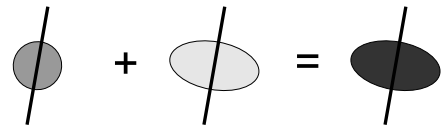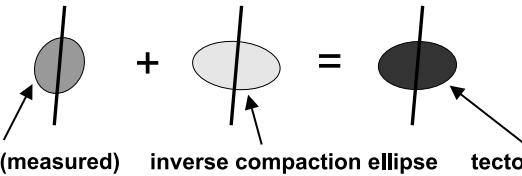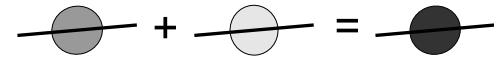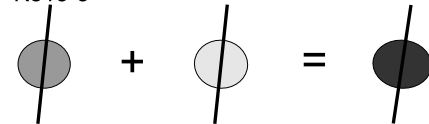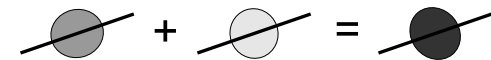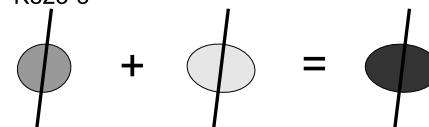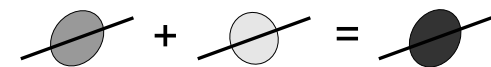
Figure 5.8: 2D decompaction of measured finite-strain ellipses in cross-section plane, see text for further explanation
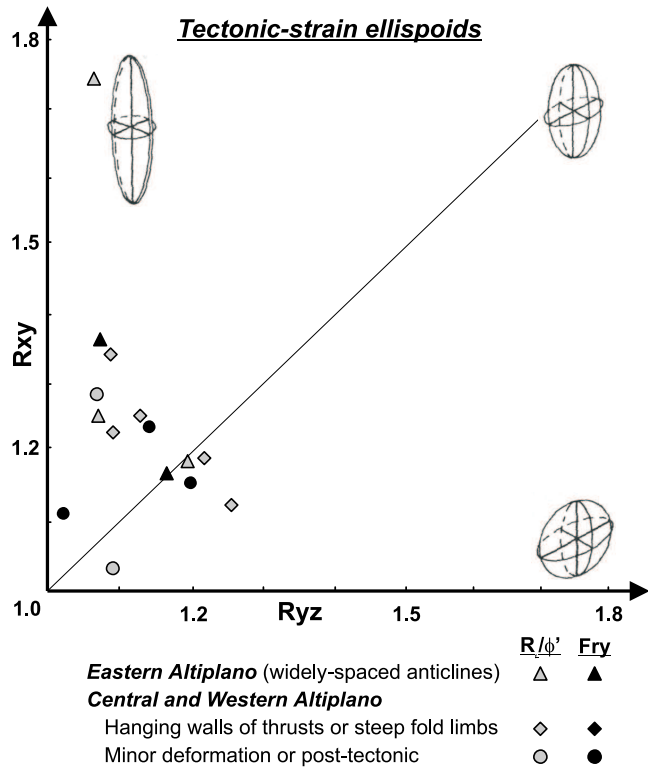
Figure 5.9: Flinn Graph of the tectonic (= decompacted) strain ellipsoids. In contrast to Fig. 5.5, the ellipsoids are relocated closer to the diagonal, representing plane strain, or to the prolate field. Legend as in Fig. 5.5.

have the long (X) or the medium axis (Y) perpendicular to the bedding. Three samples have the short axis normal to bedding, and only two ellipsoids have axes oblique to bedding. The 3D results mainly support the observations that were already reported from the 2D sections (Fig. 5.10): Most tectonic-strain ellipsoids are strongly influenced by the inverse compaction ellipsoid.

In contrast to the finite-strain ellipsoids (Fig. 5.6), the length differences between the three principal axes of the ellipsoid are significant in most cases (with exception of the post-tectonic samples ke03 and ke20, see Fig. 5.10). Thus the orientation of each axis is more significant than in the finite-strain ellipsoids (see Fig. 5.6 and section 5.3.2). As for the finite-strain ellipsoids, the main structural trend of the Southern Altiplano (N–S to NNE–SSW) is also recorded in the tectonic-strain ellipsoids.

5.5 Strain interpretation and discussion

For many samples, plotting the three principal axes of the calculated finite-strain ellipsoid in a Schmidt-net (Fig. 5.6) reveals the unexpected observation of a horizontal to very gently-dipping extension axis and a steeply-dipping compression axis — independent of the inclination of the strata. This would indicate horizontal extension and vertical shortening. At first sight this resembles a vertical compaction geometry, although this compaction would have to have occurred after folding of the strata. This could either have been caused by an enormous sedimentary loading by unconsolidated sediment, which appears unlikely because observed post-tectonic erosion rates on the Altiplano during the last ~10 Ma were very low (see section 3.3.4). Alternatively, extension may have overprinted earlier shortening fabrics. Major extensional structures, however, are not observed on the Southern Altiplano (see chapter 4).

TECTONIC-STRAIN ELLIPSOIDS

Eastern Altiplano
Widely-spaced anticlines
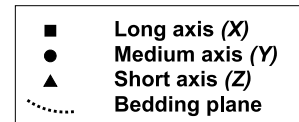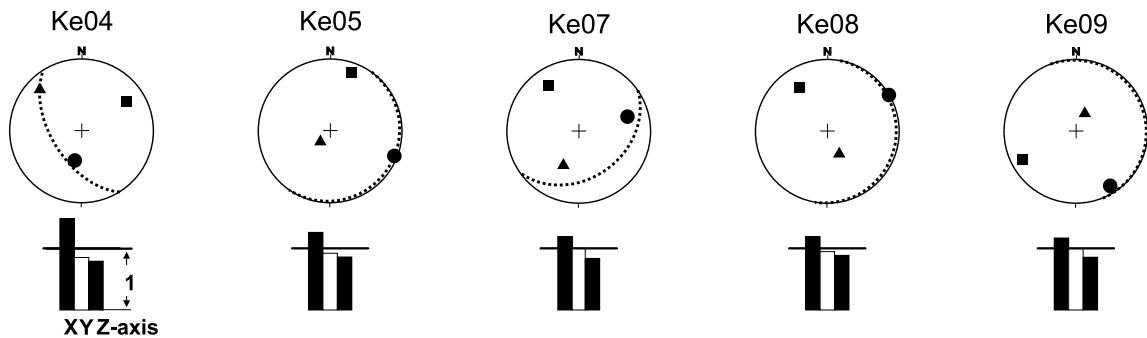
Western and Central Altiplano
Hanging walls of thrusts or steep fold-limbs
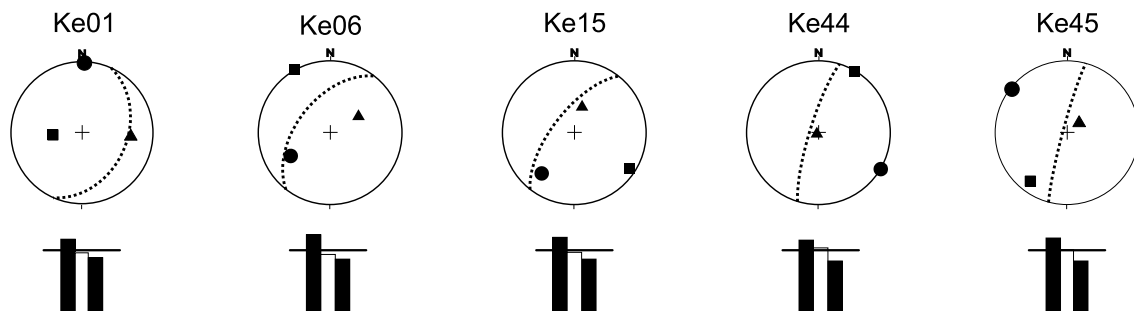
Minor deformation or post-tectonic
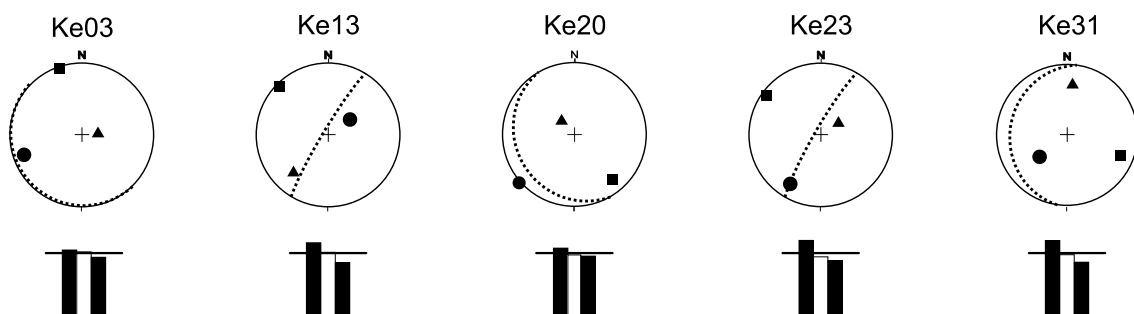
Figure 5.10: Schmidt-net projections (lower hemisphere, equal area) of the principal axis (X, Y, Z) of the tectonic-strain ellipsoids and the bedding plane of each sample. The diagram below each Schmidt-net shows the length of $X, Y,$ and Z normalised to a volume of unity. The black horizontal line marks the length 1 of the unit sphere.
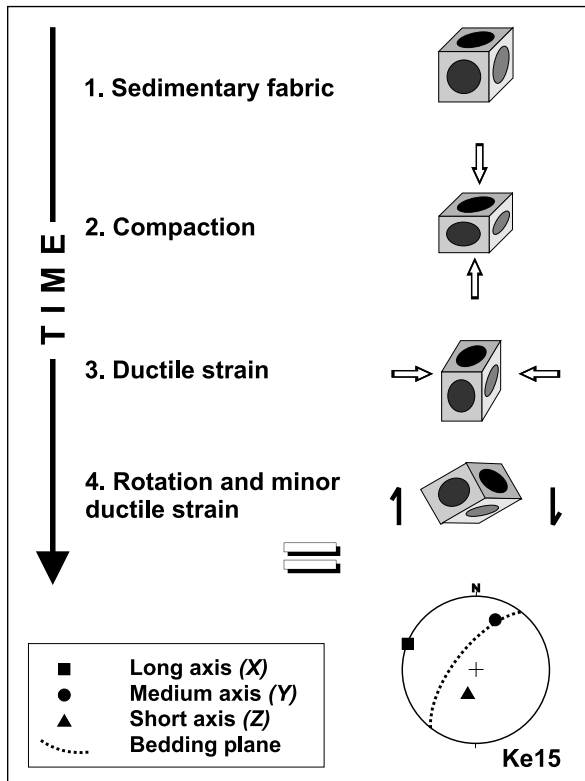
Figure 5.11: Superposition of strain increments accounting for the calculated finite strain state of sample ke15 as example.

One hypothesis to explain this observation involves three deformation stages (Fig. 5.11): (i) an early stage of sedimentary compaction generated an oblate strain ellipsoid with short axis subperpendicular to bedding. (ii) Early ductile layer-parallel shortening ahead of the approaching folding front overprints this geometry with formation of a prolate ellipsoid (long axis parallel to future fold axes) and, eventually, an exchange of the intermediate and short axes when ductile shortening exceeds earlier compaction. (iii) A strain component of probably minor importance is accumulated during folding. At this stage, the ellipsoid is largely passively rotated and probably only further deformed in the inner and outer arcs of folds.

This explanation requires that the layer-parallel ductile shortening was larger than compaction. The fact that not every finite-strain ellipsoid showed the above-mentioned exchange of axes indicates that ductile strain and compaction are on the same order of magnitude. This can be also seen in Fig. 5.8. Accordingly, some axes of the finite-strain ellipsoids have exchanged (e.g. ke07, ke15) while others have not (e.g. ke05, ke23; see Fig. 5.6).

The hypothesis also demands that the magnitude of pre-rotational strain (compaction and early ductile shortening) is higher than the strain accumulated during the folding of the strata. This can be tested by rotating all ellipsoids so that the bedding plane is horizontal. All samples that experienced a similar pre-rotational strain history should then show equivalent orientations of the three principal strain axes. Fig. 5.12A shows that the principal axes of the tectonic-strain ellipsoids do have a significantly higher correlation after the strata is flattened. The orientation of the axes (i.e. steep X, flat to horizontal Y and Z) would be expected if pre-rotational ductile strain was mainly responsible for the shape and orientation of the strain ellipsoids, and if strain during the folding of the strata was mostly negligible. The rotated state of Fig. 5.12A is equivalent to stage 2 in the hypothesis of Fig. 5.11.

A.) Tectonic-strain ellipsoids   ### B.) Finite-strain ellipsoids

| not rotated | rotated | not rotated | rotated |
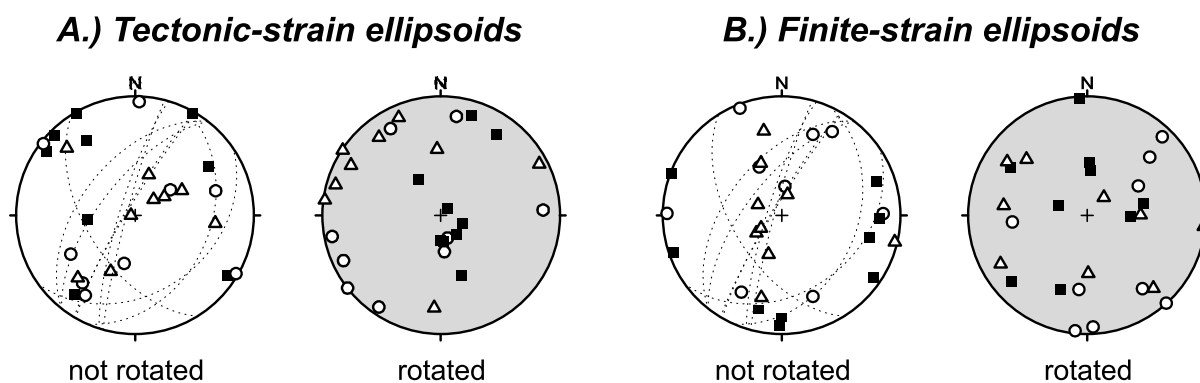
Figure 5.12: Schmidt-net projections (lower hemisphere, equal area) of the principal axes (X = black squares, Y = open circles, Z = open triangles) of the measured (not rotated) and the rotated strain ellipsoids (horizontal bedding) of all samples with X or Y perpendicular to the bedding (= ke01, ke04, ke06, ke07, ke13, ke15, ke23, ke44, and ke45, see Fig. 5.10). After rotation, the principal axes of the tectonic-strain ellipsoids (**A.**) show a very similar orientation for all samples (clustering of X in the centre, Y and Z lie on a great circle). This proves that they are mainly dominated by pre-rotational strain. This effect is not visible in the finite-strain ellipsoids (**B.**) which may be due to the very small length differences between the principal axes of each sample.

The same operation performed on the finite-strain ellipsoids (Fig. 5.12B) did not show the same result. The correlation of the principal axes of the rotated state is not higher than in the unrotated state. This could be due to the very small length differences of the principal axes in the finite-strain ellipsoids that facilitates switching of axes by very small strain inhomogeneities (Fig. 5.6). The finite-strain ellipsoids can either be interpreted as weak compaction (Z normal to bedding) or a weak ductile strain ellipsoid (X normal to bedding). After decompaction, most of the samples have a 'ductile strain ellipsoid' (X normal to bedding, cf. Fig. 5.10). Only post-tectonic samples (ke03, ke20) and three samples from the Eastern Altiplano (ke05, ke08, ke09) from an anticlinal core (shallow burial, very little rotation) have the short axis (Z) normal to the bedding, i.e. still show the compaction ellipsoid.

The two outlier in the rotated state of Fig. 5.12A have a steep medium axis (Y) and nearly horizontal X and Z in the rotated state. These are samples from the hanging wall of the San Cristóbal Fault (ke44 and ke45). The trends of the long axes parallel the NNE–SSW trending San Cristóbal Fault. This may indicate that these samples recorded some strain during folding. Furthermore, this could also be interpreted as an indicator of a strike-slip component along the San Cristóbal Fault. It is interesting to note that these are the only two sample locations where the long axes of the tectonic-strain ellipsoids parallel the structural strike of the Southern Altiplano. The remaining samples have their long axes normal to bedding and often their intermediate axes in N–S or NNE–SSW direction. This is additional evidence for the hypothesis that only small amounts of strain were accumulated during the folding. A high amount of out-of-section material loss at the grain-size scale, accumulated during the folding, would stretch the ellipsoids along strike resulting in long axes oriented parallel to strike.

The observed orientation of tectonic-strain ellipsoids, i.e. the orientation of the long axis perpendicular to the bedding and to the fold axis, requires the accumulation of ductile strain prior to folding. If the tectonic strain during folding was higher, the long axes of the strain ellipsoids would be oriented parallel to the fold axes and not perpendicular to it, as they are. The present orientations clearly show that the largest amount of ductile, i.e. pervasive, micro-scale strain
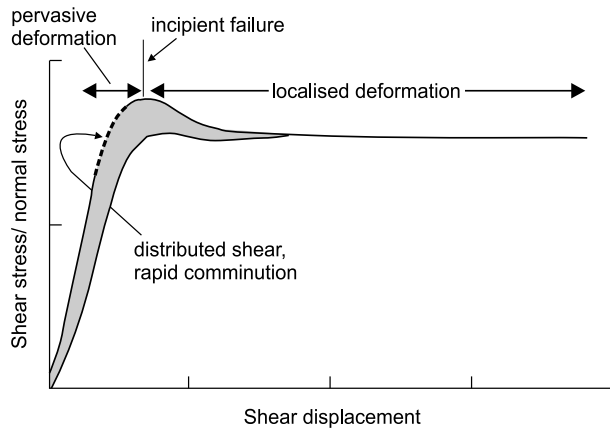
Figure 5.13: Stress vs. displacement diagram, modified after Marone (1998). It illustrates the transition from pervasive deformation to localised shear in terms of the shear stress/normal stress ratio. Dashed line marks the area where distributed shear reaches maximum values which results in rapid comminution and the accumulation of ductile strain. Localised deformation on discrete faults starts beyond the point of incipient failure and leads to the decrease of the shear stress/normal stress ratio. See text for further explanation.

was accumulated prior to folding and thrusting. Ductile strain during the folding could not reset the previously-formed strain ellipsoid; its main effect was rotation.

The observation that the highest portion of pervasive strain was accumulated prior to discrete deformation is consistent with the strain-stress graphs based on the results of rock-friction experiments and analogue modelling (Marone, 1998). Fig. 5.13 illustrates that penetrative deformation occurs only on the ascending part of the curve. Beyond the point of incipient failure deformation is localised on faults. The graph also shows that the amount of distributed (ductile) strain is highest where the shear stress/normal stress ratio reaches a maximum value.

The comparison of the Flinn Graphs of the finite (Fig. 5.5) and the tectonic-strain ellipsoids (Fig. 5.14) reveals a general shift of data points from the oblate domain to plane strain and the prolate field. The highly-prolate strains (samples ke04, ke05, ke06, and ke23) are a result of the superposition of very similar oriented finite strain and the inverse compaction ellipsoids (see Fig. 5.6 and Fig. 5.10). The E–W trend of the long axis of the finite-strain ellipsoid of sample ke04, which was derived from an anticlinal core, can be interpreted as extension in the outer arc of the anticline (above the neutral line), as described by Ramsay and Huber (1983b, p. 457ff).

A general problem of strain analysis of unconsolidated rocks is that large amounts of strain can be accumulated by grain-boundary sliding prior to the intra-grain deformation. This strain cannot be measured with the R_f/ϕ' Method because R_f/ϕ' only uses the grain shape and orientation but not the mutual relationship of the neighbouring grains. In this case, the removal of the total compaction from the finite ellipsoid would underestimate the tectonic strain.

The Fry Method, on the other hand, accounts for the distance between neighbouring particles and should therefore be able to cope with grain-boundary sliding as long as the slip vector is typically less than the mean grain size. Evidence for a very small component of grain-boundary sliding comes from the 2D strain results of the Series A samples: the similarity of the R_s values determined with the Fry and R_f/ϕ' method for grain-supported samples, varying only up to $\pm 10\%$ (see section 5.3.1 and Fig. 5.4). Thus I consider effects due to grain-boundary sliding to be negligible.

Sample ke06 is the only Paleozoic sample. It is interesting to note that the measured strain ellipsoid (with a small strain intensity, see Table D.7) does not differ significantly from the other samples in the same area. This may be additional support of the sedimentologically-derived thesis that the Silurian rocks only experienced Andean shortening, and that the Carboniferous deformation that was reported for the Eastern Cordillera of southern Bolivia (Jacobshagen et al., 1999) did not reach the Southern Altiplano (cf. section 3.1).
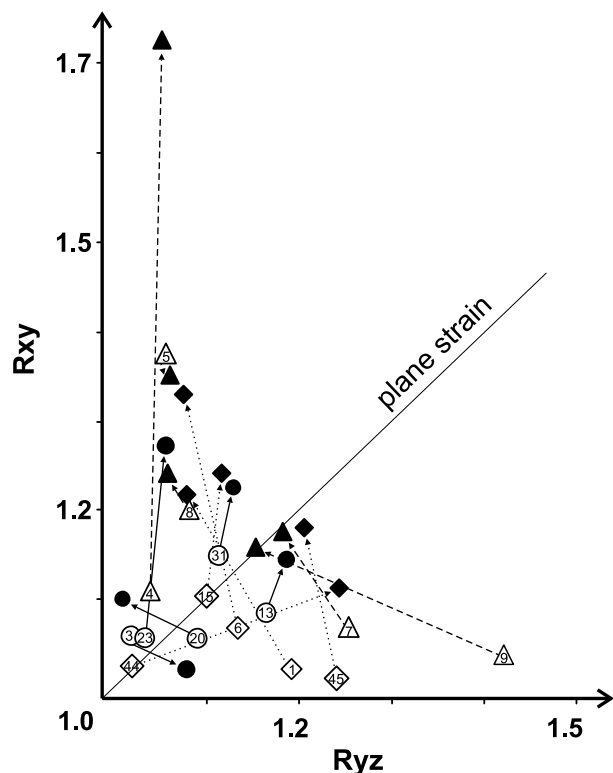
Figure 5.14: Flinn Graph of finite (white with sample number) and tectonic-strain ellipsoids (black). Arrows show the change of data points during decompaction (black arrows and circles = post-tectonic or minor deformation, dashed arrows and diamonds = samples from the Eastern Altiplano, dotted arrows and triangles = samples from the Central Altiplano).

5.6   Implications of strain for the balanced cross-section

Von Winterfeld and Oncken (1995) developed an algorithm to quantify the line length and thickness correction and the magnitude of ductile strain from 3D strain data. I used the (decompacted) tectonic-strain ellipsoid, not the finite-strain ellipsoid, because the aim was to quantify the amount of tectonic strain accumulated in the Southern Altiplano (strain during folding and thrusting but also ductile micro-scale strain).

The required line length and thickness corrections for each sample are shown in Table D.9. The input for each sample is a mixture of 2D and 3D data. The program requires that one principal plane of the strain ellipsoid parallels the cross-section plane. The program tolerates slight angles between the two planes, but gives wrong results if there is a high angle between the profile plane and the respective principal plane of the strain ellipsoid. For this study, I did not interpret samples with an angle greater than 30° between the cross-section plane and a principal plane of the strain ellipsoid. This is the case for samples ke04, ke13, ke15, and ke31 (see Fig. 5.10). Consequently, the line-length correction for these samples was not calculated.

The output is the line-length correction in percent for both the XY plane of the strain ellipsoid, which is equivalent to the 'out-of-plane mass transfer' in direction of the fold axis, and in the so-called *P90* plane, the vertical profile plane 90° to the fold axis corresponding to samples with the suffix -3. For the *P90* plane two values are given; '*in P90 ∥ bed*' is the required line-length correction for the undeformed section and '*in P90 ⊥ bed*' the corresponding thickness correction of the beds (*bed* = bedding). The output values listed in Table D.9 are with respect to the orientation of the bedding plane (*P90* is the plane orthogonal to both the bedding and the fold axis, XY the principal plane of the tectonic-strain ellipsoid). Positive values indicate that ductile strain resulted in line-length increase (= stretching), negative values indicate line-length reduction, i.e. shortening as the result of micro-scale strain.

The dip direction of the bedding does not always correspond with the direction of the balanced cross-section. Therefore the output values for the horizontal planes (*'hor in XY'* and *'in P90 ∥ bed'*, see Table D.9) were corrected in map view to values perpendicular to the cross-section plane, and to lie in the cross-section plane and horizontal. Fig. 5.15 demonstrates this correction. The percentage line-length corrections for the two directions can be transformed into an ellipse (e_x = *'hor in XY'*, e_y = *'in P90 ∥ bed'*). The correction is simply the calculation of straight lines cutting through the ellipse that are different from the principal axes (after Ramsay and Huber (1983a), see also Equation D.1). The angle between the principal axis and the new line is determined by the angle between the cross-section and the strike of bedding. The new values for horizontal line-length corrections of the undeformed profile in the cross-section plane ($∥$ *bed*) and perpendicular to the cross-section plane ($⊥ CSP$) are given in the last two columns of Table D.9.

For isovolumetric strain ($dV = 0$), the values for the length correction parallel to the bedding in the undeformed cross-section plane ('$∥$ *bed*' in Table D.9) have either positive or negative values. All samples with the short axis of the tectonic-strain ellipsoid perpendicular to the bedding (ke03, ke08, ke09, ke20, see Fig. 5.10 and Fig. 5.8) have positive values, i.e. ductile strain resulted in extension parallel to the axial trend. Sample ke05 has a slight compaction ellipsoid and a correction value around zero. Ke06 is an exception. All samples that show the ductile strain ellipsoid (ke01, ke07, ke23, ke44, ke45, see Fig. 5.10 and Fig. 5.8) have negative correction values, i.e. experienced additional shortening parallel to the bedding due to ductile strain. All samples have positive correction values perpendicular to the cross-section, i.e. parallel to the structural trend ('$⊥ CSP$', Table D.9). This indicates out-of-section material loss, and consequently, the amount of shortening from the balanced cross-section is an underestimation.

The correction of the balanced cross-section for ductile strain was achieved using an average value for the line-length correction. The structural position of each sample was important for choosing an appropriate correction factor. The samples from the Eastern Altiplano were derived mainly from anticlinal hinges, as seen from the ∼E–W direction of the ellipsoids' long or intermediate axes (samples ke04, ke05, ke08, ke09, Figs. 5.10 and 5.6), which indicate extension above the neutral line of an anticline (Ramsay and Huber, 1983b). In these cases a sample from below the neutral line should show E–W compression. To obtain an average value, strain values from above and below the neutral line have to be taken into account. Positions below the neutral line are buried beneath the surface and could not be sampled. An integration of only the samples above the neutral line in the calculation of the average value would falsify the average value. Therefore, only sample ke07, which was taken from the flank of an anticline, was used to derive the average correction value in the Eastern Altiplano. In the Central and
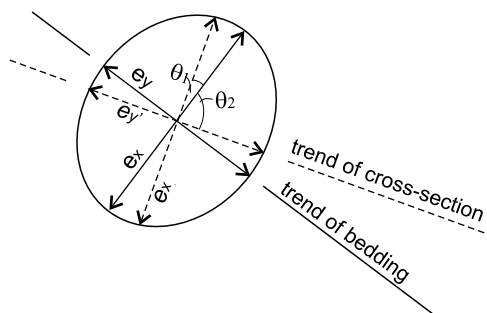
Figure 5.15: Calculation of the line-length correction values in cross-section plane in map view. e_x and e_y are the principal axes of the ellipse where e_x is perpendicular to bedding. The aim is the calculation of the length of the principal axes in the horizontal cross-section plane ($e_{x'}$) and orthogonal to the cross-section plane ($e_{y'}$, calculated with Equation D.1; $θ_1$ and $θ_2$ were used to calculate $e_{x'}$ and $e_{y'}$, respectively).
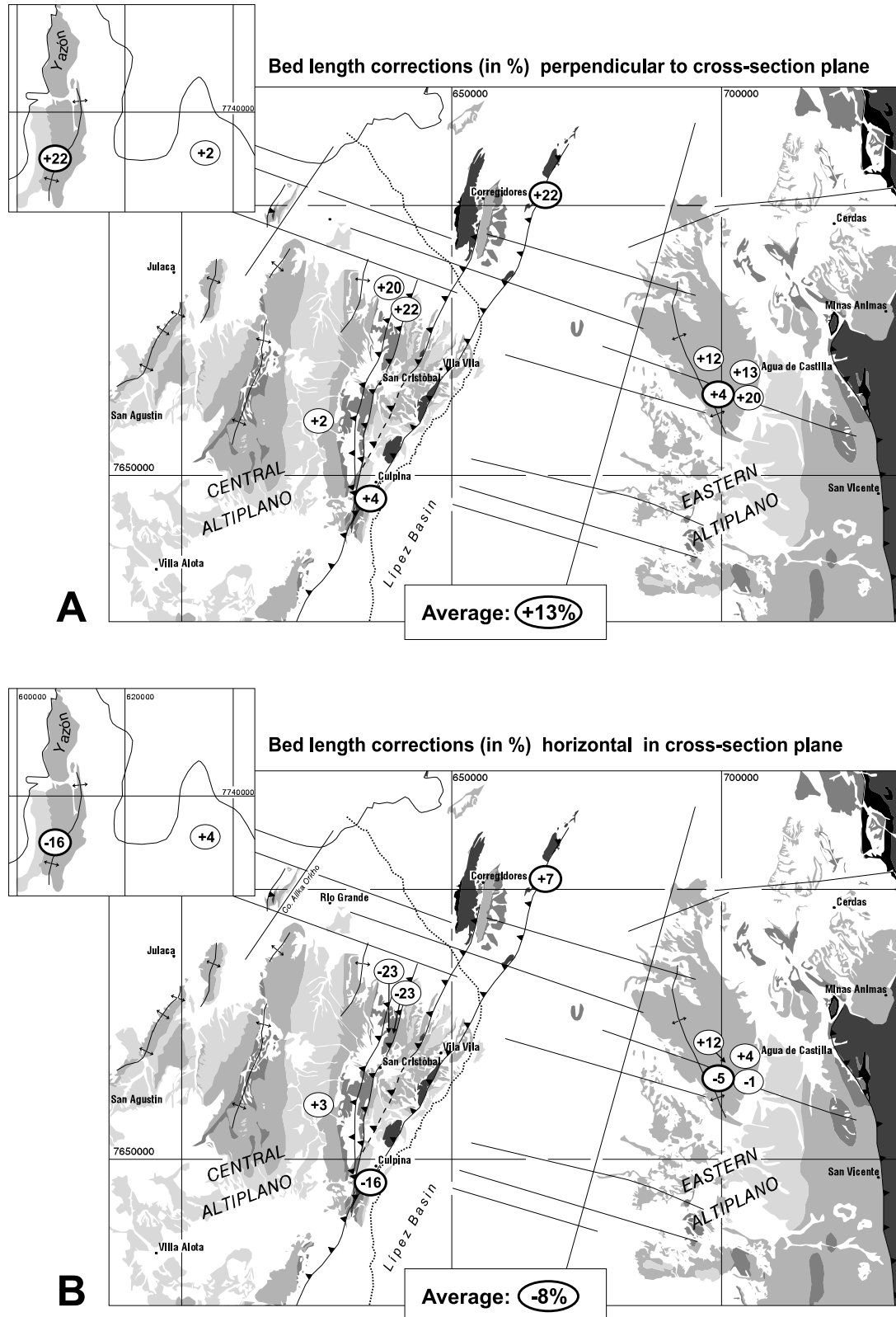
Figure 5.16: Changes of bed length in the Southern Altiplano during deformation perpendicular (a) and parallel (b) to strike (constant volume assumed). Positive numbers show stretching, negative numbers correspond to shortening. The average was calculated only using values encircled with a bold outline. See text for further explanation and Fig. 5.1 for legend.

Western Altiplano, only samples ke01, ke06, and ke23 were candidates for the calculation of the average value. Samples ke03 and ke20 are post-tectonic and did not record the entire ductile strain. Samples ke44 and ke45 are exceptional because they are from an area close to a major fault and may have been influenced by strike-slip movements (cf. section 5.5).

The average correction value for longitudinal strain of bedding in cross-section plane is $-7.7 \pm 9.3\%(1\sigma)$. The corresponding correction perpendicular to the cross-section is $+13 \pm 9.2\%$ (1σ), and the correction of the bed thickness $+9.6 \pm 6.4\%$ (1σ) (mean values of line-length corrections horizontal in the cross-section plane ($= \parallel$ bedding in the undeformed section), perpendicular to the cross-section plane ($\perp$ *CSP*), and vertical in the cross-section plane (*'in P90 $\perp$ bed'*) of samples ke01, ke06, ke07, and ke23).

The consequence for the balanced cross-section is an additional shortening of 7.7% due to ductile strain, which is equivalent to 8.6% stretching of the restored profile. The horizontal shortening was compensated by 13% orogen-parallel extension and 9.6% increase of bed thickness.

These correction values are maximum values because they were calculated assuming that the strain is isovolumetric, i.e. there was no net material change ($dV = 0$, cf. Table D.9). Dittmar (1996) showed that the amount of orogen-parallel extension decreases with increasing volume loss during deformation. Dittmar (1996) also showed that $+15\%$ orogen-parallel extension for the case of isovolumetry is equivalent to 0% orogen-parallel extension with 30% volume loss. In the case of the Southern Altiplano, a volume loss of 30% is quite unlikely, because of the absence of any indication for a significant loss of pore volume in the rock fabric (such as the existence of pressure solution shadows, crack-seal structures, indications of collapsing pore space, etc.). Consequently, this favours the existence of a certain amount of orogen-parallel extension during ductile strain.

5.7   Strain analysis — conclusions

The very small ellipticities of the finite-strain ellipsoids are because compaction and tectonic strain had the same order of magnitude. Local strain inhomogeneities were responsible for the broad range of shape and orientation of the principal axes of the finite-strain ellipsoids.

The orientation of most of the tectonic-strain ellipsoids (i.e. long axis orthogonal to the bedding) can be best interpreted with a model in which most of the strain accumulates during early ductile shortening ahead of the approaching deformation front, followed by subsequently bed rotation. During folding of the strata, only minor amounts of ductile strain were accumulated.

The general structural trend of the Southern Altiplano has an influence on the orientation of the strain ellipsoids, as shown by the N–S to NNE–SSW trend (parallel to sub-parallel to major structures) of one principal axes of the tectonic-strain ellipsoid (mostly X or Y) of many samples. Exceptions to this generalisation occur where local strain inhomogeneities exist, e.g. in fold hinges. This indicates that penetrative deformation (visible in the strain data) and localised deformation (folding and thrusting) were co-genetic, i.e. the ductile strain represents an early stage, while the formation of folds and thrusts occurred during the later stages of the same deformation increment. This is consistent with strain-stress experiments which show that the highest amount of penetrative deformation (= ductile strain) accumulates prior to the decrease of the critical shear stress due to the formation of localised shear zones (Marone, 1998, see also Fig. 5.13).

Furthermore, the observation that only minor amounts of ductile strain were accumulated during the folding of the strata is an additional indicator for the 'flexural-slip' deformation mechanism (see introduction to chapter 4). During flexural-slip folding, all deformation occurs by slip of the layers past each other, i.e. the deformation is restricted to planes between the component layers, in this case bedding planes (Twiss and Moores, 1992, p. 239ff). The layers themselves are characterised by little internal deformation (McClay, 2000, p. 55). Because all strain samples were taken from the competent layers, the results of the strain analysis do not show the complete deformation of the strata during folding. That is, the strain results show only the ductile strain which was accumulated prior to the folding of the strata. Penetrative strain and localised deformation (folds and thrusts) were probably derived in the same kinematic realm.

With exception of Population 2, the orientation of main kinematic axes, determined from local fault-striation data (Fig. 4.5), is different to that of the principal strain axes (compare Population 2 in Fig. 4.5B with the rotated state of Fig. 5.12A). Because strain ellipsoids image the finite deformation, in contrast to local fault-striation data, the similar orientation of principal strain and kinematic axes suggest that the NW–SE compression and vertical extension of Population 2 could represent the main population among the local fault-striation data, which is slightly oblique to the trend of major structures.

The strain measurements suggest 7.7% additional shortening in balanced cross-section profile plane, together with 13% orogen-parallel extension and a 9.6% increase of bed thickness.

5.8 Error discussion

Errors occur at every step of the strain analysis. They are generated while collecting the oriented sample in the field (How representative is the measured plane? Is it planar or not? How accurate is the measurement of the bedding plane?) and the sample preparation in laboratory (e.g. is the angle between all thin-sections 90°?). These errors are small ($< 5\%$), inevitable, and almost negligible because angular differences of $\pm 10°$ are negligible in trigonometric functions, especially near the principal planes of the ellipsoid, where the angle between the planes is close to 90°.

The errors during the strain measurement itself are presumably higher. These include inaccuracies during the digitisation of the samples (determination of the inscribed ellipse), errors to determine the finite-strain ellipsoid from the Fry or R_f/ϕ' Graph during the 2D strain analysis, and during the following calculation of the 3D strain ellipsoid, based on the 2D results. These errors generally decrease with an increasing number of measured grains.

The application of the least-squares ellipse algorithm in addition to the normalisation of the inter-marker distance minimises the error during the Fry analysis with INSTRAIN (Erslev and Ge, 1990, see section 5.2.1.1) and avoids the subjectivity inherent in the visual interpretation of the data.

The minimal errors for the Fry-analysis are achieved with the 'Enhanced Normalised Fry Method' (see sections 5.2.1.1 and 5.2.2). Here the 'mean radial error' for the measurement of 300 or 400 grains in a sandstone is described to be $13\% \pm 2\%$ or $\pm 1.25\%$ respectively (Erslev and Ge, 1990). For the R_f/ϕ' Methods the errors are not stated (Erslev and Ge, 1990). The χ^2 test of R_f/ϕ' after Peach and Lisle (Peach and Lisle, 1979) provides a graphical control of the

quality of the data. The errors of the R_f/ϕ' measurements are possibly of the same order of magnitude as those of the Fry analysis and are approximately lower than 20%. The effect of the error in the calculation of the 3D strain ellipsoid is definitely smaller. This is because of the insensibility for angular variations of the trigonometric functions that were used to determine the strain ellipsoid. Angular variations of$\pm\,10°$ with respect to $0°$ or $90°$ will change the result of a sine calculation to the second decimal place.

The largest error, however, lies in the determination of the inverse compaction ellipse. For the calculation, typical published values (e.g. Angenheister, 1982; Sclater and Christie, 1980) for the porosity of sandstones and siltstones were used. Table 5.1 gives an overview of these values.

Fig. 5.17 are porosity-depth-graphs calculated with the value range given in Table 5.1. The compaction modulus k determines the gradient of porosity loss with depth. Small k values indicate rapid porosity loss at shallow depths (down to $\sim 2000\,\text{m}$) and a smaller gradient below 2000 m (48% porosity at surface, 4.6% at $-2000\,\text{m}$, and 0.4% at $-4000\,\text{m}$, calculated with $k_{\max}$). A high k value leads to a more continuous porosity decrease with depth (48% porosity at surface, 19.9% at $-2000\,\text{m}$, and 8.3% at $-4000\,\text{m}$, calculated with $k_{\max}$). The higher the k-value, the smaller the porosity-loss gradient, and the shorter the length of the inverse compaction ellipsoids' long axis (see Fig. 5.17A and Table 5.2). The variations due to different initial porosity values have a noticeably smaller error (see Fig. 5.17B).

Table 5.2 and Table 5.3 show the influence of varying k values (Table 5.2) and varying initial porosity (Table 5.3) on the calculated length of the long axis of the inverse compaction ellipsoid (e_x). Both tables show that the variation of e_x increases with depth. For most samples, the maximum burial depth is $< 1500\,\text{m}$. For different initial porosity, the e_x variation at 1500 m depth is 0.165 ($e_{x(\phi_{0(\min)})} - e_{x(\phi_{0(\max)})}$). This difference is negligible because it lies within the rounding error of 'Shear3.0'. The difference due to varying k values is substantially higher at 1500 m depth ($e_{x(k_{\max})} - e_{x(k_{\max})} = 0.38$).

To determine the influence of different k values on the line length and thickness correction of the balanced cross-section, I decompacted one sample (ke06) with the maximum and minimum length of e_x of the inverse compaction ellipsoid, then calculated the 'maximum' and 'minimum' tectonic-strain ellipsoid, and the line length correction. Table 5.2 and Table 5.3 demonstrate an increasing variation of e_x with depth. Sample ke06 has a maximum burial depth of 1400 m. The 'error calculation' with this sample approximates a maximum error because most samples were more shallowly buried (see Table D.5). The three deeper-buried samples have a different lithology (silt: ke44 and ke45) or are not representative (ke04, see section 5.5).

Fig. 5.18 shows the effect of different k values on the length and orientation of the tectonic-strain ellipsoid. The table on the right gives the resulting error for the line length and thickness correction. The orientation of the principal axes of the tectonic-strain ellipsoid does not vary much. The line-length correction in the XY plane of the sample (= parallel to the trend of the fold axis) is +24.2% for the average ellipsoid, +21.14% for the minimum ellipsoid, and +31.43% for the maximum ellipsoid (minimally decompacted). The line-length correction of the average ellipsoid in direction of the trend of the fold axis is +24.2 +7.23/−3.06%. The error is slightly higher normal to the cross-section plane (= out-of-section material flow: +21.92 +7.37/−3.63). It is interesting to note that the error for the line-length correction of the cross-section plane ('*in P90*$\|$ *bed*' and (horizontal) in the cross-section plane (*in CSP*) has the same magnitude (e.g. +6.49 +7.93/−6.4%).
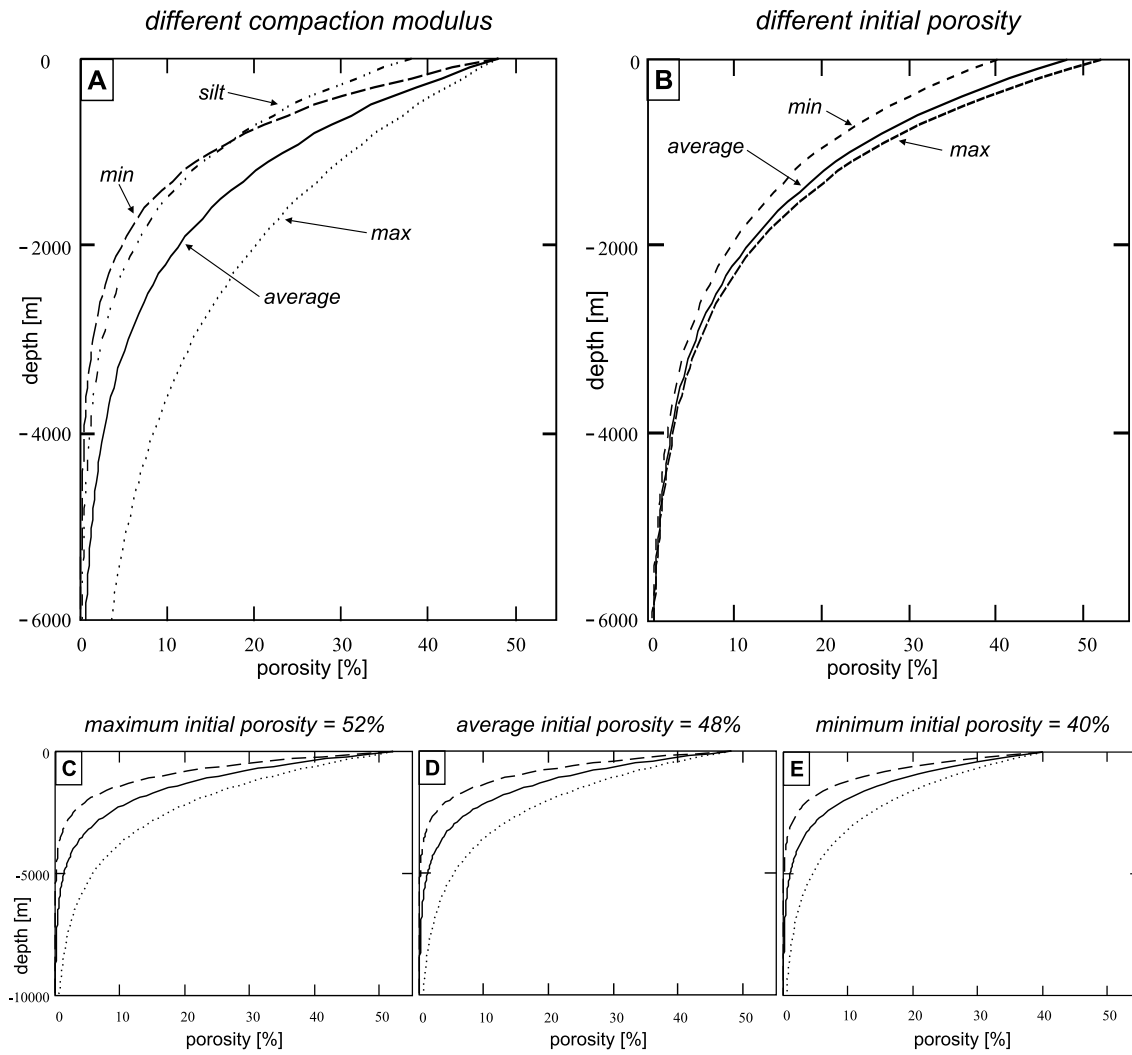
Figure 5.17: Porosity-depth-graphs calculated with different values given in Table 5.1. See text for explanation.

depth [m]	e_x $(k_{\mathrm{aver.}})$	e_x $(k_{\max})$	e_x $(k_{\max})$
100	**1.035**	0.983	1.142
300	**1.104**	1.025	1.248
500	**1.171**	1.066	1.346
1000	**1.330**	1.169	1.553
1500	**1.468**	1.267	1.647
2000	**1.582**	1.358	1.790
3000	**1.742**	1.516	1.880
4000	**1.831**	1.639	1.909

Table 5.2: The influence of different k values on the calculation of the long axis of the inverse compaction ellipsoid (e_x).

depth [m]	e_x $(\phi_{0(\mathrm{aver.})})$	e_x $(\phi_{0(min)})$	e_x $(\phi_{0(max)})$
100	**1.035**	1.029	1.038
300	**1.104**	1.085	1.113
500	**1.171**	1.139	1.188
1000	**1.330**	1.261	1.367
1500	**1.468**	1.362	1.527
2000	**1.582**	1.442	1.663
3000	**1.742**	1.550	1.856
4000	**1.831**	1.608	1.967

Table 5.3: The influence of different k values on the calculated long axis of the inverse compaction ellipsoid (e_x).

Length correction in %

sample	hor. in XY	⊥ CSP	P90 ∥ bed	in CSP	P90 ⊥ bed
ke06	+24.20	+**21.92**	+5.14	+**6.59**	−6.02
ke06min	+21.14	+**18.29**	−1.44	+**0.19**	−5.38
ke06max	+31.43	+**29.29**	+13.09	+**14.52**	−14.87
Variation	−3.06	−**3.63**	−6.58	−**6.40**	−0.64
	+7.23	+**7.37**	+7.95	+**7.93**	+8.85
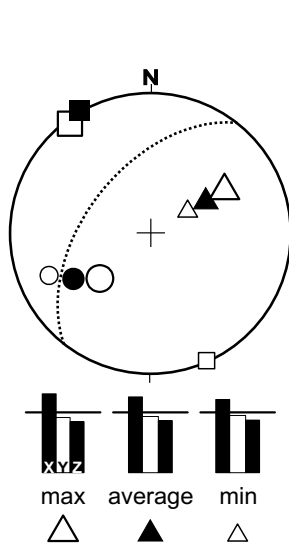
Figure 5.18: Schmidt-net projection (left) of the principal axes (X squares, Y circles, Z triangles) of the orientation of tectonic-strain ellipsoid and the normalised axes length of sample ke06 calculated with different compaction modules. The table shows the corresponding results for the line length and thickness correction with respect to the sample sections and the cross-section plane (*CSP*, see Table D.9 for nomenclature).

These errors should be regarded as maximum errors. The variation of the line-length correction for samples with a smaller maximum burial depth (see Table D.5) is smaller because of the smaller difference between the minimum and maximum length of the inverse compaction ellipsoids' long axis (e_x in Table 5.2).

The error associated with the deepest samples (ke44 and ke45) cannot be determined because there is no published range for the initial porosity or the compaction modulus k for siltstones (see Table 5.1).

Chapter 6

Isotopic age determination

One main objective of this study was to determine the ages of tectonic activity, based on isotopic age determinations of volcanic rocks (tuffs) in key structural positions. In particular the youngest deformation history of the Central Altiplano was deciphered by age dating of volcanic intercalations in syn-tectonic basins along the balanced cross-section. This chapter describes and discusses the results and the quality of isotopic age determinations using the Ar-Ar and K-Ar methods. The geological interpretation of the data and their importance for the history of the Southern Altiplano will be discussed in chapters 8 and 9.

From the known ages of two samples at different depths from the same syn-tectonic basin the sedimentation rate can be calculated. Furthermore, because the history of these basins is intimately linked to the formation of the related structures (anticlines), sedimentation rates are linked to rates of tectonic movement. This was, however, impossible to determine for all syn-tectonic basins of the Southern Altiplano. The rapid redistribution of sediments, a typical feature of the Pilkhaua Subsequence (cf. section 3.3.3.1), resulted in the preservation of only one volcanic horizon within the same basin. In addition, interbedded tuffs are typically thin (2–10 cm) and do not occur in every syn-tectonic basin of the Central and Western Altiplano.

The samples for Ar-Ar age determination are mainly from syn-tectonic basins of the Central and Western Altiplano. I analysed five samples from three different basins (ke24-00, ke30-00, ke39-00, ke40-00, and ke41-00), plus one additional post-tectonic sample (ke13-00) and one sample from the youngest pre-tectonic strata (ke28-00, see Table C.1 and App. F.1 for sample locations, bedding and structural positions).

Ke28-00 and ke24-00 are tephra from the Yazón Peninsula. Ke28-00 is a sample of the youngest pre-tectonic tuff of the San Vicente Fm. from the vertically-inclined forelimb of the Yazón Anticline (see Fig. 4.3). Ke24-00 was taken only 50 m further west in the basal part of the syn-tectonic Pilkhaua sediments, ~5 m above the basal conglomerate. The 4 cm thin tuff was tilted 48° westwards. Sample ke24-00 represents the oldest available syn-tectonic age of the Yazón Anticline. Ke01-00 and ke30-00 were interbedded in the syn-tectonic basin west of the Ines Anticline (Central Altiplano) and dip in WNW-direction with 60 and 40°, respectively (see Fig. 7.12 and Table C.1). Ke39-00, ke40-00, and ke41-00 were sampled from the syn-tectonic basin west of the Central Anticline (Cerro Paya Punta, see Fig. 3.1 for location). Ke40-00 is mildly tilted (272/15) and ke39-00 lies horizontally. They were deposited during or after the latest stages of thrusting. Ke41-00 is a volcanic clast within the steeper parts of the same basin (bedding 257/60). The post-tectonic sample Ke13-00 is from an ignimbrite of the southern Central Altiplano.

The complementary, sedimentological work of P. Silva-Gonzáles (in prep.) aims to date stratigraphic formations of the Southern Altiplano. I mainly used stratigraphic ages for correlation purposes of the Eastern and the Central Altiplano. Therefore, five samples of crystal or tephra tuffs within in the San Vicente Fm. were analysed using the K-Ar method. Samples ke06-99 and ke10-99 were taken from the eastern flank of the Vilque Anticline in the Eastern Altiplano, sample ke19-99 is from the eastern flank of the Ines Anticline in the Central Altiplano, and samples ke11-99 and ke12-99 come from the northern part of the Yazón Peninsula in the Western Altiplano.

This chapter is divided in three parts: In the first section I will give a short overview of sample characteristics and of the separation procedure to obtain the mineral concentrates (6.1), followed by the description of the K-Ar and Ar-Ar techniques (6.2). The last part (6.3) addresses the evaluation of the results and discusses their quality and geological significance. The analytical data tables are shown in Appendix C.

6.1   Samples and mineral separation

In this project, five samples were analysed with the K-Ar method and another eight using the Ar-Ar approach. Additional thirty three K-Ar ages were acquired in the parallel project (Silva-González, in prep.). The K-Ar analyses, including sample preparation, were accomplished by Geochron Laboratories, a division of Krueger Enterprises in Cambridge, USA. For Ar-Ar analyses I first checked the samples in thin section for mineral intergrowth and signs of alteration or weathering. Subsequently, minerals suitable for age determination were identified and prepared in the mineral separation laboratories at GFZ Potsdam. The mineral separates were then sent to the geochronological laboratories of the University of Vienna, Austria (Prof. Dr. W. Frank) for further processing.

Mineral separation followed standard procedures (crushing, Frantz magnetic separator, heavy liquids). The obtained concentrates were further processed as indicated in Table 6.1.

6.2   The K-Ar system

Age determinations using the K-Ar system are based on the radioactive decay of ^{40}K to ^{40}Ar. The evaluation of this decay scheme, in terms of geochronology, is only directly possible if the following conditions are met:

- No excess ^{40}Ar was incorporated into the mineral either at the time of mineral formation or at any later event. All of ^{40}Ar in the mineral is a product of the in-situ decay of ^{40}K.

- The mineral became closed to K and Ar after a specific, short-term event; either at its formation or at a specific temperature during cooling. Since this event, there was no exchange with the surrounding rock, neither assimilation nor release of K or Ar, i.e. the mineral was a closed system. Isotopic ages of tuffs are normally interpreted as extrusion ages because of the almost instantaneous cooling during extrusion.

Sample	mineral	rock type	amount [mg]	sieve fraction [mm]	Mineral enrichment and purification procedure
Ke01-00	bi	tephra	100.6	> 0.250	enriched by adhesion on paper, then ground in ethanol and sieved
Ke13-00	bi	ignimbrite	47.0	> 0.355	enriched by adhesion on paper, then ground in ethanol and sieved
Ke24-00	bi	tephra	5.4	0.160–0.355	picking of large phenocrysts
Ke28-00	hbl	tephra	46.18	0.2–0.5	picking, 2 min leaching with *HF* (20%) in an ultrasonic bath
Ke30-00	hbl	tephra clast	100.48	0.25–0.5	picking, 2 min leaching with *HF* (20%) in an ultrasonic bath. Microprobe analysis: average amount of K_2O = 0.8 weight-%
Ke39-00	bi	crystal tuff	87.7	0.355–0.5	enriched by adhesion on paper, then ground in ethanol and sieved
Ke39-00	hbl	crystal tuff	58.0	0.355–0.5	picking, 2 min leaching with *HF* (20%) in an ultrasonic bath
Ke40-00	bi	crystal tuff	169.3	0.5–1	enriched by adhesion on paper, then ground in ethanol and sieved
Ke41-00	hbl	crystal tuff	26.45	0.125–0.18, some 0.18–0.25	Picking, 2 min leaching with *HF* (20%) in an ultrasonic bath

Table 6.1: Sample preparation for isotopic age determinations. GPS co-ordinates of the samples are given in Table C.1 in the appendix. bi = biotite, hbl = hornblende (amphibole).

- The concentrations of K and Ar can be determined accurately; the isotopic composition of Ar must be measured with precision high enough to enable appropriate corrections for possible adherent atmospheric Ar.

6.2.1   The K-Ar method

K-Ar age analysis is based on two separate analyses of ^{40}K and radiogenic ^{40}Ar concentrations of the sample. For the samples of this study, [K] was determined by flame spectrophotometric methods. ^{40}Ar was determined by mass spectrometry (MS-10 static mode mass spectrometer) using isotope dilution methods. For evaluation of the results, it was assumed that no excess Ar was present. The analysis of only one mineral of a rock implies that the possible presence of excess Ar cannot be detected with this method. Ages were determined using the K-Ar age equation:

$$t = \frac{1}{\lambda} \cdot \left[\frac{^{40}\text{Ar}^*}{^{40}\text{K}} \cdot \left(\frac{\lambda}{\lambda_\epsilon} \right) + 1 \right] \tag{6.1}$$

with t = K-Ar age, ^{40}Ar* = radiogenic Ar, λ = total decay constant of ^{40}K, λ_ϵ = decay constant for the ^{40}K to ^{40}Ar decay branch.

6.2.2   The $^{39}\text{Ar}/^{40}\text{Ar}$ method

In case of Ar-Ar age determinations, K and Ar abundances are determined simultaneously from one sample aliquot. ^{39}K is converted to ^{39}Ar by irradiation with fast neutrons in a nuclear reactor. In first approximation, the amount of ^{39}Ar generated in this way is dependent on the neutron dose and the K content of the sample only. Given that the neutron dose was correctly determined, K concentrations are calculated from the amount of 'artificial' ^{39}Ar that was generated in the sample. With this approach, all parameters of the K-Ar system of a sample can be obtained simply from the analysis of the isotopic composition of the sample Ar after irradiation. For the analysis, sample Ar is liberated by heating, often in several subsequent stages, and its isotopic composition is analysed in a mass spectrometer. The comparatively long half-life of ^{39}Ar ($t_{1/2} = 269$ years) allows ^{39}Ar to be considered as a stable nuclide during the mass spectrometric analysis.

The Ar-Ar technique has several advantages over 'conventional' K-Ar age determinations:

- K and Ar concentrations can be derived from the same aliquot of sample, by simple outgassing and isotopic analysis of the sample Ar. This avoids uncertainties arising from a possible inhomogeneous distribution of K and Ar in the sample. These uncertainties are highest when only small amounts of samples are available and arise from sample splitting (see section 6.2.1).

- The step-heating technique permits the identification of anomalous sub-systems.

- Information about K/Ca ratios are accessible, since part of the sample Ca is converted to specific Ar isotopes (mainly ^{37}Ar). This information is important to judge whether or not a sample was mineralogically homogeneous, i.e. whether it consisted of only one specific phase. If the K/Ca ratios differ significantly between different degassing steps, the step-heating spectra must be interpreted as multi-phase degassing spectra.

The in-situ partial conversion of ^{39}K to ^{39}Ar allows the liberation of Ar in stages from different domains of the sample and still recovers the full age information of each step. Step heating refers to the stepwise degassing of a sample with increasing temperatures up to the melting point (or to temperatures where Ar is not released anymore). In homogeneous, undisturbed samples (the ideal case), each degassing step will produce the same age. This is not the case for heterogeneous samples. The biggest advantage of the step-heating technique over the conventional 'total fusion' is that the progressive outgassing allows the identification of anomalous sub-systems within a sample. Ideally, these sub-systems can be excluded from age calculation which is then performed using only the 'properly behaved' parts of the sample. This technique can be applied to understand samples which have suffered Ar loss, but it may also help to interpret samples with inherited (excess) Ar. In case of a partially-disturbed system, those domains which are most susceptible to diffusional Ar-loss or Ar-gain, such as the rims of a crystal, should be degassed at relatively low temperatures, whereas domains with tightly-bound argon, which are more resistant to disturbance, should release Ar at higher temperatures.

The results of the step-heating analysis are commonly presented in an Ar-Ar isochron diagram and an age-spectrum plot ('plateau plot'). This demonstrates the history of disturbed samples. According to Dickin (1997), the isochron plot is particularly useful when the presence of inherited (excess) Ar is suspected. The isotope-ratio correlation, which determines the isochron,

allows the quantification of the amount of Ar that did not originate from in-situ decay, and possibly the determination of an accurate age even in presence of excess Ar. The age-spectrum plot gives a more intuitive, direct impression of the degassing procedures' history. To construct the spectrum plot, the size of each gas release at successively higher temperatures is measured by the magnitude of the produced ^{39}Ar ion-beam. Each gas release can then be plotted as a bar, whose length represents its volume as a fraction of the total ^{39}Ar release. The ordinate of the plot shows the $^{40}Ar/^{39}Ar$ ratio, which is proportional to the geological age. Additionally, the spectrum plots contain the K/Ca ratio of each degassing step.

The determination of a reliable crystallisation (or cooling) age from the plateau plot depends on the identification of a 'plateau'. A rigorous criterion for a plateau age is the identification of a series of adjacent steps which together comprise more than 50% of the total Ar release, each of which yields an age within two standard deviations of the mean (Dalrymple and Lanphere, 1974; Lee et al., 1991).

The Ar-Ar analyses were made by Prof. Dr. W. Frank in the fully-automatised laboratory of the Institute of Geology of the University of Vienna, Austria. Detailed information about analytical techniques and age calculation algorithms of this laboratory are given in Frimmel and Frank (1998). See Appendix C for correction and calculation factors of the Ar-Ar analysis.

6.3   Evaluation of the results

The most important observation is the detection of excess Ar in almost all samples that were analysed with the Ar-Ar step-heating technique. This phenomenon occurs in all minerals that were used for age determinations, i.e. in amphiboles (hornblendes) and biotites.

The amount of excess Ar is variable. Some samples have only minor amounts (e.g. ke13-00, biotite), while for others the amount of excess Ar even exceeded the amount of in-situ radiogenic Ar (e.g. ke39-00, biotite). The spectrum plots mostly show successively-decreasing apparent ages with subsequent degassing steps, i.e. with increasing temperatures. This decrease is probably related to the presence of excess Ar particularly in the outer rims of the crystals (Wolfgang Frank, Vienna, Austria, pers. comm.). In several cases, this decrease of apparent ages is limited to the first degassing steps, and reasonable plateaus were formed during later steps (e.g. ke39-00, amphibole). For these samples, the plateau ages can be interpreted as geologically
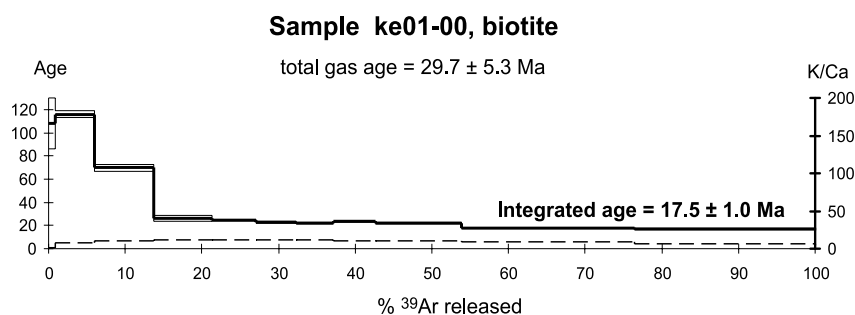
Figure 6.1: ^{39}Ar/^{40}Ar Age-spectrum plot of sample ke01-00 (biotite). Analytical uncertainties are given at the 1σ level; errors of the integrated and total gas ages include an additional error of 0.4% of the J-value. Dashed line show the K/Ca ratio.
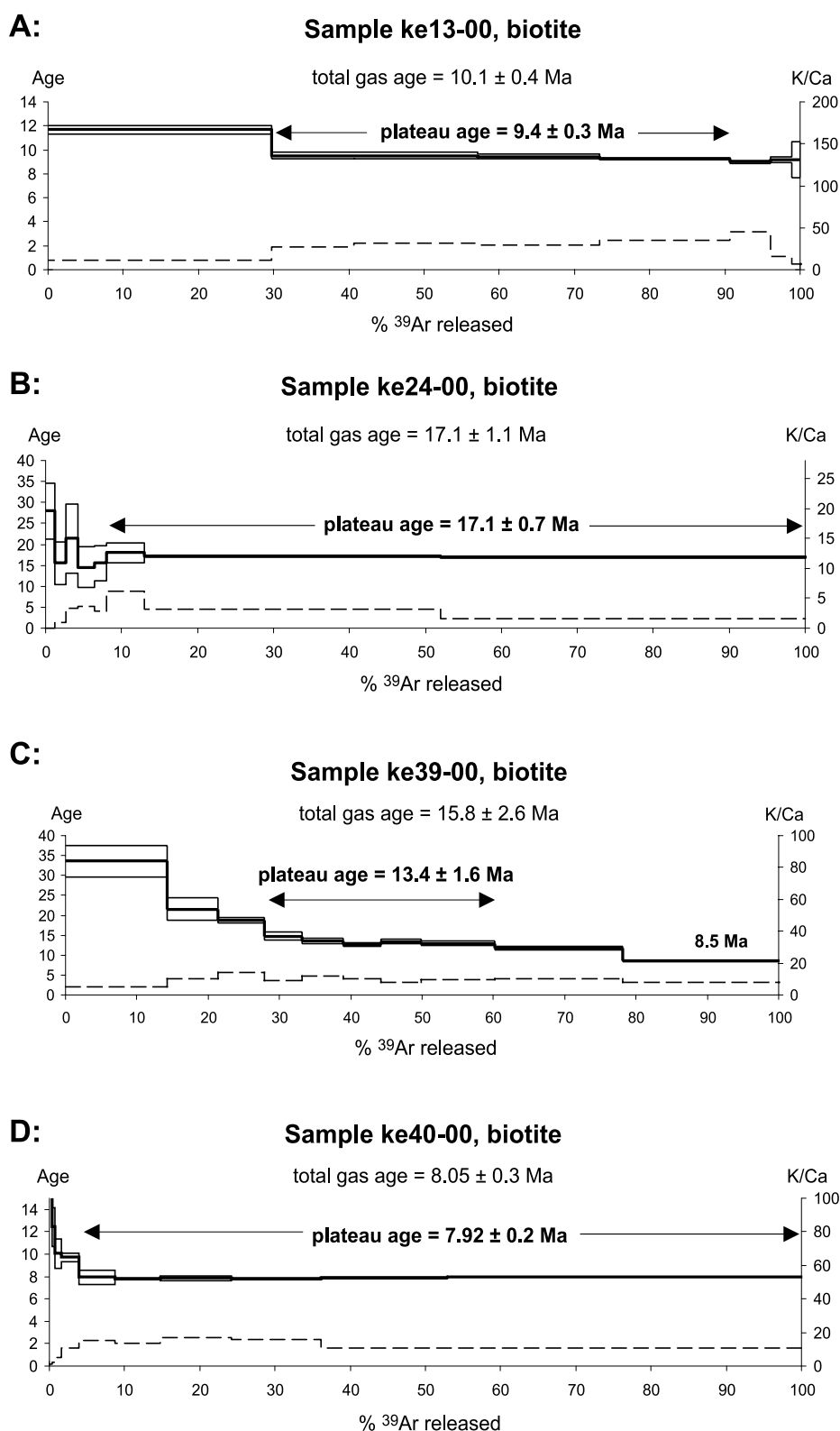
Figure 6.2: ^{39}Ar/^{40}Ar Plateau ages of biotite samples. Analytical uncertainties are given at the 1σ level; errors of the plateau and total gas ages include an additional error of 0.4% of the J-value. Dashed line show the K/Ca ratio.

A: **Sample ke28-00, amphibole**

total gas age = 24.0 ± 2.9 Ma

plateau age = 20.9 ± 2.1 Ma

% ^{39}Ar released

B: **Sample ke30-00, amphibole**

total gas age = 74.5 ± 3.6 Ma

34 Ma

% ^{39}Ar released

C: **Sample ke39-00, amphibole**

total gas age = 9.2 ± 1.4 Ma

Plateau age = 8.3 ± 1.2 Ma

% ^{39}Ar released

D: **Sample ke41-00, amphibole**

total gas age = 32.2 ± 2.1 Ma

Plateau age = 29.3 ± 1.9 Ma

% ^{39}Ar released
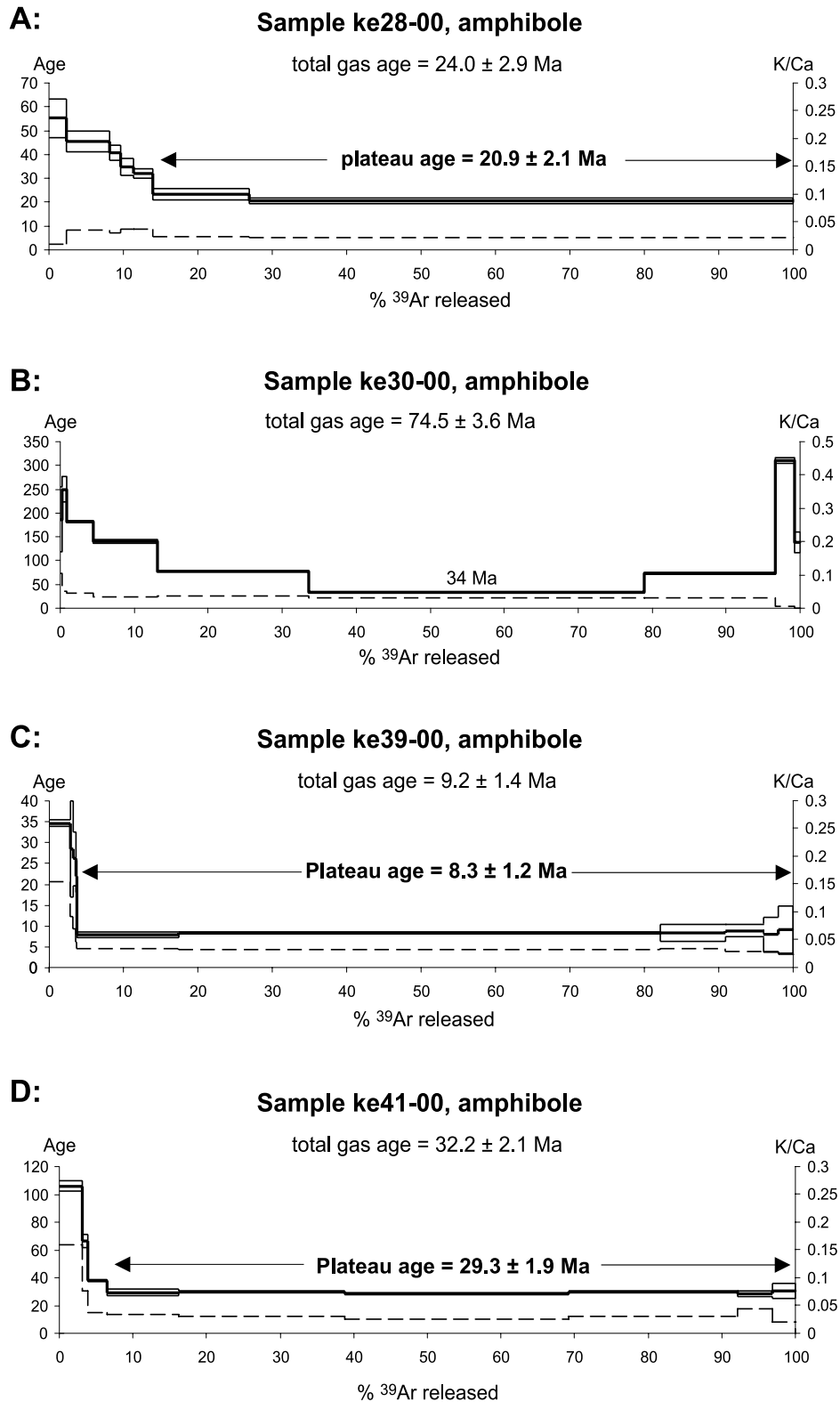
Figure 6.3: ^{39}Ar/^{40}Ar Plateau ages of amphibole (hornblende) samples. Analytical uncertainties are given at the 1σ level; errors of the plateau and total gas ages include an additional error of 0.4% of the J-value. Dashed line show the K/Ca ratio.

significant. In other samples, however, excess Ar persists up to the highest-temperature degassing steps (e.g. ke39-00 biotite). Here, the isochron age is preferred to the plateau age, if a good isotope-ratio correlation exists. If the amount of excess Ar is very high and, additionally, the isotope-ratio correlation is poor (e.g. ke30-00, amphibole), the minimum apparent age of the degassing spectrum may be taken as a maximum extrusion age of the respective tuff.

The observation of abundant presence of excess Ar sets important limitations on the geological significance of the K-Ar ages from similar rocks: Apparently, the crustal anatectic melts that formed the felsic tuffs and ignimbrites were rich in Ar, in particular rich in ^{40}Ar. This Ar was probably liberated during partial melting of geologically old crust in the magma chamber and subsequently incorporated into magma phenocrysts such as biotite and amphibole. Ar solubility is known to be particularly high in felsic, rhyolithic melts (Kelley, 2002), and the presence of excess Ar has been previously noted, e.g. by Singer and Brown (2002), in phenocrysts of rhyolitic magmas. It is very likely that the presence of excess Ar is a general phenomenon in phenocrysts from tuffs and ignimbrites that are petrologically and genetically similar to the rocks that were analysed in the present study. As outlined in section 6.2.1, it is not possible to detect excess Ar in dates that were generated by the conventional K-Ar approach (total gas ages). Its presence, however, must be suspected to contribute to at least some, if not to most of the K-Ar dates, mainly due to the petrological and genetical similarity of all tuffs from the Southern Altiplano. Consequently, all K-Ar dates must be interpreted with caution; most likely they represent maximum ages for the tuff eruption, i.e. the apparent ages may be too high in many cases (compare differences between total gas and plateau ages of the Ar-Ar samples, Table 6.2 and Appendix C).

The primary advantage of the Ar-Ar approach over conventional K-Ar age determination is that the presence of excess Ar may become 'visible'. Most of the dates were be corrected for excess Ar. Meaningful, accurate ages were derived from careful evaluation of both the degassing spectra and the isotope-ratio correlations (isochron plots).

Sample ke01-00 (biotite, Fig. 6.1) shows a 'classical' excess-Ar staircase with continuously decreasing apparent step-ages with increasing temperatures. The minimum apparent step-age is 17.0 ± 0.4 Ma, but it is very likely that the apparent ages would continue to decrease if further heating occurred. In this case, the apparent age of the last step may represent a maximum extrusion age, but not a geologically meaningful age. In contrast, the corresponding ^{40}Ar/^{36}Ar vs. ^{39}Ar/^{36}Ar isotope correlation plot yields a good isochron (correlation: 0.988) with an age of 15.8 ± 1.2 Ma. Here, the ^{40}Ar/^{36}Ar intercept of 400.6 ± 13.2 documents the presence of excess Ar. However, the isochron age, which is 'corrected' for excess Ar, is most probably a geologically-meaningful age.

Sample ke13-00 (biotite, Fig. 6.2A) shows excess Ar in the first degassing step. This higher apparent age also correlates with a variation in the K/Ca ratio and may indicate that the excess Ar is located in the rims of the biotite (W. Frank, Vienna, Austria, pers. comm.). There is consistency between the plateau and the isochron age (see Table 6.2). Consequently, the plateau age of 9.4 ± 0.3 Ma is considered to be geologically meaningful. The sample released most of the gas at low temperatures ($< 800^{\circ}$C). This may indicate a certain amount of weathering of the sample (W. Frank, Vienna, Austria, pers. comm.).

Sample ke24-00 (biotite, Fig. 6.2B) is the only sample with no significant excess Ar; i.e. the total gas, the plateau, and the isochron age are identical within limits of error (see Table 6.2). The large error bars at the beginning of the plateau diagram are due to low ion-beam intensity. In

contrast to ke13-00, most of the degassing occurs at high temperatures ($> 1000^\circ$ C). The plateau age of 17.1 ± 0.7 Ma is based on 92% of the total ^{39}Ar release and interpreted as a geological age.

Sample ke28-00 (amphibole, Fig. 6.3A) has excess Ar in the first steps. The consistency between the isochron and plateau age indicates the geological significance of the plateau age (20.9 ± 2.1 Ma).

Sample ke30-00 (amphibole, Fig. 6.3B) has a complex release diagram with a distinct saddle-shaped pattern due to various effects (mostly excess Ar). A plateau is not developed (see section 6.2.2 for definition of a plateau). Additionally, the isotope-correlation ratio is very poor (0.83, see Appendix C) and does not permit the calculation of an isochron age. The minimum apparent step-age of 34 Ma may represent a maximum age of the extrusion.

Sample ke39-00 (biotite, Fig. 6.2C) again shows an excess-Ar 'staircase' (as sample ke01-00). The minimum apparent step-age is 8.5 Ma, but it is unclear whether the apparent ages would continue to decrease if further heating occurred. The corresponding isotope-ratio correlation plot yields an acceptable isochron (correlation: 0.971) and an isochron age of 7.6 ± 0.9 Ma. As in sample ke01-00, the intercept (^{40}Ar/^{36}Ar) of 400.6 ± 13.2 documents the presence of excess Ar. The isochron age is most probably a geologically-meaningful age. This interpretation is further supported by the observation that the isochron age of the biotite analysis of sample ke39-00 is also identical to the well-defined amphibole age of the same sample.

Sample ke39-00 (amphibole, Fig. 6.3C) has excess Ar in the first steps. The anomalous steps (1–4) correlate with a variation in the K/Ca ratio (dashed line, Fig. 6.3C). This correlation indicates that the sample was probably influenced by inclusions of an adherent phase different from bulk amphibole with excess Ar content (possibly biotite or volcanic glass). In this case, the amphibole itself does not apparently have excess Ar. The very homogeneous plateau age of 8.3 ± 1.2 Ma is based on 96% of the total ^{39}Ar release and represents an analytically well-determined age.

In sample ke40-00 (biotite, Fig. 6.2D), there is a good consistency between all three ages (plateau, isochron, and total gas age, see Table 6.2). This indicates that there is very little excess Ar. This observation can also be made from the spectrum plot. The plateau age of 7.9 ± 0.2 Ma is considered to be the extrusion age.

The interpretation of sample ke41-00 (amphibole, see Fig. 6.3C) is similar to that of sample ke39-00 (amphibole, see above). The visible excess Ar in the first steps is probably related to the presence of a second phase (biotite or volcanic glass?) with excess Ar (as indicated by the K/Ca ratio). The well-defined plateau age of 29.3 ± 2.0 Ma is considered to be geologically meaningful. This sample (volcanic clast) yields the oldest age of the San Vicente Fm. from the Southern Altiplano, and does not have a Pilkhaua age. It is not a deformation age, despite the sample's location within Pilkhaua sediments.

6.4 Conclusions

Most samples of the Southern Altiplano have excess Ar, but geologically-meaningful ages can be derived. The plateau ages are trustworthy for all samples, with the exception of ke39-00 (biotite), ke01-00, and ke30-00. The spectrum plots of the biotite analysis of ke39-00 shows an

Sample	mineral, rock	plateau age [Ma]	^{39}Ar [%]	total gas age [Ma]	st	%rad. cont.	isochron age [Ma]	IC $^{40}Ar/^{39}Ar$		comment
ke01-00	bi, tephra	–	-	29.7 ± 5.3	11	7–67	15.8 ± 1.2	$366 \pm$	21	excess staircase
ke13-00	bi, ign-imbrite	9.4 ± 0.3	61	10.1 ± 0.4	8	72–89	9.8 ± 0.2	$243 \pm$	47	excess/ rims
ke24-00	bi, tephra	17.1 ± 0.7	92	17.1 ± 1.1	8	52–85	17.0 ± 0.9	$335 \pm$	49	
ke28-00	hbl, tephra	20.9 ± 2.1	86	24.0 ± 2.9	7	44–98	20.6 ± 0.1	$448 \pm$	32	excess/ rims
ke30-00	hbl, tephra	–	–	74.5 ± 3.6	10	82–98	65.1 ± 16.3	$2705 \pm$	1716	excess dom. 34 Ma min
ke39-00	hbl, crystal tuff	8.3 ± 1.2	96	9.2 ± 1.4	10	13–91	8.5 ± 0.2	$307 \pm$	46	excess/ rims
ke39-00	bi, crystal tuff	–	–	15.8 ± 2.6	10	26–58	7.6 ± 0.9	$401 \pm$	13	excess staircase
ke40-00	bi, crystal tuff	7.9 ± 0.2	96	8.1 ± 0.3	10	19–85	8.2 ± 0.1	$279 \pm$	21	excess/ rims
ke41-00	hbl, crystal tuff	29.3 ± 2.0	93	32.2 ± 2.2	9	31–95	29.2 ± 0.6	$318 \pm$	75	excess/ rims

Table 6.2: Summary of the results of the Ar-Ar step-heating analysis. $\%^{39}Ar$ is the % of plateau from total released ^{39}Ar, (exception ke28-00, ke39-00 (bi)); *st* refers to the total number of steps; *%rad. cont.* is the range of radiogenic content of all steps; *isochron age* refers to the $^{40}Ar/^{36}Ar$ vs. $^{40}Ar/^{36}Ar$ isotope correlation plot; *IC* $^{40}Ar/^{39}Ar$ is the $^{40}Ar/^{36}Ar$ intercept of the isochron plot, 'excess dom.' = excess Ar dominant, '34 Ma min' = minimum step age is 34 Ma (see Appendix C for details).

excess-Ar staircase (see Fig. 6.2C), but the isochron age is similar to the hornblende age of the same sample. The isochron age was also taken for sample ke01-00. For ke30-00 neither the plateau plot nor the isotopic age provide any meaningful age. The outgassing step with the lowest age is considered as the maximum age of the sample.

The overall presence of excess Ar indicates that the results of K-Ar dating can only be regarded as maximum ages. This study showed that excess Ar is an overall phenomenon of the felsic tuffs from the Southern Altiplano, so it is likely that the samples that were analysed with the K-Ar method also have excess Ar. A re-evaluation of the K-Ar samples with the Ar-Ar approach would probably produce more reliable ages. Alternatively, if the samples were not affected by a subsequent heating event after cooling, zircon fission-track analysis or age determinations with the (U,Th)-He approach on (U,Th)-bearing minerals (e.g. zircon, apatite) could be made.

The time frame of the youngest tectonic increment of the Southern Altiplano is constrained by Ar-Ar ages of tilted tuffs within syn-tectonic basins. Deformation ages range between 17.1 ± 0.7 Ma (ke24-00) and 7.9 ± 0.2 Ma (ke40-00).

An age for the end of deformation is given by the age of undeformed tuffs or ignimbrites overlying tilted strata (post-tectonic samples, see Table C.1). These ages range between 9.4 ± 0.3 Ma (ke13-00) and 7.6 ± 0.9 Ma (ke39-00, biotite).

Chapter 7

Analysis of reflection-seismic profiles

This chapter describes the evaluation and interpretation of the available reflection-seismic profiles, including the Main Cross-Section (see section 2.5 and Fig. 2.1) that covers the Eastern and Central Altiplano. The first part of this chapter (7.1) addresses the resolution of the seismic data (7.1.1), followed by the presentation of the velocity model used to perform the time/depth conversion of the seismic TWT-sections (7.1.2), and the description of the along-strike correlation between different seismic sections (7.1.3).

The identification of seismic facies and their correlation with stratigraphy are subject of the second part of this chapter (7.2). Major unconformities between different seismic facies reflect the basic changes in basin tectonics. Furthermore, together with the identification of faults in the seismic data, the unconformities provide important information about the relative age of deformation, the order of fault activation, and also the lateral extension of deformation increments within the profile. This topics are subject of the last part of this chapter (7.3). Fig. 7.1 shows an overview of the position of seismic profiles relative to geological outcrops, the position of the Main Cross-Section, and marks important shot points.

7.1 Methodology

7.1.1 Horizontal and vertical resolution of the seismic profiles

The resolution of seismic data refers to the minimum separation required between two features to resolve them individually. The vertical resolution is the minimum distance to show two interfaces as separate reflectors. The horizontal resolution describes how far apart two features involving a single interface must be separated to be visible as separate features (Sheriff and Geldart, 1995, pp. 172–177).

An approximation of the vertical resolution can be made from the seismic wavelength measured in the section and the interval velocity (Badley, 1985). The general formula for the wavelength (λ) is

$$\lambda = v \cdot period \tag{7.1}$$

with λ in m, v (here the interval velocity $v_{(int)}$) in m/s and the $period$ (in s) of the seismic waves, measured from the seismic section.
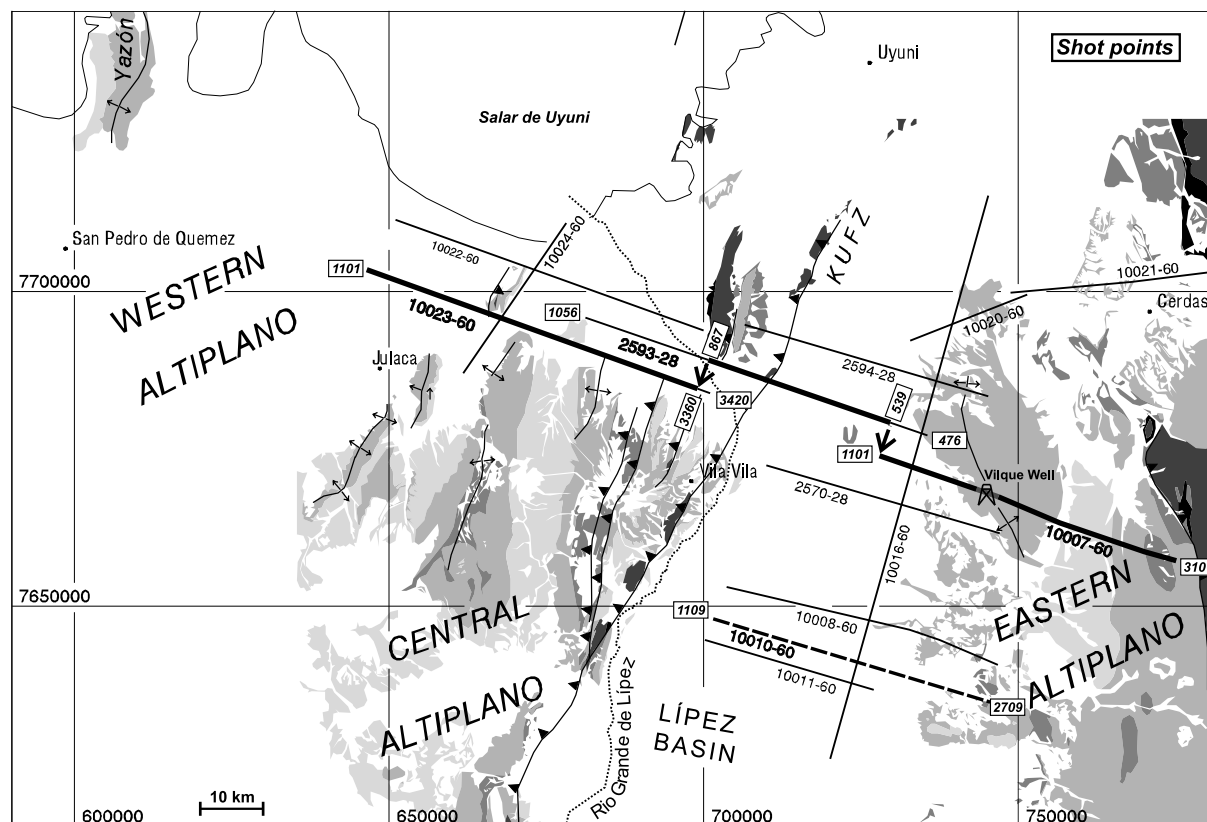
Figure 7.1: Overview of seismic profiles south of the Salar de Uyuni with respect to outcrops shown by the generalised geological map (see Fig. 3.1 for legend. The Main Cross-Section, in bold, is a combination of seismic lines 10023 (shot points 1101–3360), 2593 (shot points 867–539), and 10007 (entire section). Bold, stippled line is also shown in this thesis (line 10010); KUFZ = Khenayani-Uyuni Fault Zone. The northern lines are not shown here, but shown in Fig. 2.1.

The *tuning thickness* (= $\lambda/4$) is the thickness at which the reflections from the top and the base of a bed interfere constructively resulting in an amplitude increase. Signals from interfaces separated by a distance larger than the *tuning thickness* are visible as two separate features. Therefore the *tuning thickness* gives a useful approximation of the vertical resolution of seismic data (Badley, 1985). However, the required thickness to produce a measurable signal is significantly smaller than the resolution ($\lambda/20$–$\lambda/30$, cf. Sheriff and Geldart, 1995). An overview of the *tuning thickness* at different depths of the seismic sections from the Southern Altiplano is given in Table 7.1.1.

The horizontal resolution is generally significantly less than the vertical (Sheriff and Geldart, 1995). The Fresnel Zone (Equation 7.2) is taken as the limiting horizontal resolution on unmigrated seismic data:

$$rf = \frac{v}{2} \cdot \sqrt{\frac{t}{f}} \tag{7.2}$$

with *rf* the radius of the Fresnel Zone (in m), v the average velocity of the corresponding reflector (in m/s, here the root-mean square velocity [$v_{(RMS)}$]) of the corresponding reflector),

lithology	TWT [s]	period [s]	frequency [Hz]	$v_{(int)}$ [m/s]	tuning thickness [m]	$v_{(RMS)}$ [m/s]	Fresnel radius [m]
Sediment	0.5	0.020	51	3072	15	2753	137
Sediment	1.0	0.024	42	4328	26	3212	247
Sediment	1.5	0.031	32	4868	38	3734	406
Sediment	2.0	0.039	25	5594	55	4587	644
Basement	2.0	0.039	25	5594	55	4587	644
Basement	3.0	0.043	23	5886	64	4867	877
Basement	4.0	0.055	18	5868	81	5082	1193

Table 7.1: Estimation of the vertical and horizontal resolution of the reflection-seismic profiles. The *tuning thickness* is an approximation of the vertical resolution. The radius of the Fresnel Zone determines the horizontal resolution of unmigrated sections. See text for further explanation.

t the (one-way) travel time in s, and f the frequency in 1/s. In migrated sections, however, the size of the Fresnel Zone cannot be used as a criterion for horizontal resolution. Nevertheless to estimate the horizontal resolution, I calculated the size of the Fresnel Zone of the available seismic lines (see Table 7.1.1). Velocities are derived from shot-point 1625 of line 10007 (profile metre 100000), which is the reference track used to calculate the applied velocity model (see section 7.1.2). The period was directly measured from the section.

Similar values for the *tuning thickness* of the basement and the sediments (at 2 s depth) may be due to the sedimentary character of the basement (see section 3.1). Comparable calculations from seismic data of the Bolivian Subandean show that the vertical and horizontal resolution in crystalline basement is clearly smaller than in sediments (Hinsch, 2001). Most of the interpreted geological structures in this work do not reach depths below 2 s.

7.1.2 Velocity model and time/ depth conversion

The time-to-depth conversion of the seismic data is necessary for the construction of the balanced cross-section, because only a depth section shows the true geometries and vertical positions of stratigraphic horizons and structures.

The best available velocity model for the time/depth conversion was derived from the interval velocities used for the migration of the seismic data. The time/depth conversion was only done for the Main Cross-Section (see section 2.5 and Fig. 2.1) and was achieved with the time-to-depth conversion module of 2DMove (Midland Valley Corp.). This module uses an increasing velocity gradient with depth. The corresponding depth $z(t)$ (in m) for a given two-way-travel time (TWT) is calculated with the following equation:

$$z(t) = \frac{v_0 \cdot (e^{k \cdot 0.5 \cdot TWT} - 1)}{k} \tag{7.3}$$

v_0 (in m/s) is the initial seismic velocity at the surface and k the rate of change in velocity with increasing depth.

To perform the time-to-depth conversion, 2DMove requires two values: the initial seismic velocity v_0 and the k value. However, this simple approach is only possible for seismic profiles which do not have significant lateral variations in the velocity model.
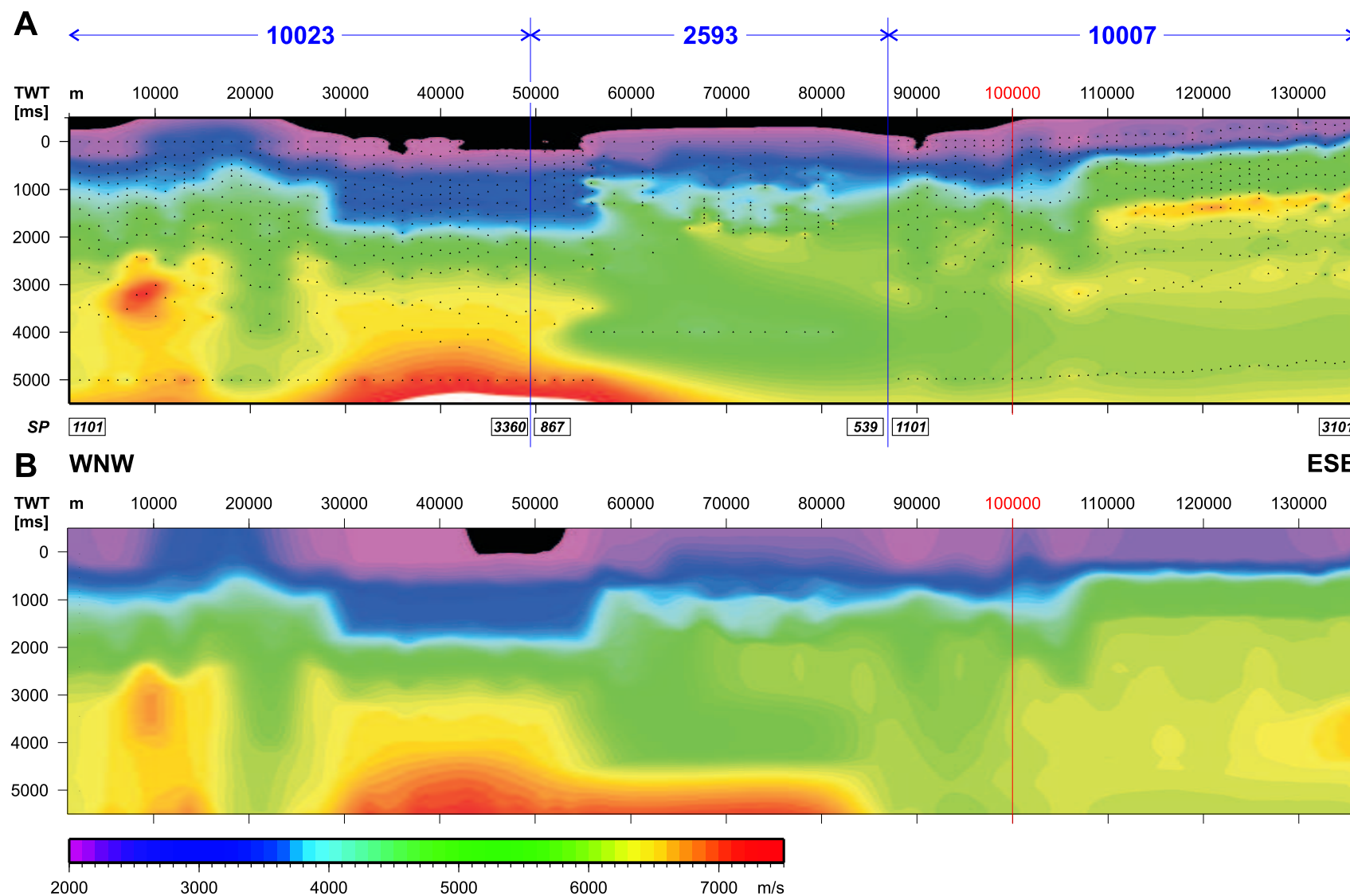
Figure 7.2: Interval-velocity model (colours, in m/s) of the Main Cross-Section, a combination of seismic lines 10023, 2593, and 10007; SP = shot points (see Fig. 7.1). Grid parameters: x-increment = 100 m, y-increment = 100 ms, x-axis = profile metres (m). **A:** Original data. Black points are data gridding points. **B:** Velocity model after smoothing with a median filter (filter width = 2000 m). Red line highlights 'Track 100000' which was used to determine the input parameters for the time-to-depth conversion.
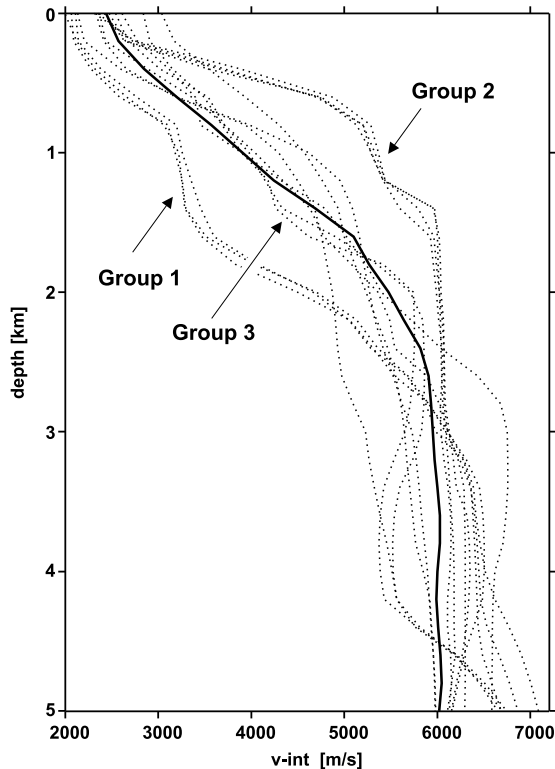
Figure 7.3: Velocity-depth graph for vertical velocity tracks every 10000 m of the main section (Fig. 7.2). Bold black line delineates 'Track 100000', the velocity depth profile that was defined as adequate to determine v_0 and k.
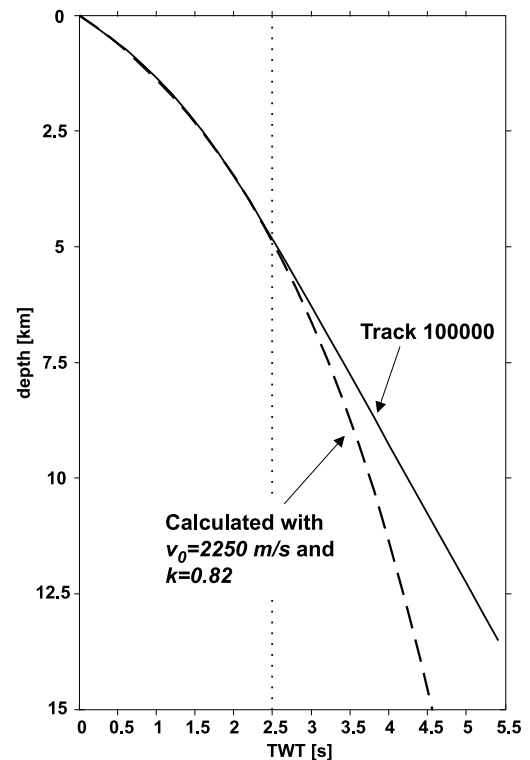
Figure 7.4: TWT-depth graph to image the result of the calculation of the best-fit time/depth graph (dashed line) to explain 'Track 100000' (solid line). Both lines are almost identical to ~2.5 s TWT. See text for explanation.

Fig. 7.2A shows the interval velocities of the Main Cross-Section. The velocity model of the entire section is quite homogeneous apart from the middle part, between 30000–55000 profile metres, with lower velocities (< 3500 m/s) reaching depths of 2 s TWT. Velocities higher than 6500 m/s are only reached in deeper portions of line 10023 (below 3 s TWT). These are not relevant for this study due to the absence of interpretable reflectors at these depths (see section 7.1.1). The area with lower velocities down to 2 s TWT (between 30000 and 55000 profile metres) corresponds to the eastern part of the bivergent thrust system of the Central Altiplano. This area is characterised by steep-dipping strata and only very few interpretable reflectors. Therefore I tolerated a rather small error (see below) in the east-vergent part of the bivergent thrust system and determined the initial velocity v_0 and k for the largest part of the section where this low-velocity zone did not occur.

To remove small heterogeneities, I applied a median filter to smooth the velocity model (see Fig. 7.2B). To evaluate the lateral variations of the velocity model, vertical velocity tracks were extracted every 10000 m. Fig. 7.3 shows these velocity-depths profiles. All tracks can be separated into three groups. Three tracks have low velocities in the upper parts and end with velocities above 6000 m/s (Group 1). These correspond to the low-velocity zone mentioned above. Another three tracks (Group 2) have a rapid velocity increase between 1 and 2 km depth and merge at ~3000 m depth with the other tracks. Eight tracks are part of the third group which falls between the others. The 100000 m velocity profile (= 'Track 100000') lies in the middle of

Group 3 and was therefore believed adequate to determine the required v_0 and k values. 'Track 100000' is in the Eastern Altiplano and corresponds to shot-point 1625 of line 10007 (see red line in Fig. 7.2).

The required input parameters (v_0 and k) for the time/depth conversion module were determined by 'trial and error'. By continuously varying v_0 and k, I tried to fit a time/depth profile, calculated with Equation 7.3, to the time/depth graph of 'Track 100000'. The best fit is shown in Fig. 7.4 and was achieved with an initial velocity of 2250 m/s and $k = 0.82$. These values were taken for the time/depth conversion of the Main Cross-Section. The diagram in Fig. 7.4 shows an almost perfect fit from 0 to 2.5 s TWT depth. Below this, the two gradients separate and the velocity of the calculated track (dashed line) increases rapidly with increasing depth. At this depth, however, no Tertiary sediments are present. Structures in the Paleozoic basement were not interpreted. The error in depth localisation that was derived from application of an average velocity gradient for the entire cross-section are ± 100 m for a reflector at 0.5 s TWT, ± 250 m, at 1 s TWT, and ± 800 m at 2 s TWT.

I did not depth-convert the original seismic data, because the seismic sections were only available as scanned versions of the paper prints (tif format). Therefore, the time/depth conversion only involved the line drawings and the interpreted stratigraphic horizons.

7.1.3   Correlation of seismic profiles

In the Eastern Altiplano, the correlation of parallel seismic lines was unproblematic, mainly due to the presence of the NNE–SSW trending cross-line 10016 and the structural continuity along strike (see section 7.2.1). In the Central Altiplano, the correlation of the parallel lines 10023 and 10024 was not necessary because of the very poor data quality of line 10024 across the Salar de Uyuni. Only line 10023 was interpreted.

The Main Cross-Section is a combination of lines 10023, 2593, and 10007 (see Fig. 7.1 and section 2.5). Lines 10023 and 10007 are situated on one WNW–ESE directed line. Line 2593 parallels them, but lies ∼5 km north. A parallel projection to close this gap was made. This was possible because of the structural continuity (there was no vertical shift in the reflectors). Furthermore, evaluation of the velocity model (Fig. 7.2A) also shows that the velocity model of line 2593 is laterally continuous with that of lines 10007 and 10023.

The correlation of the northern seismic line that crosses the Western Altiplano with the Main Cross-Section is difficult. This is mainly because of the large distance (> 50 km) between the lines without a tying cross line, and the absence of stratigraphic information due to the lack of outcrops. Furthermore, the data quality of the northern lines is far below the quality of the Main Cross-Section, because the northern lines exist only as stacked versions (cf. section 2.5 and App. B). This, in addition to the almost complete absence of Tertiary outcrops, meant that I did not attempt to balance the cross-section of the Western Altiplano.

The superposition of main structural elements onto the gravity map (Bouguer Anomaly) revealed a strong correlation between structural and gravity highs (Fig. 7.5). Structural highs refer to anticlines and hanging walls of major thrusts. This qualifies gravity data to be an appropriate subsurface mapping tool for the Southern Altiplano that was used to correlate the northern seismic lines with the Main Cross-Section. Furthermore, it can be used to estimate the number of structures in the Western Altiplano that are buried beneath post-Miocene sediments or volcanics.
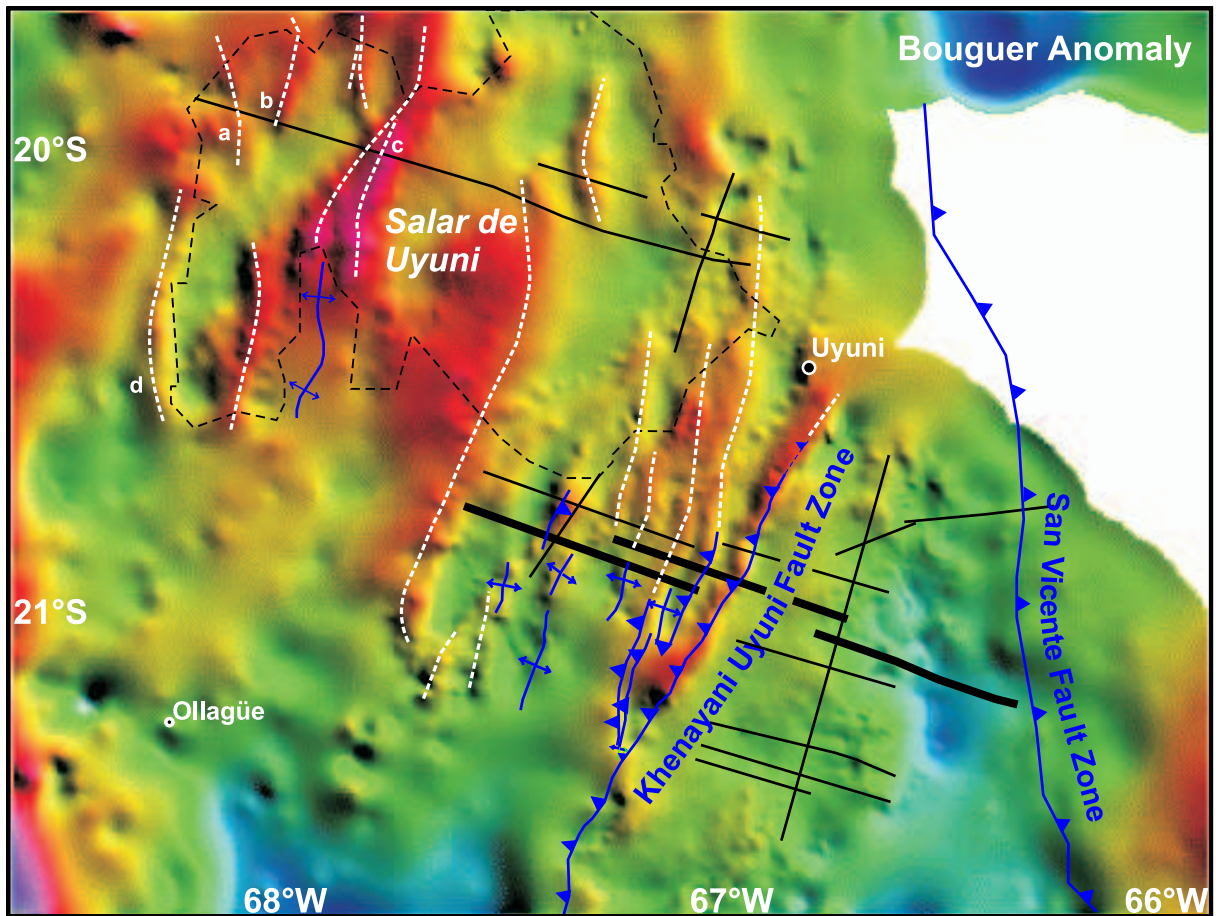
Figure 7.5: Main structural elements of the working area (blue lines) superposed onto the map of Bouguer anomaly (blue tones are gravity lows, red tones gravity highs). Gravity highs correspond to structural highs, such as hanging walls of thrusts and anticlines. This correlation was used to infer upper-crustal structure from the pattern of anomalies (white lines). The pattern of seismic lines is shown in black, bold lines delineate the Main Cross-Section. The gravity map was kindly provided by H.J. Götze and S. Schmidt (FU Berlin). The data was extracted from Götze and Krause (2002).

7.2 Seismic sequence/ facies analysis

The interpretation of the seismic data is based on the identification of seismic facies/sequences, their geometry, and the characteristics of reflections and reflector terminations. I followed the terminology of Miall (1997, p. 57–70). The identification of seismic facies and their correlation with stratigraphic formations is mainly based on data from the Eastern Altiplano (lines 10007 and 10010, see Figs. 2.1 and 7.6). Here the weakly-inclined and poorly-dissected strata provide continuous reflectors across the entire section. The sequence boundaries, identified in the seismic data (see Table 7.2), were correlated with surface outcrops and major stratigraphic boundaries identified on the surface and in the Vilque Well.

In the Central Altiplano (line 10023), stratigraphic correlation of the deeper units is difficult as steeply-dipping faults, some with large horizontal and vertical displacements, dissect the units, along with strong rotation and frequent erosion of hanging-wall cutoffs. Broad domains

of steeply-dipping strata cannot be resolved in reflection-seismic data and restrict the seismic interpretation to horizontally to weakly-dipping domains. Thus, the Central Altiplano is interpreted by linking surface data to seismic interpretation.

7.2.1   Eastern Altiplano

Seismic lines 10007 and 10010 are examples of interpreted seismic profiles of the Eastern Altiplano (Fig. 7.6). Table 7.2 summarises the characteristics of each sequence. I present two seismic sections to show the lateral (north-south) variation of the Lípez Basin (Fig. 7.6).

The identification of seismic sequences allowed the subdivision of the San Vicente Fm. into three subsequences (OMsv1, OMsv2, and Pilkhaua). The youngest sequence, here named Pilkhaua Subsequence, was syn-tectonic with respect to the youngest compressional event. It was first identified in the Central Altiplano where it forms the syn-tectonic basin fill of the M/U-Miocene thrust-front basins (see section 7.2.2). The Pilkhaua Subsequence is not equivalent to a stratigraphic unit because it describes a structural position and not a depositional period (see section 3.3.3.1 for a stratigraphic description of the Pilkhaua Subsequence). As it is syn-tectonic, its age may vary across the Altiplano. In the seismic data, its syn-tectonic character is shown by a strong increase of stratal thickness with increasing distance from the source area and by diverging strata (e.g. in the upper western part of line 10010, Fig. 7.6).

The Paleocene Santa Lucia and Cayara Formations are not listed in Table 7.2. This is due to their very small thickness (together $< 100\,\text{m}$, cf. section 3.3.1), which does not permit their resolution at depths of 1.5–2 s TWT (cf. section 7.1.1). Even if these strata had greater thickness, they still would be difficult to image because of the low impedance contrast (due to lithological similarity) between the Santa Lucía and the El Molino Fms., and the Cayara and Potoco Fms., respectively (see chapter 3).

Line 10007 is the eastern part of the Main Cross-Section. It crosscuts large parts of the Lípez Basin of the Eastern Altiplano and shows the westernmost thrusts of the west-vergent part of the Eastern Cordillera's bivergent thrust system. The buried deformation front lies ~12 km west of the Vilque Well (DF in Fig. 7.6). West of the deformation front, the fill of the Lípez Basin is undeformed, i.e. there is no unconformity between the OMsv1 and OMsv2 Subsequences.

I interpret the westward-thinning wedge of the Potoco Fm. in line 10007 as a primary depositional feature and not the result of erosion. This is indicated by concordant reflectors at both sequence boundaries of the Potoco Fm. (the top and the base). Consequently, I interpret the wedge-shaped geometry as the result of the deposition of the Potoco Fm. in the foreland basin of the early Eastern Cordillera (Fig. 7.6). This interpretation is further supported by sedimentary observations, i.e. the presence of coarser grains, including conglomerates, in the easternmost outcrops of the Potoco Fm. in the Southern Altiplano (Sempere et al., 1990; Sempere and Orstom-YPFB, 1990; see also section 3.3.2; Silva-González, in prep.).

In line 10007, the OMsv1 and OMsv2 Subsequences are characterised by relative uniform thickness across the entire section. This constant thickness excludes major changes in basin tectonics during the deposition of the OMsv1 and OMsv2 Subsequences. In contrast to the OMsv1, the OMsv2 Subsequence is characterised by downlapping reflector terminations on the lower sequence boundary in the western part of the section (see arrow 1 in Fig. 7.6). I interpret this as indication of its deposition within a westward-prograding sedimentation system.

Formation	Seismic characteristics	Geometry	Sequence stratigraphy	Interpretation
San Vicente **Pilkhaua Subsequence**	Moderate to high amplitude, high frequency, very continuous reflectors	Westward thickening wedge; CAP divergent basin fill	LB onlap, divergent reflectors, UB toplap and concordant	Small, well-defined thrust-top basins, several filling events from different directions, interpreted as syn-tectonic sediments of the latest tectonic event
San Vicente **OMsv2 Subsequence**	2 alternating seismic facies (a) high amplitude and frequency, very continuous reflectors; (b) transparent zone with moderate continuity and frequency, and low amplitude	Planar (line 10007) to westward-thinning wedge (line 10010)	LB downlap, UB concordant	The downlapping reflectors (LB) represent a westward-prograding sedimentary body with a source area east of the seismic profile (probably early stages of the Eastern Cordilleran uplift)
San Vicente **OMsv1 Subsequence**	Same characteristics as OMsv1	Planar to very slightly westward-thinning wedge; southern line shows double-wedge shape	LB concordant, locally above toplaps; UB concordant below downlap of OMsv2 or toplap (10010). 10010: progressive onlap onto basement high and divergent reflectors in the east	The almost planar-shaped geometry in line 10007 reflects continuous sedimentation with well-developed stratification; line 10007 shows the distal part of this basin. In line 10010 the entire basin is exposed. Significant decrease of basin width from N (10007 1/2 basin ~ 58 km) to S (10008 entire basin $\sim$46 km (not shown), 10010 $\sim$ 36 km). Toplap terminations below the LB are due to an erosional unconformity
Potoco	Moderately continuous to discontinuous reflectors with low amplitude. There are continuous reflectors but their low amplitude renders them discontinuous	Westward-thinning wedge; 10010: double-wedge shape	Divergent reflectors, LB concordant, UB concordant in the east, toplap in the west. Southern line shows onlap onto basement high in the east	Significant N to S decrease of sediment thickness (10007: up to 3 km, 10010: $<$ 800 m). The westward-thinning wedge is interpreted as a (possibly syn-tectonic) foreland basin of a source area in the east. Toplap terminations in the western part (UB) are interpreted as erosional unconformity. N-to-S decrease of basin width (10007: 1/2 basin $\sim$48 km, 10010: entire basin $\sim$27.5 km)
El Molino	High amplitude, continuous reflectors, moderate to high frequency	Planar, possible onlap onto basement high to the south (10010)	Parallel to sub-parallel reflectors, prominent double reflector	High-amplitude double reflector interpreted as El Molino limestone. Planar shape and continuous thickness show continuous facies and thickness with only small lateral variations
Pre-Mesozoic **Basement**	Low to moderate amplitude, low frequency, discontinuous reflectors			

Table 7.2: Seismic facies and stratigraphic analysis from the Eastern Altiplano, based on the interpretation of lines 10007 and 10010 (see Fig. 7.6). Seismic characteristics of the Pilkhaua Subsequence are from the Central and Eastern Altiplano. UB = upper boundary, LB = lower boundary, CAP = Central Altiplano.
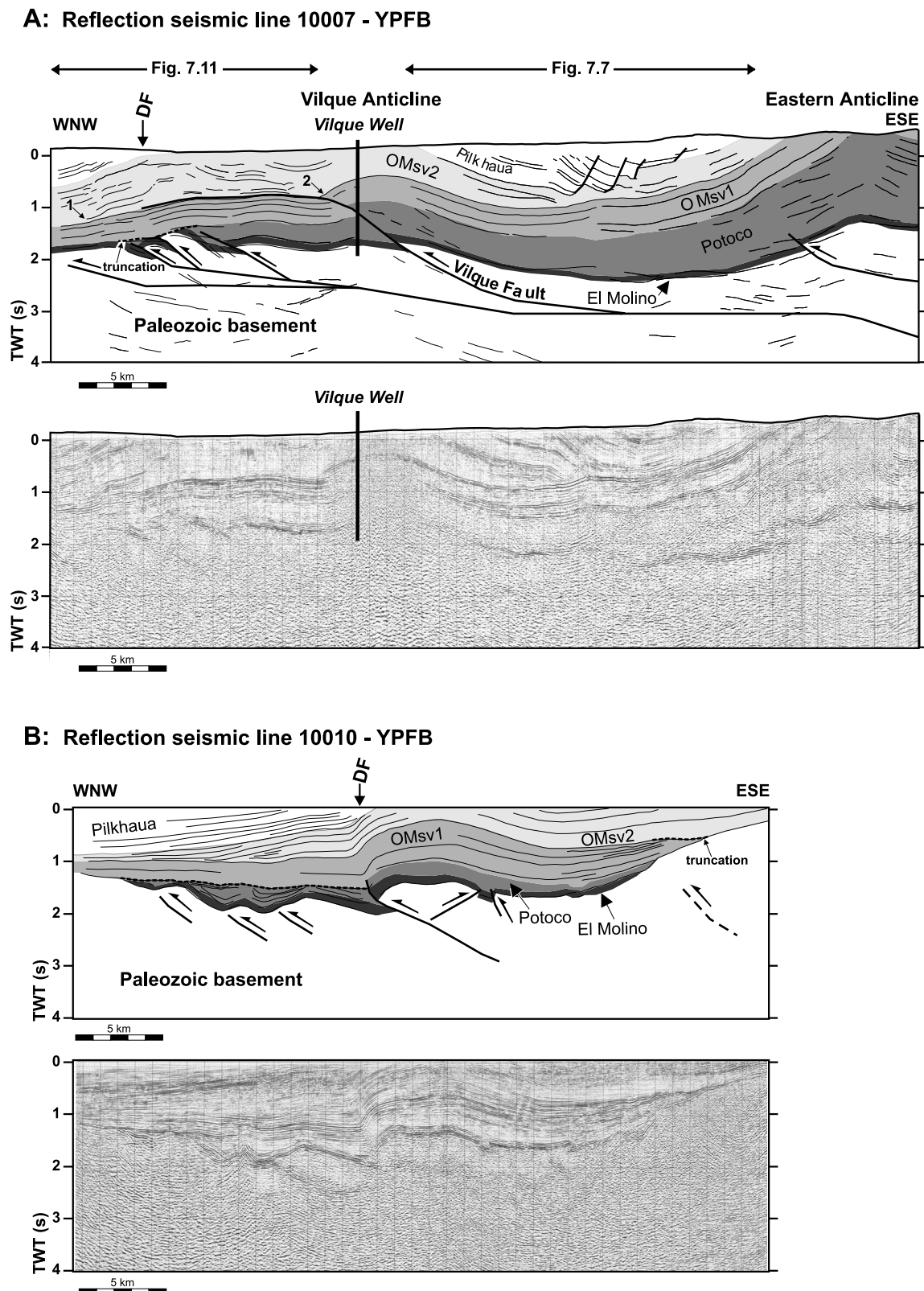
Figure 7.6: Seismic interpretation of the Eastern Altiplano (YPFB lines 10007 and 10010, time sections, complete sections, see Fig. 2.1 for location). DF = buried deformation front of the Eastern Cordillera. The vertical correlation of the two seismic sections is structural, not geographical: The western half of the sections show similar structures, i.e. buried Oligocene thrusts and a central anticline, whereas the eastern half is different (basement high only in line 10010, different deformation history; OMsv1 syn-tectonic only in line 10010).
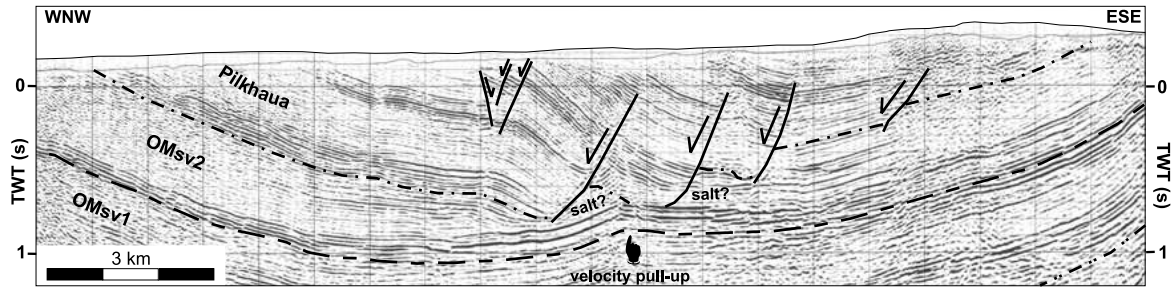
Figure 7.7: Close-up of seismic line 10007 (YPFB) from the syncline to the east of the Vilque Well, Eastern Altiplano illustrates post-Miocene extension, possibly above salt layers (see Fig. 7.6A for location). The stratigraphic horizons were derived from the Vilque Well and surface outcrops.

The diverging reflectors that normally define the Pilkhaua Subsequence (e.g. line 10010, Fig. 7.6B and line 10023, Fig. 7.8) are absent in line 10007. This could be due to the erosion of its upper part. Nevertheless, the structural position and correlation with line 10010 (where divergent reflectors are present) requires the existence of the Pilkhaua Subsequence in the upper westernmost part of line 10007, as interpreted in Fig. 7.6A. The existence of Pilkhaua sediments east of the Vilque Well is proven by field evidence (see section 3.3.3.1). The syncline east of the Vilque Well is the only place in all seismic data of the Southern Altiplano available to me where extensional structures are visible (Fig. 7.7). These small normal faults with little displacement, however, are not due to regional extensional stresses because they are not present in any of the parallel lines further south (e.g. line 10010, Fig. 7.6B). I therefore interpret these as local features, related to the collapse of the forelimb of the Eastern Anticline of line 10007, possibly above salt layers within the upper OMsv2 Subsequence. Evidence for the presence of salt derives from the Vilque Well, where 600 m salt were penetrated within the San Vicente Fm. (Fig. 2.2), from the very variable thickness of the OMsv2 near the base of the normal faults, and from the velocity pull-up of the lower reflectors (Fig. 7.7).

The most prominent unconformity of line 10007 is the truncation at the base of the OMsv1 Subsequence near the deformation front (DF, see Fig. 7.6A). The toplap terminations of the Potoco and El Molino Fms. below the truncation identify it as an erosional unconformity. A second unconformity is developed in the western part of the Vilque Anticline between the OMsv1 and OMsv2 Subsequences (see arrow 2 in Fig. 7.6A). Close to the Vilque Well this is an intra-OMsv1 unconformity. Reflectors below the unconformity are concordant (OMsv1) and downlap above it. This represents the hanging-wall ramp of the Vilque Fault and provides information about thrust displacement, which will be discussed in section 9.3. This unconformity dies out west of the deformation front. The eastern boundary of the Tertiary basin lies east of the seismic section.

The width of the basin of all units between the El Molino Fm. and the base of the OMsv2 Subsequence is smaller In the southern line (10010, Fig. 7.6B) than in the northern line (36 km total basin length in the south [10010] compared to 58 km half-basin length in the north [10007], see Table 7.2). The eastern border of the southern part of the basin is formed by a basement high (Fig. 7.6B). Progressive onlaps of reflectors of the Potoco Fm. and OMsv1 Subsequence against the basement high, and divergent reflectors (increasing bed thickness towards the basin centre) indicate either continuous uplift of the basement high or basin subsidence throughout their deposition, i.e. during the Eocene and most of the Oligocene (see Fig. 7.6 and chapter 3). It is possible that the basement high may have been a source area until the onset of the OMsv2

Subsequence. The sediment source changed significantly with the beginning of the OMsv2 Subsequence. The downlapping reflectors in the western part of the basin indicate a westward-prograding depositional system. The observation of the concordant or slightly erosive lower OMsv2 boundary in the eastern part of the basin points to a sediment source east of the section. Locally-developed toplap terminations below the OMsv2 Subsequence show that this sequence boundary was partly erosive (e.g. truncation in the eastern part of the section, Fig. 7.6B).

Major unconformities in profile 10010 are largely in the same positions as in the northern line 10007. One unconformity is at the base of the OMsv1 Subsequence in the western part of the basin. As in line 10007, it is interpreted as erosional, because of the well-developed toplap terminations below the truncation (i.e. the OMsv1 cuts the top of the underlying structures). A second unconformity developed between the OMsv1 and OMsv2 Subsequences in the western part of the basin. As mentioned above, this is due to the deposition of the OMsv2 in a westward-prograding sedimentary sequence.

The most obvious difference between the northern and the southern section (cf. Fig. 7.6) is the smaller basin width in the southern section during the deposition of the Potoco Fm. and OMsv1 Subsequence. The postulated gradual decrease of basin width towards the south is further supported by information of line 10008 (not shown). There, the basin width lies between the widths of lines 10007 and 10010 (see Table 7.2). A second difference between lines 10007 and 10010 is a decrease of thrust displacement during the younger deformation increment that resulted in the formation of the Vilque Anticline, a 'classical' fault-bend anticline, in the north. In the south, the youngest deformation only resulted in the development of a moderately-dipping thrust that partially inverted the former basin centre (see section 7.3.1 for the derivation of the relative deformation age). The latter is also responsible for the eastward shift of the deformation front in line 10010 (see Fig. 7.6B).

The most significant observation of Fig. 7.6, however, is the strong similarity between both sections. It does not only include the characteristics of seismic facies, but also similar positions of unconformities and the structural style. This indicates a similar geological history of the entire Lípez Basin and permits the transfer of information, e.g. structural observations, from one line to the other. The interpretation of seismic lines between the sections 10007 and 10010 (e.g. lines 2570-28 and 10008-60) and also the N–S directed line 10016 (see Fig. 7.1 for location, seismic lines not shown) supports the observation that there are some differences between the northern and the southern Lípez Basin, but most of these, e.g. the basin width, can be explained by gradual variations. There is no evidence for a major structure, which divides the northern part of the basin from the south.

7.2.2   Central Altiplano

Line 10023 crosscuts the bivergent thrust system of the Central Altiplano from WNW to ESE, i.e. largely perpendicular to strike. Folds and thrusts have a spacing of ~6–10 km, which is much smaller than the wavelength of structures in the Eastern Altiplano. The structural style of the Central Altiplano is described more detailed in section 4.2.

Seismic data of the Central Altiplano vary strongly in quality across the section (lines 10023 and 2593, see Fig. 7.8). Especially deeper parts of the section mostly lack coherent, interpretable reflectors. Interpretations would be arbitrary without surface data. Surface outcrops show that

Reflection seismic lines 10023 and 2593 (extract)- YPFB
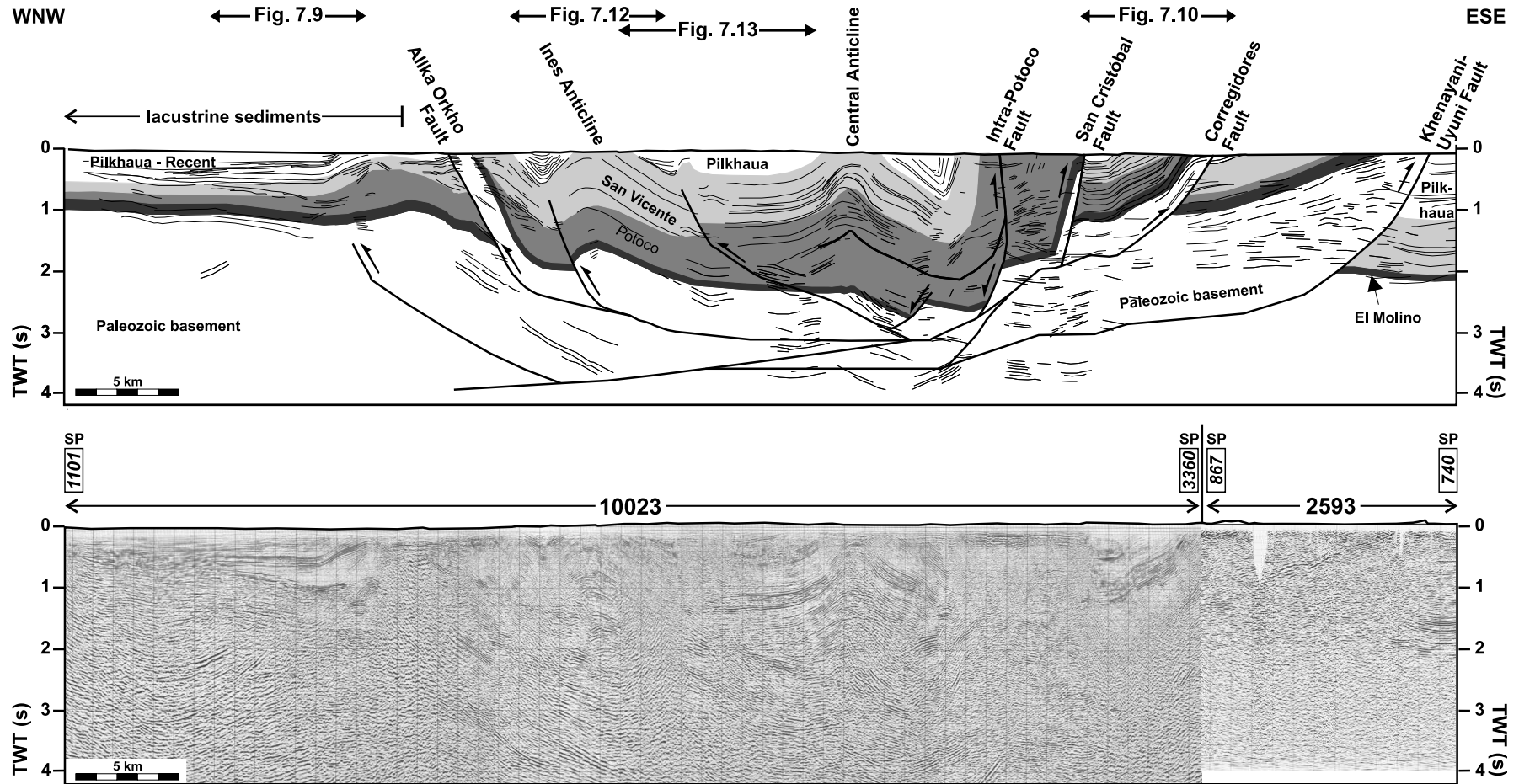
Figure 7.8: Seismic interpretation of the Central Altiplano, the western part of the main section. Complete section of line 10023 and parts of line 2593 (shot points [SP] are given above the seismic section, see Fig. 7.1 for location). The upper part of the figure shows the balanced geological interpretation of the section in TWT.
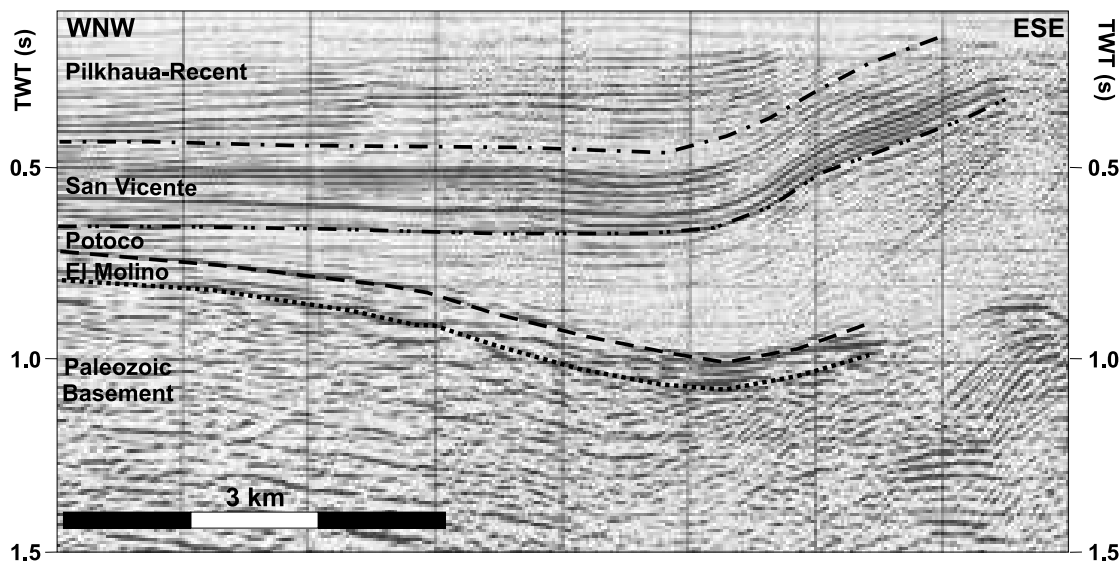
Figure 7.9: Close-up of seismic line 10023 from the Central Altiplano. The seismic sequences identified in the Eastern Altiplano can be transferred to the Central Altiplano, see Figs. 7.1 and 7.8 for location).

most parts with poor seismic quality correlate with steeply-inclined strata (see App. F.1). The strongly folded and thrusted strata of large parts of the seismic section of the Central Altiplano can be observed in almost continuous outcrops 5–10 km south of the seismic section (e.g. in the hanging wall of the San Cristóbal Fault, see Fig. 7.8 and App. F.1). Hence, the combination of surface and seismic data provided sufficient information for the construction of the starting model of the balanced cross-section. The geological interpretation, shown in Fig. 7.8, is the final version of the balanced cross-section as time-section.

The identification of seismic facies and their correlation with the Eastern Altiplano is difficult. Fig. 7.9 shows a close-up of the western part of Fig. 7.8. It demonstrates that the seismic sequences detected in the Eastern Altiplano (Fig. 7.6 and Table 7.2) also exist in the Central Altiplano. This includes the prominent double reflector of the El Molino Fm., the seismically transparent facies of the Potoco Fm., and the continuous reflectors with high amplitude of the San Vicente Fm. In the Central Altiplano, division of the San Vicente Fm. into the OMsv1 and OMsv2 Subsequences is not possible due to facies differences between the Eastern and Central Altiplano (see section 3.3.3). The Pilkhaua Subsequence will be further regarded as separate subsequence (cf. section 3.3.3).

The Potoco Fm. forms a continuously eastward-thickening wedge that reaches maximum thickness in the hanging wall of the San Cristóbal Fault (Figs. 7.8 and 7.9). Because the wedge is also present in the undeformed westernmost part of the section (Fig. 7.9), and because the top and the base the Potoco Fm. are concordant this wedge-shaped geometry is a primary syndepositional geometry. Its thickness significantly decreases east of the San Cristóbal Fault. Fig. 7.10 is a close-up of the area between the San Cristóbal Fault in the west and the Corregidores Fault in the east (see Fig. 7.8 for location). The lower sequence boundary of the San Vicente Fm. is concordant in the west, i.e. the footwall of the San Cristóbal Fault, and erosive further east, i.e. in the hanging wall of the Corregidores Fault (toplap terminations of the Potoco reflectors, see arrow in Fig. 7.10). In the geological map (App. F.1) the contact between the San Vicente Fm. and the Silurian in the hanging wall of the Corregidores and the Khenayani-
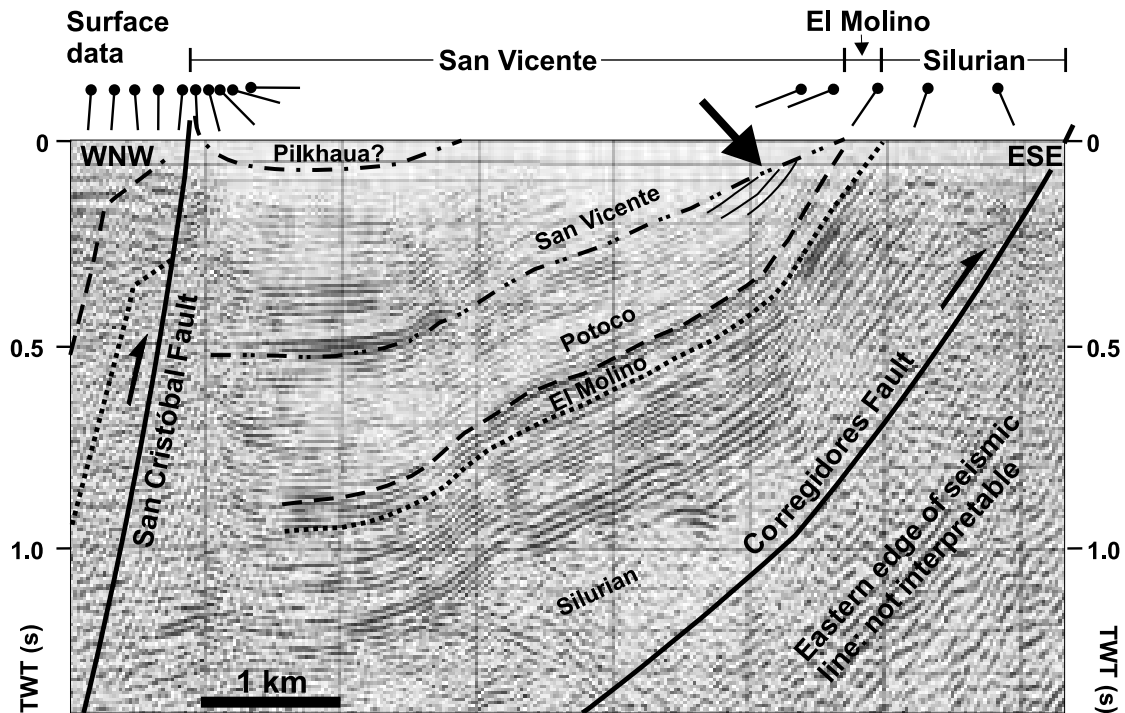
Figure 7.10: Close-up of seismic line 10023 between the San Cristóbal and the Corregidores Faults (eastern part of the bivergent thrust-system of the Central Altiplano, see Fig. 7.1 and Fig. 7.8 for location). The arrow marks an erosional unconformity between the San Vicente Fm. and the underlying Potoco and El Molino Fms. Surface data above the seismic section completes the database.

Uyuni Faults is also erosive (see also Fig. A.2D). This suggests that the smaller thickness of the Potoco Fm. to the east of the San Cristóbal Fault can only be partially explained by erosion, i.e. in the hanging wall of the Corregidores Fault (arrow in Fig. 7.10) but not in the footwall of the San Cristóbal Fault. The overlying San Vicente Fm. thins westward (Fig. 7.8). The overall conformable contact with over- and underlying strata indicates that this thinning-out is also a primary feature.

The Pilkhaua Subsequence was first recognised in the Central Altiplano, where it fills small syn-tectonic thrust-front and piggy-back basins (see section 4.2). These basins generally do not extend below 0.5–0.8 s TWT and are reasonably-well resolved in the seismic data. The syn-tectonic character is shown by strongly-divergent reflectors away form the source area, and the partly asymmetrical basin geometry (e.g. east of the Ines Anticline, see Fig. 7.8). Other syn-tectonic basins have a symmetrical geometry (e.g. west of the Ines Anticline, Fig. 7.8).

West of the westernmost anticline, the seismic profile was acquired over lacustrine sediments south of the Salar de Uyuni (see Fig. 7.8 and App. F.1). These undeformed post-tectonic sediments are represented in the uppermost horizontal reflectors. In this part of the section, the Pilkhaua Subsequence is not distinguished from the post-Pilkhaua strata (Figs. 7.8 and 7.9).

Major unconformities, such as those in the Eastern Altiplano, are not present in the Central Altiplano. However, sedimentological observations show that the San Vicente Fm. was locally deposited above an erosional unconformity (see section 3.3.3). This can partly be seen in the seismic data, e.g. in the hanging wall of the Corregidores Fault (see arrow in Fig. 7.10) and in the hanging wall of the Allka Orkho Fault (Fig. 7.8). Both unconformities are similar in that they are related to basement outcrops at surface (see Fig. 7.8).
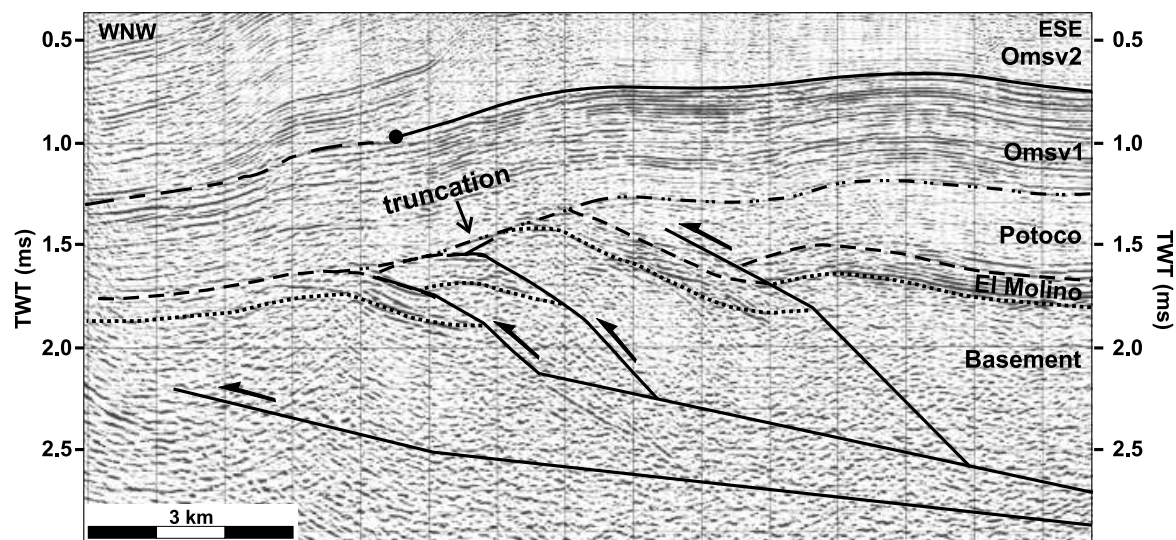
Figure 7.11: Close-up of YPFB-seismic line 10007 from the Eastern Altiplano. The truncation below the basal OMsv1 reflector is interpreted as erosion of pre-San Vicente anticlines, see Fig. 7.6A for location.

7.3   Relative age of deformation

Major unconformities between seismic sequences, folds, and faults are key indications of deformation in the seismic data. This section will give a short overview of relative deformation ages of the Eastern and Central Altiplano, derived directly from the interpretation of the seismic sections.

7.3.1   Eastern Altiplano

The structures of the Eastern Altiplano, shown in line 10007 (Fig. 7.6), were formed during two independent compressional events. The oldest shortening affected only the older formations (Basement, El Molino, and Potoco Fms., see Fig. 7.11). The anticlines above the west-vergent, thin-skinned thrusts were partly eroded prior to the sedimentation of the basal parts of the OMsv1 Subsequence. The same deformation increment formed the small basins in the western part of line 10010 (between ~1.5–2 s depth, see Fig. 7.6B). The different geometry of the 'older structures' in the two lines are probably only due to variable deformation intensity and erosion depth from N to S. Compressional deformation must have ceased prior to the deposition of the OMsv1 Subsequence, because the OMsv1 and overlying units are not deformed by the older increment.

The overall-concordant reflectors at the sequence boundaries and the relative uniform thickness of the OMsv1 and OMsv2 Subsequences in line 10007 (Fig. 7.6) indicate that there was tectonic quiescence in this region during their sedimentation. In contrast, the progressive onlaps on the basement high in line 10010 (Fig. 7.6) indicate continuous basement uplift or basin subsidence throughout the deposition of the OMsv1 Subsequence in the south (see Fig. 7.6B and section 7.2.1). However, there is no evidence for significant compressional movements.

The second compressional event involved all units except the post-tectonic cover. This deformation increment was responsible for the formation of the Vilque Anticline (line 10007, Fig. 7.6A) and the corresponding anticline in the southern seismic line (10010, Fig. 7.6B). The

uniform thickness of the OMsv1 and OMsv2 Subsequence and the concordant transition to the underlying Potoco Fm. in the Eastern Anticline of line 10007 show that the formation of this anticline also occurred during the younger compressional event, i.e. post-OMsv2.

The weakly westward-diverging reflectors of the Pilkhaua Subsequences in the front of the central anticline of line 10010 (Fig. 7.6B) indicate sedimentation syn-tectonic with respect to the formation of the anticline in a thrust-front basin. Accordingly, the younger compressional increment in the Eastern Altiplano also has a 'Pilkhaua age'. The similar geological history of the entire Lípez Basin (see section 7.2.1) suggests that this is also the case for the younger compressional structures observed in the northern line (10007). The small normal faults in the syncline of line 10007 (Figs. 7.6A and 7.7) are the only structures that dissect Pilkhaua sediments. They represent the youngest, post-Pilkhaua, tectonic movements in the Eastern Altiplano.

7.3.2 Central Altiplano

Although seismic interpretation on a regional scale is difficult due to the lack of well-dated key stratigraphic horizons, seismic-sequence analysis in smaller thrust-front basins of the Pilkhaua sequence unravel the youngest tectonic history of the Central Altiplano. The interpretation of reflector terminations is used to investigate the succession of faults and to examine the pattern of propagation of deformation to constrain the incremental section-balancing procedure. Absolute time marks are given by isotopic age determination of sampled volcanic rocks in the thrust-top basins (see chapters 6 and 8).

The syn-tectonic basin west of the Ines Anticline has a complex depositional history (Fig. 7.12): the oldest syn-tectonic unit (ST1) is characterised by onlap terminations in the west and in the east (**1** and **2** of Fig. 7.12D). Onlapping reflectors in the west (**1**) are slightly older than in the east (**2**), where the lowermost reflectors parallel the pre-tectonic unit. After the deposition of ST1, the western part of the basin was partly eroded (toplapping pre-tectonic [PT] sequence, **3**), followed by a stage of post-tectonic sedimentation with almost consistent thickness (PST). The younger syn-tectonic sequence (ST2) shows onlapping terminations in the east (**4**) and concordant reflectors in the west. The latter were subsequently rotated (**5**). At the surface, a westward increase in bed thickness of the Pilkhaua sediments in the eastern basin is noticeable (Fig. 7.12E). The inclination of the strata decreases significantly with increasing distance from the pre-tectonic San Vicente Fm. At the pre-tectonic/syn-tectonic boundary, no angular unconformity is developed, but their lithification is different (Fig. A.2B).

I interpret the structural position of this basin as a thrust-front basin of the eastern anticline and concurrently as a piggy-back basin of the western anticline. The first tectonic uplift occurred in the west and led to the deposition of the ST1 that onlaps the new topographic high and shows normal contact in the east (**1**, Fig. 7.12D). The first movements in the east began slightly later, as shown by the onlap in ST1 (**2**). The end of the first movements is followed by erosion of the pre-tectonic sediments (PT) in the west (**3**) and the overall sedimentation of PST. The first onlap of ST2 (**4**) is interpreted as the next deformation step for the formation of the fault propagation fold in the east (Fig. 7.12B). Divergent and rotated reflectors indicate syn-tectonic sedimentation. However, the presence of tilted reflectors in the western part of the basin indicate that tectonic movements had not yet terminated there. A post-depositional rotation must have occurred, otherwise one would expect onlap terminations at the lower boundary of ST2 in the western part of the basin.
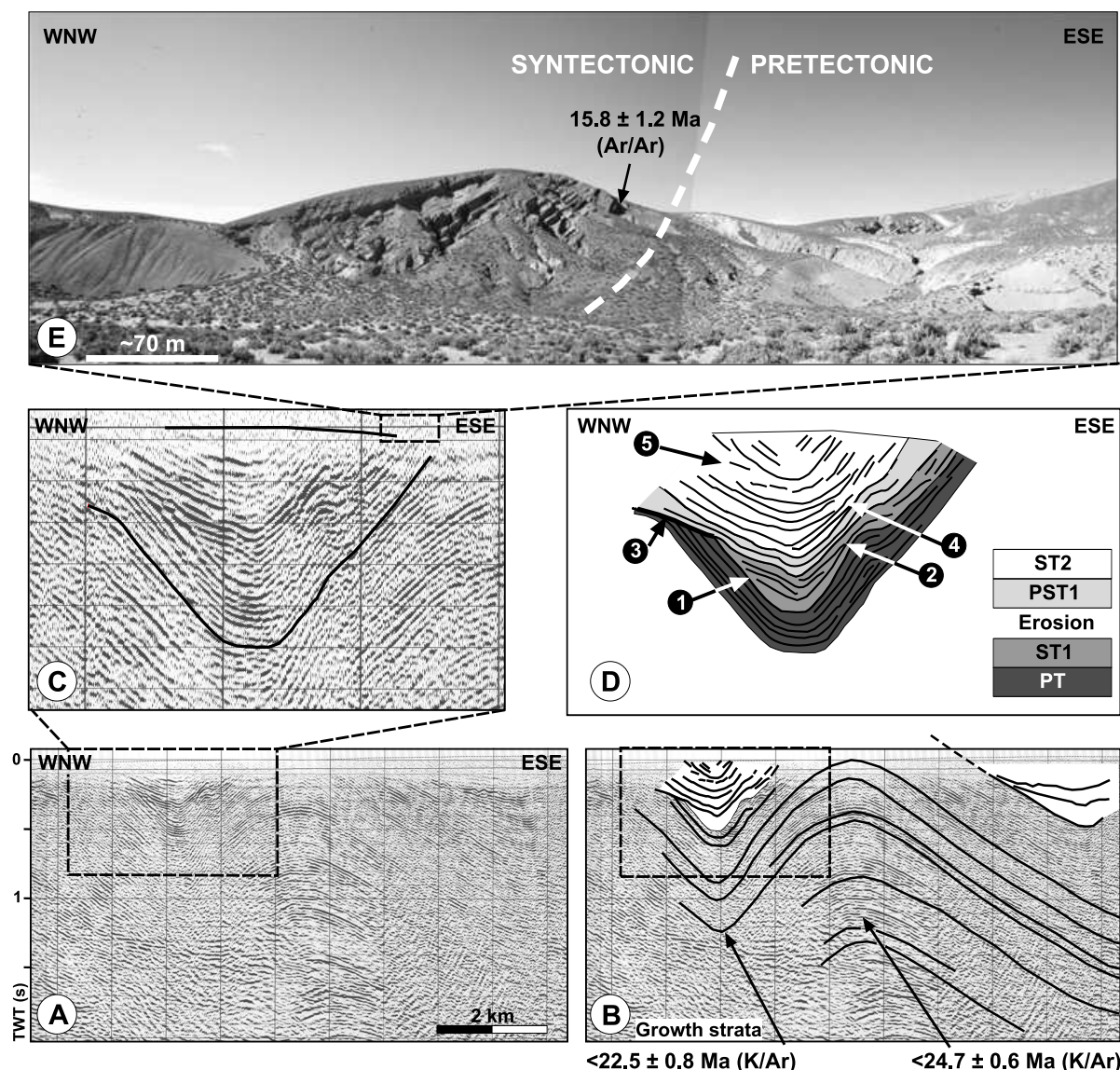
Figure 7.12: Detailed seismic analysis of the syn-tectonic basin west of the Vilque Anticline (line 10023). The basin is interpreted as thrust-front basin of the Ines Anticline and as piggy-back basin of the next thrust sheet. The pre-tectonic is part of the San Vicente Fm., the syn-tectonic part of the Pilkhaua Subsequence. **A:** Uninterpreted seismic data; **B:** Interpreted version of A imaging the fault-propagation fold of the Ines Anticline with the thrust-front basin; **C:** Close-up of A showing the syn-tectonic basin; **D:** Interpretation of C, line drawing and sequence identification (PT = Pre-tectonic, ST1 = first syn-tectonic unit, PST1 = post-tectonic unit 1 [post-ST1], ST2 = second syn-tectonic unit), numbers 1–5 refer to the succession of events discussed in the text; **E:** Surface data showing the eastern part of the syn-tectonic basin. See text for further explanation and Fig. 7.8 for location within the Main Cross-Section.

The analysis of the syn-tectonic basin fill shows that the basin development is related to both adjacent structures. Tectonic movements alternate between locations and were contemporaneous on either side of the basin. They cannot be explained by a simple progradation or retrogradation of a deformation front.
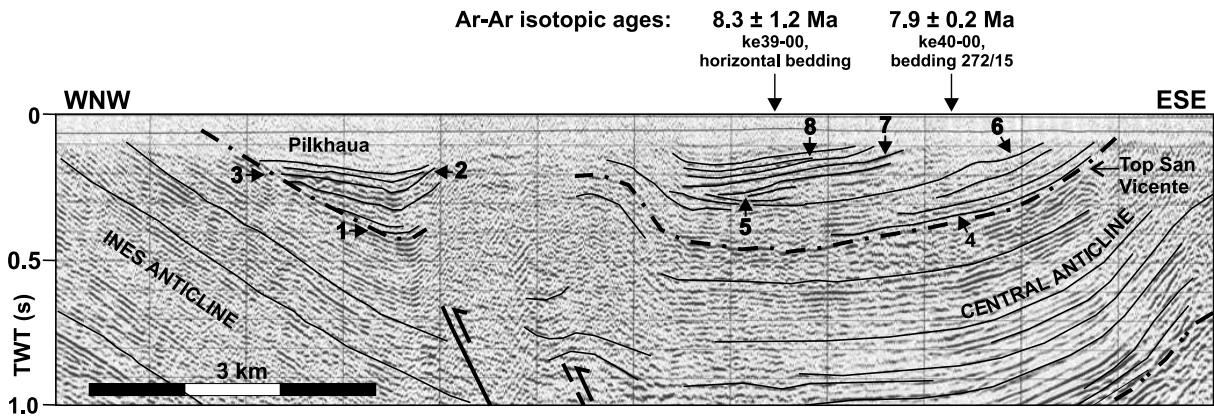
Figure 7.13: Line-drawing of the syn-tectonic 'Pilkhaua' basins between the Ines and the Central Anticlines of the Central Altiplano to illustrate the sequence of fault activation over time, as indicated by onlaps of syn-tectonic sediments (see Fig. 7.8 for location). See text for interpretation.

Seismic stratigraphic analyses of other thrust-front basins in the Central Altiplano domain show a similar deformation pattern: Fig. 7.13 shows the syn-tectonic 'Pilkhaua' basins to the east of the Ines Anticline. They are related to the formation of the Central and Ines Anticlines (see Fig. 7.8 for location). The detailed analysis of seismic data revealed the following sequence of fault activation: the oldest onlaps are in the western part of the western sub-basin, adjacent to the Ines Anticline (arrow **1**). This marks the beginning of the formation of the Ines Anticline. During a later stage, from arrow **2** onward, seismic reflectors also onlap on the eastern border of the same sub-basin, while movement in the west continued (arrow **3**).

In the eastern sub-basin, next to the Central Anticline, the lower syn-tectonic sediments were deposited concordant to the underlying San Vicente Fm. (arrow **4**). This indicates that the formation of the Ines Anticline predates the formation of the Central Anticline. The first onlaps formed during later stages of syn-tectonic sedimentation, again first in the west (arrow **5**), while the eastern sub-basin edge is still characterised by concordant reflectors (arrow **6**). The latest movements are coevally with the formation of the Central Anticline. They resulted in the observed tilting of the older, concordantly deposited syn-tectonic sediments (arrow **7**), and the formation of the eastward-onlapping reflectors (arrow **8**).

This diagram demonstrates again an irregular fault-activation sequence of the west-vergent part of the Central Altiplano's thrust-system. This includes the formation of western anticlines prior to eastern anticlines, which can be seen in both sub-basins (compare arrows **1** with **2**, **1** with **4**, and **5** with **7**), and synchronous fault activity on both sides of a single syn-tectonic basin (e.g. arrows **2** and **3**). I also suggest that during the latest stage of basin formation (from arrows **2** and **5** onward), the entire section, shown in Fig. 7.13, was characterised by active deformation, which was more or less coeval. A rapid deformation rate during this later stage is indicated by the sedimentary facies (see section 3.3.3.1) and by two isotopic ages of volcanic rocks interbedded in sediments, which are identical within error, despite a difference of 15° in dip angle (Ar-Ar samples ke39-00 and ke40-00, see Table C.1 for details and Fig. 7.13.)
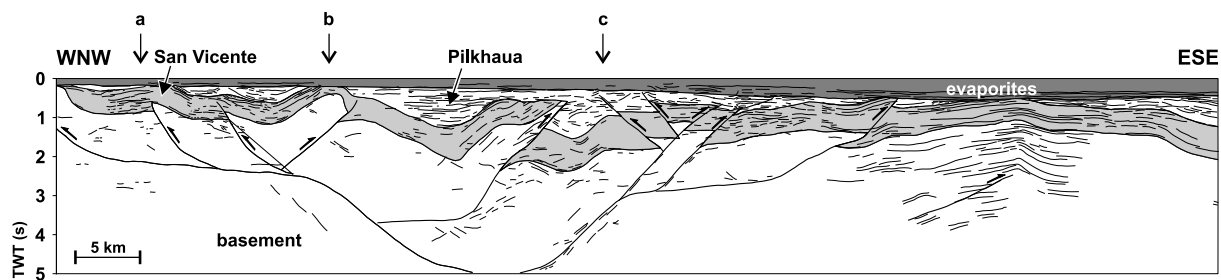
Figure 7.14: Line-drawing and preliminary structural interpretation of the western part of seismic line 2553 (west of A, see Fig. 2.1), depth section. The structures strongly resemble the Miocene structures of the Central Altiplano; **a**, **b**, and **c** correspond to gravity anomalies of Fig. 7.5.

7.4 Western Altiplano

A preliminary interpretation of the northern seismic line 2553 indicates that the structural inventory consists of east- and west-vergent structures, i.e. fault-propagation folds and thrusts with associated syn-tectonic basins overlain by horizontally-bedded evaporites of the Salar de Uyuni (Fig. 7.14). The thickness of the evaporites, which are characterised by horizontal reflectors and concordant boundaries, slowly decreases westward towards the edge of the Salar. Locally-developed truncations below the evaporites are interpreted as erosional unconformities. Divergent reflectors and progressive onlaps towards the rims of the basins characterise the syn-tectonic basins below the evaporites. They reach depths between 1–2 s TWT. The underlying unit is characterised by a weakly-folded reflective band of 0.5–1 s TWT thickness. Its uniform thickness and the concordant boundary with the overlying syn-tectonic basins indicate that no deformation occurred before the deposition of the overlying basins.

With the exception of the central part of the section (Fig. 7.14), the depth of the syn-tectonic basins of the Western Altiplano is similar to that of the 'Pilkhaua' basins of the Central Altiplano. This, together with their similar seismic facies favours the same Middle/Late Miocene age. Consequently, I interpret the underlying reflective part of the section (Fig. 7.14), in analogy to the Central Altiplano, as San Vicente Fm. The rather poor data quality of the stacked section does not permit the differentiation of the pre-San Vicente formations. The existence of similar stratigraphy and structures in the Western and Central Altiplano also suggests that these two regions were deformed more or less coevally during the younger deformation increment.

Chapter 8

Age and pattern of deformation

This section summarises and combines all available relative and absolute age information from the Southern Altiplano cross-section at 21° S to determine the time frames of the deformation increments. Relative ages were mainly derived from the interpretation of seismic lines (reflector geometry, truncations, etc., cf. section 7.3) and from field evidence (erosional unconformities, provenance of clasts, etc., cf. chapters 3 and 4). Isotopic age determinations of volcanic intercalations within Late Miocene syn-tectonic basins directly date the formation of the related structure (cf. section 3.3.3.1 and chapter 6). Absolute deformation ages are key boundary conditions and were used for the definition of restoration steps and target horizons for the incremental cross-section balancing. They were derived from the combination of seismic interpretation with isotopic ages and stratigraphy.

This chapter will show that the Southern Altiplano structure formed during two independent compressional increments, Middle/Late Miocene ($\sim$17–8 Ma, see section 8.2) and Late Oligocene (>27.4 Ma Central Altiplano [see section 8.3.1]; >26 Ma Eastern Altiplano [see section 8.3.2]). The youngest movements are small normal faults in the Eastern Altiplano, which are possibly related to salt tectonics (see section 8.1).

Furthermore, deformation ages of growth strata in syn-tectonic basins and the interpretation of seismic-reflector geometry have enabled me to examine the order of fault activation of neighbouring structures within the given time frame. In section 8.4 I will illustrate that the Southern Altiplano shows a diffuse spatial and temporal distribution of deformation. It was possible to distinguish several phases of westward propagation and eastward retreat of the active deformation front as well as along-strike variation of deformation activity.

8.1   Post-Miocene tectonics

The youngest structures are small normal faults that dissect the syn-tectonic sediments of the Pilkhaua Subsequence in the Eastern Altiplano (to the east of the Vilque Anticline, Figs. 7.6 and 7.7). These faults are local features and could only be observed in the eastern part of the Main Cross-Section (line 10007). Major extensional structures could not be detected in the field and from map observations.

8.2   Miocene compression

The duration of Miocene compression (17–8 Ma) is well-defined by isotopic dating of volcanic
rocks which are interbedded in syn-tectonic thrust-front or piggy-back basins of the Central
Altiplano (Fig. 8.2). Similar ages of the underlying San Vicente Fm. (see section 3.3.3) and
similarities in the seismic facies suggest a similar duration for the deformation in the Eastern
and the Central Altiplano (Fig. 8.2).

8.2.1   Eastern Altiplano

In the Eastern Altiplano, the formation of the Vilque and the Eastern Anticlines can be at-
tributed to Miocene shortening (see Fig. 7.6 for location). The laterally-uniform thickness and
overall concordant boundaries of the OMsv1 and OMsv2 Subsequences show that Miocene de-
formation did not start before the deposition of the Pilkhaua Subsequence (see Fig. 7.6A). The
youngest OMsv2 age in the Eastern Altiplano (16–17 Ma, see section 3.3.3) is a maximum age of
Miocene shortening. In the eastern part of the Main Cross-Section, the Pilkhaua Subsequence
does not show the 'typical' growth structure, as in the Central Altiplano (see section 7.2.1).
However, locally-developed onlaps onto the western limb of the Eastern Anticline as well as
divergent reflectors to the west of the southern extension of the Vilque Anticline (line 10010,
see Fig. 7.6B), indicate that the formation of the Vilque and Eastern Anticlines was coeval with
the deposition of the Pilkhaua Subsequence.

8.2.2   Central and Western Altiplano

Middle/Late Miocene compressional tectonics were responsible for the formation of the biver-
gent thrust system of the Central Altiplano. The age of the formation of single structures during
the Miocene deformation increment is well defined by dating of syn-tectonic thrust-front and
piggy-back basins that are abundant throughout the Central and Western Altiplano (see sec-
tions 3.3.3.1, 4.2, 4.3, and 7.4). The available (due to outcrop) ages of volcanic rocks within the
syn-tectonic basins mostly date the start of shortening rather than the end. This is indicated by
steep to moderately steep dip of most of the dated strata (see Table C.1 and App. F.1 and F.2).
It was impossible to date the end of Miocene shortening for many syn-tectonic basins because
of the absence of tuffs in their higher parts.

First indications of Miocene shortening were derived from the Yazón Anticline in the West-
ern Altiplano. Here, it was possible to date the youngest pre-tectonic tuff (20.9 ± 2.0 Ma, Ar-
Ar, ke28-00) of the vertically-dipping forelimb and the oldest syn-tectonic tuff (17.1 ± 0.6 Ma,
Ar-Ar, ke24-00) which dips 65° west and was found only 50 m west of the former sample
(Fig. 4.3). Syn-tectonic sedimentation in the bivergent thrust system of the Central Altiplano be-
gan slightly later: the oldest syn-tectonic age (15.8 ± 1.1 Ma, Ar-Ar, ke01-00) was derived from
a 60° WNW-dipping tephra in the thrust-front basin west of the Ines Anticline, in the west-
vergent part of the bivergent thrust-system (see App. F.2). Deformation in the east-vergent
part started slightly later: the oldest K-Ar maximum age was derived from a vertically-inclined
tuff in the footwall of the San Cristóbal Fault (13.7 ± 0.4 Ma, sample ps99-17, Silva-González, in
prep., see App. F.2).

Three samples indicate the end of deformation in the Central Altiplano. The maximum age of an undeformed dacitic lava, which unconformably overlies folded San Vicente strata in the hanging wall of the Intra-Potoco Fault, is 11.0 ± 0.5 Ma (K-Ar, sr99-10, Silva-González, in prep.). Sub-horizontal to horizontal tuffs in syn-tectonic basins yielded 8.3 ± 1.2 Ma (Ar-Ar, ke39-00), to the west of the Central Anticline of the bivergent system, and 11.0 ± 0.3 Ma (K-Ar maximum age, ps99-26, Silva-González, in prep.) in the footwall of the San Cristóbal Fault (see App. F.2).

The rate of Miocene deformation possibly also varies across the bivergent system of the Central Altiplano. In the east-vergent domain, volcanic intercalations in the thrust-front basin of the San Cristóbal Fault indicate active thrusting between 13–11 Ma (K-Ar maximum ages, ps99-17 and ps99-26, see above). In contrast, in the west-vergent domain, the ages of two samples within the growth strata west of the Central Anticline (see App. F.2 and Fig. 7.13) are identical within the error, despite the difference of 15° in dip angle of the bedding (ke41-00: 7.9 ± 0.2 Ma, Ar-Ar, 272/15; ke39-00: 8.3 ± 1.2 Ma, Ar-Ar, horizontal bedding). A higher deformation rate in the western part of the bivergent thrust system is also suggested by the absence of stratification and the extremely immature facies of the higher parts of the growth strata, indicating rapid re-deposition of sediments (see section 3.3.3.1).

8.3 Oligocene compression

The locally-developed erosional unconformity below the San Vicente/OMsv1 Fm. is the only 'hard evidence' for Oligocene, i.e. pre-San Vicente deformation. The identification of the unconformity was mainly achieved by interpretation of reflection-seismic data and from field evidence. The determination of the absolute age of Oligocene tectonics is less precise than for the Miocene event. This is mainly because most evidence is buried under post-Oligocene rocks. Furthermore, the almost complete lack of volcanic intercalations in the Potoco Fm., which was deposited prior to the Oligocene deformation increment, renders the age determination of this shortening event difficult. A single tuff age within intensely-folded Potoco sediments in the footwall of the Corregidores Fault yields a K-Ar maximum age of 40.4 ± 1.1 Ma (sr99-03, Silva-González, in prep.). Volcanic activity in the Southern Altiplano began with the onset of the San Vicente Fm. around 29 Ma ago (ke41-00, Ar-Ar, oldest volcanic rock of the San Vicente Fm.). The oldest San Vicente age represents a minimum age for the Oligocene deformation increment.

8.3.1 Eastern Altiplano

In the Eastern Altiplano, Oligocene deformation is observed between 1–2 s TWT, to the west of the Vilque Anticline (see Fig. 7.6A). The truncation below the lowermost reflector of the OMsv1 Subsequence is interpreted as an erosional unconformity (see Fig. 7.11). Anticlinal hinges, formed during Oligocene thrusting, were eroded prior to the deposition of the lowermost OMsv1 sediments. Consequently, the formation of the thrust system and its partial erosion pre-dates the oldest OMsv1 sediments of the Eastern Altiplano, i.e. occurred prior to 25.3 ± 1 Ma (an14-2000, Silva-González, in prep.). The presence of the same erosional unconformity in the southern seismic section of the Eastern Altiplano (see Figs. 7.6B and 8.1) indicates that the Oligocene compressional tectonic event regionally affected large parts of the Eastern Altiplano.

8.3.2   Central Altiplano

In the Central Altiplano, Oligocene shortening occurred in the external parts of the bivergent thrust system as indicated by the direct superposition of higher San Vicente strata onto folded Silurian sediments. In the east-vergent part, this was observed in the hanging wall of the Khenayani-Uyuni Fault (field evidence, see Fig. A.2D) and in the hanging wall of the Corregidores Fault (seismic evidence, see Fig. 7.10). In the west-vergent part, Oligocene shortening only affected the Allka Orkho Fault (see Fig. 7.8 for location). The eastern ridge of the Co. Allka Orkho is formed by eastward-dipping (20–22°) San Vicente sediments with overlying Pilkhaua sediments (see App. F.1). These San Vicente strata directly overlie steeply-inclined, eastward-dipping Paleozoic basement ($\sim$60°) which was raised by the Allka Orkho Fault. The erosional unconformity is further constrained by the absence of Potoco and El Molino sediments in the hanging wall of the Allka Orkho Fault.

The principal evidence of the minimum age of Oligocene shortening in the Central Altiplano was derived from a stratigraphic observation: the oldest OMsv1 conglomerates in the hanging wall of the Intra-Potoco Fault contain Silurian clasts from the adjacent basement highs to the east. This requires that Silurian sediments were partly eroded and re-deposited within the lower San Vicente conglomerates in the Middle Oligocene. The conglomerates are conformably overlain by a basaltic-andesitic tuff with a maximum age of 27.4 ± 0.6 Ma (K-Ar, sr99-12, Silva-González, in prep.).

8.4   Pattern of deformation

To investigate the pattern of deformation, I combined several approaches: The projection of the deformation ages of single structures onto the Main Cross-Section revealed the large-scale lateral distribution of deformation along the >200 km long cross-section (see Fig. 8.2). Detailed seismic sequence and reflector-geometry analysis provided additional information about relative deformation ages at smaller scale and revealed the lateral extent of a deformation increment. In the Eastern Altiplano, seismic-sequence analysis of line 10010 (Figs. 7.1 and 7.6B) suggested a deformation history of the southern Lípez Basin ($\sim$40 km wide), which partly differs from the deformation history of the Main Cross-Section. The analysis of the fill of a single syn-tectonic basin in the Central Altiplano exposed the tectonic relationship of the neighbouring structures at a small scale (i.e. <5 km). Isotopic ages were also used to correlate relative with absolute deformation ages (see Fig. 8.2).

The symmetrical syn-tectonic basin west of the Ines Anticline formed due to Miocene movements on the adjacent Ines and Allka Orkho Faults. Because a very detailed analysis of seismic reflectors of the syn-tectonic basin fill was possible, and syn-tectonic sediments are very sensitive to tectonic events, high-resolution of the events related to both structures were seen (Fig. 7.12). The oldest onlaps were detected in the western part of the basin (reflecting tectonic movements of the Allka Orkho Fault); they predate the first movements along the Ines Fault. The deformation history of this basin was characterised by alternating and contemporaneous tectonic activity of both faults. The data also show that phases of tectonic activity alternate with phases of tectonic quiescence (see section 7.3.2 and Fig. 7.12). This is further supported by the analysis of Miocene syn-tectonic basins to the east of the Ines Anticline (see Fig. 7.13).
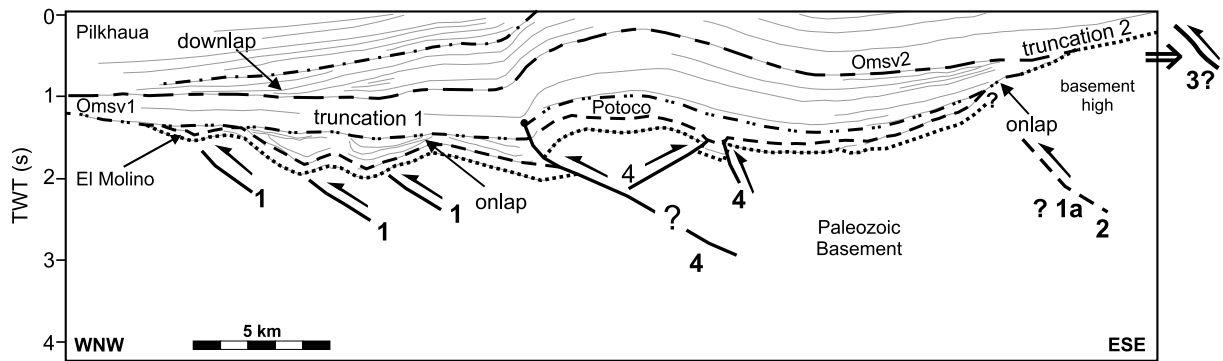
Figure 8.1: Interpretation of YPFB line 10010 from the Eastern Altiplano (seismic section is shown in Fig. 7.6). The line drawing clearly rules out the existence of any unilaterally migrating deformation front. The numbers beside the thrusts indicate the order of activation. The oldest tectonics can be observed in the west (**1**), probably synchronous to relative uplift of the basement high in the east (**1**). Prior to the start of sedimentation of the OMsv1 Subsequence, deformation ceased in the west, but basement uplift in the east continued (**2**), as seen in progressive onlaps of the divergent OMsv1 reflectors. The downlapping reflectors of the OMsv2 Subsequence indicate a westward-prograding sediment body. The weak truncation in the eastern part shows that the sediment source was located to the east of the present section (**3**). The youngest deformational increment inverted the former basin centre (**4**).

The analysis of seismic section 10010 (see Fig. 7.1 for location) determined the spatial and temporal distribution of deformation of the southern Lípez Basin in the Eastern Altiplano (Fig. 8.1): The eastern basement high acted as a topographic barrier, following the deposition of the El Molino formation in the uppermost Cretaceous, until the end of the OMsv1 Subsequence (**1a**). The subordinate El Molino and Potoco basins in the western part of the section were the result of Oligocene, west-vergent thrusting (**1**). This thrusting caused a topographic relief which was leveled prior to the deposition of the OMsv1 Subsequence (see 'truncation 1' in Fig. 8.1), i.e. prior 25.3 ± 1.0 Ma (K-Ar, an14-2000, Silva-González, in prep.). Evidence that these basins are thrust-related, and not extensional, was derived from seismic line 10007 (the eastern part of the Main Cross-Section) where anticlines are preserved more completely than in the southern line (see section 7.3.1 and Figs. 7.6 and 7.11). The present data cannot resolve whether the older compressional movements occurred during or after the deposition of the Potoco Fm., since reflector terminations allow both interpretations (see Fig. 8.1).

By the end of the OMsv1 deposition, the basin fill reached the level of the basement high, the former topographic barrier was leveled out and covered by new sediments from uplifted areas further to the east (**3**, Fig. 8.1), which form a westward-prograding sedimentary body. 'Truncation 2' in the east indicates partial erosion of the basin fill prior to the onset of the OMsv2 Subsequence. The development of an eastern source area is probably related to the uplift of the Eastern Cordillera (i.e. along the San Vicente Fault Zone) and therefore may indicate the deformation age of the latter. Tectonic movements at the San Vicente Fault Zone were dated between 27–17 Ma (Müller et al., 2002). However, the existence of a westward-prograding sedimentary body does not suffice on its own to conclusively prove tectonic activity along the San Vicente Fault Zone. It is also possible that topographic relief in the Eastern Cordillera existed prior to the onset of the OMsv2 Subsequence, and that the related sediments were deposited to the east of the basement high. The youngest tectonic increment affected the former basin centre where west-vergent thrust faults and minor back-thrusts are localised (**4**, Fig. 8.1). I interpret this increment to be synchronous with the development of the Vilque Anticline in line 10007 because

the central anticline in Fig. 8.1 is the southern continuation of the Vilque Anticline. Divergent reflectors within the Pilkhaua Subsequence indicate an age syn-tectonic to the Miocene increment. The tilted OMsv2 reflectors above the basement high (in the east of the section) show that there were also post-OMsv2 movements of the basement high.

This seismic analysis of the southern line 10010 revealed a very similar deformation history, as described for the eastern part of the Main Cross-Section (cf. sections 8.2.1 and 8.3.1). The only exception to this was observed in the OMsv1 Subsequence: In the northern line (10007, Main Cross-Section), the OMsv1 Subsequence is characterised by constant thickness and overall concordant sequence boundaries. In contrast, in the southern line, the OMsv1 Subsequence shows progressive onlaps onto the basement high to the east, which indicate either uplift of the basement high or basin subsidence (see Fig. 7.6).

This analysis of reflection-seismic lines in the Eastern and Central Altiplano, in combination with isotopic ages of syn-tectonic basins, shows that compressional deformation was active during most of the Tertiary except during deposition of the OMsv2 Subsequence. Individual deformation events were mostly restricted to local areas. The regional deformation history cannot be related to a simple tectonic pattern such as a westward- or eastward-prograding deformation front (see Fig. 8.2 and App. F.2). Instead, the sites and initiation of the sequential activation of thrust faults, as imaged by the thrust top basin fills, seem to be irregularly distributed across the profile. Several steps of westward progradation and eastward retreat of the active major deformation front can be distinguished. This observation is valid for the entire cross-section even at different scales (Fig. 8.2). The existence of a migrating deformation front is only a local phenomenon appears to exist only in the east-vergent part of the Central Altiplano during the Miocene deformation increment (cf. section 9.4.1.1 and App. F.2). In addition, the comparison of two seismic sections in the Eastern Altiplano (10007 and 10010, Fig. 7.6) revealed along-strike variations of fault activity.
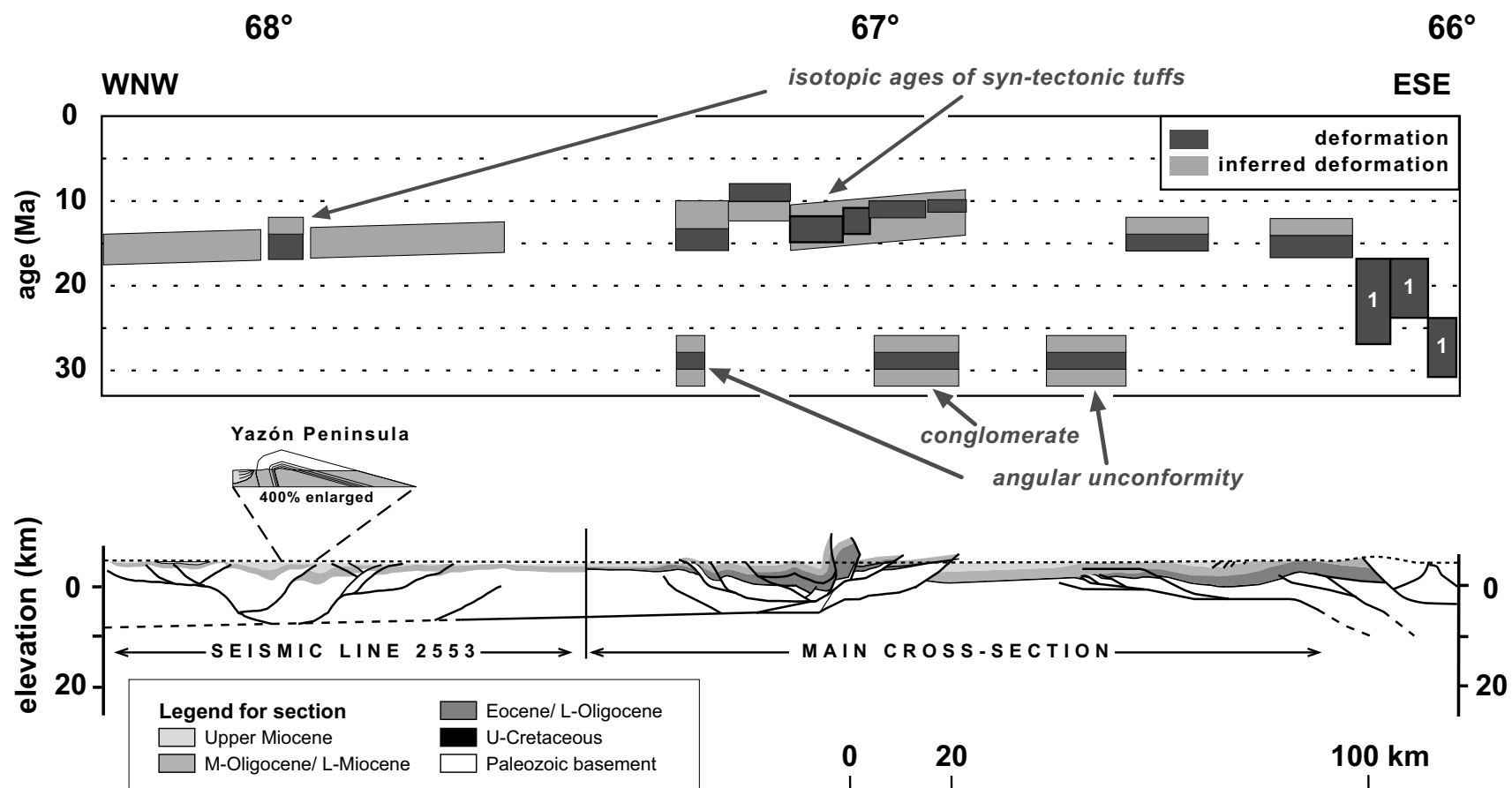
Figure 8.2: Age of deformation across the Southern Altiplano (based on isotopic ages, seismic stratigraphy, and field observations). Seismic line 2553 is projected from 50 km northward from, the Yazón Peninsula is parallel to, the Main Cross-Section (cf. Fig. 2.1). The section east of the Main Cross-Section, i.e. the edge of the Eastern Cordillera, is modified after Müller et al. (2002). The diagram above the cross-section shows the lateral distribution of fault activity over time, 1: data from Müller et al. (2002). This diagram excludes the existence of any unilaterally-migrating deformation front. Instead, the spatial and temporal pattern of tectonic activity is irregular. See chapter 6 for details about isotopic age determination and Table C.1 for structural position and bedding of dated volcanic rocks of this project. All ages, sample numbers and locations, including those ages that were derived from Silva-González (in prep.), are also shown on the geological map (F.1) and were projected on the balanced cross-section (App. F.2).

Chapter 9

Incremental cross-section balancing

The technique of 'balanced cross-sections' permits the quantification of deformation by the construction of restorable (i.e. retro-deformable) geological cross-sections (e.g. Dahlstrom, 1969; Elliott, 1983; Hossack, 1979; Woodward et al., 1989). A balanced cross-section is not necessarily an unique solution, but validates the interpretation by offering a viable and admissible solution (Woodward et al., 1989).

Two-dimensional balancing is only possible when the profile plane is strictly parallel to the plane of tectonic transport, i.e. there is no out-of-section material flow due to tectonic transport oblique to the cross-section. This plane is generally perpendicular to the strike of major thrusts and the trend of large-scale fold (Woodward et al., 1989). The assumption of plane strain in the cross-section is necessary to fulfill the geological volume-conservation law for 2D balanced cross-sections (Dahlstrom, 1969).

In nature, the requirement of plane-strain deformation is almost never fulfilled. Hence, to balance the entire deformation, additional quantitative information about the amount of out-of-plane mass transfer is required. These include, e.g., displacements along faults crossing the profile obliquely, or the shape and orientation of 3D strain ellipsoids (see sections 5.6 and 9.1, and Table D.9). Generally, 2D balanced cross-sections are constructed assuming plane strain and subsequently corrected for out-of-section mass transfer, i.e. by line length or strata-thickness changes.

Incrementally-balanced cross-sections imply the stepwise restoration of each deformation increment. In this study, the total Cenozoic shortening occurred during two distinct deformation increments, i.e. Miocene and Oligocene (see chapter 8). For the entire section, three different restoration steps will be presented: The deformed present-day status, the partially-restored section prior to the Miocene deformation increment, and the fully restored section before the Oligocene.

9.1 Construction technique and boundary conditions

The cross-section was constructed parallel to the Main Cross-Section, which was determined by the position of seismic reflection lines (2.5). In the Central Altiplano, the Main Cross-Section is perpendicular to large-scale structures, i.e. in the optimal orientation to construct a balanced

cross-section. In the Eastern Altiplano, the seismic lines cross the structures obliquely (with an angle of ∼27–40° to the preferred orientation; orientation of the seismic line 10007 = 110°; strike of two anticlines [Vilque Anticline 173°, Eastern Anticline 160°] that are directly on the seismic trace, see Schmidt nets g and h in Fig. 4.1). Consequently, in the seismic profiles, the fabrics of the Eastern Altiplano are shown with shallower apparent dips and larger interlimb angles of folds than perpendicular to the structural strike. In addition, the obliquity of the seismic section to the structural trend implicates that the acquired shortening values in percent are minimum values. Horizontal shortening perpendicular to the fold axes is possibly 10–20% higher than the values from the oblique section.

Seismic lines were the most important database for the profile construction, because they image subsurface structures and their geometry. Therefore the balanced cross-section was not constructed in the 'classical' way, i.e. from surface data, but based on the line drawings of the seismic data. The seismic information was completed and adjusted, especially in the uppermost portion, to fit surface observations (bedding, stratigraphy, fault position and kinematics), well data from the Vilque Well, which lies directly on the profile trace (see App. F.1), and by map analysis. Geological outcrops generally do not coincide spatially with the position of seismic profiles. This is mainly due to logistical reasons of acquisition: The seismic lines where acquired in places without steep topography, and these are mainly covered by Recent sediments. Consequently, in doubt, seismic reflectors were given a higher priority for the profile interpretation than surface data which were projected from several kilometres north or south of the Main Cross-Section.

The Late Cretaceous El Molino Fm. represents the last marine episode of the Southern Altiplano prior to plateau formation (cf. section 3.2). It is the most important paleostructural marker of the balanced cross-section because the widespread presence of oolites and stromatolites in its limestones indicate that it was deposited in shallow water near sea-level.

The combination of all available data produced a starting model which was subsequently improved during the restoration procedure. Every significant change in thrust geometry was cross-checked for consistency with line-drawings and surface data. Surface observations of stratigraphic boundaries, bedding, and faults positions were regarded as first-order boundary conditions for the uppermost part of the cross-section. Furthermore, they were used to calibrate the observed seismic facies with stratigraphy. The northward plunge of structures of the Central Altiplano beneath the Salar de Uyuni permits insight into progressively deeper structural levels south of the cross-section (cf. chapter 4). This provided additional control concerning deep levels, especially regarding eroded or partially-eroded hanging-wall cutoffs, or branch points of faults.

The strategy I used for the cross-section construction was the conservative approach to assume minimal displacement. Consequently, eroded hanging-wall beds were constructed to meet the thrust as soon as possible within the boundary conditions from surface data and seismic reflectors.

9.2   Balancing algorithms

To restore a balanced cross-section the first essential step is to choose the correct algorithm that sufficiently matches the observed structural styles. Many restoration tools are based on one of two different algorithms: 'flexural slip' and 'inclined shear'. 'Flexural slip' implies that the

shear surfaces are parallel or nearly parallel to bedding. Typical indications for this algorithm are flexural-slip folds (parallel folds with slickensides on the bedding planes). In contrast, evidence for 'inclined shear' would consist of spaced or penetrative shear at oblique angles to the bedding or horizontal (Egan et al., 1999). This is not seen in the study area.

The widespread presence of flexural-slip folds in the working area (see introduction to chapter 4) is the strongest reason to use the 'flexural-slip' algorithm. In addition, the observation that the folding of the strata was accompanied by little layer-internal deformation (cf. section 5.7), supports this choice.

The different structural styles between the Eastern and the Central Altiplano required that a different balancing procedure that was applied to the two parts of the Southern Altiplano. The gently-folded or flat-lying strata with shallowly to moderately-dipping thrusts, well-defined fault traces, and conserved hanging-wall cutoffs of the Eastern Altiplano allows the use of a kinematic restoration tool ('fault-parallel flow') of 2DMove (Midland Valley Corp.) that is described by Egan et al. (1999) and Tanner et al. (2003). This algorithm is an extension of 'flexural slip' to cope with variable fault geometry. Kinematic restoration was impossible in the Central Altiplano where narrow anticlines and steep to overturned reverse faults are abundant and where the sequence of fault activation is difficult to assess, but nevertheless necessary for a kinematic restoration. Therefore the non-kinematic 'flexural-slip' algorithm of GeoSec2D (Paradigm Geotechnology B.V.) was the appropriate restoration tool for the Central Altiplano domain. Due to the different restoration methods, the Eastern and the Central Altiplano are described separately.

9.2.1 Kinematic restoration of the Eastern Altiplano ('fault-parallel flow')

'Fault-parallel flow' is a 'move-on-fault' restoration tool, which considers the effects of fault geometry on hanging-wall deformation. Volume is conserved during deformation. Line length and area conservation is achieved when the correct angular 'post' shear is chosen. 'Fault-parallel flow' is based on the assumptions of flexural-slip folding and strain localisation above changes in fault plane angles.

The 'fault-parallel flow' algorithm is designed to kinematically model geological structures in the hanging wall of faults where deformation is accommodated by fault-parallel shear. It is based on particulate laminar flow over a fault ramp. The fault plane is divided into discrete dip domains. Particles in the hanging wall are translated along flow lines, which are parallel to the fault plane, spaced at a user-defined distance. The footwall is not restored.

The 'fault-parallel flow' algorithm is best suited for modelling hanging-wall movement on faults from fold-and-thrust belts where the majority of the deformation occurs discretely between bed interfaces (i.e. flexural slip) and above rapid changes in fault dip. The algorithm assumes particle flow parallel to the fault surface and to the plane of cross-section (plane strain assumption, see introduction to chapter 9). The practical advantage of the 'fault-parallel flow' algorithm in 2DMove is that the entire movement along the fold can be observed in several steps (see Fig. 9.1). Control of the structural geometry is always possible, not only at the beginning and the end stage. This assists in localising error.
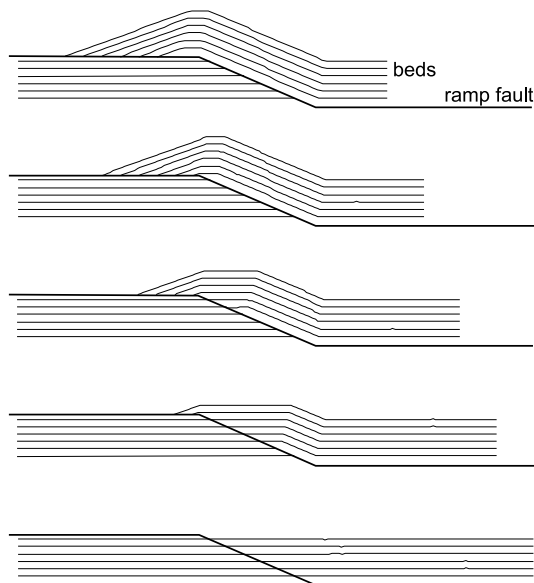
Figure 9.1: Example of the stepwise retro-deformation of a ramp anticline with the 'fault-parallel flow' algorithm (shear angle = 0°). The biggest advantage of the kinematic restoration tool is that changes in the geometry of the hanging wall can be continuously monitored during the entire restoration.

9.2.2   'Classical' restoration of the Central Altiplano ('flexural slip')

The Central Altiplano was balanced with the 'flexural-slip' transfer module of GeoSec2D (Paradigm Geotechnology B.V.) that is described below. The incremental balancing was realised by stepwise restoration. The first step consisted in flattening of the Top San Vicente horizon to restore the Miocene (post-San Vicente) deformation increment. During the second step, Oligocene (pre-San Vicente) shortening was restored using the Top Potoco reflector as a reference horizon (i.e. flattening of the Top Potoco horizon).

GeoSec2D requires the determination of fault or pin-line bordered components (see section 9.2.2.1) that will be restored separately. To fulfill this requirement, all blind thrusts were extended to the surface or connected to other faults.

9.2.2.1   The 'flexural-slip' transfer module of GeoSec2D

'Flexural slip' is one of the modules of GeoSec2D which transfer components from one geometry into another. A component comprises a domain, generally bordered by faults, that is assumed to have been deformed as a single entity. When the source component is in a deformed state and the target component in an undeformed or less deformed state, the transfer process is equivalent to the restoration of a deformed cross-section. Furthermore, the 'flexural-slip' module can also be used to modify any geometry into another, e.g. to transfer the undeformed state into any given deformed geometry. This provides an excellent tool to evaluate the effect of changes in either the deformed or the undeformed state in the balanced cross-section. Changes in the undeformed state can easily be transferred into the deformed state to check the newly-created geometry for consistency and fit with seismic reflectors and/or neighbouring components.

The 'flexural-slip' transfer module transfers components under the assumption that the sliding surfaces are parallel or close to parallel to bedding. This is consistent with surface observations (see introduction to chapter 4 and sections 5.7 and 9.2). For each transfer several reference
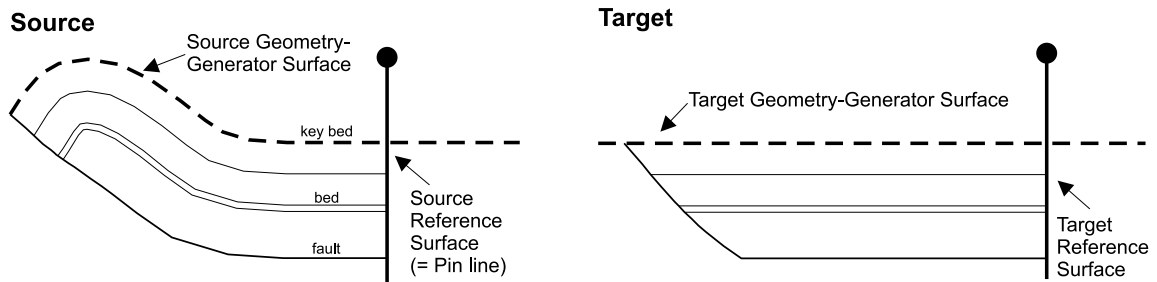
Figure 9.2: Unfolding of a component using the 'flexural-slip' transfer module of GeoSec2D. The Geometry-Generator Surface is the surface from which the internal slip system geometry is created; the Reference Surface is the pin line. Key bed describes the stratigraphic horizon to be flattened.

surfaces (e.g. stratigraphic horizons, fault lines, pin lines, etc.) have to be chosen to determine the internal geometry (by the Geometry-Generator Surface) and the slip system (by the Reference Surface) of the transferred component (Fig. 9.2). The 'flexural-slip' module preserves both bed-length and area.

I typically used the pin line as a Reference Surface. A pin line is a line across which no slip occurred during deformation. Ideal positions for pin lines are undeformed parts of the section (where the pin line is vertical), e.g. the undeformed foreland of a thrust system or at the 'return to regional' (Woodward et al., 1989). In addition, axial surfaces of anticlines or synclines are also acceptable positions of pin lines, especially in the internal parts of the thrust system where no undeformed strata are present within a component.

9.3   Restoration of the Eastern Altiplano

The Eastern Altiplano was kinematically balanced with the 'fault-parallel flow' algorithm. The general assumption of this algorithm is that all deformation takes place parallel to bedding or fault surfaces. A shear angle of 0° was applied. Most faults of the Eastern Altiplano have a flat-ramp-flat geometry. Therefore, no shear correction is required due to changes in fault-plane dip because the shear effect of two bends in opposite directions cancel each other out (Tanner et al., 2003).

The aim of the restoration was to flatten the top of the Late Cretaceous El Molino Fm., which represents the last marine ingression prior to plateau formation. The uniform facies of the El Molino Fm. on the Southern Altiplano, as seen in both outcrop and seismic profiles, precludes the existence of significant topography during its deposition. This qualifies the El Molino horizon as the only valid marker horizon for the entire cross-section. In contrast, large parts of the overlying Tertiary formations are syn-tectonic, as indicated by abundant lateral thickness variations and wedge-shaped sediment bodies (see Table 7.2).

I tried to balance the section with the least number of faults. Regional undulations of the Cretaceous marker were corrected by small angle variations of the basal detachment. The presented structural model is not the unique solution for the cross-section, but can be considered as a preferred model. After the description of the balanced cross-section I will briefly discuss alternative models (see section 9.3.3).
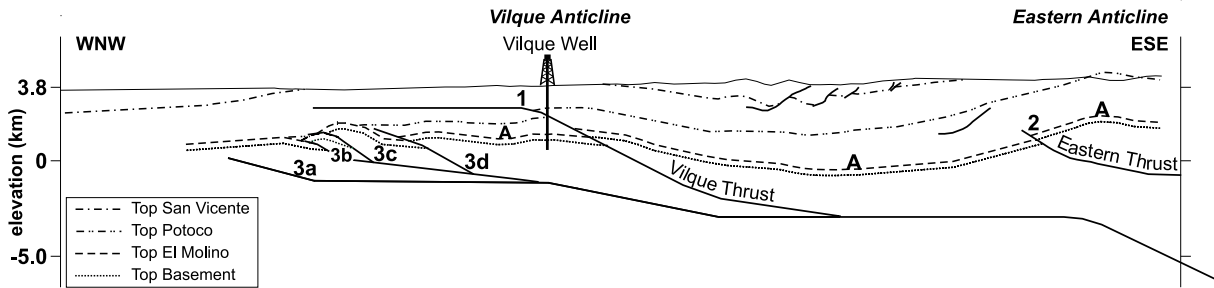
Figure 9.3: Cross-section of the Eastern Altiplano. Numbers indicate deformation domains, see text for explanation. This figure shows the complete (non-eroded) anticlines (above thrusts No. 3a-d) that were constructed during the restoration.

The Eastern Altiplano is the outermost part of a 'classical' thin-skinned fold-and-thrust belt with widely-spaced ramp anticlines and open fault-bend folds that were formed during two independent compressional increments (cf. chapter 8 and section 7.3). The following describes the construction and restoration of the balanced section, beginning with the Miocene movement along the Vilque Fault (No. 1 in Fig. 9.3) and in the core of the Eastern Anticline (No. 2 in Fig. 9.3). The oldest compressional structures are visible in deeper parts of the section, slightly west of the present Vilque Anticline (No. 3a-d in Fig. 9.3). They were partially eroded prior to the deposition of the basal San Vicente Fm. In the presented model (Fig. 9.4), the flattening of the gently anticline ($\sim$40 km wavelength, 175° interlimb angle), represented by the El Molino horizon (A in Fig. 9.3), was achieved by the presence of two shallow ramps in the basal detachment. This construction is reasonable from a structural point of view, but there are some difficulties concerning the timing of the formation of the Eastern Anticline. I will discuss this in section 9.3.3.

9.3.1   Miocene deformation

Fig. 9.4 shows the stepwise restoration of the Eastern Altiplano. Miocene compression took place along two thrusts (No. 1 and No. 2, Fig. 9.3). The geological database to define the Eastern Thrust (No. 2 in Fig. 9.3) is rather poor, whereas the geometry and fault displacement of the Vilque Fault (No. 1 in Fig. 9.3) was easy to constrain due to the good resolution of the seismic data and full stratigraphic control from the Vilque Well that was drilled only 1.5 km west of the anticlinal core (Figs. 9.3 and 2.2).

Tectonic transport along the Vilque Thrust (No. 1, Fig. 9.3) was responsible for the formation of the Vilque Anticline, a 'classical' westward-verging ramp anticline. The ramp angle (28°) was determined from the opening angle of the Vilque Anticline (162°), measured from field data and seismic reflectors, using the geometrical analysis chart for fault-bend folds of Jamison (1992). The lower end of the ramp is indicated by the synclinal core to the east of the ramp anticline. Here the Vilque Thrust merges into the sub-horizontal detachment of the Oligocene deformation. The restoration required 985 m movement along the fault which corresponds to $\sim$1 km horizontal shortening (see Table 9.1 and Fig. 9.4B). For the Eastern Thrust, 450 m of fault displacement was required to restore the hanging wall to the footwall strata. This corresponds to $\sim$0.5 km horizontal contraction (Table 9.1, Fig. 9.4C). The total of Miocene horizontal shortening equals approximately 1.5 km (Table 9.1).

A: Starting model (present day state)

B: 985 m displacement on Vilque Thrust (Miocene) removed

C: 450 m displacement at the Eastern Thrust (Miocene) removed

D: 1700 m displacement at Potoco-3a Thrust (Oligocene) removed

E: 950 m displacement at Potoco-3b Thrust (Oligocene) removed

F: 1400 m displacement at Potoco-3c Thrust (Oligocene) removed

G: 1000 m displacement at Potoco-3d Thrust (Oligocene) removed

WNW   10 km   ESE

Figure 9.4: Stepwise restoration of the Eastern Altiplano. Active faults at each respective deformation step are shown in bold. The displacement along each fault and the corresponding horizontal shortening is given in Table 9.1. See Fig. 9.3 for legend of stratigraphic horizons.

Fault	*Age*	*Displacement*	*Shortening*[1]
Vilque ramp-1	Miocene	985 m	1.0 km
Eastern Fault-2	Miocene	450 m	0.5 km
	Σ *Miocene shortening*		1.5 km
Potoco-3a	Oligocene	1700 m	1.5 km
Potoco-3b	Oligocene	950 m	0.9 km
Potoco-3c	Oligocene	1400 m	1.2 km
Potoco-3d	Oligocene	1000 m	0.9 km
	Σ *Oligocene shortening*		4.5 km
	Total horizontal shortening		**6.0 km**

Table 9.1: Horizontal shortening and fault displacement derived from the kinematic restoration of the Eastern Altiplano (2DMove, 'fault-parallel-flow' algorithm). See Table 9.3 for relative shortening values.
[1] horizontal shortening (rounded).

9.3.2   Oligocene deformation

The highest amount of shortening in the Eastern Altiplano was accumulated in the western part of the section. Compressional tectonics along four west-vergent thrusts (No. 3a–3d in Fig. 9.3, Fig. 9.4d–g) caused 4.5 km horizontal shortening. The upper parts of the anticlines were eroded prior to the deposition of the basal San Vicente Fm., as clearly imaged by the truncation beneath the lowermost San Vicente reflector (Fig. 7.11). Indeed, the seismic image of the partially-eroded anticlines was always sharp enough to determine the fore and back limbs of each anticline (Fig. 7.11). The opening angle exceeds 130° at all locations. Therefore, only 'mode I' fault-bend folds are possible (Jamison, 1992). The ramp angles were again determined with the help of the geometrical analysis charts of Jamison (1992). I interpret the Oligocene thrust system as a westward-prograding in-sequence thrust system. This is indicated by the generally westward increase in ramp angle of the Oligocene thrusts (3a = 15°, 3b = 29°, 3c = 35°, 3d = 29°, Fig. 9.3), which is possibly the result of passive rotation of the older thrusts (to the east) by the younger thrusts (to the west), i.e. piggy-back thrusting. Accordingly, the restoration was carried out from west to east (Fig. 9.4D to G). The displacements along each thrust and the corresponding horizontal shortening values are given in Table 9.1.

All thrusts join a shallowly-eastward dipping, sub-horizontal detachment, which is characterised by a double flat-ramp geometry descending eastwards in two steps from six to nine kilometres depth.

9.3.3   Discussion of the Eastern Altiplano cross-section

The balanced cross-section, shown in Fig. 9.4, is based on the assumption that the complete deformation was accommodated by localised fault zones, as required by the restoration algorithm used ('fault-parallel flow'). This can explain the structures and the timing of their formation in the western part of the section (i.e. the Oligocene thrust system and the Vilque Fault), but
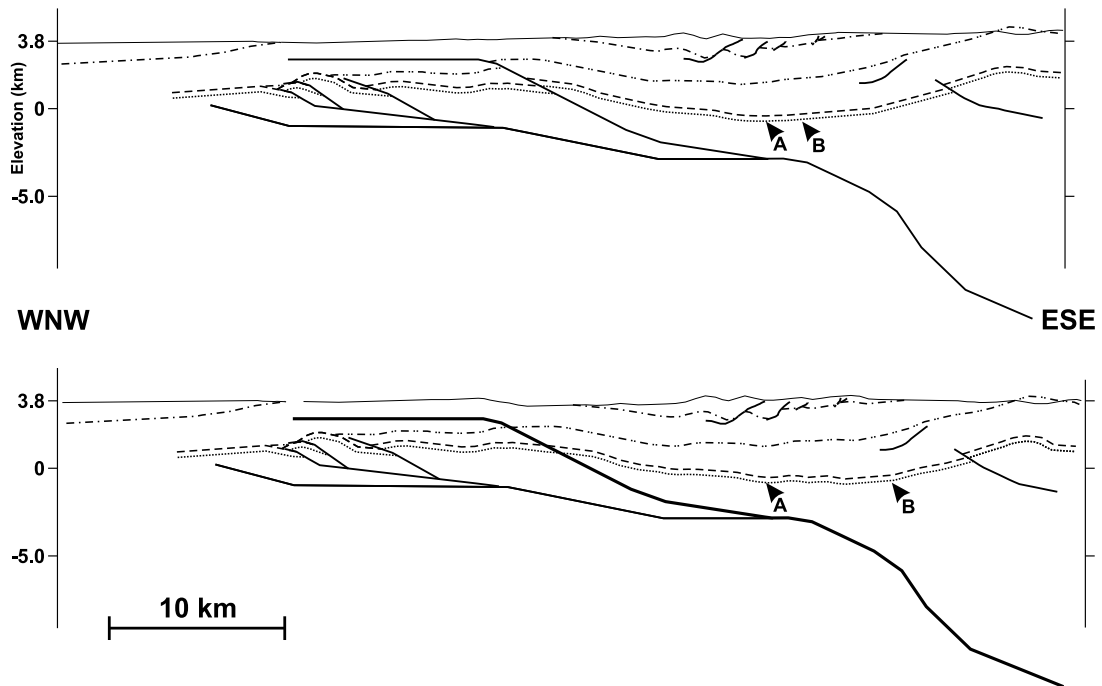
Figure 9.5: The attempt to explain the formation of the Eastern Anticline only with the Miocene short-
ening increment led to a very improbably fault trajectory of the eastern part of the Miocene detachment
(ramp angle far too steep) and still does not sufficiently flatten the Eastern Anticline with the applied
'fault-parallel flow' algorithm. The upper figure shows the deformed, present-day state, the lower fig-
ure the result of 1 km back-stripping above the Vilque Fault and its eastward continuation. See Fig. 9.3
for legend of stratigraphic horizons and text for further explanations, no vertical exaggeration.

there is a problem with the Eastern Anticline. In the structural model shown in Fig. 9.4, the
wide anticline of the El Molino Fm. (A in Fig. 9.3) was mostly the result of Oligocene defor-
mation. The presence of two shallow ramps in the basal detachment is sufficient to flatten the
regional anticline. However, the existence of the Eastern Anticline after the Oligocene defor-
mation increment (i.e. prior to the onset of the OMsv1 Subsequence) should be reflected in
the sedimentary record. One would expect to see onlap terminations of seismic reflectors of
the OMsv1 Subsequence against the anticline. I would further expect the bed thickness of the
OMsv1 to increase towards the basin centre, west of the Eastern Anticline. These observations
can be made in the southern line 10010, but not for the Main Cross-Section (line10007, Fig. 7.6),
where the basal sequence boundary of the OMsv1 Subsequence is overall concordant (Fig. 7.6).
There is not one single onlap developed within the OMsv1 Subsequence. Furthermore, the
OMsv1 has constant thickness throughout the entire section. It is therefore very unlikely that
the Eastern Anticline was a product of the Oligocene shortening increment. Earliest indica-
tions for formation of the Eastern Anticline are onlapping reflectors in the lower part of the
Pilkhaua Subsequence (see Fig. 7.6). This is additional evidence for the Miocene age of the
Eastern Anticline. The associated fault is blind and characterised by increasing displacement
with increasing depth.

To check this interpretation, I attempted to flatten the Eastern Anticline only during the
Miocene increment. This led to absurd fault trajectories (see Fig. 9.5). The restoration of the
anticline with only 1.5 km horizontal shortening (Vilque Fault and Eastern Anticline, see Ta-
ble 9.1) requires a very steep to nearly vertical angle of the basement ramp. The ~60° angle

of the basement ramp, shown in Fig. 9.5, is improbable with respect to the regional structural style in the Eastern Altiplano, characterised by shallow-dipping thrusts and sub-horizontal detachments. In addition, a $60°$-dipping basement ramp is still too flat to completely flatten the Eastern Anticline during the Miocene increment. The result of 1 km horizontal extension, i.e. the retro-deformation of the displacement of the Vilque Fault (Table 9.1), above the $\sim60°$-dipping basement ramp is illustrated by different distances between arrows A and B in the upper and lower part of Fig. 9.5.

Consequently, one of the assumptions previously made (either the application of the 'fault-parallel flow' algorithm and/or the necessity to appropriate the entire deformation onto one basal fault which did not change its position since its formation during the Oligocene deformation increment) is not valid. Possible reasons for this could be:

- Deformation was not restricted to a single basal detachment which was stationary throughout both deformation increments. Instead, total shortening in the Eastern Anticline was distributed between several smaller-scale faults. A large number of smaller faults require smaller displacements along each fault to accommodate the total shortening. Such a structure would have led to distributed deformation, especially in areas above ramp/flat bends in the master fault. An increased number of faults would be less visible in the seismic data and below seismic resolution (cf. Table 7.1.1).

- The lack of data near the eastern edge of seismic line 10007, where the geometry of structures cannot be exactly imaged. If the seismic profile extended further east, and did not end within the anticline, it would be possible to better define the internal geometry of the Eastern Anticline.

The available database favours the former. In the seismic data there is one, possibly two, discrete faults visible in the lower core of the Eastern Anticline. The displacements along these are not sufficient to restore the Eastern Anticline (see Fig. 9.5). It is therefore possible that the deformation was accommodated by several subseismic faults. In this case, this part of the profile is not balanceable employing line-length preservation strategies, because there is no constraint on the number of faults and the typical displacement at depths of 3–4 km beneath the Eastern Anticline.

To summarise: Field and seismic data clearly show that the Eastern Anticline is the result of Miocene shortening (possibly syn-Pilkhaua). This is not restorable with these assumptions ('flexural slip', one stationary basal detachment) that satisfactorily explain the structures in the western part of the section. Nevertheless, the estimated shortening values (Fig. 9.7, Table 9.1) remain valid because they are based on line length and area conservation between the finite deformed and undeformed state and hence independent of the deformation mechanism.

Fig. 9.4G shows that, even in the restored stage, the El Molino horizon is slightly folded. The wavelength of this bend is ~60 km, which is larger than the profile length, and the amplitude less than 1.5 km. It is very unlikely that this extremely weak bending is the result of any deeper-located detachments. The slightly eastward dip, which is the dominant feature of this bending, could be explained by flexural bending of the foreland due to loading by the Eastern Cordillera. It is also possible that this bending is an artefact of the 'fault-parallel flow' algorithm.
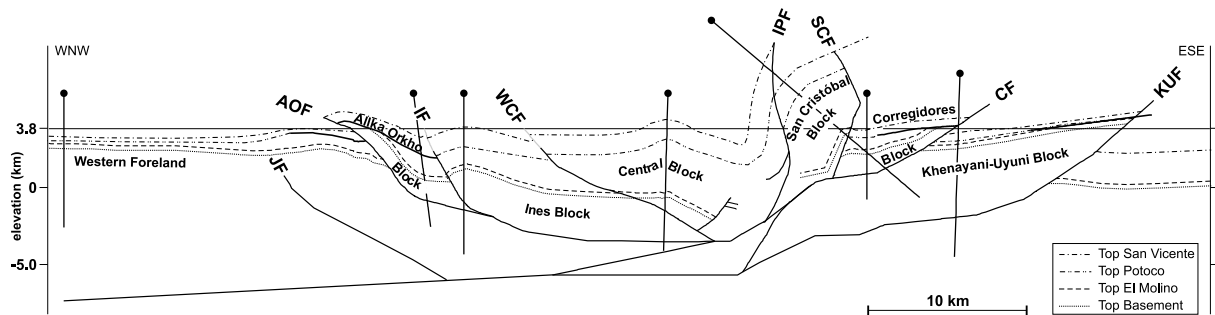
Figure 9.6: Balanced cross-section of the Central Altiplano with block names and pin lines of each block. JF = Julaca Fault (blind), AUF = Allka Orkho Fault, IF = Ines Fault (blind), WCF = Western Central Fault (blind), IPF = Intra-Potoco Fault SCF = San Cristóbal Fault, CF = Corregidores Fault, KUF = Khenayani-Uyuni Fault.

9.4 Restoration of the Central Altiplano

The western part of the Main Cross-Section, the transect of the Central Altiplano, was balanced with the 'flexural-slip' transfer module of Geosec2D. A kinematic restoration, such as for the Eastern Altiplano, was not possible due to widespread erosion of hanging-wall cut-offs and steep to overturned thrusts. Additionally, seismic observations of syn-tectonic basins revealed a complex deformation history with several phases of movement and quiescence during the formation of a single anticline and also partially synchronous movements on two folds bordering the same syn-tectonic basin (e.g. Fig. 7.12). This also made a kinematic restoration impossible.

The restoration of the cross-section will show that most shortening in the Central Altiplano was accumulated during the Miocene compressional event and was responsible for the present architecture of the Central Altiplano. Structures formed during the Oligocene increment were mainly eroded and are therefore difficult to detect. Evidence for Oligocene shortening is mainly derived from unconformities, as observed in the field and seismic data. It was also possible to determine the position of the sub-horizontal detachment which was active during both compressional deformation increments.

The Khenayani-Uyuni Fault Zone forms the eastern part of the bivergent thrust system (Fig. 9.6). It is characterised by four steeply westward-dipping to overturned thrusts with steep to moderately-dipping hanging-wall strata (KUF, CF, SCF, IPF, see Fig. 9.6). Large parts of the hanging walls were eroded during thrusting. The less deformed, west-vergent part is characterised by fault-propagation folds above four moderately to steeply eastward-dipping, mostly blind, thrusts.

There are often inconsistencies between the structures shown in the balanced cross-section and the geological map. The geological map is far more detailed than the balanced cross-section (e.g. in the hanging wall of the Khenayani-Uyuni Fault). The scale of many of these mapped features, however, is below seismic resolution (see section 7.1.1).

In the following I present the balanced cross-section and its retro-deformation. The first step of the incremental balancing was to restore the Miocene deformation (see section 9.4.1); the second step was the retro-deformation of the Oligocene shortening increment (see section 9.4.2).

The third part discusses possible and impossible positions of the basal detachment, and some general problems that occurred during the construction of this part of the cross-section (see section 9.4.3). Fig. 9.6 shows the balanced cross-section of the Central Altiplano and gives an overview of block names and the positions of pin lines in each block.

9.4.1   Miocene deformation

This section describes the construction of the balanced cross-section and the restoration of the Miocene deformation increment. I will illustrate the east-vergent and the west-vergent parts separately (see sections 9.4.1.1 and 9.4.1.2 respectively) and start each section with a summary of boundary conditions that were derived from field and seismic observations.

9.4.1.1   East-vergent part

The eastern part of the bivergent thrust system is formed by the Khenayani-Uyuni Fault Zone, a splay of four moderately to steep westward-dipping thrusts that define three blocks (Khenayani-Uyuni, Corregidores, and San Cristóbal Block) and the eastern part of the Central Block (see Fig. 9.6).

The Khenayani-Uyuni Block is bordered by the Khenayani-Uyuni Fault to the east and the Corregidores Fault to the west (Fig. 9.6). The hanging wall is formed by shallow eastward-dipping (10–15°) Silurian strata which are visible in the seismic data as prominent reflectors (Fig. 7.8). Surface outcrops often show smaller scale, hanging-wall anticlines which are partially dissected by faults (see App. F.1). The size of these features, however, is below the resolution of the seismic data; consequently, they were not considered in the balanced cross-section. South of the cross-section, the Silurian quartzite is directly overlain by higher San Vicente sediments (OMs) above an erosional unconformity (Fig. A.2D). North of the section, folded pelites of the Potoco Fm. crop out in the footwall of the Corregidores Fault. There is no outcrop of the El Molino Fm. in this block (see App. F.1). At the surface, the Khenayani-Uyuni Fault dips 20–30° westward (Co. Khala Huasi, ~30 km south of the Main Cross-Section, see Fig. A.3A).

The Corregidores Block lies west of the Khenayani-Uyuni Block (Fig. 9.6). It is bordered by the Corregidores Fault in the east and the San Cristóbal Fault in the west. At the surface, the hanging wall of the Corregidores Fault is formed by folded Silurian quartzites which are overlain by Cretaceous (El Molino Fm.) and Oligocene-Miocene sediments (San Vicente Fm., OMs). The Silurian and the Cretaceous strata are best exposed in the Serranía Corregidores (see App. F.1). The regional dip of the Silurian and El Molino sediments in the hanging wall of the Corregidores Fault is 35–40° west. Further south, San Vicente sediments (OMs) directly overlie Silurian strata above an erosional unconformity (see App. F.1). The Potoco Fm. does not crop out in this block. The Corregidores Block is well resolved in the seismic data, which show a stepwise flattening of the hanging-wall strata with increasing depth. The trace of the Corregidores Fault is well-defined by the geometry of the hanging-wall strata. A syn-tectonic thrust-front basin in the footwall of the San Cristóbal Fault is filled with sediments of the Pilkhaua Subsequence. Their inclination is vertical, close to the thrust, but almost horizontal 1000–1500 m further east (see section 4.2).

The next block to the west is the San Cristóbal Block which lies between the San Cristóbal and the Intra-Potoco Faults (Fig. 9.6). This block is very poorly resolved in the seismic data. The
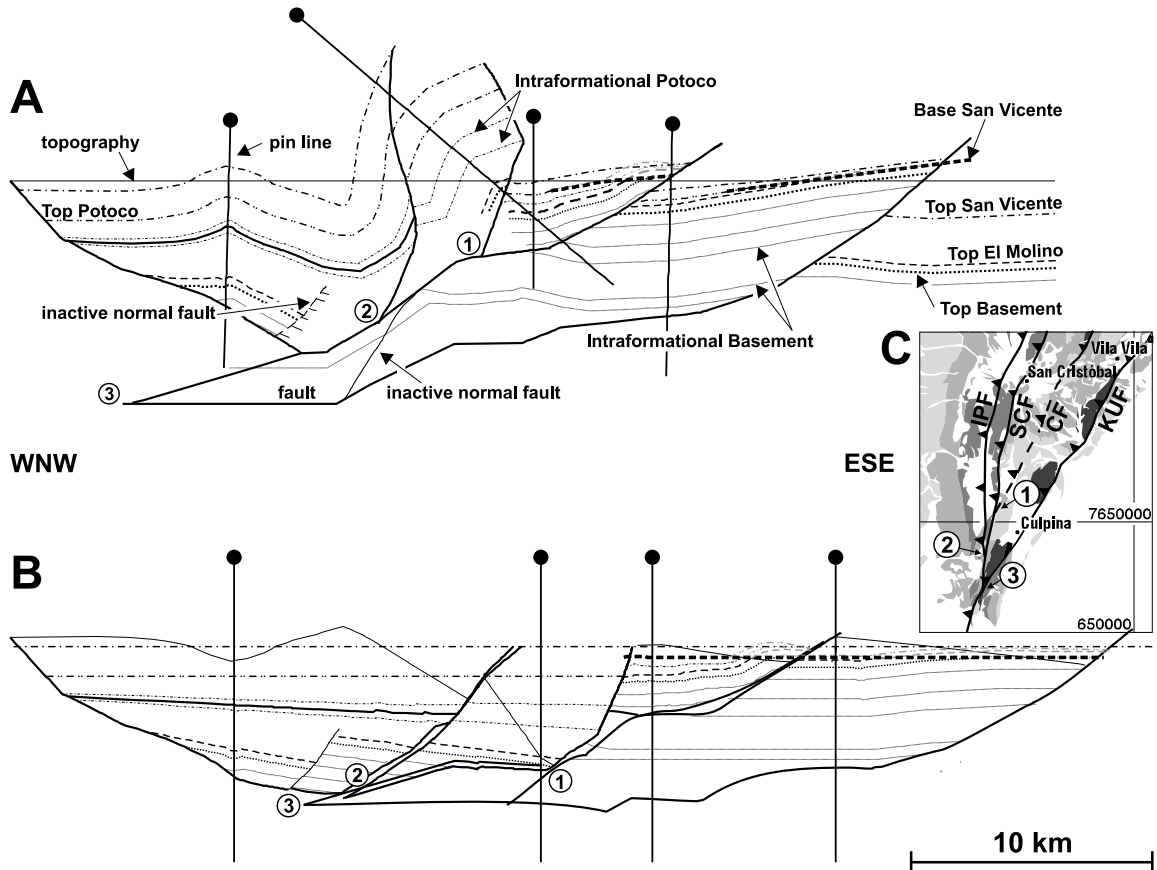
Figure 9.7: Balanced cross-section of the eastern part of the bivergent thrust system of the Central Altiplano (i.e. the Khenayani-Uyuni Fault Zone in the broader sense). **A** shows the deformed state, numbers 1–3 mark branch points of faults. **B** the restoration of the Miocene compressional event, i.e. flattening of the San Vicente horizon. Both figures show the complete, non-eroded hanging-wall cutoffs that were constructed in the course of the profile construction. Grey lines mark those parts that were eroded prior to the deposition of the basal San Vicente Fm. 'Base San Vicente' indicates the basal San Vicente Fm. above an erosional unconformity. **C** Generalised geological map of the southern part of the Khenayani-Uyuni Fault Zone with branch points of major faults (numbers 1–3). See text for further explanation. No vertical exaggeration.

few visible reflectors are very short, discontinuous, and dip gently westward (see line drawing in Fig. 7.8, at depths between ~0.5–1.5 s TWT). In contrast to this, the along-strike projection of outcropping strata ~10 km south of the section defines the surface part of the entire San Cristóbal Block (see App. F.1). At the surface, the hanging wall is formed by a 3500 m thick succession of nearly vertically inclined to overturned, westward-younging pelites of the Potoco Fm. and a few metres of underlying pre-Potoco strata (see section 3.3.1 and Silva-González, in prep.). The surface outcrop of the Intra-Potoco Fault is ~3500 m west of the San Cristóbal Fault. The Intra-Potoco Fault is characterised by a ~100 m wide, intensely-folded zone within vertically-dipping Potoco sediments (see section 4.2). In the balanced cross-section, the Intra-Potoco Fault is overturned and dips 85° to the east. Further south, it dips steeply westward (see App. F.1). The balanced cross-section requires a curved fault trace of the Intra-Potoco Fault which also continues in the eroded hanging wall above the surface.

The construction of the eroded hanging wall of the San Cristóbal Fault fulfilled the boundary conditions given by surface data (i.e. overall vertical strata) and also follows the conservative

approach in constructing the balanced cross-section (see section 9.1). This includes the positions of the Top El Molino horizon which just crops out in the easternmost part of the San Cristóbal Block (representing the few metres pre-Potoco strata below the base of the Potoco Fm., cf. section 4.2), and the Top Potoco horizon, which would meet the surface directly east of the Intra-Potoco Fault (indicating that no San Vicente strata crops out in the San Cristóbal Block). The position of the eastward bend of the hanging-wall strata towards the San Cristóbal Fault was constructed as close to the topographic surface as possible without violating the condition of overall vertical strata at the surface. The hanging-wall cutoff angles could be determined from surface data further south (48–54°, see App. F.1). Indications for the gently westward-dipping strata in deeper parts of the San Cristóbal Block were derived from seismic reflectors (see App. F.2 and Fig. 7.9).

The surface outcrop of the Top Potoco horizon is ∼1500 m west of the Intra-Potoco Fault in the Central Block (Fig. 9.6). Here the nearly vertically-inclined, westward-younging Potoco pelites are conformably overlain by the basal San Vicente Fm. Approximately 1000 m west of the Potoco/San Vicente contact is the core of a open syncline (80° opening angle). To the west, the syncline is followed by a symmetrical, gentle anticline which forms the centre of the bivergent thrust system (see section 4.2).

A consequence of the general northward plunge of the structures in the Central Altiplano is that the branch points of thrusts crop out south of the section. The geological map shows that the branch points of the three western faults (Corregidores, San Cristóbal and Intra-Potoco Faults) crop out slightly north of the branch point between the southern prolongation of the three merged western faults and the Khenayani-Uyuni Fault (see Fig. 9.7C). This indicates that the three western faults branch at higher levels than the Khenayani-Uyuni Fault.

The three western thrusts (Intra-Potoco, San Cristóbal and Corregidores Faults) were formed in-sequence, i.e. from west to east. This is indicated by increasingly steeper dip angles of each thrust towards the west which is the result of passive rotation during piggy-back thrusting (see Fig. 9.6).

The balanced cross-section (Fig. 9.7) shows the branch point of the Khenayani-Uyuni Fault and the master fault at ∼9 km depth, vertically below the western edge of the Central Block (Fig. 9.6). East of the branch point, the master fault forms a basement ramp and rises to a shallower depth. The Khenayani-Uyuni Fault continues horizontally and then climbs stepwise to shallower levels. East of the pin line, it rapidly ascends to the surface with a listric fault trace. This stepwise ascent to shallower levels (from 9 to 5.8 km depth) is a consequence of the profile reconstruction. The fault geometry, together with the geometry of the hanging-wall strata, results in a horizontal position of the basal detachment in the undeformed section. This is not conclusive evidence, however. It is also possible that the basal detachment continues at an acute angle parallel to the basal detachment. This would shift the branch point of the two faults slightly westward. The strata in the deeper parts of the Khenayani-Uyuni Fault were constructed such that the upper limit of the Khenayani-Uyuni Block fits best to the lower boundaries of the Corregidores and San Cristóbal Blocks.

The dip angle of the Khenayani-Uyuni Fault (42°) in the balanced cross-section is steeper than in surface outcrops further south (e.g. Co. Khala Huasi, 20–30°, Fig. A.3A), but resulted in hanging-wall cutoff-angles between 30–40°. Similar cutoff angles were also observed in the neighbouring blocks. A significantly shallower thrust angle of, for example, 15–20° would result in much higher horizontal shortening (∼24 km shortening along the Khenayani-Uyuni

Fault), 'unusual' hanging-wall cutoff-angles below 10°, and a rather unlikely footwall geometry. Therefore I consider the steeper thrust angle as more reliable. Nevertheless, it was observed that the fault plane of the Khenayani-Uyuni Fault flattens at the surface.

The master fault climbs to shallower crustal levels from the branch point of the Khenayani-Uyuni Fault eastwards. After an initial gentle rise (15° dip), it forms a ~40°-dipping basement ramp with a vertical heave of ~3.5 km. The Intra-Potoco Fault branches off the master fault in the middle of the basement ramp. The very strong uplift and erosion of the San Cristóbal Block and adjacent areas is a direct consequence of tectonic transport over the basement ramp. Note that this region is the only part of the Main Cross-Section without associated Late Miocene syn-tectonic sediments. The top of the ramp lies beneath the eastern part of the San Cristóbal Block. The branch point of the San Cristóbal and the Corregidores Faults is in the eastern half of the upper flat. While the San Cristóbal Fault ascends at an angle of 70° to the surface, the Corregidores Fault steepens eastward after ~3 km of sub-horizontal detachment to reach the surface at an angle of ~35° (Fig. 9.7).

The model presented here shows two inactive normal faults which are located at the eastern edge of a half graben filled with sediments from the Potoco Fm. A normal fault between the San Cristóbal and the Corregidores Blocks is required to explain the extreme decrease in thickness of the Potoco Fm. east and west of the San Cristóbal Fault (see Fig. 9.6). In the hanging wall, the thickness of the Potoco pelites reaches 3650 m; 3500 m vertically-inclined Potoco pelites crop out at the surface (see section 4.2). In the footwall of the San Cristóbal Fault, the thickness of the Potoco Fm. is reduced to ~800 m. Erosion of the Potoco Fm. is improbable because of the concordant transition between seismic reflectors of the Potoco and the San Vicente Fms. in the footwall of the San Cristóbal Fault, i.e. the western part of the Corregidores Block (Fig. 7.10). The top of the Potoco Fm. was eroded prior to the onset of the San Vicente Fm. only in the eastern part of the Corregidores Block, i.e. in the hanging wall of the Corregidores Fault, as indicated by the erosional unconformity imaged in the seismic data (Fig. 7.10).

A consequence of the balanced cross-section is that this thickness reduction of 2850 m must occur within a horizontal distance of only ~3000 m. This is not explicable without a syn-sedimentary normal fault that borders the Eocene/Oligocene half graben. Further indications for the existence of an active half-graben system during 'Potoco' times were derived from the westernmost part of the section, where the Potoco Fm. has a wedge-shaped geometry in the undeformed foreland (Fig. 7.9). An inverted normal fault could also explain the very steep angle of the San Cristóbal Fault, which is the steepest fault of the entire section in the undeformed state (Fig. 9.7B). The thickness reduction of the overlying San Vicente Fm. west and the east of the San Cristóbal Fault is possibly a result of differential compaction. I will discuss this in section 9.4.3.

The existence of the second normal fault west of the Intra-Potoco Fault can only be inferred. It is very likely that the half graben was not only bordered by one single normal fault but by several. Therefore the inactive fault perhaps could represent a number of faults.

The lower parts of the San Cristóbal and Central Blocks do not contain detailed information of the stratigraphic fill (Fig. 9.7). This is because I could not construct a balanced cross-section with the algorithms, which yielded consistent results for the rest of the cross-section. Some of the 'unsuccessful' attempts to construct a balanced cross-section of the contact between the Central and the San Cristóbal Blocks are given in Appendix E. I will discuss possible reasons
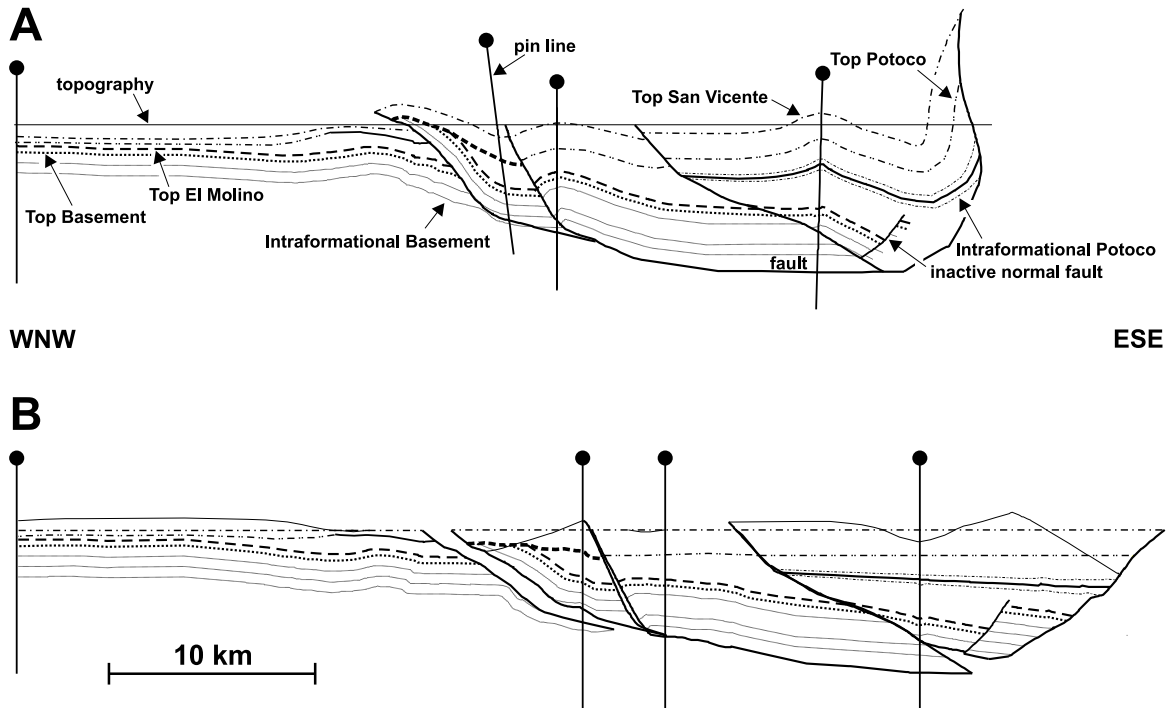
Figure 9.8: Balanced cross-section of the western part of the bivergent thrust system of the Central Altiplano. **A** shows the deformed state, **B** the restoration of the Miocene compressional event, i.e. flattening of the San Vicente horizon. Both figures show the complete, non-eroded hanging-wall cutoffs that were constructed in the course of the profile construction. See text for further explanation. No vertical exaggeration.

for this outcome in section 9.4.3. It is important to note that those areas, i.e. the lower portions of the San Cristóbal and Central Blocks, are only area-balanced.

However, despite of the fact that it was impossible to construct a detailed restorable cross-section for the lower parts of some blocks, it was always possible to determine the line-length shortening from the better-defined upper parts of these blocks. Furthermore, the restored section (Fig. 9.7B) contains the stratigraphic fill of the entire section to illustrate the structural model of the Central Altiplano.

9.4.1.2 West-vergent part

The structural inventory of the western part of the Central Altiplano consists of one thrust and three west-vergent fault-propagation folds with blind thrusts. For the construction and the restoration of the balanced cross-section all faults were extended to the surface (i.e. they also formed borders of blocks). The blocks of the west-vergent part of the thrust system are, from east to west, the Central, the Ines, and the Allka Orkho Blocks, and the Western Foreland (see Fig. 9.6). The fault-propagation folds have associated syn-tectonic basins which are filled with poorly-consolidated sediments of the Pilkhaua Subsequence. The anticlines and the syn-tectonic basins of the western part are mostly well-defined in the seismic data (see Figs. 7.8 and 7.12). The amount of shortening decreases westward, as indicated by the increasing opening angle of the anticlines towards the west (130° Central Anticline, 142° Ines Anticline, 160° Julaca Anticline, see App. F.2).

In the Allka Orkho Block, steeply eastward-inclined Paleozoic basement (e.g. 100/60) is directly overlain by gently eastward-dipping, upper San Vicente sediments above an erosional unconformity (OMs, e.g. 125/20 dip angle). Neither the Potoco nor the El Molino Fms. crop out at the surface. As in the east-vergent part, the existence of an erosional unconformity below the San Vicente Fm. was interpreted as indication of Oligocene shortening. The tilting of the San Vicente strata is the result of Miocene deformation (see chapter 8 and Fig. 7.12). At the surface, the slightly arcuate thrust to the west of Co. Allka Orkho dips 20° to the east. It rapidly steepens with increasing depth and finally dips 50–55° east. The lower end of the ramp is determined by the flattening of the overlying El Molino horizons. To construct the westward increasing thickness of the Potoco wedge I used a thickness gradient between the better-defined Potoco thicknesses of the neighbouring blocks.

The footwall of the Allka Orkho Fault (Western Foreland) is not well-defined in the seismic data. The presented geometry is a result of progressive adjustment of the less-defined footwall of the Allka Orkho Fault to the better-defined hanging wall during the stepwise retrodeformation and the forward-deformation of the best-fit-undeformed section to the deformed stages. This procedure is further described in Fig. 9.10.

9.4.2 Oligocene deformation

Oligocene shortening only affected the external parts of the bivergent thrust system, namely the Khenayani-Uyuni and the Corregidores Blocks in the east and the Allka Orkho Block in the west (Fig. 9.9). The main evidence for Oligocene shortening are erosional unconformities below the San Vicente Fm. (8.3.2). Consequently, the Oligocene hanging-wall cutoffs were completely eroded and had to be reconstructed.

For the construction of the eroded hanging walls I used the following constraints: The top of the Paleozoic basement was defined from surface outcrops, the Late Cretaceous El Molino Fm. was given a uniform thickness of 300 m. The variable thickness of the Potoco Fm. was interpolated between two points with well-defined thickness. I followed an overall conservative strategy and brought the hanging-wall strata to the fault as early as possible without violating constraints from surface and seismic data.

In the east-vergent part of the thrust-system, seismic data show that erosion only affected the hanging walls of the thrusts and not the footwalls (e.g. Fig. 7.10). Consequently, the observed thicknesses of the Potoco Fm. in the footwalls of the thrusts are considered to be the original thickness. The balanced cross-section of the Eastern Altiplano shows a westward thinning of the Potoco Fm. (Fig. 9.13). The tip of the Potoco wedge lies to the west of the Vilque Well. In the east-vergent part of the Central Altiplano, the presence of Potoco sediments is mapped in the footwall of the San Cristóbal and the Corregidores Faults (see App. F.1). East of the San Cristóbal Fault, the thickness of the Potoco Fm. decreases eastward (i.e. from 800 m in the footwall of the San Cristóbal Fault to 220 m in the footwall of the Corregidores Fault). The Potoco Fm. does not crop out in the footwall of the Khenayani-Uyuni Fault. I therefore assume that, similar to the Eastern Altiplano, the Potoco Fm. was not deposited there. Consequently, to construct the eroded hanging walls of the Oligocene deformation I used a Potoco Fm. thickness varying from 800 m at the western edge of the erosional unconformity in the Corregidores Block to 0 m in the hanging wall of the Khenayani-Uyuni Fault. The geometry of the hanging-wall anticlines above both faults were partially defined by seismic reflectors imaging the Silurian strata (Fig. 9.9).
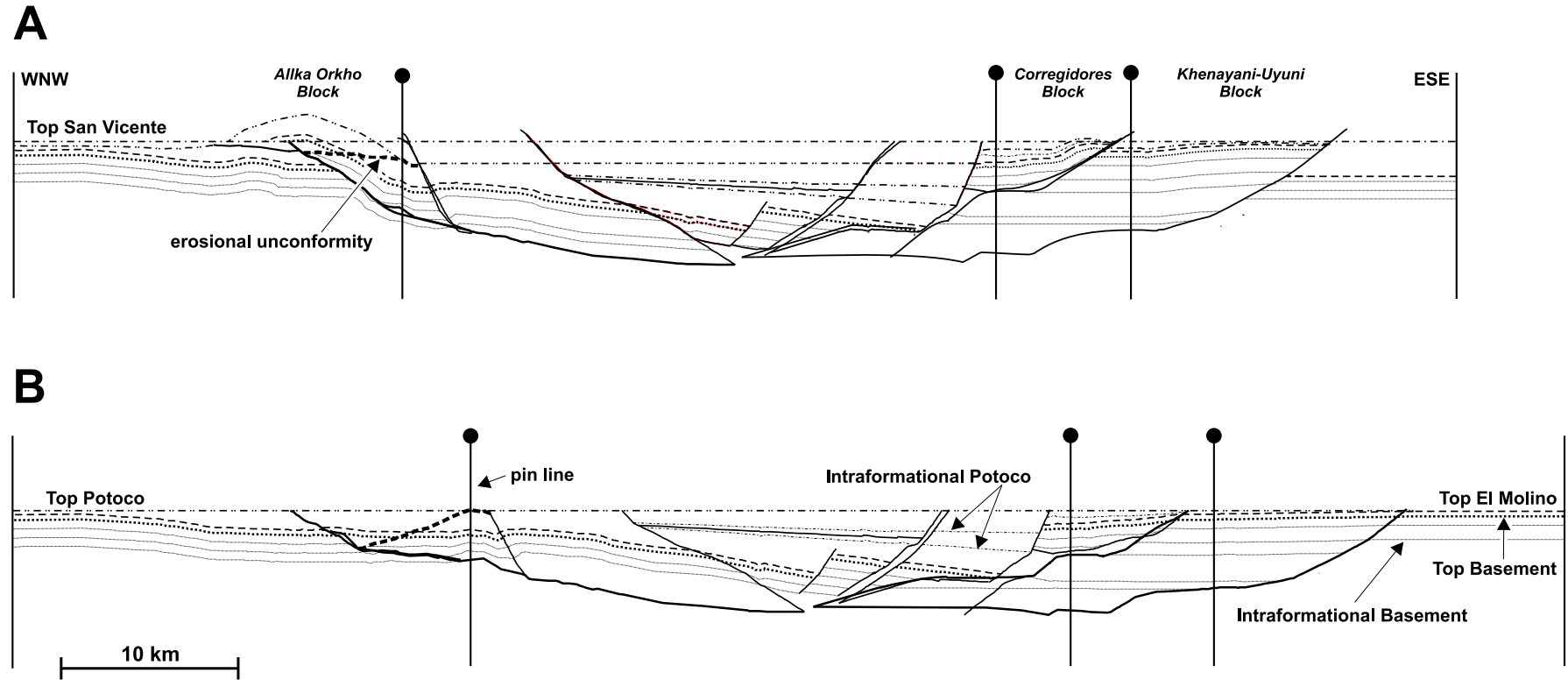
Figure 9.9: **A:** Reconstruction of the Pre-Miocene cross-section of the Central Altiplano with complete, non-eroded hanging walls (newly constructed above the erosional unconformity); **B:** Restoration of the Oligocene deformation increment. No vertical exaggeration.

In the west-vergent part of the thrust system, Oligocene deformation only affected the Allka Orkho Block. Here, I also used a constant thickness-gradient to infer the thickness of the Potoco Fm. The end points were defined by the thicknesses in the neighbouring blocks (940 m at the western end of the erosional unconformity in the Western Foreland and 1250 m in the hanging wall of the Ines Fault, see Fig. 9.6). The detailed construction of the eroded hanging-wall of the Allka Orkho Fault is described in Fig. 9.10.

9.4.3   Discussion of the Central Altiplano cross-section

The stepwise restoration of the balanced cross-section of the Central Altiplano revealed the following values of horizontal shortening:

Restoration steps	profile length	shortening
deformed profile length	78.2 km	
after restoration of the Miocene increment	91.6 km	13.4 km
after restoration of the Oligocene increment	97.9 km	6.3 km
Total		**19.7 km**

Table 9.2: Results of the incremental cross-section balancing of the Central Altiplano. Shortening values in percent are given in Table 9.3.

Table 9.2 shows that most of the shortening (i.e. 68% of the total 19.7 km) accumulated during the Miocene deformation increment. This is in contrast to the Eastern Altiplano, where Miocene shortening only accounted for 33% of the total (cf. Table 9.1).

The profile restoration revealed that the two compressional deformation increments were preceded by an extensional regime that led to the formation of a half graben during deposition of the Eocene/Oligocene Potoco Fm. The syn-tectonic character is shown by an eastward-thickening wedge of Potoco sediments (from below 250 m in the undeformed Western Foreland to 3650 m in the hanging wall of the San Cristóbal Fault). The eastern border of the half graben is formed by a precursor of the San Cristóbal Fault, which was active during the sedimentation of the Potoco Fm. The mostly pelitic sediments of the Potoco Fm. make the existence of a significant topographic relief during the extensional regime highly unlikely. This, in turn, indicates very small strain rates during the Eocene/Oligocene.

The locally-developed erosional unconformities at the base of the San Vicente Fm. indicate that the deposition of the San Vicente Fm. postdates post-Oligocene shortening. The reduced thickness of the San Vicente Fm. in the Corregidores and Khenayani-Uyuni Blocks is required by the presence of Late Miocene, syn-tectonic sediments of the Pilkhaua Subsequence at the surface: the vertical strata in the footwall of the San Cristóbal Fault have a maximum age of 13.7 ± 0.4 Ma (K-Ar, Silva-González, in prep.). It is commonly observed that the thickness of post-extensional sediments thins out toward the graben shoulders. This is often explained by thermal subsidence. In the Central Altiplano, however, there is no evidence of thermal subsidence. Therefore I suggest that the thickness reduction of the San Vicente sediments in the Corregidores and Khenayani-Uyuni Blocks is due to differential compaction. Recently published studies (Krzywiec, 2001; Skuce, 1996) showed that significant thickness variations above normal faults must not always indicate syn-depositional fault activity. Instead, they can also be due to differential compaction above the hanging wall and the footwall of normal faults
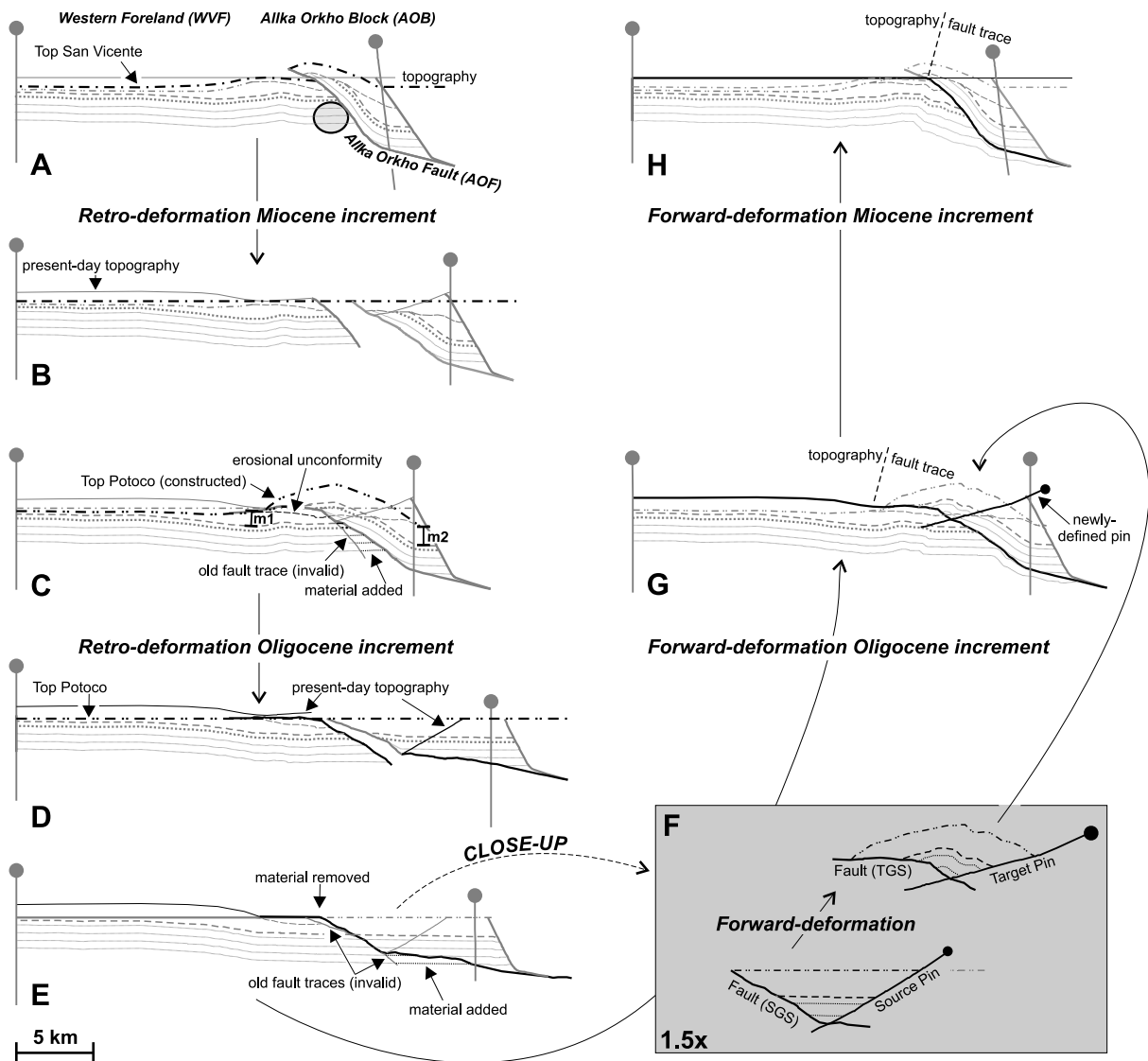
Figure 9.10: Work-flow of the construction of the eroded hanging wall of the Allka Orkho Block (AOB) and the eastern part of the Western Foreland (WFL). **A:** Starting model, based on line-drawing of seismic profiles and surface data. The footwall of the Allka Orkho Fault (AOF) (circle) is very poorly resolved in the seismic data and therefore only inferred. The erosional unconformity in the hanging wall is consistent with surface observations (see section 4.2). **B:** Restoration of the Miocene deformation increment, i.e. flattening of the Top San Vicente horizon. The fault trace of the AOB is better constrained than in the WFL. **C:** Extrapolation of the footwall horizons to the AOB, and construction of the eroded hanging wall of the AOB. The Oligocene trace of the AOF continues along the Top Potoco horizon westward. The thickness of the Potoco Fm. was constructed with a gradient between **m1** = 940 m and **m2** = 1230 m. **D:** Retro-deformation of the Oligocene increment, i.e. flattening of the Top Potoco horizon. **E:** Completion of the undeformed state by extrapolation of the WFL below, and removal of part of the AOB below, the topography, respectively. The deformed states of the WFL and of the eroded hanging wall were determined by successively forward-deforming stage E. **F:** Construction of the post-Oligocene hanging-wall of the AOB with newly-defined geometry generator surface (fault) and reference surface (pin = topography). **G:** Combination of the eroded (H) and the non-eroded part (from B) to complete the forward deformation of the Oligocene increment for the AOB. The WFL was forward-deformed with the combination of fault-trace and topography as geometry-generator surface. **H:** Forward-deformation of the Miocene increment (final version). The WFL was again projected onto the fault trace and topography.

without their tectonic activity (Skuce, 1996). In the Central Altiplano it is very likely that compaction of the thick Potoco pelites in the footwall (i.e. San Cristóbal Block and westwards) is much higher than in the hanging wall (i.e. San Corregidores Block and eastward). This may explain the lateral thickness variation of the post-extensional and post-first-compressional San Vicente sediments.

A consequence of the balanced cross-section is that all thrusts merge into a basal detachment. Indications for the detachment geometry were derived from the Late Cretaceous El Molino Fm., which was deposited prior to the onset of plateau formation. The Main Cross-Section shows that the El Molino Fm. still forms a sub-horizontal regional around sea level. Exceptions to this are the strongly-deformed external parts of the bivergent thrust system, i.e. the Khenayani-Uyuni Fault Zone and the Allka Orkho Fault. There, the El Molino Fm. was uplifted along discrete faults and locally crops out at the surface at an altitude of ∼3800 m (see App. F.1 and F.2). Despite this, the elevation of the El Molino horizon is significantly higher (2300 m) in the undeformed Western Foreland than in the footwall of the Khenayani-Uyuni Fault (0 m). I take this as further indication for a shallow westward-dipping detachment. The dip angle α of the detachment was determined with the following equation:

$$\alpha = \arctan \frac{x}{h} \tag{9.1}$$

where x is the horizontal contraction and h is the height difference of the Top El Molino horizon between the Western Foreland and the footwall of the Khenayani-Uyuni Fault. The basal detachment of the bivergent thrust system of the Central Altiplano dips 1.5° westward (x= 20 km [see Table 9.2], h= 2.3 km) and lies at depths between 9–10 km (see App. F.2).

Additional evidence for a westward-dipping detachment is given by the age of Late Miocene, syn-tectonic sediments. The deformation-age diagram of Fig. 8.2 shows that Miocene deformation started in the Western Altiplano (Yazón Anticline, 17.1 ± 1.1 Ma ago) and migrated eastward. Consequently, deformation in the west-vergent (back-thrust) part of the bivergent thrust system started earlier (i.e. 15.8 ± 1.2 Ma to the west of the Ines Anticline) than in the strongly folded and uplifted east-vergent (fore-thrust) part of the Khenayani-Uyuni Fault Zone, where shortening did not start before 13.7 ± 0.4 Ma (K-Ar maximum age, see App. F.1, F.2, and Silva-González, in prep.). This eastward migration of deformation onset possibly reflects the eastward progradation of the basal detachment during the Late Miocene.

The eastward migration of deformation is also the principal reason I consider an eastward-dipping detachment unlikely. If the detachment continued towards the east, I would expect the El Molino Fm. to be shallower in the east than in the west, which is not the case. Furthermore, an eastward-dipping basement ramp in the basal detachment would result in extremely strong uplift of those crustal parts that are above the basement ramp. The only part of the entire balanced cross-section, however, which experienced very strong uplift is the Khenayani-Uyuni Fault Zone. This uplift can be fully explained by the basement ramp of the master fault beneath the San Cristóbal and the Central Block (see App. F.2).

The existence of one or several ramp bends in the basal detachment is also unlikely, because every change in the dip angle of the basal detachment should have an effect on all overlying parts of the crust and therefore should be visible in the seismic or surface data. The presence of Late Miocene syn-tectonic basins throughout the Main Cross-Section, which are all at a constant altitude, except for the Khenayani-Uyuni Fault Zone, forbids major changes in the dip angle of the basal detachment.
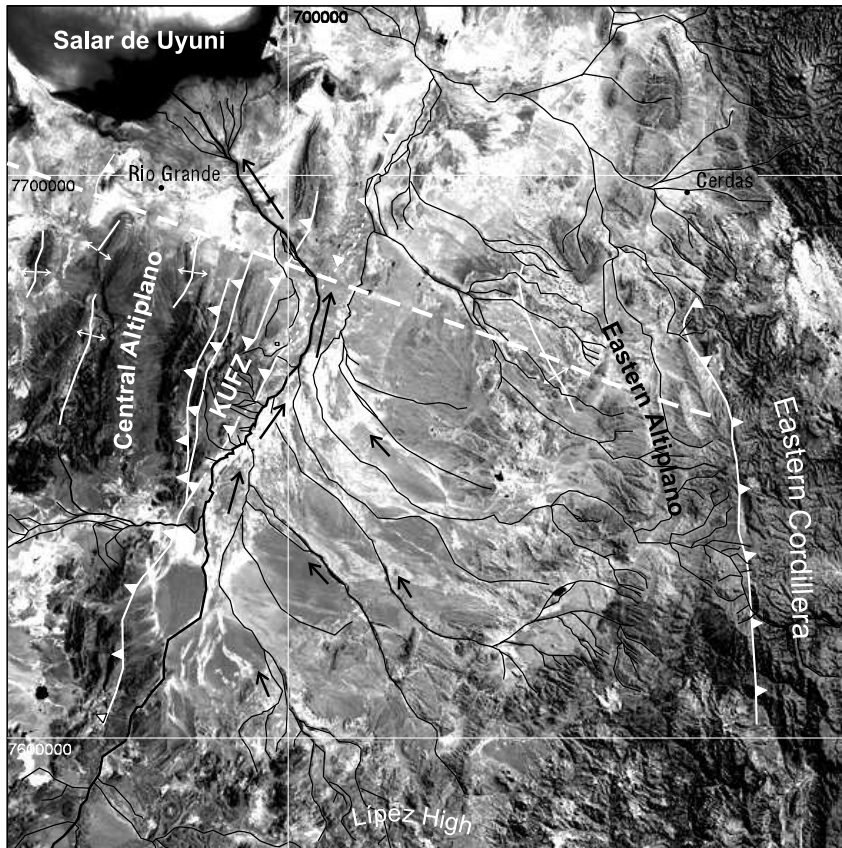
Figure 9.11: Drainage system (black lines) superimposed onto the satellite image of the Lípez Basin and adjacent areas of the Southern Altiplano. Arrows show the direction of sediment transport, arrow length correlates to the amount of sediments, stippled white line delineates the Main Cross-Section, main structural elements are shown in white. Note the significant bend of the rivers in the footwall of the Khenayani-Uyuni Fault Zone (KUFZ), which acts as a topographic hindrance.

The thickness of syn and post-tectonic sediments (Pilkhaua Subsequence to Recent) reach maximum values (1500 m) in the footwall of the Khenayani-Uyuni Fault. This is approximately one and a half times the thickness reached in the rest of the Main Cross-Section. Today, the Lípez Basin drains into the Salar de Uyuni. Main sediment sources are the Eastern Cordillera in the east and the Lípez High to the south of the basin (Fig. 9.11). Consequently, the main drainage direction of the Lípez Basin is to the NW. However, Fig. 9.11 shows that the NNE–SSW trending hills of the hanging-wall of the Khenayani-Uyuni Fault Zone act as a barrier, forcing the rivers to bend towards the N–NNE, follow the trend of the hills, and only reassume their original NW-direction north of the Main Cross-Section. This has caused sediment transport on the footwall and parallel to the Khenayani-Uyuni Fault Zone which is equivalent to material transport into the balanced cross-section. A further effect of this topographic hindrance is a sediment concentration in the footwall of the Khenayani-Uyuni Fault which may also contribute to the observed increased sediment thickness in the Main Cross-Section. This study shows that this topographic hindrance was the result of Late Miocene shortening. I therefore assume that the increased thicknesses of Pilkhaua and younger sediments in the footwall of the Khenayani-Uyuni Fault are a direct consequence of the formation of the relief in the hanging wall of the Khenayani-Uyuni Fault Zone.
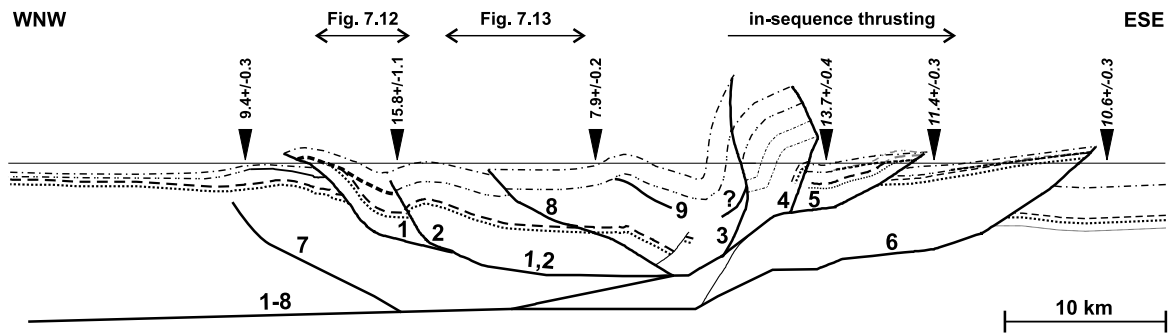
Figure 9.12: Onset of fault activation in the bivergent thrust system of the Central Altiplano. Numbers indicate the sequence of fault activation, based on various constraints: isotopic age determination of syn-tectonic sediments (2, 5, 6, 7, 8), seismic-sequence analysis (1, 2, Fig. 7.12), and constraints from the balanced cross-section (in-sequence formation of 3–5). Black triangles mark sample location for isotopic age determination with the corresponding age; normal font: Ar-Ar age (own data), italic font: K-Ar age (Silva-González, in prep.); no vertical exaggeration.

The geometry of the bivergent thrust system of the Central Altiplano favours the interpretation of an east-vergent fore-thrust system and a west-vergent back-thrust system. They are kinematically coupled because both parts developed between ∼16 and ∼8 Ma, as indicated by the age of volcanic intercalations in syn-tectonic sediments (see Fig. 9.12 and App. F.2).

Isotopic ages of tilted syn-tectonic sediments, detailed seismic analysis (e.g. Fig. 7.12), and consequences of the balanced cross-section reveal the sequence of fault activation during the Late Miocene formation of the bivergent thrust system of the Central Altiplano. Fig. 9.12 shows that the oldest compressional movements occurred in the west-vergent part of the thrust-system (1 and 2). The oldest isotopic age (15.8 ± 1.1 Ma, ke01-00) was derived from the eastern edge of the syn-tectonic basin above fault number 2. Detailed seismic-sequence analysis of this syn-tectonic basin reveals that compressional tectonics at fault 1 started slightly earlier than at fault 2 (cf. Fig. 7.3.2). The observation that the oldest syn-tectonic sediments on the Southern Altiplano are from the Western Altiplano (Yazón Peninsula, 17.1 ± 1.1 Ma, ke24-00), and that the beginning of deformation in the bivergent thrust system of the Central Altiplano was also in the west-vergent part, images the eastward progradation of the basal detachment. The in-sequence thrusting of faults 3–5 is a consequence of the balanced cross-section (see section 9.4.1.1). This is further supported by isotopic ages (Fig. 9.12). Isotopic ages also show, that fault 6 was active earlier than faults 7 and 9. The age for fault 6, however, is a maximum age (K-Ar). In contrast, movements along faults 7 and 9 are well-defined by Ar-Ar ages of syn-tectonic sediments. The seismic analysis of the Pilkhaua basins between faults 2 and 9 showed that the activity of fault 8 began earlier than of fault 9 (cf. Fig. 7.13).

To conclude, the early phases of Miocene shortening were characterised by an eastward-prograding triangle zone which led to movements along the Yazón Fault around 17 Ma ago, followed by the activation of the Allka Orkho (1, Fig. 9.12) and Ines Faults (2) in the west-vergent part of the bivergent thrust system. It is possible that pre-existing basement structures, which parallel the future fault (cf. Fig. 7.8), could have influenced the formation of the triangle zone. The second phase started with the onset of deformation in the east-vergent part where most of the net horizontal shortening accumulated. Furthermore, interpretation of seismic data indicates that especially during the later stages of Miocene shortening the entire bivergent thrust system was deformed more or less coevally (see Figs. 7.12 and 7.13).

9.5   Final discussion

The construction of the balanced cross-section and its retro-deformation yielded 26 km (14.5%) horizontal shortening of the Main Cross-Section which was accumulated during two independent compressional events: (i) Oligocene age, corresponding to the transition between the Potoco and the San Vicente Fm., and (ii) Middle/Late Miocene, syn-tectonic to the deposition of the Pilkhaua Subsequence. The magnitude of shortening and its distribution within the increments varies between the Eastern and the Central Altiplano. The less-shortened Eastern Altiplano accumulated 6 km of shortening, two thirds of this during the Oligocene increment (see Table 9.3). In contrast Miocene shortening was twice as high (13.5 km) as Oligocene shortening (6.5 km) in the Central Altiplano (see Table 9.3 and Fig. 9.13).

3D strain analysis showed that an additional 7.7% of shortening was accumulated as ductile, micro-scale strain. This is equivalent to 8.6% stretching of the undeformed section and yielded ~14 km additional shortening (see Table 9.3). The total shortening of the Main Cross-Section is 40 km or 21% (see also Fig. 9.13).

Horizontal shortening of the Main Cross-Section (folding and thrusting)

Eastern Altiplano	profile length	shortening	in %
Pre-Oligocene (undeformed section)	62.7 km		
Post-Oligocene shortening	58.2 km	4.5 km	2.5
Post-Miocene shortening	56.7 km	1.5 km	0.8
Total shortening of the Eastern Altiplano		6.0 km	3.3[1]
Central Altiplano			
Pre-Oligocene (undeformed section)	97.9 km		
Post-Oligocene shortening	91.6 km	6.5 km	3.5
Post-Miocene shortening	78.1 km	13.5 km	7.5
Total shortening of the Central Altiplano		20.0 km	11.0
Main Cross-Section (total thrusting)			
Pre-Oligocene (undeformed section)	165 km		
Post-Oligocene shortening	154 km	11 km	6.1
Post-Miocene shortening	139 km	15 km	8.4
Total shortening of the Main Cross-Section		26 km	14.5
Main Cross-Section (thrusting plus ductile strain)			
Deformed section (post Miocene)	139 km	26 km	14.5
Pre-Oligocene (undeformed section)	165 km		
Stretching due to ductile strain	179 km	14[2] km	7.7
Grand total (thrusting and ductile strain)		**40 km**	**21.2**

Table 9.3: Summary of shortening values for the Main Cross-Section. Total thrusting refers to the results of the incremental cross-section balancing (Tables 9.1 and 9.2). The reference for all percentage values is the undeformed section which was corrected for ductile strain (i.e. 179 km length). See section 5.6 for the origin of 7.7% of ductile strain. [1] = 3.35%, rounded to 3.3%. [2] 13.8 km rounded to 14 km.

A further result of the balanced cross-section is that the two compressional events were preceded by an Eocene/Oligocene extensional event which led to the formation of a half-graben system. The eastern border of the half graben was formed by one or several normal faults which were active during the deposition of the Potoco Fm. The mostly uniform thickness of the San Vicente Fm. indicates the post-tectonic character of this formation.

A general observation of the entire cross-section is that deeper parts of thrust bodies are generally not well resolved in the seismic data. Furthermore, for some of these regions it is impossible to construct a balanced cross-section with the available algorithms of the software used and to fulfill structural and age constraints given by surface and seismic data. Such was the case for the Eastern Anticline of the Eastern Altiplano, where it was impossible to reconcile the structural modelling with the timing of the formation of the anticline (see section 9.3.3). In the Central Altiplano, east and west of the Intra-Potoco Fault, it was impossible to construct a balanced cross-section for the lower portions of the San Cristóbal and the Central Blocks, which fulfilled both line length and area conservation requirements with a comprehensible, consistent kinematic model. This especially affects those areas which were transported above the steep basement-ramp of the master fault in the east-vergent part of the thrust system during Miocene shortening (i.e. parts of the Central, San Cristóbal and Corregidores Blocks, Fig. 9.7) because they have no coherent reflectors in the seismic data. A possible reason for this may be that deeper parts of thrust bodies, especially when they were transported over ramp/flat bends in the detachment, were deformed by a different deformation mechanism than the shallower parts. The deformation mechanism within the deeper parts could possibly be 'inclined shear'. The parallel existence of two different deformation mechanisms surpasses the limits of the structural-modelling programs used. In addition, there is generally no possibility to better define this penetrative deformation and its lateral extension within the profile, because there is no surface control and these structures are below seismic resolution. Inspite of this, the main part of the cross-section yielded consistent results with the 'flexural-slip' algorithm. The determination of line-length shortening was also possible for near-surface areas.

The balanced cross-section shows the existence of two different structural domains in the Eastern and Central Altiplano. The Eastern Altiplano is the tip of the 'classical' foreland fold-and-thrust belt of the Eastern Cordillera, which developed above a gently eastward-dipping detachment that continues below the Eastern Cordillera. The Central Altiplano structure, in contrast, is a bivergent thrust system with a strongly-folded, east-vergent part and a lesser-deformed, west-vergent part. The bivergent thrust system developed during the Middle/Late Miocene shortening event above a shallow, westward-dipping detachment, which was possibly kinematically coupled with the west-vergent thrusts of the Western Altiplano, as indicated by the age of Middle/Late Miocene syn-tectonic sediments. It is possible that the sub-horizontal detachment continues further west beneath the Western Cordillera. Apart from mostly contemporaneous deformation of the Eastern and Central Altiplano, a kinematic coupling of the two parts of the Main Cross-Section is not likely.

Total thrusting   **20 km**   **+**   **6 km**

= 26 km (14.5%)

= 14 km (7.7%)

= 40 km (21.2%)

Microscale strain

A: 8 Ma

3.8
0
-5
-10

0   10   20   30   50 km

elevation (km)
3.8
0
-5
-10

M-U Miocene
Oligocene/ Miocene
Eocene/ Oligocene
U Cretaceous
Basement

13.5 km   **1.5 km**

B: 17 Ma

6.5 km   **4.5 km**

C: 30 Ma

WNW   blue faults = active, black faults = inactive, dashed = future faults   **ESE**
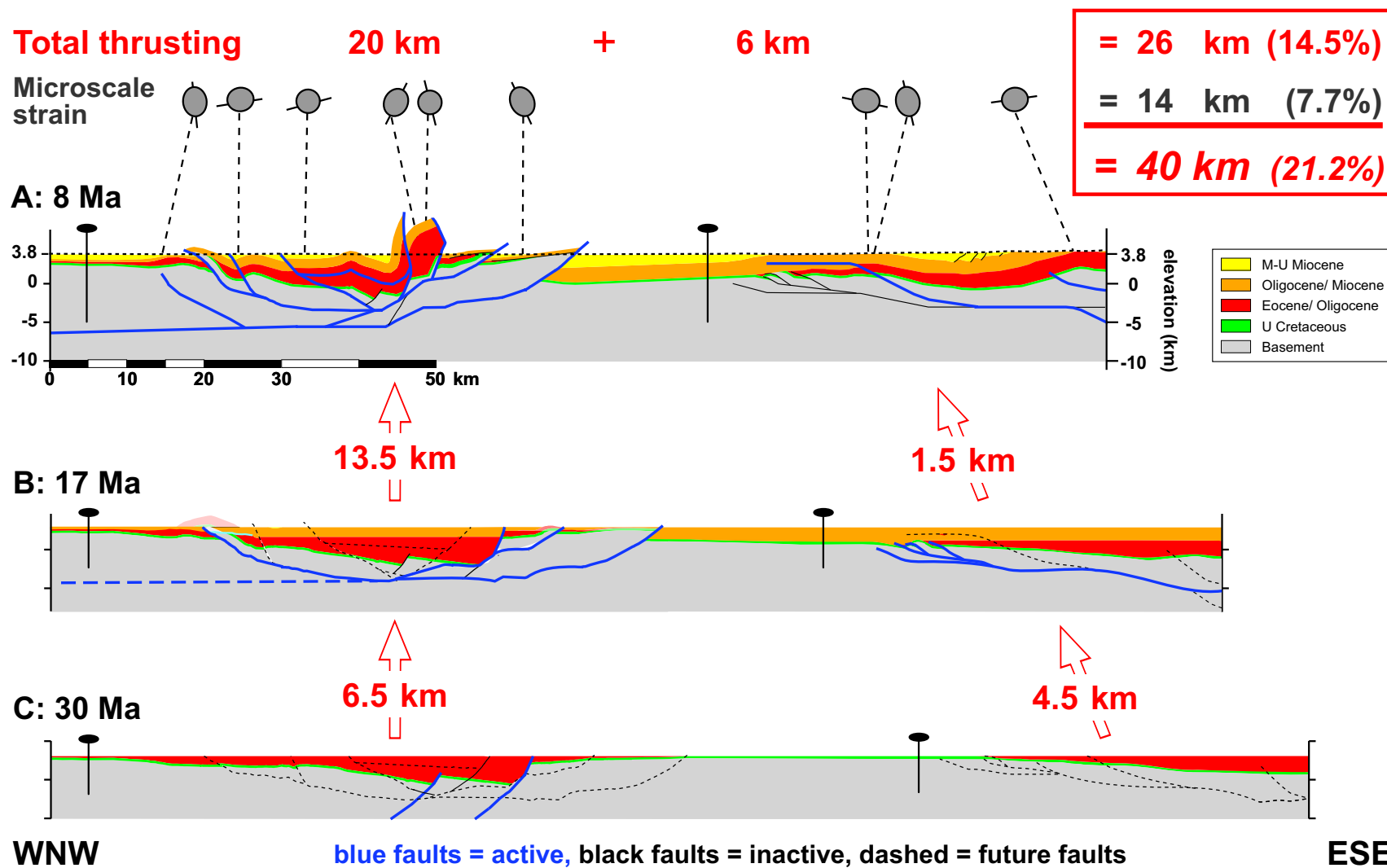
Figure 9.13: Combination of both parts of the Main Cross-Section. **A:** Deformed state: post-Miocene compression, i.e. post 8 Ma. **B:** Post San Vicente stage: i.e. ~17 Ma ago. Hanging walls of Oligocene thrusts were eroded ~17 Ma ago. **C:** The Pre-Oligocene, i.e. post-extensional stage shows the geometry of the Potoco half graben.

Chapter 10

Discussion

10.1 Horizontal shortening and structural style

10.1.1 Structural style of the Andean Plateau (21° S)

The new data in this study from the Southern Altiplano complete the cross-section of the Central Andean Plateau and its margins at 21° S, except for a ~40 km-long segment of the Western Cordillera (the Recent magmatic arc), which cannot be completed due to the lack of data. The most important observation of the compiled cross-section of Fig. 10.1 is that the structural style of the entire Andean Plateau is very similar. It can be described as a series of three to four bivergent thrust systems, which vary in size and amount of shortening. The only exceptions are the Interandean and Subandean foothills, which form a 'classical' east-vergent foreland fold-and-thrust belt detached along Lower Silurian shales (Dunn et al., 1995). The bivergent systems are, from east to west, the Eastern Cordillera/Eastern Altiplano, the Central Altiplano, the Western Altiplano, and probably another in the Western Cordillera/Western Flank.

The first bivergent system: The main focus of tectonic shortening and crustal thickening in the Central Andes was the 220 km wide, bivergent thrust system of the Eastern Cordillera/Eastern Altiplano. Recent balanced cross-sections yielded 95 km (41–45%) horizontal shortening across the Eastern Cordillera (Müller et al., 2002; see Fig. 10.1). This study shows that the Eastern Altiplano belongs structurally to the Eastern Cordillera. The buried deformation front of the west-vergent part of the Eastern Cordillera is ~50 km west of the San Vicente Fault in the Eastern Altiplano (see sections 4.1 and 9.3). The shallow, eastward-dipping detachment lies at 7–9 km depth and continues into the Eastern Cordillera (Fig. 10.1). This thrust-dominated interpretation is consistent with some of the previously-published data (e.g. Baby et al., 1990; 1997; Kley et al., 1997). However, inversion of an Late-Cretaceous rift basin, postulated by Welsink et al. (1995), or the existence of major normal faults as the result of Miocene extension in the Eastern Altiplano (Baby et al., 1997; Welsink et al., 1995) is not supported by the results of this study. In contrast, re-evaluation of reflection-seismic lines (Fig. 7.6A) demonstrates the compressional nature of faults previously interpreted as normal faults (Baby et al., 1997; Welsink et al., 1995).
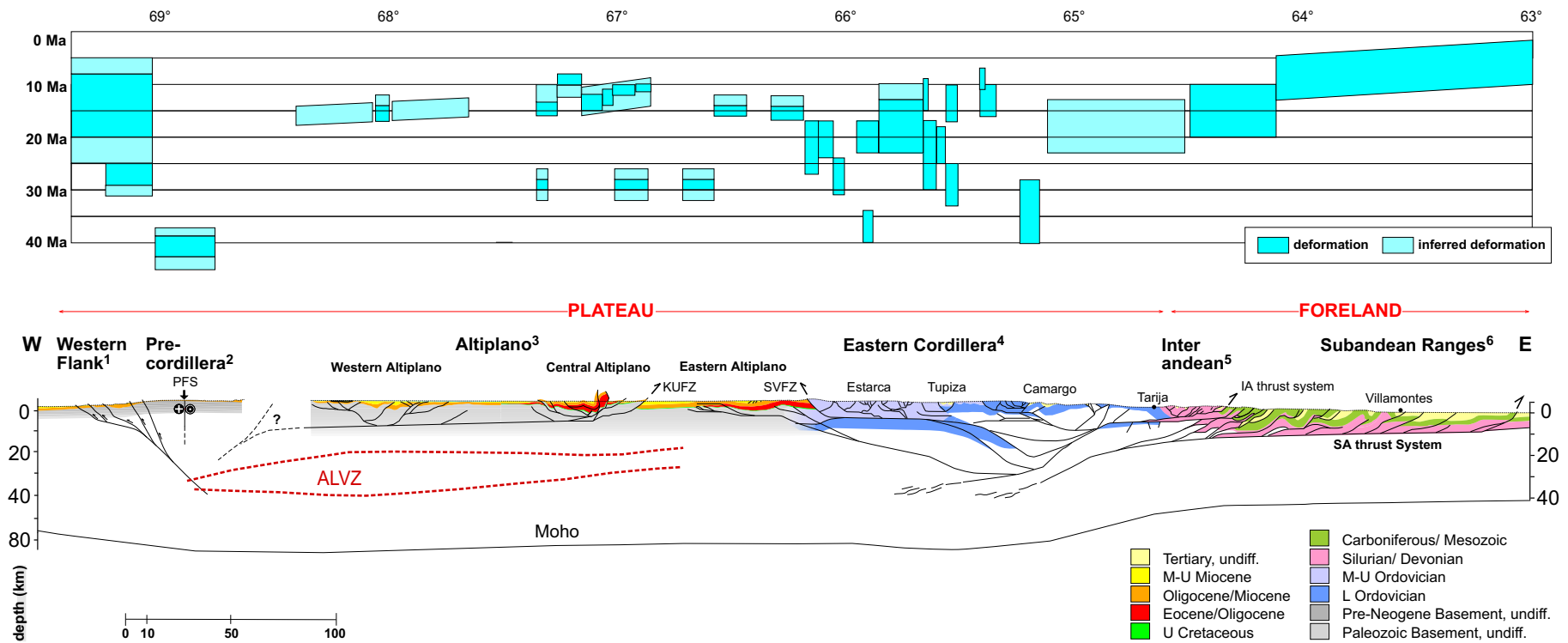
Figure 10.1: Compilation of balanced cross-sections of the Andean Plateau and its margins at ∼21° S: Eastern Cordillera, Interandean, and Subandean from Müller et al. (2002), Western Flank from Victor et al. (2003), Altiplano (own data). The diagram above shows the spatial distribution of deformation over time, based on published and own data. Moho from receiver function data (Yuan et al., 2000). Compilation of deformation ages: (1) Western Flank (Victor et al., 2003), (2) Precordillera (Günther, 2001), (3) Altiplano (this study), (4) Eastern Cordillera (Gubbels et al., 1993; Müller et al., 2002), (5) Interandean (Kley, 1996; Kley et al., 2001), (6) Subandean (Kley et al., 2001). The Western Altiplano cross-section was projected 50 km southward. PFS = Precordilleran Fault System, KUFZ = Khenayani-Uyuni Fault Zone, SVFZ = San Vicente Fault Zone, IA = Interandean, SA = Subandean, ALVZ = Andean Low Velocity Zone (Yuan et al., 2000).

The second bivergent system: The Central Altiplano is the next bivergent system to the west. It is much narrower than the Eastern Cordillera (~60 km) and was less shortened (21%, see Table 9.3). The results of this study show that the Central Altiplano is characterised by steep to moderately-dipping, emergent or blind thrusts with associated fault-propagation folds that merge into a sub-horizontal, westward-dipping detachment at 9–10 km depth (see sections 4.2 and 9.4). This rather shallow detachment is in contrast to previously published cross-sections, where the inversion of steep, crustal-scale normal faults was envisaged (e.g. Baby et al., 1997; Martínez et al., 1994). The shallow depth of the detachment as well as its sub-horizontal geometry is a constraint of the balanced cross-section and of surface data (see section 9.4.3).

The third bivergent system: The preliminary interpretation of a seismic line across the Salar de Uyuni (line 2553, see Fig. 2.1 for location) detected the existence of an additional bivergent thrust system in the Western Altiplano (Fig. 7.14). The structural inventory of bivergent structures at different scales, fault-propagation folds, thrusts, and associated syn-tectonic basins, is very similar to the Central Altiplano structure. Preliminary line-length balancing, based on the Top-San-Vicente horizon, revealed 12 km shortening due to thrusting and folding. Assuming a similar amount of micro-scale strain as for the Eastern and Central Altiplano (since similar lithologies exist throughout the Altiplano), the estimated shortening value for the Western Altiplano reaches 20 km, which is equivalent to 19%. This is the same order of magnitude as the rest of the Southern Altiplano (compare with Table 9.3). However, the bivergent system of the Western Altiplano cannot be directly considered as the western extension of the Central Altiplano. The only compressional structure cropping out in the direct continuation of the Main Cross-Section is the west-vergent fault-propagation fold of the Yazón Peninsula.

Is it possible to add the shortening value of the northern seismic line to that of the Main Cross-Section? Or does the northern bivergent thrust system of the Western Altiplano represent the lateral equivalent of the Central Altiplano thrust system? In the latter case, the addition of the northern shortening value would mean that the shortening of the respective parts of the Altiplano was counted twice.

The following line of thought makes a case for the addition of shortening values to be permissable. In Fig. 7.5, a strong correlation is shown between gravity highs and structural highs for the Central Altiplano thrust system. Preliminary interpretation of the Western Altiplano supports this thesis, especially in the western part of the seismic section (compare the position of anomalies a, b, and c of Fig. 7.5 with the positions of anticlines or other structural highs in Fig. 7.14). Consequently, this implies that the size and/or the magnitude of gravity highs correlates with the amount of vertical thickening due to horizontal shortening, if the nature of the basal detachment does not change significantly between the Central and Western Altiplano, as is the case. I therefore suggest that the thrusts have the highest displacement in the Western Altiplano, between the western extension of the Main Cross-Section and the northern seismic line, as indicated by the largest gravity anomaly (Fig. 7.5). The observation that the northern seismic line and the western continuation of the Main Cross-Section cross a similar pattern of gravity anomalies tentatively suggests that the amount of shortening may also be similar. In this case, I can add the 20 km shortening of the northern seismic line to the Main Cross-Section.

Because the base level of the Middle/Late Miocene syn-tectonic basins, which crop-out throughout the section, except in the Khenayani-Uyuni Fault Zone, does not vary significantly, no major ramps exist in the basal detachment of the Central and Western Altiplano (Woodward

et al., 1989, see Fig. 10.1). Moreover, the overall flat topography requires a flat-lying basal detachment (cf. section 9.4.3 and App. F.2). This shows that the upper crustal fault system of the Central and Western Altiplano does not reach below ∼10 km depth.

A possible fourth bivergent system: The Western Flank of the plateau is characterised by a west-vergent, thick-skinned basement ramp and only minor tectonic shortening (García and Hérail, 2001; Muñoz and Charrier, 1996; Victor, 2000). The kinematic model of Victor (2000) showed that the ramp-flat-ramp geometry of the basement detachment was able to generate ∼2500 m of plateau uplift with only 2.5 km horizontal shortening. The prevalence of bivergent structures in the Central Andean Plateau suggests the possible existence of an east-vergent thrust acting as back-thrust of the Western Flank. East-vergent structures in the Chilean Western Cordillera were described from García et al. (2002) for the Andes of Arica at 19° S (e.g. the Chucal Anticline with active deformation between 21–17 and 5 Ma). For the cross-section at 21° S, the existence of an emergent east-vergent thrust is excluded by surface and map observations. However, the very straight, N–S striking western border of the Salar de Uyuni strongly contrasts with the irregular, bay-like outline of the rest of the Salar. In addition, it correlates with a narrow, N–S trending, symmetrical gravity high with steep flanks (d in Fig. 7.5). I interpret this as a potential east-vergent structure which might complete the fourth bivergent system of the Central Andean Plateau. An alternative model to the east-vergent back-thrust could be a westward-dipping ramp in the basal detachment, along which the Paleozoic basement was uplifted near the surface (Fig. 10.1).

Synopsis: The dominance of bivergent thrust systems across the entire plateau is in contrast to several published balanced cross-sections (Baby et al., 1997; McQuarrie and DeCelles, 2001; Schmitz, 1994), which explain the present crustal thickness by dominantly east-vergent, crustal-scale thrusts in the Eastern Cordillera and Subandean Ranges, and interpret the Altiplano as a broad piggy-back basin carried over a basement duplex system. New data from the Eastern Cordillera, however, clearly image the bivergent character and even detected that west-vergent structures in the south Bolivian Eastern Cordillera dominate over east-vergent thrusts (Kley, 1996; Kley et al., 1997; Müller et al., 2002). Furthermore, the east-vergent piggy-back models (Baby et al., 1997; McQuarrie and DeCelles, 2001; Schmitz, 1994) implicate that the entire system is kinematically coupled. This would require a continuously eastward-migrating deformation front over time. This is not possible with the new deformation ages from the Southern Altiplano (this study), the Eastern Cordillera (Müller et al., 2002), and the Western Flank (Victor et al., 2003) which were compiled in Fig. 10.1 (see also section 10.2).

10.1.2   Amount of shortening

The estimated 60 km shortening of the entire Altiplano area (40 km calculated for the Main Cross-Section [see Table 9.3] plus 20 km estimated for the Western Altiplano) is significantly higher than proposed from other studies of the Southern Altiplano (e.g. 20 km, Baby et al., 1997). One reason for this difference is the kind of kinematic model assumed, i.e. extension vs. compression-dominated. Adding these 60 km to the published shortening estimates for the plateau flanks (15–20 km Precordillera and Western Flank, 95 km Eastern Cordillera, 30–40 km Interandean, and 100 km Subandean; Dunn et al., 1995; Günther, 2001; Kley, 1996; Müller

et al., 2002; Victor, 2000) yields a total shortening of 300–315 km for the cross-section of the entire Andean Plateau and its margins at 21° S. This shortening estimate is slightly less than the 326 km of a recently-published balanced cross-section between 19–20° S (McQuarrie and Davis, 2002).

Microscale strain: These shortening values, however, do not account for micro-scale strain, with exception of the values taken from this study of the Altiplano (see chapter 5). This study shows that even the weakly deformed, Cenozoic sediments of the Southern Altiplano were additionally shortened in the transport direction by 7.7% of ductile, micro-scale strain (see section 5.6). The amount of ductile strain should be significantly higher in those areas that are much stronger deformed than the Altiplano, e.g. the Subandean Ranges. Published data from foreland thrust belts (e.g. Hogan and Dunne, 2001; Plessmann, 1965) revealed 17–30% of micro-scale-strain contribution to the total shortening. In contrast to this, the Eastern Cordillera possibly did not accumulate much 'Andean' micro-scale strain, because of the previous slaty cleavage, which was the result of a Pre-Andean metamorphic event (Jacobshagen et al., 2002; Kley et al., 1997). The negligence of micro-scale strain for most of the Andean cross-section suggests that most of the published shortening estimates underestimate the total strain and therefore represent minimum values.

Outcrop-scale strain: In addition, none of the balanced cross-sections, including this study of the Altiplano, regard the strain contribution due to outcrop-scale structures that are commonly not incorporated in geological maps, and therefore not taken into account to assess deformation. In orogeny, however, deformation typically occurs at all scales, ranging from atomic lattices to mountain ranges (Mitra, 1994; Ramsay and Huber, 1983a; Smart et al., 1997). Neglecting minor structures (at outcrop- and micro-scale) will therefore always underestimate the deformation (Mitra, 1994; Smart et al., 1997). A case study of the Alleghenian foreland thrust belt in the Central Appalachians, which systematically determined the strain at different scales (map-, outcrop-, and micro-scale), revealed that outcrop-scale structures contribute about 17–25% of total regional shortening, which was similar to micro-scale shortening (Hogan and Dunne, 2001). A regional mapping of outcrop-scale structures is not possible for most parts an orogen, because continuous exposures, which would provide representative samples are not present (Williams, 1970). The extrapolation of measured outcrop-scale structures from isolated outcrops to the regional cross-section may even overestimate the strain contribution of outcrop-scale strain, because the distribution of outcrop-scale structures anti-correlates with that of map-scale structures (Hogan and Dunne, 2001).

Synopsis: For the Central Andes, especially the Altiplano, the sparse outcrop situation does not permit the determination of regional outcrop-scale strain. Nevertheless, for the case study of the Central Appalachians, Hogan and Dunne (2001) showed that the contribution of outcrop-scale structures to the total shortening nearly equals the micro-scale-shortening contribution. Should this also be the case for the Southern Altiplano, I would assume an additional 7–8% of shortening due to outcrop-scale structures. For the rest of the plateau cross-section I therefore assume a minimum of 10–15% additional shortening due to micro-scale and outcrop-scale strain. This would result in a minimum of 20 km additional shortening (i.e. 7%) for the Altiplano and 77 km (i.e. 10%) for the remaining cross-section (Western Flank, Precordillera, East-

ern Cordillera, Interandean, Subandean, see Fig. 10.3). Adding these values to the previous shortening values of 300–315 km results in at least 397–412 km horizontal shortening across the Andean Plateau and its margins at 21° S.

10.1.3   The crustal-thickening problem

Orogen-normal shortening is widely believed to be the single most important mechanism for thickening the crust of the Central Andes (Allmendinger and Gubbels, 1996; Allmendinger et al., 1997; Isacks, 1988; Kley and Monaldi, 1998; Roeder, 1988; Sheffels, 1990). Consequently, many authors calculated the contribution of tectonic shortening to crustal thickness, based on two-dimensional balanced cross-sections (e.g. Kley and Monaldi, 1998; Lamb and Hoke, 1997; McQuarrie, 2002; Müller et al., 2002; Sheffels, 1990). They suggest that the present shortening values can account for 70–80% of the required crustal volume (e.g. Kley and Monaldi, 1998; Lamb and Hoke, 1997). McQuarrie (2002) estimated 320 km of shortening for a cross-section at 19–20° S. Adding the new data from the Southern Altiplano (this study) and the estimated shortening contribution due to outcrop and micro-scale strain, the shortening for the 21° S section would reach 397–412 km (see section 10.1.2 and Fig. 10.3). This would be more than enough to explain the observed crustal thickness of the plateau by tectonic shortening for the cross-section at 21° S.

The question arises, however, whether the calculation of the mass balance based on two-dimensional balanced cross-sections for the Central Andes is permissible. The strain analysis (chapter 5) of this study showed that the 7.7% of micro-scale strain in the cross-section plane were accompanied by 13% orogen-parallel extension (see section 5.6). Thus a principal assumption for the construction of balanced cross-sections, i.e. plane-strain deformation, is not valid in this case. Consequently, if orogen-parallel extension is not taken into account in 2D approaches, the results are always over- or underestimates.

First indications for orogen-parallel mass transfer were derived from the observed along-strike variation of the amount of tectonic shortening with respect to the observed crustal thickness (e.g. Kley and Monaldi, 1998). This correlation is good in the central parts of the plateau (between 18–21° S), where the known shortening values can more than fully explain the observed crustal thickness in cross-section plane (i.e. there is material gain), but this is not possible towards the northern and southern ends of the Altiplano-Puna Plateau (Kley and Monaldi, 1998). Ductile lower-crustal flow from the central areas into areas with a deficit of shortening was discussed as possible process contributing to crustal thickness (Kley and Monaldi, 1998). Surface structural evidence for upper-crustal orogen-parallel extension was also reported from the Argentine Puna (Riller and Oncken, 2003). It is unclear whether the major rhomb-shaped strike-slip fault zones of the Puna, which were produced by orogen-parallel extension (Riller and Oncken, 2003), continue into the Southern Altiplano. Major strike-slip faults were not mapped on the Southern Altiplano (see section 4.5), but some could be buried beneath post-Miocene sediments of e.g. the López Basin, or covered by the thick, vertically-inclined pelites of the Potoco Fm. in the hanging wall of the San Cristóbal Fault. It is also possible that there is no need for additional strike-slip structures, because 13% of micro-scale strain are already sufficient to accommodate all orogen-parallel extension.

10.1.4 Nature of the 'Proto-Eastern Cordillera'?

One of the open questions pertaining to Altiplano and Eastern Cordilleran geology concerns the existence of an Early Tertiary topographic high in the western part of the Eastern Cordillera, the so-called 'Proto-Eastern Cordillera'. It was first described by Lamb and Hoke (1997) for the Central Bolivian Altiplano (~18° S) as a narrow mountain belt formed by Eocene shortening. Apatite and zircon fission-track cooling ages for the western edge of the Eastern Cordillera at 16–17° S indicate rapid cooling around 40 Ma ago, which were interpreted as indication for Eocene uplift and erosion (Benjamin et al., 1987). In the Southern Altiplano (near San Vicente, at the transition to the Eastern Altiplano), Marocco et al. (1987) assigned a local intra-Paleocene angular unconformity to compressional movements related to the 'Proto-Eastern Cordillera' (see also Marshall et al., 1997; Sempere et al., 1997). The lack of Early Paleocene to Early Eocene sediments in the Tupiza area was also interpreted as indication of uplift and exhumation of the central part of the Eastern Cordillera (Müller et al., 2002).

This study suggests that the 'Potoco wedge' of the Eastern Altiplano required an eastern sediment source at least during the Eocene and the lower parts of the Oligocene, i.e. during sedimentation of the Potoco Fm. (see sections 3.3.2 and 7.2.1). In section 7.2.1 I interpreted the westward-thinning Potoco wedge of the Eastern Altiplano as a foreland-basin wedge of the early Eastern Cordillera. This is in agreement with Sempere (1995). The simple existence of a sediment wedge, however, does not indicate the nature or origin of the sediment source.

An alternative model for the origin of the Eocene topographic high east of the Altiplano can be developed from a comparison with the Central Altiplano. This study shows that the eastward-thickening Potoco wedge of the Central Altiplano was the result of an Eocene/Oligocene half graben (cf. sections 7.2.1 and 9.4.1.1). The undeformed cross-section reveals a strong similarity in geometry between the two Potoco wedges of the Eastern and Central Altiplano (Fig. 9.13C). This may suggest the existence of a second half-graben system in the Eastern Altiplano, which could also be bordered by steep, westward-dipping, normal faults in the present-day, westernmost Eastern Cordillera. This model is not in conflict with the sedimentological observation of westward-decreasing grain size of Potoco sediments (see section 3.3.2). The existence of a second half-graben system in the east could possibly be proved by a reduced thickness of syn-extensional sediments on the potential graben shoulders, i.e. in the Eastern Cordillera. Published tectonic and stratigraphic data (Fiedler, 2001; Müller, 2000), however, as well as a preliminary map analysis of some of the few remnants of Eocene/Oligocene sediments in the Eastern Cordillera (most sediments have been eroded or were not deposited) is ambiguous. Consequently, it is not possible using the present data to decide whether the eastern sediment source of the Potoco Fm. of the Eastern Altiplano was the result of thrusting or extension.

10.2 Deformation age and pattern — how significant?

A special focus of this study was to constrain the age of deformation. In chapter 8 I demonstrated that the Southern Altiplano structure formed during two independent compressional events (during the Early Oligocene [≥ 27 Ma] and the Middle/Late Miocene [17–8 Ma]) which were preceded by an Eocene/Oligocene extensional event. The age of the first compressional deformation is further supported by apatite fission-track ages which range between 33–29 Ma for Silurian quartzite in the hanging walls of the Khenayani-Uyuni and Corregidores Faults

(Ege, in prep.). Isotopic age determination of syn-tectonic thrust-top basins, as well as detailed seismic-sequence interpretation, allow a closer examination of the activation of single structures. The results of sections 7.3 and 8.4 reveal an irregular spatial and temporal distribution of deformation of the Altiplano (cf. Fig. 8.2).

A synopsis of published and own data across the cross-section of the entire plateau suggests that an irregular tectonic activity is also characteristic for the entire plateau area during the past ∼40 Ma (see Fig. 10.1). The oldest compressional events were recorded in the Eastern Cordillera and in the Chilean Precordillera around 40 Ma ago (e.g. Günther, 2001; Kley et al., 1997; Müller et al., 2002; Sempere et al., 1997). Slightly later, local deformation started in the Eastern and Central Altiplano, but only for a short period between ∼30–25 Ma (see section 8.3). The subsequent tectonic quiescence in the Altiplano (25–17 Ma) correlates temporally with the main period of shortening in the Eastern Cordillera (Müller et al., 2002). Approximately 20 Ma ago, the Western Flank began to deform at peak rates (Victor et al., 2003) and around 17 Ma ago, the formation of the bivergent thrust systems of the Western and Central Altiplano began, locally with high strain rates (see Fig. 10.3, section 7.3, and chapter 8). During this time, active compressional tectonics affected the entire plateau area, from the Western Flank to the Eastern Cordillera. This increment lasted until 12–8 Ma ago. Since then there has been no active deformation on the entire plateau. Instead, it has shifted to the eastern foreland, where eastward-migrating deformation led to the formation of the broad, thin-skinned thrust belt of the Interandean and Subandean Ranges (see Fig. 10.1). This last stage is the only phase during which an eastward-migrating deformation front can be observed. It could possibly represent the second, simple-shear plateau stage of the model of Allmendinger and Gubbels (1993).

An important observation of Fig. 10.1 is that the overall irregular pattern of deformation over time excludes the existence of any large-scale eastward- or westward-migrating deformation front over the entire plateau, i.e. between the Western Flank and the Eastern Cordillera. This is in contrast to DeCelles and Horton (1999), Horton and Decelles (2001) and Horton et al. (2002) who postulate, based on sedimentological observations, a continuously eastward-migrating deformation front, which began in the Early Tertiary at the western edge of the Altiplano and subsequently migrated eastward. The dominantly east-vergent cross-sections of the plateau (e.g. Baby et al., 1997; Schmitz, 1994) also implicate that the entire system is kinematically coupled, which requires an eastward-migrating deformation front. In this study I can definitely exclude any unidirectionally-migrating deformation front in the Andean Plateau at 21° S (Fig. 10.1).

The observed diffuse pattern of deformation, i.e. without a migrating deformation front, can be used to infer the mechanical behaviour of the crust during plateau formation. It is known that orogenic plateaus may evolve from initially doubly-vergent orogens (Willett et al., 1993). The increase in temperature in the lower crust as a result of continuous crustal thickening changes the dominant deformation mechanism from a frictional to a thermally-activated viscous flow, which causes a decrease in shear strength at base of the orogen (Willett et al., 1993). The newly-formed weak base of the orogen decreases the taper angle in the upper crust; progressive heating of the lower crust produces an intra-orogenic plateau (Willett et al., 1993). The extremely weak detachment at the base of the orogen cannot support any topographic relief any longer, i.e. the surface of the orogen levels out, and consequently the stress field depolarises. Subsequent shortening would be delocalised with an irregular pattern in time and space.

Such a two-stage behaviour is not supported by the present data of the Andean Plateau at 21°S. A 'first stage of localised deformation', i.e. the compressional, doubly-vergent orogen stage is not observed. The irregular sequence of fault activation was a characteristic feature since the beginning of the compressional deformation in the plateau domain in the Oligocene (cf. Figs. 10.1 and 10.3). This observation implies that the lower-crustal weak zone was an *a priori* feature of the Andean Plateau which averted the formation of a polarised doubly-vergent orogen and, instead, a plateau was formed directly. The observed diffuse pattern of deformation also possibly implies that the plateau has remained flat since its formation.

10.3 Magmatism and deformation — a possible correlation?

The evolution of the Altiplano was largely accompanied by volcanic activity, i.e. since the Late Oligocene (cf. sections 3.3.3 and 8.3). This enabled the dating of deformation (see chapter 8). The question arises, whether there is any correlation between magmatic and tectonic activity. A direct connection between volcanic and tectonic activity was reported from the Argentine Puna (Riller et al., 2001), where it could be shown that the eruption of collapse calderas was triggered by tectonic activity of major faults. A causal relationship between deformation and the eruption of large-volume ignimbrites was also suggested for the western flank of the plateau north of 21°S (Victor, 2000).

For the Southern Altiplano, the correlation between deformation and magmatism is not definite: the absence of volcanic intercalations in the Potoco Fm. indicates that the formation of the Eocene/Oligocene half graben in the Central Altiplano occurred without coeval magmatism. The beginning of volcanic activity on the Altiplano (27–29 Ma ago, see section 3.3.3) roughly correlates with the end of the first compressional increment and the beginning of the San Vicente Fm., as indicated by interbedded tuffs (see section 3.3.3). The San Vicente Fm. is characterised by an increasing amount of volcanic intercalations upsection (Silva-González, in prep.). Major tectonic events did not occur throughout the deposition of the San Vicente Fm. (cf. section 7.3 and chapter 8). An episode of strong volcanic activity, which affected the entire Southern Altiplano and adjacent parts of the Eastern Cordillera, started 25–24 Ma ago (Evernden et al., 1977; Fornani et al., 1989; Fornani et al., 1993; Hoke et al., 1993; Kussmaul et al., 1975; Soler and Jimenez Ch., 1993) and continued until 10–8 Ma ago. The Middle/Late Miocene deformation (17–8 Ma) of the Eastern and Central Altiplano was coeval with the later stage of this volcanic activity.

In addition to these observations, my study also demonstrated that faults were not used as pathways for ascending magmas, with exception of the San Cristóbal Volcano of the Central Altiplano. The volcanic centres for the Oligocene/Miocene intra-stratified tuffs are mostly located in the westernmost part of the Eastern Cordillera and in the Western Altiplano (Fornani et al., 1989; Grant et al., 1979).

This shows that a direct correlation between magmatism and deformation is not observed in the Southern Altiplano, especially not during the early stages of plateau formation until the Late Oligocene. The influence of magmatism on the Miocene deformation (17–8 Ma) also remains speculative: it is possible that the continuous magmatic and volcanic activity for more than 10 Ma (since 29 Ma ago, see section 3.3.3) may have sufficiently weakened the upper crust of the Altiplano to trigger deformation (Babeyko et al., 2002; Tanner et al., 2000).

10.4   Surface uplift and plateau formation

The results of this study generally agree with Isacks' (1988) and Allmendinger and Gubbels' (1996) models of plateau formation. In particular, the kinematic two-stage model of initially widespread, pervasive horizontal shortening and coeval vertical thickening (i.e. 'pure shear'), which could be expressed by the observed irregular pattern of deformation, followed by concentrated deformation along the eastern side of the Andes, where the Brazilian Craton is thrusted beneath the Subandean in a 'simple shear' manner (see Figs. 10.1 and 10.3 for the lateral distribution of active deformation), is supported.

However, the very thin post-Miocene sediment cover of the Altiplano and especially the absence of deformation on the Western Flank of the plateau (Victor et al., 2003) stands in contrast to Gregory-Wodzicki (2000) who proposed, based on paleo-botanical evidence, that the plateau had attained no more than half of its present elevation by 10 Ma. The present data rather supports the model of Wdowinski and Bock (1994a; 1994b) which implies that the plateau crust thickened until the plateau reached a critical elevation, upon which it resisted further accumulation of shortening. Consequently, the locus of crustal compressional deformation migrated eastward.

It is interesting to note that the Late Cretaceous El Molino Fm., a shallow marine to lacustrine deposit formed around sea level, still forms a sub–horizontal regional and is close to sea level (see Fig. 10.3). Accordingly, plateau surface-uplift was mainly achieved by sedimentary infill of tectonically-controlled, internally-drained basins, and not by tectonic uplift.

The surface observations made during this study, especially the diffuse pattern of deformation and the complete absence of compressional tectonics in the entire plateau domain at 21°S during the past 8 Ma, support the numerical models proposed by Vietor (2001), Vietor and Oncken (submitted), Wdowinski and Bock (1994a; 1994b), and Willet et al. (1993, cf. section 10.2). All these models require shear-stress decoupling within or at the base of the crust to produce a plateau topography.

The finite element, temperature dependent, viscoplastic-flow models of Wdowinski and Bock (1994a) only produce an isostatically compensated, highly-elevated plateau when the lithosphere is *a priori* thermally weakened. The flat plateau topography develops above the thermally weakened zone. During early stages, compressional deformation of the crust and mantle are localised above the thermally-weakened zone. Persistent heating at the base of the crust progressively weakens the lower crust. A thickness increase of the weak lower crust subsequently decreases the thickness of the strong upper crust, which results in a very diffuse crustal compressional pattern (Wdowinski and Bock, 1994a). As the crust thickens and reaches a critical elevation, buoyancy forces resist further thickening of the crust and the locus of deformation migrates eastward.

The distinct-element models of Vietor and Oncken (submitted) require a horizontal free-slip zone of a distinct length to build plateaus. Deformation is concentrated in the two wedge-shaped flanks of the incipient plateau, the width of which is defined by the width of the free-slip zone. Deformation occur only episodically within the limit of the decoupled crust (Vietor, 2001). Only if the free-slip zone is allowed to expand to one direction, possibly as the result of an increase in crustal thickness, deformation becomes focussed to the respective flank of the plateau and completely dies out in the plateau area (Vietor, 2001). The complete absence of deformation in the plateau area could not be reproduced in the model of Wdowinski and Bock (1994a).
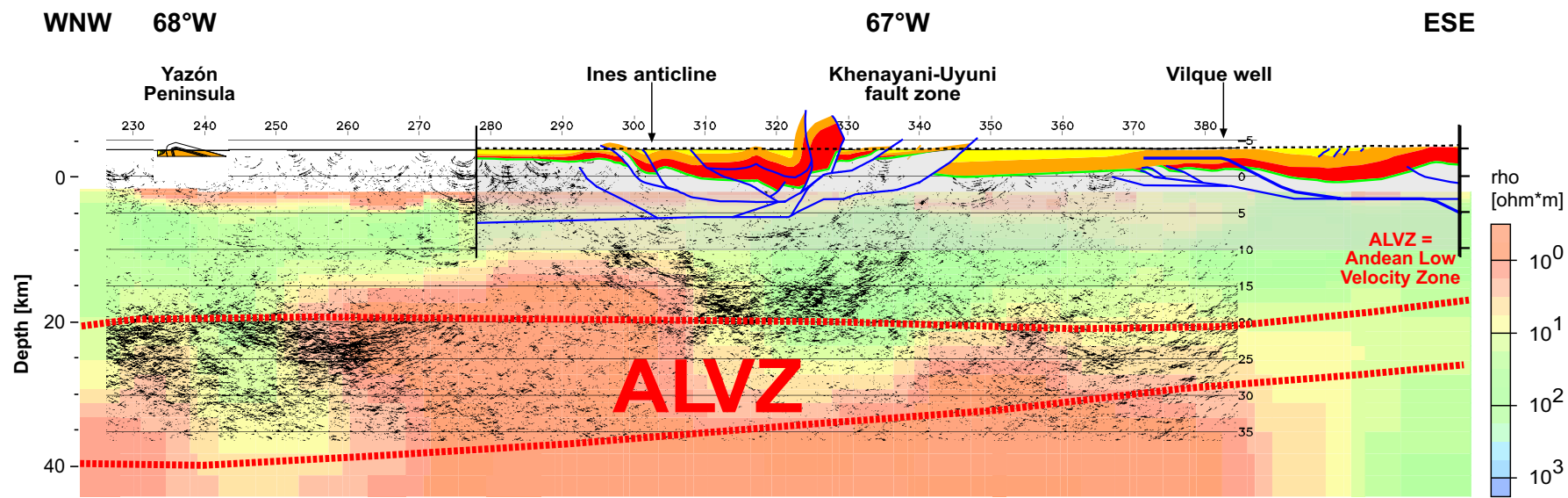
Figure 10.2: Combination of the balanced cross-section of the Southern Altiplano with the upper parts of the ANCORP'96 seismic section (automatic line-drawing of depth-migrated section, ANCORP-Working Group, 2003), magnetotelluric model results, i.e. conductivity (Brasse et al., 2002), and the Andean Low Velocity Zone (ALVZ) from receiver functions (Yuan et al., 2000). See Fig. 9.13 for legend of geological cross-section.

Timing, distribution, and geometry of Central Andean Deformation (~21° S)
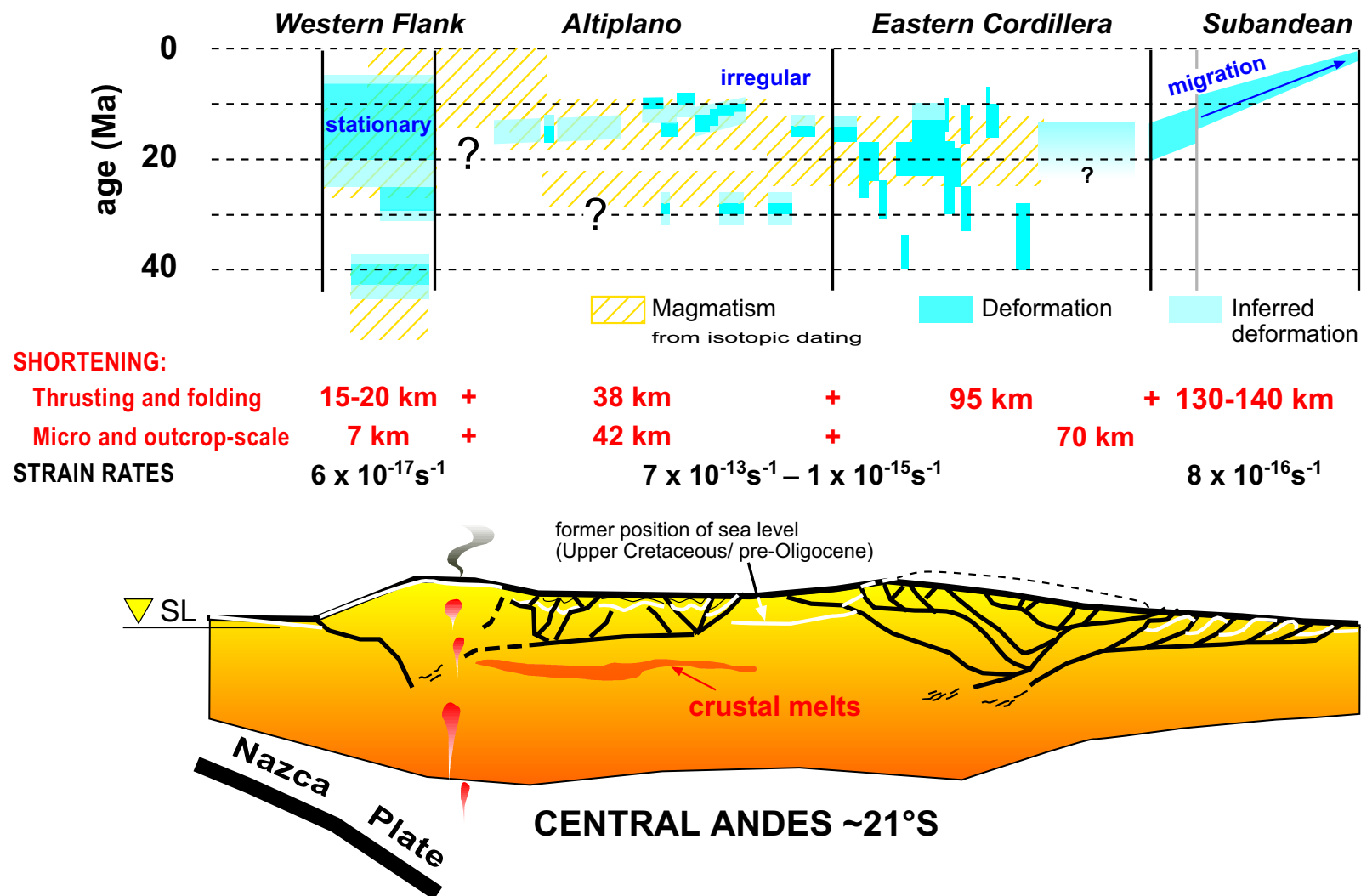
Figure 10.3: Schematic cross-section of the Altiplano Plateau at ~21°S. The diagram above shows the spatial distribution of deformation over time, based on published and own data: Western Flank and Precordillera (Günther, 2001; Victor et al., 2003), Altiplano: own data, Eastern Cordillera (Kley, 1996; Müller et al., 2002), Subandean Ranges, including the Interandean (Dunn et al., 1995; Kley, 1993).

The observed pattern of deformation in the Altiplano could be interpreted as the direct consequence of long-term thermal weakening of the crust, corresponding to the first stage of Wdowinski and Bock (1994a). Additional evidence for the existence of a thermally-weakened crust during plateau formation may come from the strong Oligocene/Miocene magmatic activity which affected the entire region between the Western and the Eastern Cordillera (e.g. Baldellon et al., 1994; Fornani et al., 1993; Grant et al., 1979; Kay et al., 1994; Wdowinski and Bock, 1994b).

Fig. 10.3 shows that, on a larger scale, plateau deformation was active during most of the time in the Western and Eastern Cordilleras, and only short-term deformation events affected the internal plateau area (Fig. 10.3). This observation strongly supports the first stage of the model of Vietor and Oncken (submitted), because the Eastern and Western Cordilleras would correspond to the two wedge-shaped plateau flanks in their model (where most of the deformation is localised) and the Altiplano would correspond to the inner plateau area, that was only episodically affected by deformation. In addition, the lack of deformation between the Western Flank and the eastern edge of the Eastern Cordillera during the second stage since 10–8 Ma, while the entire deformation was concentrated on the eastern foreland of the plateau, i.e. the Subandean, also supports the model of Vietor (2001). Alternatives to lateral extension of the free-slip zone, which could also terminate the deformation in the plateau area, could involve the end of convergence between the Nazca Plate and the South American continent (which is not the case), or large-scale out-of-section mass transfer (Tim Vietor, pers. comm.).

The present-day picture of the Andean Cross-Section at 21° S shows that the bivergent systems of the Central and Western Altiplano correlate with a variety of geophysical anomalies (Fig. 10.2). The Andean Low Velocity Zone (ALVZ) from receiver functions (Yuan et al., 2000) is considered to be a partial melt zone. The top of the ALVZ at 15–20 km depth correlates with a bright seismic reflector from the ANCORP'96 section (ANCORP-Working Group, 1999; ANCORP-Working Group, 2003) and with the upper limit of the extremely high conductivity anomaly of the Southern Altiplano for whose origin partial melts are also favoured (Brasse et al., 2002; Partzsch et al., 2000). This is a first-order candidate for the present-day weak zone underneath the plateau. This, in addition to the still flat topography of the Altiplano, cf. Fig. 1.2A, indicates that the process of plateau formation is still active and has not ended yet.

In summary, this study supports the generic geodynamic models of Vietor (2001), Vietor and Oncken (submitted), and Wdowinski and Bock (1994a; 1994b). In a structural sense, the results of this study agree with the kinematic models of Allmendinger and Gubbels (1996) and Isacks (1988), but contrast the structural models of Baby et al. (1997), McQuarrie (2002), McQuarrie and Decelles (2001), and Schmitz (1994).

10.5 Conclusions

Bivergent systems of various sizes are the dominant structures of the Central Andean Plateau at 21° S. The Southern Altiplano, i.e. the inner plateau area, can be structurally divided in three domains; the Eastern, Central, and Western Altiplano. The Eastern Altiplano is the thin-skinned, west-vergent, buried deformation front of the western part of the Eastern Cordillera's bivergent thrust system. The 20–40° dipping, blind faults merge into a shallow, eastward-dipping detachment at 7–9 km depth that continues below the Eastern Cordillera. The Central

Altiplano forms a bivergent system with 30–90° dipping, basement-involving thrusts in the east, and fault-propagation folds in the west. The shallow, westward-dipping detachment lies in 9–10 km depth and possibly continues into the Western Altiplano, which forms a separate bivergent thrust-system.

The Southern Altiplano structure formed during two independent compressional increments (Early Oligocene [$\geq$27 Ma] and Middle/Late Miocene [17–8 Ma]), which were preceded by an Eocene/Oligocene extensional event. The latter led to the formation of a half graben in the Central Altiplano, and possibly a second in the Eastern Altiplano. Horizontal contraction on the Southern Altiplano ended between 11–8 Ma as indicated by the age of undeformed volcanic rocks.

The balanced cross-section revealed that the buried deformation front of the Eastern Cordillera, i.e. the Eastern Altiplano, accumulated a minimum of 6 km (3.5%) of shortening due to folding and thrusting, mostly during the Oligocene increment. The bivergent thrust system of the Central Altiplano was shortened by 20 km (11%), mostly during the Miocene. Preliminary line-length balancing of the Western Altiplano yielded 12 km (11%) shortening. 3D strain analysis showed that an additional 7.7% of shortening was accumulated as ductile, micro-scale strain. This augments the total shortening in the entire cross-section of the Southern Altiplano at 21° S to 60 km or 21%. In addition, I suggest that the contribution of outcrop-scale structures may account for an additional 20 km. Assuming a similar amount of micro- and outcrop-scale strain for the entire plateau cross-section results in 397–412 km horizontal shortening across the Central Andean Plateau at 21° S, i.e. from the western flank of the plateau to the eastern edge of the Subandean Ranges. 3D strain analysis further showed that the 7.7% micro-scale strain were accompanied by 13% orogen-parallel extension.

The Andean Plateau at 21° S is characterised by a spatially and temporally irregular fault activity, which excludes the existence of systematically eastward- or westward-migrating deformation during plateau formation. Therefore, the plateau has probably remained flat since its formation and did not evolve from an initially doubly-vergent orogen.

The tectonic evolution of the Southern Altiplano was largely accompanied by magmatic activity. An episode of intense volcanism affected the entire width of the Altiplano and adjacent parts of the Eastern Cordillera between 25–8 Ma. However, a causal relationship between magmatism and deformation could not be shown for the Southern Altiplano. Strong Oligocene/Miocene volcanic activity, together with the diffuse pattern of deformation, suggests that the formation of the Altiplano Plateau was initiated by magmatically-controlled thermal weakening of the crust, possibly as the result of the removal of the mantle lithosphere (Babeyko et al., 2002; Wdowinski and Bock, 1994a; Yuan et al., 2002). At present, the Central and Western Altiplano has a flat topography, high heat-flow ($\sim$80 mW/m^2, Springer and Förster, 1998), and is spatially related to a variety of geophysical anomalies that are interpreted as partial melting of the middle crust (20–40 km depth, Yuan et al., 2000). From this evidence, I propose that the process of plateau formation is still active (*sensu* Isacks, 1988; Vietor and Oncken, submitted; Wdowinski and Bock, 1994a).

References

Allmendinger, R.W. and Gubbels, T., 1996. Pure and simple shear plateau uplift, Altiplano-Puna, Argentina and Bolivia. Tectonophysics, 259(1-3): 1-13.

Allmendinger, R.W., Gubbels, T., Isacks, B. and Cladouhos, T., 1993. Lateral variations in Late Cenozoic deformation, Central Andes, 20–28° S, Second ISAG, Colloques et Seminaires Institut de Recherche Scientifique pour le Développement en Cooperation, Oxford, pp. 155-158.

Allmendinger, R.W., Jordan, T.E., Kay, S.M. and Isacks, B.L., 1997. The evolution of the Altiplano-Puna Plateau of the Central Andes. Annual Reviews Earth Planet Sciences, 25: 139-174.

Alpers, C.N. and Brimhall, G.H., 1988. Middle Miocene climatic change in the Atacama Desert, northern Chile; evidence from supergene mineralization at La Escondida; with Suppl. Data 88-21. Geological Society of America Bulletin, 100(10): 1640-1656.

ANCORP-Working Group, 1999. Seismic reflection image revealing offset of Andean subduction-zone earthquake locations into oceanic mantle. Nature (London), 397(6717): 341-344.

ANCORP-Working Group, 2003. Seismic imaging of an active continental margin — the Central Andes (ANCORP '96). Journal of Geophysical Research, in press.

Angenheister, G.E., 1982. Physikalische Eigenschaften der Gesteine (Physical properties of rocks). Landolt-Börnstein: Zahlenwerte und Funktionen in Zahlen, Neue Serie, Gruppe V: Geophysik und Weltraumforschung, V/1a. Springer, Heidelberg, New York, 374 pp.

Argollo, J. and Mourguiart, P., 2000. Late Quaternary climate history of the Bolivian Altiplano. Quaternary International, 72: 37-51.

Babeyko, A.Y., Sobolev, S.V., Trumbull, R.B., Oncken, O. and Lavier, L.L., 2002. Numerical models of crustal scale convection and partial melting beneath the Altiplano-Puna Plateau. Earth and Planetary Science Letters, 199(3-4): 373-388.

Baby, P., Rochat, P., Mascle, G. and Herail, G., 1997. Neogene shortening contribution to crustal thickening in the back arc of the Central Andes. Geology, 25(10): 883-886.

Baby, P., Sempere, T., Oller, J., Barrios, L., Herail, G. and Marocco, R., 1990. Un bassin en compression d'âge oligomiocène dans le sud de l'Altiplano bolivien. C. R. Acad. Sci. Paris, Série II: 341-347.

Badley, M.E., 1985. Geology and seismic section. In: M.E. Badley (Editor), Practical seismic interpretation — seismic interpretation techniques. Int. Haman Resources Development Corp., pp. 71-129.

Bahlburg, H., 1990. The Ordovician basin in Puna of NW Argentinia and N Chile: geodynamic evolution from back-arc to foreland basin. Geotektonische Forschungen, 75: 1-107.

Baker, M.C.W. and Francis, P.W., 1978. Upper Cenozoic volcanism in the central Andes; ages and volumes. Earth and Planetary Science Letters, 41(2): 175-187.

Baldellon, E., Fornani, M., Espinoza, F. and Soler, P., 1994. Sucesion estructural de la zona Serranía de las Minas. In: YPFB (Editor), XI Congreso Geológico de Bolivia. YPFB, Santa Cruz de la Sierra, Bolivia, pp. 238-247.

Beck, S.L., Zandt, G., Myers, S.C., Wallace, T.C., Silver, P.G. and Drake, L., 1996. Crustal-thickness variations in the Central Andes. Geology (Boulder), 24(5): 407-410.

Benjamin, M.T., Johnson, N.M. and Naeser, C.W., 1987. Recent rapid uplift in the Bolivian Andes: evidence from fission- track dating. Geology, 15(7): 680-683.

Bills, B.G., de Silva, S.L., Curry, D.R., Emenger, R.S., Lillquist, K.D., Donnellan, A. and Worden, B., 1994. Hydro-isostatic deflection and tectonic tilting in the Central Andes; initial results of a GPS survey of Lake Minchin shorelines. Geophysical Research Letters, 21(4): 293-296.

Brasse, H., Lezaeta, P., Rath, V., Schwalenberg, K., Soyer, W. and Haak, V., 2002. The Bolivian Altiplano conductivity anomaly. Journal of Geophysical Research, 107(B5): 10.1029/2001B000391.

Braun, H.-M., 1999. Untersuchungen zur Strukturgeologie und Metamorphose in den Read Mountains und den nördlichen Haskard Highlands, Shackleton Range (Antarktis). Frankfurter geowissenschaftliche Arbeiten : Serie A, Geologie - Paläontologie, A19: 1-171.

Castaños, I.A. and Saavedra, M.A., 1979. Determinación de edades absolutas en Bolivia. Revista de la Academia Nacional de Ciencias de Bolivia, 1(2): 81-102.

Dahlstrom, C.D.A., 1969. Balanced cross sections. Canadian Journal of Earth Sciences = Journal Canadien des Sciences de la Terre, 6(4, Part 1): 743-757.

Dalrymple, G.B. and Lanphere, M.A., 1974. ^{40}Ar/^{39}Ar age spectra of some undisturbed terrestrial samples. Geochimica et Cosmochimica Acta, 38(5): 715-738.

De Paor, D.G., 1988. R_f/ϕ_f strain analysis using an orientation net. Journal of Structural Geology, 10(4): 323-333.

DeCelles, P.G. and Horton, B.K., 1999. Implications of Early Tertiary foreland basin development for orogenesis in the Central Andes. EOS Transactions (AGU 1999 fall meeting), 80; 46, Suppl.: 1052.

Dickin, A.P., 1997. K-Ar and Ar-Ar age dating. Radiogenic isotope geology. Cambridge University Press, Cambridge, pp. 245-276.

Dittmar, D., 1996. Profilbilanzierung und Verformungsanalyse im südwestlichen Rheinischen Schiefergebirge — Zur Konfiguration, Deformation und Entwicklungsgeschichte eines passiven varistischen Kontinentalrandes. Beringeria, 17: 1-346.

Dittmar, D., Meyer, W., Oncken, O., Schievenbusch, T., Walter, R. and Von, W.C., 1994. Strain partitioning across a fold and thrust belt: the Rhenish Massif, mid-European Variscides. Journal of Structural Geology, 16(10): 1335-1352.

Dorbath, C. and Granet, M., 1996. Local earthquake tomography of the Altiplano and the Eastern Cordillera of northern Bolivia, Geodynamics of the Andes. Elsevier, Amsterdam, Netherlands, pp. 117-136.

Dunn, J.F., Hartshorn, K.G. and Hartshorn, P.W., 1995. Structural styles and hydrocarbon potential of the Subandean thrust belt of southern Bolivia. In: A.J. Tankard, R. Suárez S. and H.J. Welsink (Editors), Petroleum basins of South America. AAPG Memoir 62. American Association of Petroleum Geologists, Tulsa, OK, United States, pp. 523-543.

Dunnet, D., 1969. A technique of finite strain analysis using elliptical particles. Tectonophysics, 7(2): 117-136.

Dunnet, D. and Siddans, A.W.B., 1971. Non-random sedimentary fabrics and their modification by strain. Tectonophysics, 12(4): 307-325.

Duyster, J., 2000. StereoNett. Shareware programme, Bochum, Germany.

Echternacht, F., Tauber, S., Eisel, M., Brasse, H., Schwarz, G. and Haak, V., 1997. Electromagnetic study of the active continental margin in northern Chile. Physics of the Earth and Planetary Interiors, 102(1-2): 69-87.

Egan, S.S., Kane, S., Buddin, T.S., Williams, G.D. and Hodgetts, D., 1999. Computer modelling and visualisation of the structural deformation caused by movement along geological faults. Computers and Geosciences, 25(3): 283-297.

Ege, H., in prep. Exhumationsgeschichte des Altiplano und der Ostkordillere Süd-Boliviens anhand von Apatit Spaltspur-Datierungen. PhD Thesis, Freie Universität, Berlin, Germany.

Egenhoff, S., 2000. Faziesanalyse, Bio- und Sequenzstratigraphie in ordovizischen siliziklastischen Abfolgen der Ostkordillere Südboliviens. Berliner Geowissenschaftliche Abhandlungen, A207. Selbstverlag Fachbereich Geowissenschaften, FU, Berlin, 173 pp.

Elliott, D., 1983. The construction of balanced cross-sections, Balanced cross-sections and their geological significance; a memorial to David Elliott. Pergamon, Oxford-New York, International, pp. 101.

Erslev, E.A. and Ge, H., 1990. Least-squares center-to-center and mean object ellipse fabric analysis. Journal of Structural Geology, 12(8): 1047-1059.

Evernden, J.F., Kriz, S.J. and Cherroni, M.C., 1966. Correlaciones de las formaciones terciarias de la cuenca altiplanica a base de edades absolutas, determinadas por el método Potasio-Argon. Hoja inf. Serv. Geol. Bolivia, 1.

Evernden, J.F., Kriz, S.J. and Cherroni, M.C., 1977. Potassium-argon ages of some Bolivian rocks. Economic Geology, 72(6: Mineral deposits in the South American Cordillera): 1042-1061.

Fiedler, K., 2001. Die kretazisch-alttertiäre Entwicklung des südlichen Potosí Beckens (Südbolivien). Berliner Geowissenschaftliche Abhandlungen, A215 ('der Schwanensang'). Selbstverlag Fachbereich Geowissenschaften, FU, Berlin, Germany, 185 pp.

Flinn, D., 1979. The deformation matrix and the deformation ellipsoid. Journal of Structural Geology, 1(4): 299-307.

Fornani, M., Hérail, G., Pozzo, L. and Viscarra, G., 1989. Los Yacimientos de oro de Los Lípez (Bolivia). Tomo I: Estratigrafía y dinámica de emplazamiento de las volcanitas del area de Guadalupe. Informe Orstrom 19.

Fornani, M., Pozzo, L., Bailly, L., Leroy, J. and Bonhomme, M.G., 1993. Miocene volcanic centers in the southern Altiplano of Bolivia. The Cerro Morokho & Cerro Bonete area (Sur Lípez), Second ISAG, Colloques et Seminaires Institut de Recherche Scientifique pour le Développement en Cooperation, Oxford, pp. 363-366.

Fornari, M., Risacher, F. and Feraud, G., 2001. Dating of paleolakes in the central Altiplano of Bolivia. Palaeogeography, Palaeoclimatology, Palaeoecology, 172(3-4): 269-282.

Frimmel, H.E. and Frank, W., 1998. Neoproterozoic tectono-thermal evolution of the Gariep Belt and its basement, Namibia and South Africa. Precambrian Research, 90(1-2): 1-28.

Fry, N., 1979. Random point distributions and strain measurement in rocks. Tectonophysics, 60(1-2): 89-105.

Gagnier, P.Y., Blieck, A., Emig, C.C., Sempere, T., Vachard, D. and Vanguestaine, M., 1996. New paleontological and geological data on the Ordovician and Silurian of Bolivia. Journal of South American Earth Sciences, 9(5-6): 329-347.

García, M. and Hérail, G., 2001. Comment on 'Geochronology (Ar-Ar, K-Ar and He-exposure ages) of Cenozoic magmatic rocks from northern Chile (18-22° S): implications for magmatism and tectonic evolution of the central Andes' by Wörner et al. (2000). Revista Geológica de Chile, 28(1): 127-130.

García, M., Hérail, G., Charrier, R., Mascle, G., Fornani, M. and de Arce, C.P., 2002. Oligocene–Neogene tectonic evolution of the Altiplano of Northern Chile (18-19° S), Fifth ISAG. Institut de Recherche pour le Développement (IRD), Université Paul Sabatier, Toulouse, pp. 235-238.

Gayet, M., Marshall, L.G. and Sempere, T., 1991. The Mesozoic and Paleocene vertebrates of Bolivia and their stratigraphic context: a review. Revista Técnica de Yacimientos Petrolíferos Fiscales Bolivianos, 12(3-4): 393-433.

Giles, M.R., 1995. Diagenesis: a quantitative perspective. RKMR: 95.034.

Götze, H.-J. and Kirchner, A., 1997. Interpretation of gravity and geoid in the Central Andes between 20 and 29° S. Journal of South American Earth Sciences, 10(2): 179-188.

Götze, H.-J. and Krause, S., 2002. The Central Andean Gravity High, a relic of an old subduction complex? Journal of South American Earth Sciences, 14(8): 799-811.

Götze, H.-J., Lahmeyer, B., Schmidt, S. and Strunk, S., 1994. The lithospheric structure of the Central Andes (20-26° S) as inferred from interpretation of regional gravity. In: K.J. Reutter, E. Scheuber and P.J. Wigger (Editors), Tectonics of the southern Central Andes; structure and evolution of an active continental margin. Springer-Verlag, Berlin, Federal Republic of Germany, pp. 7-21.

Gräber, F.M. and Asch, G., 1999. Three-dimensional models of P wave velocity and P-to-S velocity ratio in the southern central Andes by simultaneous inversion of local earthquake data. Journal of Geophysical Research, B, Solid Earth and Planets, 104(9): 20,237-20,256.

Grant, J.N., Halls, C., Salinas, W.A. and Snelling, N.J., 1979. K-Ar ages of igneous rocks in mineralization in part of the Bolivian tin belt. Economic Geology, 74: 838-851.

Gregory-Wodzicki, K.M., 2000. Uplift history of the Central and Northern Andes: a review. GSA Bulletin, 112(7): 1091-1105.

Gubbels, T.L., Isacks, B.L. and Farrar, E., 1993. High-level surfaces, plateau uplift, and foreland development, Bolivian central Andes. Geology, 21: 695-698.

Günther, A., 1994. Gefügestatistik und Strain-Analyse der Ostharz-Decke und der Harzgeröder Zone am Beispiel des Straßenprofils Stiege-Hasselfelde (Unterharz). Unpublished diplomal Thesis, Technische Universität, Braunschweig, 96 pp.

Günther, A., 2001. Strukturgeometrie, Kinematik und Deformationsgeschichte des oberkretazisch-alttertiären magmatischen Bogens (nord-chilenische Präkordillere, 21,7-23° S). Berliner Geowissenschaftliche Abhandlungen, A213. Selbstverlag Fachbereich Geowissenschaften, FU, Berlin, Germany, 170 pp.

Haberland, C. and Rietbrock, A., 2001. Attenuation tomography in the western Central Andes; a detailed insight into the structure of a magmatic arc. Journal of Geophysical Research, B, Solid Earth and Planets, 106(6): 11,151-11,167.

Hinsch, R., 2001. Frontale Akkretion und Verformungsaufteilung eines gebogenen Falten- und Überschiebungsgürtels (Räumliche Strukturanalyse im Subandin Boliviens). Scientific Technical Report, STR01/15. Geoforschungszentrum, Potsdam, Germany, 127 pp.

Hoeppener, R., 1955. Tektonik im Schiefergebirge. Geologische Rundschau, 44: 26-58.

Hogan, J.P. and Dunne, W.M., 2001. Calculation of shortening due to outcrop-scale deformation and its relation to regional deformation patterns. Journal of Structural Geology, 23(10): 1507-1529.

Hoke, L., Lamb, S. and Entenmann, J., 1993. Volcanic rocks from the Bolivian Altiplano; insights into crustal structure, contamination, and magma genesis: Comment and reply. Geology (Boulder), 21(12): 1147-1148.

Holst, T.B., 1982. The role of initial fabric on strain determination from deformed ellipsoidal objects. Tectonophysics, 82(3-4): 329-350.

Horton, B.K. and DeCelles, P.G., 2001. Modern and ancient fluvial megafans in the foreland basin system of the central Andes, southern Bolivia: implications for drainage network evolution in fold-thrust belts. Basin Research, 13: 43-63.

Horton, B.K., Hampton, B.A., Lareau, B.N. and Baldellon, E., 2002. Tertiary provenance history of the northern and central Altiplano (Central Andes, Bolivia); a detrital record of plateau-margin tectonics. Journal of Sedimentary Research, 72(5): 711-726.

Horton, B.K., Hampton, B.A. and Waanders, G.L., 2001. Paleogene synorogenic sedimentation in the Altiplano Plateau and implications for initial mountain building in the Central Andes. Geological Society of America Bulletin, 113(11): 1387-1400.

Hossack, J.R., 1979. The use of balanced cross-sections in the calculation of orogenic contraction; a review. Journal of the Geological Society of London.

Isacks, B.L., 1988. Uplift of the Central Andean Plateau and bending of the Bolivian Orocline. Journal of Geophysical Research, 93(B4): 3211-3231.

Jacobshagen, V., Müller, J., Ahrend, H. and Wemmer, K., 1999. Hercynian deformation and metamorphism in the Eastern Cordillera of southern Bolivia, Fourth ISAG, Göttingen, pp. 364-366.

Jacobshagen, V., Müller, J., Wemmer, K., Ahrendt, H. and Manutsoglu, E., 2002. Hercynian deformation and metamorphism in the Cordillera Oriental of Southern Bolivia, Central Andes. Tectonophysics, 345(1-4): 119-130.

James, D.E., 1971. Plate tectonic model for the evolution of the Central Andes. Geological Society of America Bulletin, 82: 3325-3346.

Jamison, W.R., 1992. Stress controls on fold thrust style. In: K.R. McClay (Editor), Thrust tectonics. Chapman & Hall, London, United Kingdom, pp. 155-164.

Kay, S.M., Coira, B. and Viramonte, J., 1994. Young mafic back arc volcanic rocks as indicators of continental lithospheric delamination beneath the Argentine Puna Plateau, central Andes. Journal of Geophysical Research, 99(B12): 24323-24329.

Kelley, S., 2002. Excess argon in K-Ar and Ar-Ar geochronology. Chemical Geology, 188(1-2): 1-22.

Kennan, L., Lamb, S. and Rundle, C., 1995. K-Ar dates from the Altiplano and Cordillera Oriental of Bolivia; implications for Cenozoic stratigraphy and tectonics. Journal of South American Earth Sciences, 8(2): 163-186.

Kley, J., 1993. Der Übergang vom Subandin zur Ostkordillere in Südbolivien (21° 15'-22° S): Geologische Struktur und Kinematik. Berliner Geowissenschaftliche Abhandlungen, A156. Selbstverlag Fachbereich Geowissenschaften, FU, Berlin, Germany, 88 pp.

Kley, J., 1996. Transition from basement-involved to thin-skinned thrusting in the Cordillera Oriental of southern Bolivia. Tectonics, 15(4): 763-775.

Kley, J., Gangui, A.H. and Krüger, D., 1996. Basement-involved blind thrusting in the eastern Cordillera Oriental, southern Bolivia: evidence from cross-sectional balancing, gravimetric and magnetotelluric data. Tectonophysics, 259(1-3): 171-184.

Kley, J., Kocks, H., Silva-González, P., Monaldi, C.R. and Hindle, D., 2001. Thrust-front propagation and increasing deformation rates in the Central Andes. In: S. Roth and A. Rüggeberg (Editors), 2001 MARGINS Meeting. Schriftenreihe der Deutschen Geologischen Gesellschaft, Christian-Albrechts-Universität, Kiel, Germany, pp. 108.

Kley, J. and Monaldi, C.R., 1998. Tectonic shortening and crustal thickness in the Central Andes: How good is the correlation? Geology, 26(8): 723-726.

Kley, J., Müller, J., Tawackoli, S., Jakobshagen, V. and Manutsoglu, E., 1997. Pre-Andean and Andean-age deformation in the Eastern Cordillera of southern Bolivia. Journal of South American Earth Sciences, 10(1): 1-19.

Kley, J. and Reinhard, M., 1994. Geothermal and tectonic evolution of the Eastern Cordillera and the Subandean Ranges of Southern Bolivia. In: K.-J. Reutter, E. Scheuber and P.J. Wigger (Editors), Tectonics of the Southern Central Andes, New York, pp. 155-170.

Klügel, A., 1993. Shear 3.0 (MSDOS software programme).

Krzywiec, P., 2001. Contrasting tectonic and sedimentary history of the central and eastern parts of the Polish Carpathian Foredeep basin; results of seismic data interpretation. Thematic set on sedimentary basins and hydrocarbon habitat at the margin of Pannonian Basin system. Elsevier, Oxford, United Kingdom, pp. 13-38.

Kussmaul, S., Jordan, L. and Ploskonka, E., 1975. Isotopic ages of Tertiary volcanic rocks of SW-Bolivia. Geolologisches Jahrbuch, B14: 111-120.

Lamb, S. and Hoke, L., 1997. Origin of the high plateau in the Central Andes, Bolivia, South America. Tectonics, 16(4): 623-649.

Lamb, S., Hoke, L., Kennan, L. and Dewey, J., 1997. Cenozoic evolution of the central Andes in Bolivia and northern Chile. In: J.P. Burg and M. Ford (Editors), Orogeny through time. Geological Society, London; Special Publication, pp. 237-264.

Lee, J.K.W., Onstott, T.C., Cashman, K.V., Cumbest, R.J. and Johnson, D., 1991. Incremental heating of hornblende in vacuo; implications for $^{40}Ar/^{39}Ar$ geochronology and the interpretation of thermal histories. Geology (Boulder), 19(9): 872-876.

Leturmy, P., Mugnier, J.L., Vinour, P., Baby, P., Colletta, B. and Chabron, E., 2000. Piggyback basin development above a thin-skinned thrust belt with two detachment levels as a function of interactions between tectonic and superficial mass transfer: the case of the Subandean Zone (Bolivia). Tectonophysics, 320(1): 45-67.

Lisle, R.J., 1985a. Geological strain analysis: a manual for the R_f/ϕ_0 method. Pergamon Press, Oxford.

Lisle, R.J., 1985b. The use of the orientation tensor for the description and statistical testing of fabrics. Journal of Structural Geology, 7(1): 115-117.

Lisle, R.J., 1994. Palaeostrain analysis. In: P.L. Hancock (Editor), Continental deformation. Pergamon Press, Tarrytown, NY, pp. 28-42.

Marocco, R., Sempéré, T., Cirbian, M. and Oller, J., 1987. Mise en évidence d'une déformation paléocène en Bolivie du Sud. Sa place dans l'évolution géodynamique des Andes Centrales. Comptes Rendus de l'Academie des Sciences Paris, Serie II, 304: 1139-1143.

Marone, C., 1998. Laboratory-derived friction laws and their application to seismic faulting. Annual Reviews Earth Planet Sciences, 26: 643-696.

Marshall, L.G., Sempere, T. and Butler, R.F., 1997. Chronostratigraphy of the mammal-bearing Paleocene of south America. Journal of South American Earth Sciences, 10(1): 49-70.

Martínez, C., Soria, E., Uribe, H., Escobar, A. and Hinojosa, A., 1994. Estructura y evolución del Altiplano suroccidental; el sistema de cabalgamiento de Uyuni-Khenayani y su relación con la sedimentación Terciaria. Revista Técnica de Yacimientos Petrolíferos Fiscales Bolivianos, 15(3-4): 247-264.

Masson, F., Dorbath, C., Martinez, C. and Carlier, G., 2000. Local earthquake tomography of the Andes at 20° S: Implications for the structure and building of the mountain range. Journal of South American Earth Sciences, 13(1-2): 3-19.

McClay, K.R., 2000. The mapping of geologcial structures. The Geological Field Guide Series. Geological Society of London, John Wiley and Sons, London, United Kingdom, 161 pp.

McQuarrie, N., 1999. Balanced cross sections across the Altiplano: implications for amounts of shortening in the Bolivian Andes. EOS Transactions, 80(46): F1058.

McQuarrie, N., 2002. The kinematic history of the central Andean fold-thrust belt, Bolivia: Implications for building a high plateau. Geological Society of America - Bulletin, 114(8): 950-963.

McQuarrie, N. and Davis, G.H., 2002. Crossing the several scales of strain-accomplishing mechanisms in the hinterland of the central Andean fold-thrust belt, Bolivia. Journal of Structural Geology, 24(10): 1587-1602.

McQuarrie, N. and DeCelles, P., 2001. Geometry and structural evolution of the Central Andean backthrust belt, Bolivia. Tectonics, 20(5): 669-692.

Mertmann, D., Scheuber, E., Ege, H., Silva, P., Reutter, K.-J., Sobel, E. and Jacobshagen, V., 2001. Tectono-sedimentary evolution of the southern Altiplano: basin evolution, thermochronology, and structural geology, SFB 267 „Deformation Processes in the Andes"(internal report), p. 23-50, Berlin, Germany.

Miall, A.D., 1997. The Geology of stratigraphic sequences. Springer, Berlin Heidelberg New York, 433 pp.

Milton, N.J., 1980. Determination of the strain ellipsoid from measurements on any three sections. Tectonophysics, 64(1-2): T19-T27.

Mitra, G., 1994. Strain variation in thrust sheets across the Sevier fold-and-thrust belt (Idaho-Utah-Wyoming); implications for section restoration and wedge taper evolution, Applications of strain; from microstructures to orogenic belts. Pergamon, Oxford-New York, International, pp. 585-602.

Müller, J.P., 2000. Tektonische Entwicklung und Krustenverkürzung der Ostkordillere Südboliviens (20.7-21.5° S). Ph. D. Thesis, Freie Universität Berlin, Berlin, 197 pp.

Müller, J.P., Kley, J. and Jacobshagen, V., 2002. Structure and Cenozoic kinematics of the Eastern Cordillera, southern Bolivia (21° S). Tectonics, 21(5): 1037, doi:10.1029/2001TC001340.

Munier, K. and Gôni, P., 2000. Zum Titelbild: Pastos Grandes – Landsat-7 (ETM+) Daten aus den bolivianischen Anden — verbesserte Information durch den panchromatischen Kanal. Photogrammetrie, Fernerkundung, Geoinformatik, H6: 449-450.

Muñoz, N. and Charrier, R., 1996. Uplift of the western border of the Altiplano on a west-vergent thrust system, northern Chile. Journal of South American Earth Sciences, 9(3-4): 171-181.

Partzsch, G.M., Schilling, F.R. and Arndt, J., 2000. The influence of partial melting on the electrical behavior of crustal rocks; laboratory examinations, model calculations and geological interpretations. Tectonophysics, 317(3-4): 189-203.

Paterson, S.R. and Hao, Y., 1994. Primary fabric ellipsoids in sandstones: implications for depositional processes and strain analysis. Journal of Structural Geology, 16(4): 505-517.

Paterson, S.R., Hao, Y. and Oertel, G., 1995. Primary and tectonic fabric intensities in mudrocks. Tectonophysics, 247(1-4): 105-119.

Peach, C.J. and Lisle, R.J., 1979. A Fortran IV program for the analysis of tectonic strain using deformed elliptical markers. Computers and Geosciences, 5(3-4): 325-334.

Plessmann, W., 1965. Laterale Gesteinsverformung vor Faltungsbeginn im Unterkarbon des Edersees (Rheinisches Schiefergebirge). Geologische Mitteilungen, 5(3): 271-284.

Plessmann, W., 1966a. Diagenetische und kompressive Verformung in der Oberkreide des Harz-Nordrandes sowie im Flysch von San Remo. Neues Jahrbuch für Geologie und Paläontologie. Monatshefte, 8: 480-493.

Plessmann, W., 1966b. Lösung, Verformung, Transport und Gefüge (Beiträge zur Gesteinsverformung im nordöstlichen Rheinischen Schiefergebirge). Zeitschrift der Deutschen Geologischen Gesellschaft, 115(2-3): 650-663.

Ramsay, J.G., 1967. Folding and fracturing of rocks. McGraw-Hill, New York, 568 pp.

Ramsay, J.G. and Huber, M.I., 1983a. The techniques of modern structural geology: 1. Strain analysis. 1;. Acad. Press, London, United Kingdom, 307 pp.

Ramsay, J.G. and Huber, M.I., 1983b. The techniques of modern structural geology: 2. Folds and fractures. 2. Acad. Press, London, United Kingdom, 391 pp.

Ratschbacher, L., Meschede, M., Sperner, B. and Pfänder, J., 1994. Die Computerprogrammbibliothek zur Strainanalyse der Universität Tübingen. Tübinger Geowissenschaftliche Arbeiten, A21: 5-22.

Ressetar, R. and Alfonso, C., 1990. Geological reconnaissance of the southern Altiplano, Bolivia. 90-23-369, Earth Sciences and Ressources Institut, University of South Carolina.

Reutter, K.-J., Döbel, R., Bogdanic, T. and Kley, J., 1994. Geological Map of the Central Andes between 20 and 26° S. In: K.-J. Reutter, E. Scheuber and P.J. Wigger (Editors), in: Tectonics of the Southern Central Andes. Springer, Berlin, Heidelberg, New York.

Riller, U. and Oncken, O., 2003. Growth of the Central Andean Plateau by tectonic segmentation is unrelated to the direction of Nazca-South American Plate convergence. Journal of Geology, in press.

Riller, U., Petrinovic, I., Ramelow, J., Strecker, M. and Oncken, O., 2001. Late Cenozoic tectonism, collapse caldera, and plateau formation in the Central Andes. Earth and Planetary Science Letters, 188: 299-311.

Riller, U., Strecker, M. and Oncken, O., 1999. Andean deformation mechanisms in the eastern Puna, NW Argentina, Fourth ISAG, Göttingen, pp. 618-620.

Rochat, P., Baby, P., Hérail, G., Mascle, G., Aranibar, O. and B., C., 1996. Genesis and kinematic of the northern Bolivian Altiplano, Third ISAG, St. Malo (France), pp. 473-476.

Rochat, P., Herail, G., Baby, P. and Mascle, G., 1999. Bilan crustal et contrôle de la dynamique érosive et sédimentaire sur les mécanismes de formation de l'Altiplano. Comptes Rendus de l'Academie des Sciences, Serie II. Sciences de la Terre et des Planetes, 328(3): 189-195.

Roeder, D., 1988. Andean-age structure of the Eastern Cordillera (Province of La Paz, Bolivia). Tectonics, 7(1): 23-39.

Schilling, F.R. and Partzsch, G.M., 2001. Quantifying partial melt fraction in the crust beneath and Central Andes and the Tibetan Plateau. Physics and Chemistry of the Earth Part A: Solid Earth and Geodesy, 26(4-5): 239-246.

Schmitz, M., 1994. A balanced model of the southern central Andes. Tectonics, 13(2): 484-492.

Schrader, F., 1988. Das regionale Gefüge der Drucklösungsdeformation an Geröllen im westlichen Molassebecken. Geologische Rundschau, 77(2): 347-369.

Schurr, B., Asch, G., Rietbrock, A., Kind, R., Pardo, M., Heit, B. and Monfret, T., 1999. Seismicity and average velocities beneath the Argentine Puna Plateau. Geophysical Research Letters, 26(19): 3025-3029.

Schwarz, G. and Krüger, D., 1997. Resistivity cross section through the southern Central Andes as inferred from magnetotelluric and geomagnetic deep soundings. Journal of Geophysical Research, B, Solid Earth and Planets, 102(6): 11,957-11,978.

Sclater, J.G. and Christie, P.A.F., 1980. Continental stretching: an explanation of the post-Mid-Cretaceous subsidence of the Central North Sea basin. Journal of Geophysical Research, 85(B7): 3711-3739.

Sempere, T., 1994. Kimmeridgian? to Paleocen tectonic evolution of Bolivia. In: J.A. Salfity (Editor), Cretaceous tectonics of the Andes. IGCP, IUGS UNESCO 242, Braunschweig, Wiesbaden, pp. 168-212.

Sempere, T., 1995. Phanerozoic evolution of Bolivia and adjacent regions. In: A.J. Tankard, R. Suárez S. and H.J. Welsink (Editors), Petroleum Basins of South America. AAPG Memoir 62. American Association of Petroleum Geologists, Tulsa, OK, United States, pp. 207-230.

Sempere, T., Butler, R.F., Richards, D.R., Marshall, L.G., Sharp, W. and Swisher III, C.C., 1997. Stratigraphy and chronology of Upper Cretaceous/Lower Paleogene strata in Bolivia and northwest Argentina. Geological Society of America Bulletin, 109(6): 709-727.

Sempere, T., Herail, G., Oller, J. and Bonhomme, M.G., 1990. Late Oligocene-Early Miocene major tectonic crisis and related basins in Bolivia. Geology, 18(10): 946-949.

Sempere, T. and Orstom-YPFB, C., 1990. Cuadros estratigráficos de Bolivia: propuestas nuevas. Revista Técnica de YPFB, 11(2-3): 215-227.

Sheffels, B.M., 1990. Lower bound on the amount of crustal shortening in the central Bolivian Andes. Geology, 18: 812-815.

Sheriff, R.E. and Geldart, L.P., 1995. Exploration seismology. Cambridge University Press, Cambridge, 592 pp.

Siddans, A.W.B., 1980. Elliptical markers and non-coaxial strain increments. Tectonophysics, 67(3-4): T21-T25.

Silva-González, P., in prep. Der südliche Altiplano im Tertiär: Sedimentäre Entwicklung und tektonische Implikationen. PhD Thesis, Freie Universität, Berlin, Germany.

Singer, B. and Brown, L.L., 2002. The Santa Rosa Event; $^{40}Ar/^{39}Ar$ and paleomagnetic results from the Valles rhyolite near Jaramillo Creek, Jemez Mountains, New Mexico. Earth and Planetary Science Letters, 197(1-2): 51-64.

Skuce, A.G., 1996. Forward modelling of compaction above normal faults; an example from the Sirte Basin, Libya, Modern developments in structural interpretation, validation and modelling. Geological Society of London, London, United Kingdom, pp. 135-146.

Smart, K.J., Dunne, W.M. and Krieg, R.D., 1997. Roof sequence response to emplacement of the Wills Mountain duplex; the roles of forethrusting and scales of deformation. Journal of Structural Geology, 19(12): 1443-1459.

Soler, P., Carlier, G., Bonhomme, M.G. and Fornani, M., 1993. Field observations and K-Ar dating of the Cerro Chiar Kkollu (southern Altiplano, Bolivia), Second ISAG, Colloques et Seminaires Institut de Recherche Scientifique pour le Développement en Cooperation, Oxford, pp. 443-446.

Soler, P. and Jimenez Ch., N., 1993. Magmatic contraints upon the evolution of the Bolivian Andes since late Oligocene times, Second ISAG, Colloques et Seminaires Institut de Recherche Scientifique pour le Développement en Cooperation, Oxford, pp. 447-451.

Somoza, R., 1998. Updated Nazca (Farallon)-South America relative motions during the last 40 My: Implications for mountain building in the central Andean region. Journal of South American Earth Sciences, 11(3): 211-215.

Springer, M. and Förster, A., 1998. Heat flow density across the Central Andean subduction zone. Tectonophysics, 291: 123-139.

Suárez-Soruco, R., 1995. Comentarios sobre la edad de la Formacion Cancañiri. Revista Técnica de Yacimientos Petrolíferos Fiscales Bolivianos, 16(1-2): 51-54.

Swenson, J.L., Beck, S.L. and Zandt, G., 2000. Crustal structure from broadland regional waveform modeling: implications for the composition of thick continental crust. Journal of Geophysical Research, 105(B1): 607-621.

Tanner, D., Henk, A., Wörner, G. and Weihkamp, C., 2000. Forward, thermal, finite-element modelling of the Andes at 21° S over the last 30 Ma (keynote lecture), Geowissenschaftliches Lateinamerika-Kolloquium, Stuttgart, Germany, pp. 17-20.

Tanner, D.C., Behrmann, J.H. and Dresmann, H., 2003. Three-dimensional retro-deformation of the Lechtal Nappe, Northern Calcareous Alps. Journal of Structural Geology, 25(5): 737-748.

Turner, F.J., 1953. Nature and dynamic interpretation of deformation lamellae in calcite of three marbles. American Journal of Science, 251(4): 276-298.

Twiss, R.J. and Moores, E.M., 1992. Structural Geology. Freemann & Co., Davis, University of California, 532 pp.

Unzog, W., 1990, 1992. STRAIN — eine Sammlung verschiedener Strainprogramme, Graz, Austria.

Victor, P., 2000. Die Entwicklung der Altiplano Westflanke und ihre Bedeutung für die Plateaubildung und Krustenverdickung in N-Chile (20-21° S). Scientific Technical Report, STR00/13. Geoforschungszentrum, Potsdam, Germany, 89 pp.

Victor, P., Glodny, J. and Oncken, O., 2003. Uplift of the Altiplano western flank — timing, processes, and kinematics of plateau uplift. Submitted to Tectonics.

Vietor, T., 2001. Numerical modeling of plateau growth including some similarities to the Central Andes. In: S. Roth and A. Rüggeberg (Editors), 2001 MARGINS Meeting. Schriftenreihe der Deutschen Geologischen Gesellschaft, Christian-Albrechts-Universität, Kiel, Germany, pp. 223.

Vietor, T. and Oncken, O., submitted. Shape and kinematics of orogenic plateau flanks inferred from numerical modelling. Tectonophysics.

Von Winterfeld, C. and Oncken, O., 1995. Non-plane strain in section balancing: calculation of restoration parameters. Journal of Structural Geology, 17(3): 447-450.

Wang, K., 2000. Stress-strain 'paradox', plate coupling, and forearc seismicity at the Cascadia and Nankai subduction zones. Tectonophysics, 319(4): 321-338.

Wdowinski, S. and Bock, Y., 1994a. The evolution of deformation and topography of high elevated plateaus 1. Model, numerical analysis, and general results. Journal of Geophysical Research, 99(B4): 7103-7119.

Wdowinski, S. and Bock, Y., 1994b. The evolution of deformation and topography of high elevated plateaus 2. Application to the Central Andes. Journal of Geophysical Research, 99(B4): 7121-7130.

Welsink, H., Martínez, E.A., Aranibar, O.R. and Jarandilla, J.N., 1992. Marco estructural y estratigrafigo del Altiplano Sur. Internal Report, YPFB (ACDI/ YPFB Informe Geológico No. 92-1): 1-45.

Welsink, H.J., Martinez, E., Aranibar, O. and Jarandilla, J., 1995. Structural inversion of a Cretaceous rift basin, southern Altiplano, Bolivia. In: A.J. Tankard, R. Suárez S. and H.J. Welsink (Editors), Petroleum Basins of South America. AAPG Memoir 62. American Association of Petroleum Geologists, Tulsa, OK, United States, pp. 305-324.

Wessel, P. and Smith, W.H.F., 1998. New, improved version of Generic Mapping Tools released. EOS Transactions, 79(47): 579.

Wheeler, J., 1986. Strain analysis in rocks with pretectonic fabrics. Journal of Structural Geology, 8(8): 887-896.

Wigger, P., Schmitz, M., Araneda, M., Asch, G., Baldzuhn, S., Giese, P., Heinsohn, W.-D., Martinez, E., Ricaldi, E., Röwer, P. and Viramonte, J., 1994. Variations of the crustal structure of the Southern Central Andes deduced from seismic refraction investigations. In: K.-J. Reutter, E. Scheuber and P.J. Wigger (Editors), Tectonics of the Southern Central Andes. Springer, Berlin, Heidelberg, New York, pp. 23-48.

Willett, S., Beaumont, C. and Fullsack, P., 1993. Mechanical model for the tectonics of doubly vergent compressional orogens. Geology, 21(4): 371-374.

Williams, P.F., 1970. A criticism of the use of style in the study of deformed rocks. Geological Society of America Bulletin, 81(11): 3283-3295.

Wilson, G. and Cosgrove, J.W., 1982. Introduction to small-scale geological structures. George Allen and Unwin Ltd., London WC1A 1LU, UK, 128 pp.

Woodward, N.B., Boyer, S.E. and Suppe, J., 1989. Balanced geological cross-sections; an essential technique in geological research and exploration. Am, Geophys. Union. Washington, DC, United States, 132 pp.

Wörner, G., Hammerschmidt, K., Henjes-Kunst, F., Lezaun, J. and Wilke, H., 2000a. Geochronology ($^{40}Ar/^{39}Ar$, K-Ar and He-exposure ages) of Cenozic magmatic rocks from northern Chile (18-22° S): implications for magmatism and tectonic evolution of the Central Andes. Revista Geológica de Chile, 27(2): 205-240.

Wörner, G., Lezaun, J., Beck, A., Heber, V., Lucassen, F., Zinngrebe, E., Rossling, R. and Wilke, H.G., 2000b. Precambrian and early Paleozoic evolution of the Andean basement at Belén (northern Chile) and Cerro Uyarani (western Bolivian Altiplano). Journal of South American Earth Sciences, 13(8): 717-737.

Yuan, X., Sobolev, S.V. and Kind, R., 2002. Moho topography in the Central Andes and its geodynamic implications. Earth and Planetary Science Letters, 199(3-4): 389-402.

Yuan, X., Sobolev, S.V., Kind, R., Oncken, O., Bock, G., Asch, G., Schurr, B., Gräber, F., Rudloff, A., Hanka, W., Wylegalla, K., Tibi, R., Haberland, C., Rietbrock, A., Giese, P., Wigger, P., Roewer, P., Zandt, G., Beck, S., Wallace, T., Pardo, M. and Comte, D., 2000. Subduction and collision processes in the Central Andes constrained by converted seismic phases. Nature, 408: 958-961.

Zandt, G., Velasco, A.A. and Beck, S.L., 1994. Composition and thickness of the southern Altiplano crust, Bolivia. Geology (Boulder), 22(11): 1003-1006.

Appendix A

Picture Gallery
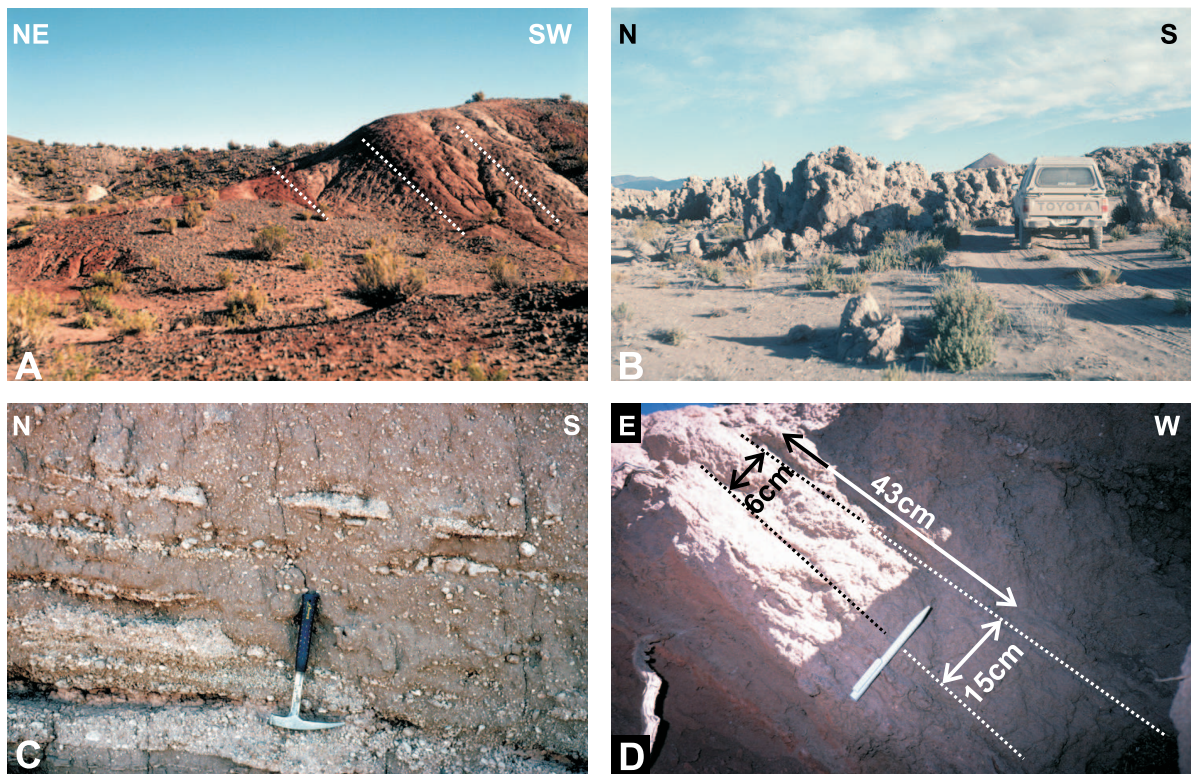
Figure A.1: **A:** Higher San Vicente strata in the western limb of the Central Anticline, Central Altiplano. **B:** Pliocene algal bioherms south of the Yazón Peninsula. **C:** Lahar, part of the Pilkhaua Subsequence in the Eastern Altiplano. **D:** Syn-tectonic sediments of the Pilkhaua Subsequence (detail). Note the strong westward increase in bank thickness.
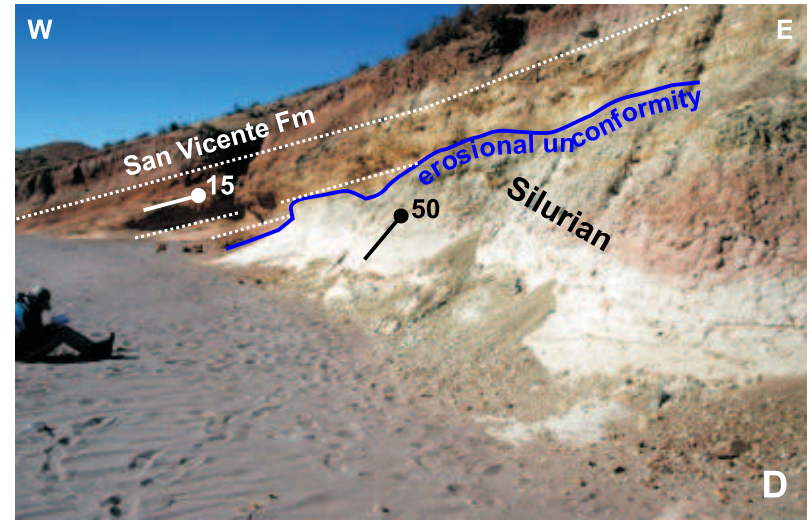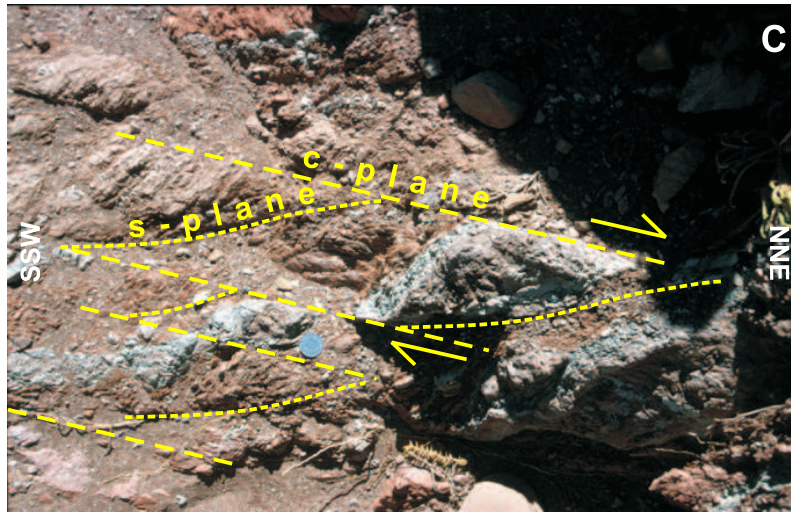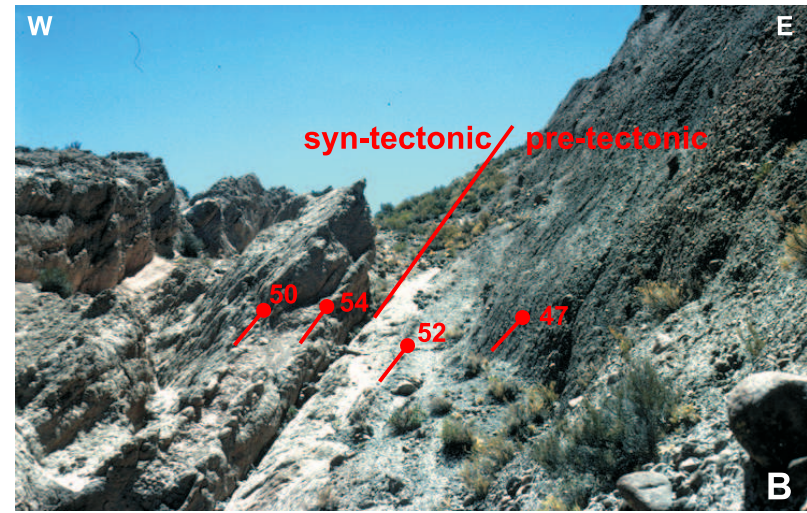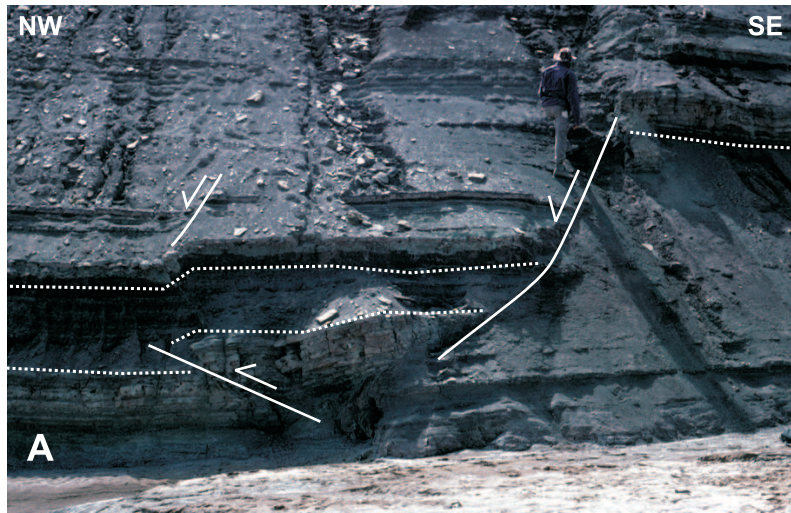
Figure A.2: **A:** Small normal faults in the Eastern Altiplano (close to the edge of the Eastern Cordillera; fault plane 138/48, displacement ~3 m; south-eastern fault). **B:** The transition of the 'pre-tectonic' San Vicente Fm. to the 'syn-tectonic' Pilkhaua Subsequence is only a facies change; no unconformity developed (west of the Ines Anticline); **C:** Gouge fabric of a dextral, 36° trending strike-slip shear zone near the southern branch of the Khenayani-Uyuni Fault, north of Soniquera (c-plane: 143/90, lineation: 50/10). **D:** Shallow, WNW-dipping San Vicente sediments directly onlapping Silurian quartzite above an erosional unconformity, photograph kindly provided by Ekkehard Scheuber (FU Berlin).
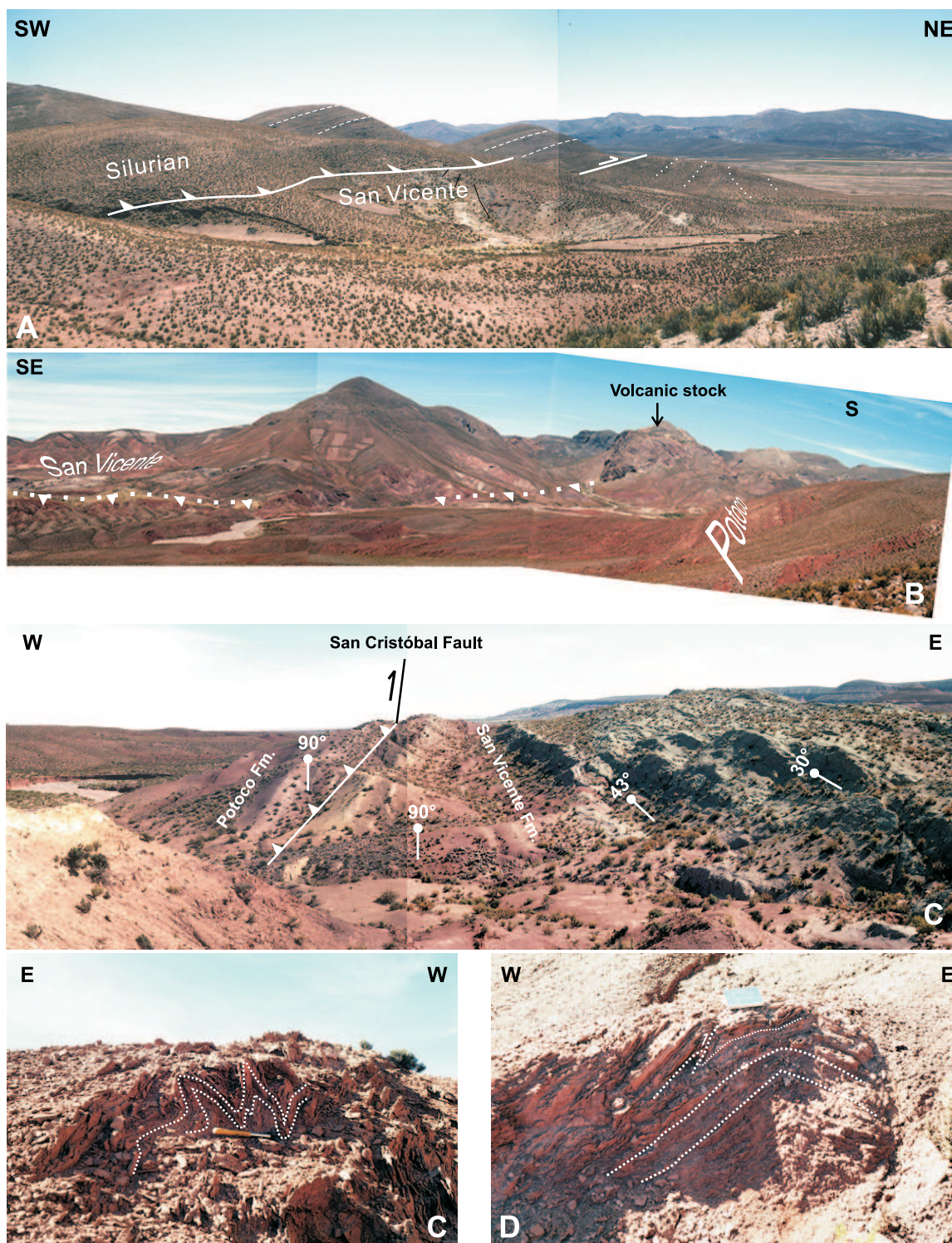
Figure A.3: **A:** Khenayani-Uyuni Fault at Cerro Khala Huasi. **B–E:** San Cristóbal Fault (SCF): **B:** vertically-inclined Potoco pelites in the hanging wall of the SCF. Note the position of the San Cristóbal volcanic complex on the thrust. **C:** syn-tectonic San Vicente strata in the footwall of the SCF. **D, E:** small folds in the thrust zone, narrow kink folds (**D**) or open folds (**E**), depending on lithology.
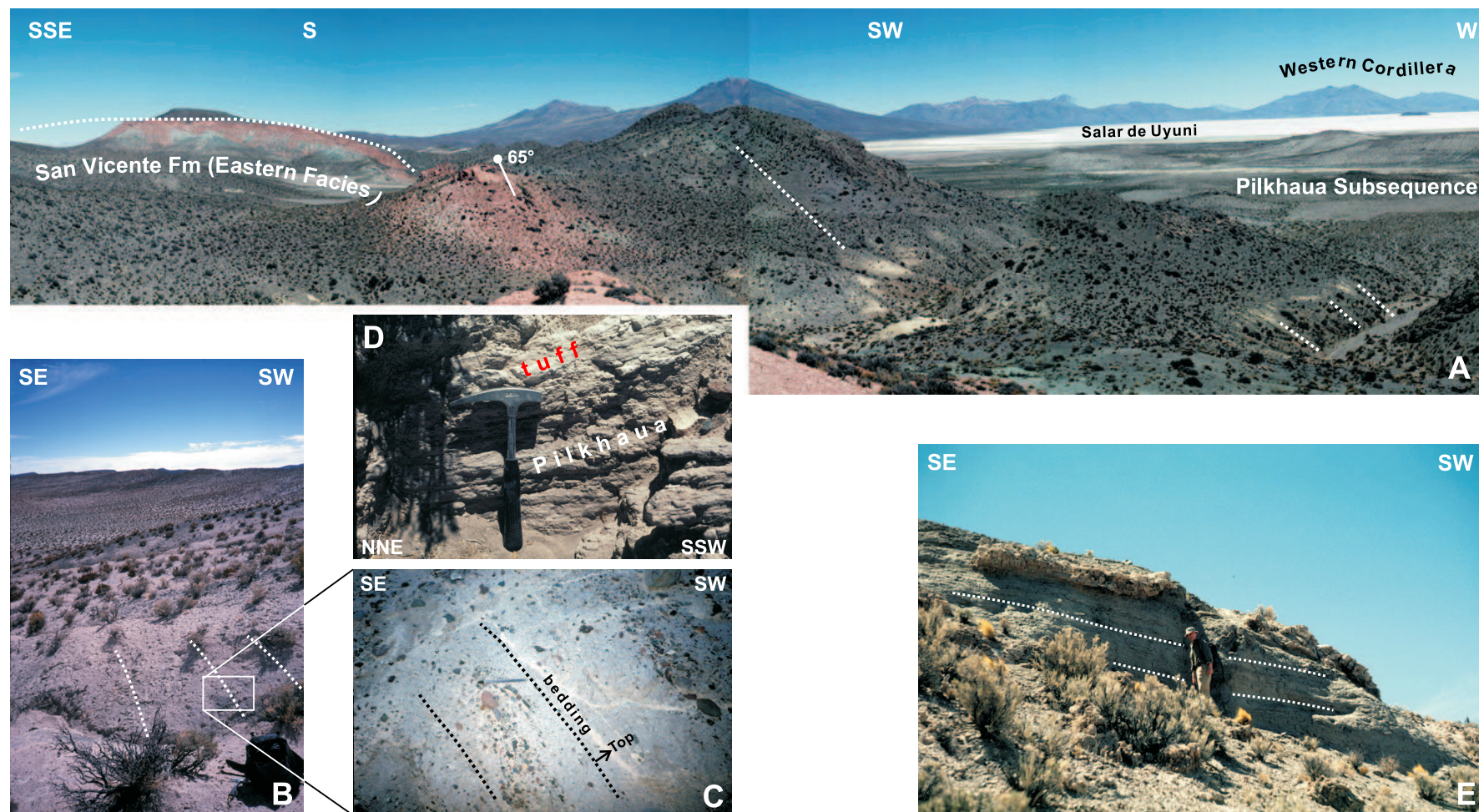
Figure A.4: **A:** View from the north to the steep, western limb of the Yazón Anticline, with associated syn-tectonic sediments to the west (Pilkhaua Subsequence). **B:** immature proto-sandstones with occasionally conglomerates are characteristic of the Pilkhaua Subsequence, steep westward-dipping strata close to the eastern basin edge. **C:** close-up of B. **D:** Small ash-flow tuffs are interbedded in the basal part of the basin. **E:** shallow, westward-dipping Pilkhaua sediments in the upper part of the syn-tectonic basin, the very weakly-developed stratification is only visible from afar.

Appendix B

Database

Reflection seismic lines (provided by YPFB)

Number	year	start point (UTM x,y)		end point (UTM x,y)		length	shot points		processing
10007–60	1994	727919	7673887	775038	7657258	50.009	1101.5 – 3101.5		migrated
10008–60	1994	703593	7653061	746721	7640699	44.976	–		migrated
10010–60	1994	701461	7647932	745514	7634749	45.984	1109.5 – 2709.5		migrated
10011–60	1994	700190	7644655	727020	7636671	27.992	–		migrated
10016–60	1994	720115	7625699	745159	7715264	93.002	1172.5 – 4821.5		migrated
10020–60	1994	751376	7699453	732749	7692169	20.003	1101.5 – 1901.5		migrated
10021–60	1994	783554	7703458	748754	7699771	35.000	1101.5 – 2501.5		migrated
10022–60	1994	650990	7711368	699933	7693823	51.993	1101.5 – 3181.5		migrated
10023–60	1994	646473	7703403	701034	7683781	57.983	1101.5 – 2005.5		migrated
10024–60	1994	678097	7710897	661783	7686936	28.987	1101.5 – 1537.5		migrated
2553–28	1972	583948	7798096	713054	7759432	135.038	188	– 1647	stack/
							315	– 1064	migrated
2554–28	1972	663636	7782861	705217	7770212	20.502	185	– 395	stack
2554–28	1972	705217	7770212	722163	7765279	17.660	530	– 797	stack
2564–28	1972	695406	7739087	709145	7780735	43.892	245	– 709	stack
2570–28	1972	747041	7661578	709894	7672331	38.672	–		stack
2593–28	1972	735511	7677171	681200	7695767	57.406	–		migrated
2594–28	1972	745210	7683297	706474	7694673	40.371	–		stack

Table B.1: Available reflection-seismic database ($\sim$844 km, paper prints) of the Southern Altiplano: UTM co-ordinates, length (m), shot points, and processing. Seismic data was kindly provided by YPFB, Santa Cruz, Bolivia. See next page for field parameters and processing sequence of seismic sections.

Field parameters and processing sequence of the seismic sections

- **For lines with suffix -60 (Dip move-out (DMO)-corrected, migrated time sections):**

  → **Field parameters:** 480 traces per record, sampling rate 2 ms, trace length 7 s. Source parameters: (a) Vibroseis, 4 vibes, sweep repetition 8, sweep length 12 s, sweep frequency 8–72 Hz, shot-point distance 50 m. (b) Borehole shots, depth 6–16 m, shot size 2–3 kg, shot-point distance 50 m, 60-fold. Receiver distance 25 m.

  → **Processing sequence:** Demultiplex, manual trace-editing, geometry description and application, phase conversion to minimum-phase signals (vibroseis only), spherical divergence corrections, refraction statics, deconvolution, common-depth point (CDP)-sorting, velocity analysis, (surface-consistent) residual statics, velocity analysis, residual statics, DMO correction, DMO-velocity analysis, DMO application, muting, time variant scaling (AGC, gate length: t=1 s), finite-differences (FD) migration, F-X random noise attenuation, pass-band filtering, AGC (t=1 s). Datum elevation 3750 m.

- **For lines with suffix -28, with exception of lines 2553-28 and 2593-28 (stacked time sections):**

  → **Field parameters:** 48 traces per record, sampling rate 4 ms, trace length 13 s, group interval 100 m, 24 geophones/group. Source parameters: Vibroseis, 3 vibes, sweep length 7 s, sweep frequency 10-40 Hz (sporadic 8–56 Hz), 16 sweeps/profile, VP interval 100 m.

  → **Processing sequence:** Demultiplex, CDP-sorting, normal move-out (NMO) analysis, NMO correction, muting, stacking (24-fold), deconvolution, filtering, AGC (t=0.5 s), trace mixing. Datum elevation 3750 m.

- **For reprocessed line 2553-28 (shot points 315–1064, DMO migration):**

  → **Field parameters:** same as sections with suffix -28

  → **Processing sequence:** Demultiplex, geometry description and application, trace editing, surface-consistent deconvolution, spectral balance, relative datum statics (datum elevation 3900 m), sorting, velocity analysis, residual statics, velocity analysis, residual statics, AGC (t=0.5 s), DMO correction, DMO-velocity analysis, NMO correction, muting, datum statics (mean), stack, FD migration, F-X random noise attenuation, bulk shift, bandpass filtering, AGC (t=1 s).

- **For reprocessed line 2593-28 (wave-equation migration):**

  → **Field parameters:** same as sections with suffix -28

  → **Processing sequence:** Demultiplex, pre-stack deconvolution, residual statics, velocity analysis, multiple suppression, DMO-correction, DMO-velocity analysis, trim statics, stacking (24-fold), F-X deconvolution, wave-equation migration (Koehler operator), bandpass filtering. Datum elevation 3700 m.

Name	Year	No.	Longitude	Latitude
Geological Maps (YPFB), scale 1:50 000				
Mapa Geológico Nor Lípez	1973	—	67°45′–66°45′	21°40′–20°00′
Geological Maps (SERGEOMIN)				
Scale 1: 1 000 000				
Mapa Geológico de Bolivia	2000	—	70°00′–57°50′	24°00′–09°00′
Scale 1: 250 000				
San Pablo de Lípez	1999	SF 19-8	67°30′–66°00′	22°00′–21°00′
Uyuni	1997	SF-19-4	67°30′–66°00′	21°00′–20°00°
Salinas de Garcí Mendoza	1995	SE 19-5	69°00′–67°30′	20°00′–19°00′
Scale 1: 100 000				
Abra de Napa/	1997	5932/		
Yonza	1997	5832	68°45′–68°00′	20°40′–20°20′
Alota/	1997	5929/		
Canapa	1997	6029	68°11′–67°30′	21°40′–21°20′
San Pedro de Quemez	1997	5931	68°35′–68°00′	21°00′–20°40′
Canquella	1967	5933	68°30′–68°00′	20°20′–20°00′
Ollagüe/	1997	6030/		
San Agustín	1997	5030	68°20′–67°30′	21°20′–21°00′
Río Grande	1967	6131	67°30′–67°00′	21°00′–20°40′
Jay	1962	6134	67°30′–67°00′	20°00′–19°40′
Tambillo	1962	6135	67°30′–67°00′	19°40′–19°20′
Pampa Aullagas	1963	6136	67°30′–67°00′	19°20′–19°00′
Tolapampa	1967	6231	67°00′–66°30′	21°00′–20°40′
Uyuni	1966	6232	67°00′–66°30′	20°40′–20°20′
Río Mulatos	1962	6234	67°00′–66°30′	20°00′–19°40′
Sevaruyo	1962	6235	67°00′–66°30′	19°40′–19°20′
Huari	1962	6236	67°00′–66°30′	19°20′–19°00′
Quechisla	1966	6331	66°30′–66°00′	21°00′–20°40′
Ubina	1966	6332	66°30′–66°00′	20°40′–20°20′
Kilpani	1962	6334	66°30′–66°00′	20°00′–19°40′
El Condor	1962	6335	66°30′–66°00′	19°40′–19°20′
Soniquera	1997	6128	67°30′–67°00′	22°00′–21°40′
San Pablo de Lípez	1997	6228	67°00′–66°30′	21°40′–22°00′
Lagunillas	1962	6336	66°30′–66°00′	19°20′–19°00′
Scale 1: 50 000				
Santiago de Agencha	1965	6032	68°00′–67°30′	20°40′–20°20′
Salar de Uyuni	1965	6033	68°00′–67°30′	20°20′–20°00′
Serranía de las Minas	1965	6129	67°30′–67°00′	21°40′–21°20′
San Cristóbal	1965	6130	67°30′–67°00′	21°20′–21°00′

Table B.2: Available geological maps from YPFB and SERGEOMIN. Additional regional overview gave the Geological Map of the Southern Central Andes (Reutter et al., 1994).

FAULT PLANES WITH LINEATIONS

Population 1 — Normal faults (NW–SE extension)

No.	Locality	Fault plane	Lineation	Sense	Formation
267	EAP, Vilque Anticline	345/72	298/67	normal	San Vicente
269	EAP, Vilque Anticline	143/75	136/75	normal	San Vicente
320	CAP, Yazón Peninsula	309/29	317/24	normal	San Vicente
320	CAP, Yazón Peninsula	340/70	346/68	normal	San Vicente
320	CAP, Yazón Peninsula	320/63	339/63	normal	San Vicente
399	EAP, EC-AP border	288/60	304/55	normal	El Molino
400	EAP, EC-AP border	290/55	313/48	normal	El Molino
623	CAP, Ines Anticline	195/85	120/10	normal	San Vicente
624	CAP, Ines Anticline	198/88	104/2	normal	San Vicente
734	CAP, Yazón Peninsula	311/48	234/51	normal	San Vicente
759	CAP, Yazón Peninsula	125/85	182/81	normal	San Vicente
808	CAP, Yonza	160/75	55/29	normal	post Miocene
808	CAP, Yonza	14/65	285/10	normal	post Miocene
1617	EAP, EC-AP border	157/40	111/20	normal	Chaunaca

Population 2 — Reverse faults (NW–SE compression)

No.	Locality	Fault plane	Lineation	Sense	Formation
265	EAP, Vilque Anticline	115/70	132/68	reverse	San Vicente
265	EAP, Vilque Anticline	135/58	131/56	reverse	San Vicente
265	EAP, Vilque Anticline	125/59	130/57	reverse	San Vicente
265	EAP, Vilque Anticline	124/50	120/50	reverse	San Vicente
317	CAP, Yazón Peninsula	290/62	244/50	reverse	San Vicente
320	CAP, Yazón Peninsula	343/48	314/45	reverse	San Vicente
320	CAP, Yazón Peninsula	327/52	313/46	reverse	San Vicente
320	CAP, Yazón Peninsula	297/14	310/14	sinistral	San Vicente
335	CAP, Yazón Peninsula	48/14	124/4	sinistral	San Vicente
335	CAP, Yazón Peninsula	113/15	120/11	sinistral	San Vicente
758	CAP, Yazón Peninsula	109/86	162/82	reverse	San Vicente
916	CAP, Yazón Peninsula	142/56	111/45	reverse	San Vicente
982	CAP, Yazón Peninsula	310/70	265/60	reverse	San Vicente
1649	EAP, syncline east of Vilque	128/45	138/48	reverse	M/L Miocene
1649	EAP, syncline east of Vilque	125/55	138/48	reverse	M/L Miocene
1626	EAP, EC-AP border	140/22	128/26	reverse	El Molino
1626	EAP, EC-AP border	165/56	122/42	reverse	El Molino

Table B.3: continues next page

Population 3 — Strike-slip faults (NE–SW compression, NW-SE extension)

No.	Locality	Fault plane	Lineation	Sense	Formation
84	CAP, Corregidores Fault	225/55	261/50	reverse	Silurian
230	CAP, Khenayani-Uyuni Fault	143/90	50/10	dextral	Potoco
435	EAP, EC-AP border	66/87	332/44	normal?	Potoco
436	EAP, EC-AP border	302/34	27/35	normal	Potoco
639	CAP, Khenayani-Uyuni Fault	296/70	40/02	?	Silurian
641	CAP, Khenayani-Uyuni Fault	308/70	36/17	dextral	Silurian
654	CAP, San Cristóbal Fault	210/75	264/36	?	Potoco
1625	EAP, EC-AP border	135/68	83/47	normal	El Molino
1625	EAP, EC-AP border	165/70	289/07	dextral	El Molino
1626	EAP, EC-AP border	145/27	82/09	sinistral	El Molino
1626	EAP, EC-AP border	178/41	81/04	sinistral	El Molino
1626	EAP, EC-AP border	342/80	257/17	sinistral	El Molino
1626	EAP, EC-AP border	138/48	215/07	sinistral	El Molino
1628	EAP, EC-AP border	185/65	95/00	sinistral	El Molino
1628	EAP, EC-AP border	174/80	80/02	sinistral	El Molino
1628	EAP, EC-AP border	145/76	257/10	sinistral	El Molino

Table B.3: (continued) Measured fault planes with lineations (mostly slickensides) of the Southern Altiplano. CAP = Central Altiplano, EAP = Eastern Altiplano, EC-AP border = border between the Eastern Cordillera (EC) and the Southern Altiplano (AP). See Table B.4 for UTM co-ordinates from outcrop numbers (No.).

CENTRAL ALTIPLANO   *EASTERN ALTIPLANO*

No.	Long.	Latitude	Locality	No.	Long.	Latitude	Locality
84	704615	7699138	KUFZ	265	754834	7664177	Vilque Anticline
230	684442	7645568	KUFZ	267	754816	7664366	Vilque Anticline
317	607302	7758174	Yazón Peninsula	269	754774	7664366	Vilque Anticline
320	611492	7734306	Yazón Peninsula	399	776599	7713618	EC-AP border
335	606651	7729002	Yazón Peninsula	400	776547	7713652	EC-AP border
623	668960	7670105	Ines Anticline	435	759063	7692139	EC-AP border
624	668991	7670082	Ines Anticline	436	759022	7692206	EC-AP border
639	716658	7701944	KUFZ	1617	781507	7712216	EC-AP border
641	716481	7701958	KUFZ	1625	777775	7715122	EC-AP border
654	682817	7655242	KUFZ	1626	777547	7715266	EC-AP border
734	609831	7733952	Yazón Peninsula	1628	777315	7715565	EC-AP border
758	606766	7730761	Yazón Peninsula	1649	761957	7663722	E' Vilque
759	606807	7730738	Yazón Peninsula				
808	601382	7719780	Yonza				
916	607570	7730866	Yazón Peninsula				
982	680798	7670977	Yazón Peninsula				

Table B.4: UTM co-ordinates of measured striated faults.

Appendix C

Isotopic age determination

The following pages contain the ^{40}Ar/^{39}Ar analytical data from incremental heating experiments on biotite and hornblende of volcanic rocks from the Southern Altiplano. Calculation and correction factors for the Ar-Ar analyses are Daly/Hf = 133±5%, ^{40}Ar/^{36}Ar$_{air}$ = 299±1.0%, K/Ca$_{conv.}$ = 0.247, ^{40}K/^{39}K = 0.0254, ^{39}Ca/^{37}Ca = 0.00039, and ^{36}Ca/^{37}Ca varies for hornblende between 0.00021 (samples ke30-00, ke39-00, ke41-00) and 0.00022 (ke28-00), and for biotite between 0.00022 (ke40-00), 0.00023 (ke13-00), and 0.000336 (ke24-00 and ke39-00). Analytical uncertainties for each step are given at the 1σ level, plateau and total gas ages contain an additional 0.4% error **of** the J-value.

The last table contains the available analytical results of the K-Ar method. Errors are given at the 1σ level.

Table C.1 gives a summary of sample locations, ages, methods and bedding of the samples.

WPT	UTM-x	UTM-y	sample	age	method	mineral	bedding	position
607	662592	7677470	**ke01-00**	15.8 ± 1.2	Ar-Ar[2]	bi	290/60	syn-tectonic
287	750589	7664554	**ke06-99**	18.2 ± 0.5	K-Ar[3]	bi	108/20	pre-tectonic
308	751833	7668609	**ke10-99**	17.8 ± 0.5	K-Ar[3]	bi	069/03	pre-tectonic
317	607111	7757827	**ke11-99**	23.6 ± 0.6	K-Ar[3]	bi	270/55	pre-tectonic
317	607111	7757827	**ke12-99**	24.2 ± 1.2	K-Ar[3]	fsp	275/55	pre-tectonic
319	605967	7730893	**ke28-00**	20.9 ± 2.0	Ar-Ar[1]	bi	323/88	pre-tectonic
367	667540	7669542	**ke19-99**	24.7 ± 0.6	K-Ar[3]	glass	120/55	pre-tectonic
707	644433	7669689	**ke13-00**	9.4 ± 0.3	Ar-Ar[1]	bi	315/15	post-tectonic
919	605882	7731505	**ke24-00**	17.1 ± 0.7	Ar-Ar[1]	bi	288/48	syn-tectonic
961	662592	7677470	**ke30-00**	< 34	Ar-Ar[3]	hbl	303/40	syn-tectonic
988	675418	7678968	**ke39-00**	8.3 ± 1.2	Ar-Ar[1]	hbl	horizontal	syn-tectonic
988	675418	7678968	**ke39-00**	7.6 ± 0.9	Ar-Ar[2]	bi	horizontal	syn-tectonic
989	679815	7684634	**ke40-00**	7.9 ± 0.2	Ar-Ar[1]	bi	272/15	syn-tectonic
998	680936	7682507	**ke41-00**	29.3 ± 2.0	Ar-Ar[1]	hbl	257/60	syn-tectonic

Table C.1: Location, ages, bedding of Cenozoic tuffs from the Southern Altiplano, own data (*WPT* = waypoint number (cf. App. F.1), bi = biotite, hbl = hornblende). *Position* refers to the structural position. [1] = plateau age, [2] = isochron age, [3] = maximum age.

---

[4]next pages: steps used for calculating plateau or integrated ages

Sample ke01-00, biotite J=0.004773 ± 0.4%

step	$T[^\circ C]$	$^{39}Ar\,[\%]$	$^{40}Ar\,[mV]$	$Rad\,[\%]$	$^{39}Ar/^{37}Ar$	$^{36}Ca\,[\%]$	$^{40}Ca/^{39}Ar$	$age\,[Ma]$
1	580	0.9	22.76	6.8	4	0.01	12.93 ± 20.9	108.0 ± 21.9
2	620	5.1	136.39	24.8	30	0.01	13.92 ± 2.9	116.1 ± 3.3
3	660	7.7	122.01	22.4	40	0.01	8.25 ± 4.5	69.6 ± 3.0
4	720	7.7	45.69	19.8	47	0.01	3.07 ± 8.6	26.2 ± 2.2
5	770	5.6	31.42	36.5	49	0.03	2.89 ± 2.5	24.7 ± 0.6
6	820	5.2	26.62	34.9	46	0.04	2.64 ± 3.6	22.6 ± 0.8
7	870	4.9	24.65	38.6	48	0.04	2.60 ± 3.0	22.2 ± 0.7
8	920	5.5	29.03	42.9	45	0.05	2.73 ± 1.2	23.4 ± 0.3
9	980	11.1	55.44	58.3	43	0.10	2.58 ± 2.1	22.1 ± 0.5
10[4]	1060	22.6	91.06	54.8	38	0.12	2.09 ± 0.8	17.9 ± 0.1
11[4]	1250	23.6	90.42	67.0	28	0.31	1.99 ± 2.3	17.0 ± 0.4

Total gas age								29.7 ± 5.3
46% integrated age[4]								17.5 ± 1.0

$^{40}Ar/^{36}Ar$ vs. $^{39}Ar/^{36}Ar$ isochron parameters:
Age = 15.8 ± 1.2 Ma; $^{40}Ar/^{36}Ar$ intercept = 366.1 ± 20.6; correlation = 0.987814

Sample ke13-00, biotite J=0.005137 ± 0.4%

step	$T[^\circ C]$	$^{39}Ar\,[\%]$	$^{40}Ar\,[mV]$	$Rad\,[\%]$	$^{39}Ar/^{37}Ar$	$^{36}Ca\,[\%]$	$^{40}Ca/^{39}Ar$	$age\,[Ma]$
1	620	29.7	31.88	75.6	44	0.40	1.26 ± 3.3	11.7 ± 0.4
2[4]	660	10.9	9.53	81.9	108	0.31	1.03 ± 3.0	9.5 ± 0.3
3[4]	700	16.4	14.36	89.5	128	0.56	1.03 ± 3.0	9.5 ± 0.3
4[4]	740	16.2	14.09	89.3	117	0.60	1.02 ± 2.0	9.5 ± 0.2
5[4]	790	17.3	14.71	86.9	143	0.38	1.00 ± 1.0	9.2 ± 0.1
6	845	5.4	4.46	84.7	182	0.25	0.97 ± 1.5	9.0 ± 0.1
7	915	2.9	2.45	82.0	65	0.55	0.99 ± 2.5	9.2 ± 0.2
8	980	1.0	0.88	71.6	25	0.74	0.99 ± 16.4	9.1 ± 1.5

Total gas age								**10.1 ± 0.4**
61% plateau age[4]								**9.4 ± 0.3**

$^{40}Ar/^{36}Ar$ vs. $^{39}Ar/^{36}Ar$ isochron parameters:
Age = 9.8 ± 0.2 Ma; $^{40}Ar/^{36}Ar$ intercept = 242.7 ± 47.2; correlation = 0.998995

Sample ke24-00, biotite J=0.005137 ± 0.4%

step	$T[^\circ C]$	$^{39}Ar\,[\%]$	$^{40}Ar\,[mV]$	$Rad\,[\%]$	$^{39}Ar/^{37}Ar$	$^{36}Ca\,[\%]$	$^{40}Ca/^{39}Ar$	$age\,[Ma]$
1	620	1.2	1.04	49.9	0.3	7.41	2.93 ± 24.7	27.0 ± 6.6
2	660	1.5	0.79	47.4	4	1.03	1.67 ± 33.5	15.4 ± 5.1
3	700	1.5	1.10	67.2	14	0.45	2.32 ± 38.5	21.4 ± 8.2
4	740	2.2	1.04	59.2	15	0.44	1.58 ± 32.9	14.5 ± 4.8
5	760	1.5	0.79	54.4	12	0.43	1.68 ± 26.7	15.5 ± 4.1
6[4]	845	5.0	2.97	80.1	25	0.60	1.95 ± 12.9	18.0 ± 2.3
7[4]	1080	39.1	22.24	83.1	13	1.50	1.86 ± 1.6	17.1 ± 0.3
8[4]	1250	47.9	26.87	84.9	7	3.38	1.83 ± 1.8	16.9 ± 0.3

Total gas age								**17.1 ± 1.1**
92% plateau age[4]								**17.1 ± 0.7**

$^{40}Ar/^{36}Ar$ vs. $^{39}Ar/^{36}Ar$ isochron parameters:
Age = 17.0 ± 0.9 Ma; $^{40}Ar/^{36}Ar$ intercept = 330.5 ± 47.8; correlation = 0.993287

Sample ke28-00, amphibole   43.7 mg, J=0.005137 ± 0.4%

step	$T[^\circ C]$	$^{39}Ar\,[\%]$	$^{40}Ar\,[mV]$	$Rad\,[\%]$	$^{39}Ar/^{37}Ar$	$^{36}Ca\,[\%]$	$^{40}Ca/^{39}Ar$	$age\,[Ma]$
1	840	2.3	1.38	44.4	0.044	16.48	6.06 ± 14.8	55.3 ± 8.1
2	880	5.9	2.92	53.9	0.145	9.72	4.97 ± 10.0	45.4 ± 4.5
3	930	1.5	0.65	39.9	0.127	7.20	4.45 ± 7.7	40.7 ± 3.1
4	980	1.7	0.65	36.4	0.148	6.34	3.78 ± 10.5	34.7 ± 3.6
5	1050	2.6	0.90	47.9	0.149	10.51	3.48 ± 6.6	32.0 ± 2.1
6[4]	1140	13.0	3.30	87.3	0.097	66.18	2.54 ± 10.1	23.4 ± 2.3
7[4]	1300	73.1	16.22	98.3	0.091	98.23	2.22 ± 5.3	20.5 ± 1.1

Total gas age								**24.0 ± 2.9**
86% plateau age[4]								**20.9 ± 2.1**

$^{40}Ar/^{36}Ar$ vs. $^{39}Ar/^{36}Ar$ isochron parameters:
Age = 20.6 ± 0.1 Ma; $^{40}Ar/^{36}Ar$ intercept = 447.9 ± 31.8; correlation = 0.999993

Sample ke30-00, amphibole   69.6 mg, J=0.005137 ± 0.4%

step	$T[^\circ C]$	$^{39}Ar\,[\%]$	$^{40}Ar\,[mV]$	$Rad\,[\%]$	$^{39}Ar/^{37}Ar$	$^{36}Ca\,[\%]$	$^{40}Ca/^{39}Ar$	$age\,[Ma]$
2	880	0.3	1.21	82.0	0.427	3.23	21.12 ± 37.5	185.8 ± 66.2
3	930	0.5	2.93	86.6	0.203	6.90	28.39 ± 11.0	245.6 ± 25.3
4	980	3.6	14.52	97.6	0.186	42.67	20.61 ± 1.4	181.5 ± 2.4
5	1015	8.7	27.21	97.6	0.137	56.43	15.86 ± 3.2	141.3 ± 4.4
6	1050	20.5	35.15	95.8	0.145	55.80	8.73 ± 1.7	79.1 ± 1.4
7	1090	45.3	32.97	92.6	0.127	65.76	3.71 ± 3.4	34.0 ± 1.2
8	1140	17.8	28.74	98.5	0.123	83.87	8.23 ± 3.4	74.7 ± 2.5
9	1210	2.6	17.91	95.0	0.021	63.22	35.66 ± 2.0	303.4 ± 5.7
10	1300	0.7	2.06	43.8	0.003	49.98	16.54 ± 14.8	147.1 ± 20.9

Total gas age								**74.5 ± 3.6**

$^{40}Ar/^{36}Ar$ vs. $^{39}Ar/^{36}Ar$ isochron parameters:
Age = 65.1 ± 16.3 Ma; $^{40}Ar/^{36}Ar$ intercept = 2705.2 ± 1716.4; correlation = 0.833059

Sample ke39-00, amphibole   54 mg, J=0.005137 ± 0.4%

step	$T[^\circ C]$	$^{39}Ar\,[\%]$	$^{40}Ar\,[mV]$	$Rad\,[\%]$	$^{39}Ar/^{37}Ar$	$^{36}Ca\,[\%]$	$^{40}Ca/^{39}Ar$	$age\,[Ma]$
1	840	2.9	2.62	45.1	0.626	2.15	3.78 ± 2.4	34.7 ± 0.8
2	880	0.3	0.21	27.4	0.369	2.04	3.09 ± 41.0	28.4 ± 11.6
3	930	0.4	0.25	29.6	0.282	3.20	2.84 ± 25.0	26.1 ± 6.5
4	980	0.1	0.08	13.1	0.182	2.14	2.37 ± 17.8	21.8 ± 3.9
5[4]	1015	13.7	2.81	84.6	0.138	77.74	0.86 ± 7.8	7.9 ± 0.6
6[4]	1050	64.7	13.92	91.3	0.129	88.99	0.90 ± 2.4	8.3 ± 0.2
7[4]	1090	8.7	1.88	71.9	0.140	57.76	0.91 ± 23.2	8.4 ± 1.9
8[4]	1140	5.2	1.19	83.4	0.116	76.40	0.96 ± 15.7	8.9 ± 1.4
9[4]	1210	2.0	0.41	65.3	0.118	54.63	0.88 ± 32.7	8.1 ± 2.7
10[4]	1300	2.0	0.46	23.9	0.095	17.82	0.96 ± 40.2	8.9 ± 3.6

Total gas age								**9.2 ± 1.4**
96% plateau age[4]								**8.3 ± 1.2**

$^{40}Ar/^{36}Ar$ vs. $^{39}Ar/^{36}Ar$ isochron parameters:
Age = 8.5 ± 0.2 Ma; $^{40}Ar/^{36}Ar$ intercept = 307.0 ± 45.5; correlation = 0.999151

Sample ke39-00, biotite   19.8 mg, J=0.005137 ± 0.4%

step	$T[^\circ C]$	$^{39}Ar\,[\%]$	$^{40}Ar\,[mV]$	$Rad\,[\%]$	$^{39}Ar/^{37}Ar$	$^{36}Ca\,[\%]$	$^{40}Ca/^{39}Ar$	$age\,[Ma]$
1	620	14.3	42.60	30.2	21	0.04	3.65 ± 11.7	33.5 ± 3.9
2	660	7.1	13.53	26.2	41	0.02	2.34 ± 12.9	21.5 ± 2.8
3	700	6.6	10.94	36.1	56	0.03	2.03 ± 3.9	18.7 ± 0.7
4[4]	740	5.2	6.80	44.4	37	0.09	1.60 ± 6.8	14.8 ± 1.0
5[4]	790	5.8	7.05	50.7	47	0.10	1.48 ± 4.8	13.6 ± 0.6
6[4]	845	5.2	5.92	46.5	41	0.10	1.38 ± 3.6	12.7 ± 0.5
7[4]	915	5.6	6.70	39.2	32	0.09	1.45 ± 3.6	13.4 ± 0.5
8[4]	980	10.3	11.85	42.0	38	0.09	1.40 ± 4.7	13.0 ± 0.6
9	1060	17.9	18.52	44.8	41	0.10	1.276 ± 3.6	11.7 ± 0.4
10	1250	21.9	16.56	58.3	33	0.31	0.92 ± 1.7	8.5 ± 0.1

Total gas age	**15.8 ± 2.6**
32% plateau age[4]	**13.4 ± 1.6**

^{40}Ar/^{36}Ar vs. ^{39}Ar/^{36}Ar isochron parameters:
Age = 7.6 ± 0.9 Ma; ^{40}Ar/^{36}Ar intercept = 400.6 ± 13.2; correlation = 0.970956

Sample ke40-00, biotite   19.5 mg, J=0.005137 ± 0.4%

step	$T[^\circ C]$	$^{39}Ar\,[\%]$	$^{40}Ar\,[mV]$	$Rad\,[\%]$	$^{39}Ar/^{37}Ar$	$^{36}Ca\,[\%]$	$^{40}Ca/^{39}Ar$	$age\,[Ma]$
1	620	0.3	0.93	35.3	4	0.30	2.76 ± 9.4	25.39 ± 2.4
2	660	0.4	0.62	19.4	9	0.14	1.35 ± 14.1	12.43 ± 1.7
3	700	0.9	1.01	27.7	21	0.11	1.09 ± 12.9	10.05 ± 1.3
4	740	2.3	2.59	53.9	44	0.17	1.05 ± 3.8	9.71 ± 0.4
5[4]	790	4.9	4.51	73.7	62	0.38	0.86 ± 7.7	7.93 ± 0.6
6[4]	845	6.0	5.50	77.6	55	0.55	0.84 ± 1.3	7.81 ± 0.1
7[4]	915	9.4	8.65	82.3	68	0.61	0.85 ± 2.6	7.87 ± 0.2
8[4]	980	11.9	10.90	81.8	63	0.63	0.85 ± 1.2	7.82 ± 0.1
9[4]	1080	16.7	15.40	85.1	43	1.22	0.85 ± 1.2	7.90 ± 0.1
10[4]	1250	47.2	44.01	85.3	43	1.24	0.86 ± 0.3	7.98 ± 0.0

Total gas age	**8.05 ± 0.3**
96% plateau age[4]	**7.92 ± 0.2**

^{40}Ar/^{36}Ar vs. ^{39}Ar/^{36}Ar isochron parameters:
Age = 8.2 ± 0.1 Ma; ^{40}Ar/^{36}Ar intercept = 279.1 ± 20.9; correlation = 0.999697

Sample ke41-00, amphibole 25 mg, J=0.005137 ± 0.4%

step	$T[^\circ C]$	^{39}Ar [%]	^{40}Ar [mV]	Rad [%]	$^{39}Ar/^{37}Ar$	^{36}Ca [%]	$^{40}Ca/^{39}Ar$	age [Ma]
1	840	3.2	2.86	63.7	0.65	1.44	11.76 ± 3.6	105.9 ± 3.7
2	880	0.7	0.42	49.9	0.31	2.68	7.31 ± 7.6	66.5 ± 5.0
3	980	2.6	0.83	83.7	0.15	34.81	4.16 ± 1.5	38.1 ± 0.5
4^4	1015	9.7	2.35	86.5	0.14	49.51	3.18 ± 8.1	29.2 ± 2.4
5^4	1050	22.6	5.59	94.7	0.12	76.87	3.23 ± 2.4	29.6 ± 0.7
6^4	1090	30.4	7.25	95.3	0.10	82.75	3.11 ± 1.9	28.6 ± 0.6
7^4	1140	22.9	5.72	93.5	0.12	71.61	3.25 ± 2.8	29.9 ± 0.8
8^4	1210	4.7	1.11	79.9	0.18	31.56	3.09 ± 7.7	28.4 ± 2.2
9^4	1300	3.1	0.79	30.6	0.08	9.46	3.32 ± 17.8	30.5 ± 5.4

Total gas age **32.2 ± 2.2**
93% plateau age[4] **29.3 ± 2.0**

$^{40}Ar/^{36}Ar$ vs. $^{39}Ar/^{36}Ar$ isochron parameters:
Age = 29.2 ± 0.6 Ma; $^{40}Ar/^{36}Ar$ intercept = 317.6 ± 75.2; correlation = 0.999441

K-Ar age determination — results

Sample	mineral	$^{40}Ar'$ [ppm]	$^{40}Ar'/$ $^{40}Ar_{total}$	aver. ^{40}Ar [ppm]	K [%]	aver. K [%]	^{40}K [ppm]	$^{40}Ar'/$ ^{40}K	age [Ma]
ke06-99	bi	0.007841	0.302		6.242				
		0.008093	0.112	0.007967	6.291	6.266	7.476	0.001066	**18.2 ± 0.5**
ke10-99	bi	0.005046	0.227		4.124				
		0.005200	0.222	0.005123	4.137	4.130	4.927	0.001040	**17.8 ± 0.5**
ke11-99	bi	0.010510	0.274		6.298				
		0.010850	0.298	0.010680	6.065	6.182	7.375	0.001381	**23.6 ± 0.6**
ke12-99	fsp	0.000626	0.066		0.343				
		0.000550	0.077	0.000588	0.353	0.348	0.415	0.001417	**24.2 ± 1.2**
ke19.99	glass	0.005949	0.325		3.348				
		0.005676	0.281	0.005812	3.380	3.367	4.017	0.001447	**24.7 ± 0.6**

Constants used: $\lambda_\beta = 4.962 \cdot 10^{-10}/year$; $\lambda_0 + \lambda'_0 = 0.581 \cdot 10^{-10}/year$; $^{40}K/K = 1.193 \cdot 10^{-4}g/g$;
$^{40}Ar'$ refers to radiogenetic ^{40}Ar; errors are given at the 1σ level.

Appendix D

Strain analysis

Microscopic description of strain samples

ke01	moderately sorted, clast-supported oolithic limestone, bimodal grain-size 0.2–0.4 mm and 0.6–1.2 mm, elliptical grain shape
ke03	very immature, poorly-sorted, fine to coarse sandstone (grain size 0.1–1.3 mm, mostly < 0.6 mm), 50% quartz, 30–35% feldspar, 10–15% matrix, biotite and hornblende (< 5%)
ke04	well-sorted, medium sandstone (0.3–0.5 mm), subrounded to rounded grains, 80–90% quartz, rock fragments, ~10% matrix (0.1–0.2 mm) containing calcite
ke05	moderately to well-sorted, clast-supported, medium sandstone (0.3–0.5 mm) with angular grains, 50% quartz, 30–35% feldspar, plus rock fragments, biotite, 15–20% silt matrix, many elongated grains show preferred orientation (long axis parallel to bedding)
ke06	moderately-sorted quartzite, bimodal distribution of subangular quartz grains (0.1–0.2 mm and 0.4–1.6 mm, calcite in matrix
ke07	moderately-sorted, fine to medium sandstone (0.15–0.5 mm grain size), > 50% quartz, 20–30% rock fragments, < 5% feldspar
ke08	poorly-sorted, clast-supported, fine sandstone (0.1–0.3 mm) with some larger clasts (up to 1.5 mm), 30–40% matrix, 40–50% quartz, plus biotite and some feldspars
ke09	tephra, 60–70% glassy matrix with embedded crystals of quartz (20–30%), hornblende and biotite (max 10%), average crystal size 0.1–0.9 mm
ke13	poorly-sorted, bimodal, matrix-supported, fine to medium sandstone (grain size 0.1–0.3 mm, some 0.5–1 mm), 30–35% quartz, 15–20% feldspar, 50% matrix containing calcite
ke15	well-sorted, medium sandstone (average grain size 0.2–0.4 mm) 40% quartz, 30% volcanic rock fragments, 20% feldspar, 10% matrix, plus hornblende and some alterated biotites
ke20	crystal tuff, 85–90% matrix of crystallised glass, 10–15% small blasts (0.06–0.2 mm, mainly quartz (~10%), biotite, feldspar
ke23	moderately-sorted, clast-supported, medium to coarse sandstone (grain size 0.3–1 mm, most grains ~0.6 mm), 40–50% volcanic rock fragments, 20–30% feldspar, 10–15% quartz, 10–15% matrix, plus magnetite, calcite (in matrix)
ke31	crystal tuff, 50–60% crystallised matrix with 0.1–0.5 mm large crystals of 50–55% feldspar, 40–45% quartz, 10% hornblende and biotite
ke44	very well-sorted, clast-supported, very fine sandstone (grain size 0.05–0.1 mm, some up to 0.15 mm), 85–90% quartz, 5–10% rock fragments, 5–10% Fe^{3+}-dominated matrix
ke45	very well-sorted, clast-supported, fine sandstone (average grain size 0.1–0.2 mm, max 0.4 mm), 90–95% quartz, < 5% feldspar

Table D.1: Lithology of strain samples

sample	sr	UTM-x	UTM-y	Fm./age	lithology	structural position	bedding	fabric	additional information
ke01	A	684528	7645617	El Molino	oolith	CAP, FW Khena-yani-Uyuni Fault	114/37	gs	oolites slightly deformed
ke03	B	668991	7670082	Pilkhaua	sandstone	CAP, top of syn-tectonic basin	45/01	gs	undeformed
ke04	A	771397	7655896	Potoco	sandstone	EAP, Eastern Anti-cline, western flank	238/56	gs	upper part of the Potoco Fm.
ke05	A	754054	7663950	OMsv2	sandstone	EAP, Vilque Anti-cline, eastern flank	125/05	ms	beginning of pressure solution at grain boundaries between different minerals
ke06	B	716481	7701958	Silurian	quartzite	CAP, HW Khena-yani-Uyuni Fault	308/52	gs	unmetamorphic, no texture
ke07	B	749450	7664707	OMsv2	sandstone	EAP, Vilque Anti-cline, eastern flank	145/35	gs	closest to the hinge
ke08	B	753639	7668753	OMsv2	sandstone	EAP, Vilque Anti-cline, eastern flank	100/05	gs	upper OMsv2
ke09	B	751848	7668581	OMsv2	tephra	EAP, Vilque Ant., north-eastern flank	69/03	ms	
ke13	A	605967	7730893	San Vicente	sandstone	WAP, Yazón Anti-cline, western flank	301/84	ms	upper San Vicente Fm.
ke15	A	664222	7676259	San Vicente	crystal tuff	CAP, Ines Ant., western flank	308/66	gs	lower San Vicente Fm.
ke20	B	634343	7732614	Post-Miocene	crystal tuff	CAP, post-tectonic	240/19	ms	inclination due to deposition on slope of volcano
ke23	B	607017	7730936	San Vicente	sandstone	WAP, Yazón Anti-cline, western flank	300/83	gs	east of ke13
ke31	B	656855	7690252	San Vicente	crystal tuff	CAP, Julaca Anti-cline, western flank	278/20	ms	near the anticlinal hinge
ke44	B	689433	7673471	Potoco	sandstone	CAP, HW San Cristóbal Fault	278/80	gs	lower Potoco Fm., interbedded in silt-stone
ke45	B	688405	7673638	Potoco	sandstone	CAP, HW San Cristóbal Fault	285/85	gs	lower Potoco Fm., interbedded in silt-stone

Table D.2: sr = series, gs = grain-supported fabric, ms = matrix-supported fabric, EAP = Eastern Altiplano, CAP = Central Altiplano, WAP = Western Altiplano, HW = hanging wall, FW = footwall, see text for further explanation

Samples from the Eastern Altiplano

Sample	n	X/Y	ϕ'	aver. error %
ke05-1	338	1.424	12.71	19.89
ke05-2	376	1.334	−21.75	18.88
ke05-3	351	1.168	−12.42	21.73
ke09-1	333	1.174	89.70	19.48
ke09-2	333	1.375	−7.39	16.44
ke09-3	333	1.488	−11.16	23.00

Samples from the Central Altiplano

Sample	n	X/Y	ϕ'	aver. error %
ke13-1	360	1.215	−20.80	17.30
ke13-2	247	1.188	56.52	22.66
ke13-3	357	1.087	−0.32	18.57
ke20-1	317	1.156	1.25	19.04
ke20-2	333	1.100	14.14	18.10
ke20-3	305	1.109	−42.15	13.38
ke31-1	352	1.193	0.43	17.10
ke31-2	252	1.174	−32.87	23.40
ke31-3	301	1.246	49.85	16.81

Table D.3: Fry results from INSTRAIN for matrix-supported samples. Enhanced normalised Fry (SF = 1.10)

Samples from the Eastern Altiplano

Sample	n	$R_{f(harm)}$	θ	R_s from χ^2	χ^2	$R_{i(harm)}$
ke04-1	283	1.68	-19.61	1.18	9.76	1.66
ke04-2	254	1.59	-19.61	1.09	12.93	1.58
ke04-3	249	1.71	10.24	1.11	7.59	1.69
ke07-1	329	1.67	8.14	1.22	23.61	1.66
ke07-2	333	1.72	3.12	1.32	12.98	1.67
ke07-3	333	1.74	-7.50	1.29	12.52	1.69
ke08-1	333	1.69	-4.85	1.19	23.43	1.68
ke08-2	333	1.71	0.94	1.16	38.98	1.68
ke08-3	322	1.76	12.37	1.26	13.40	1.75

Samples from the Khenayani-Uyuni Fault Zone

Sample	n	$R_{f(harm)}$	θ	R_s from χ^2	χ^2	$R_{i(harm)}$
ke01-1	350	1.54	-75.16	1.04	15.71	1.54
ke01-2	336	1.68	-5.88	1.28	12.75	1.61
ke01-3	325	1.6	23.98	1.15	4.14	1.59
ke06-1	428	1.58	27.81	1.08	18.68	1.57
ke06-2	333	1.72	-2.54	1.17	10.51	1.70
ke06-3	333	1.78	0.20	1.28	24.81	1.73
ke44-1	333	1.59	0.71	1.09	6.37	1.58
ke44-2	446	1.62	89.90	1.07	17.23	1.62
ke44-3	333	1.71	85.48	1.01	14.12	1.71
ke45-1	333	1.69	22.10	1.24	60.24	1.68
ke45-2	360	1.72	39.39	1.12	21.72	1.70
ke45-3	333	1.75	-7.38	1.20	63.49	1.71

Samples from the Central Altiplano

Sample	n	$R_{f(harm)}$	θ	R_s from χ^2	χ^2	$R_{i(harm)}$
ke03-1	500	1.54	-17.14	1.04	33.12	1.54
ke03-2	357	1.57	4.05	1.17	5.66	1.54
ke03-3	350	1.61	88.73	1.06	15.03	1.61
ke15-1	352	1.67	-31.17	1.22	10.78	1.63
ke15-2	374	1.68	-3.64	1.18	14.50	1.67
ke15-3	353	1.62	23.90	1.12	9.12	1.61
ke23-1	333	1.77	-30.10	1.12	7.99	1.76
ke23-2	350	1.68	-13.68	1.28	7.49	1.62
ke23-3	291	1.67	81.63	1.12	10.68	1.66

Table D.4: R_f/ϕ' results after Peach und Lisle (1979) for grain-supported samples

D.1 Projection of section planes through the compaction ellipsoid

To determine the length of the compaction ellipsoids principal axes in a section that is not parallel to the principal planes, the method of Ramsay and Huber (1983a) was applied. This method was originally designed to determine the three-dimensional strain from two sections which are not principal planes. In the present case, the three-dimensional strain, i.e. the compaction, was fully known as axial ratios and orientation. The aim was to calculate the change of the length of the principal strain axes of the compaction ellipsoid for two sections that are not principal planes. These are the two sections of each sample of Series A that are oblique to the bedding, i.e. the horizontal section (e.g. ke01-1) and the vertical section containing the fold axis (e.g. ke01-2). The values of $e_{x'}$ and $e_{z'}$ are given in Table D.5.

In Fig. D.1, the dip direction and dip angle of the bedding is 114/37. x, y, and z are the principal axes of the inverse compaction ellipsoid, the corresponding length are $e_x > 1$, $e_y = e_z = 1$. x is normal to the bedding, y and z in bedding plane. The aim is to project x, y, and z into the required sections ($x \rightarrow x', y \rightarrow y', z \rightarrow z'$). y and y' are identical in this special case. The third section of each sample is in the XZ plane of the compaction ellipsoid (cross-section plane).

The length of the new principal axes ($e_{x'}, e_{z'}$) is calculated with

$$e_{x',z'} = \left[\frac{\left(\cos\theta_{(x,x'),(x,z')}\right)^2}{(e_x)^2} + \frac{\left(\sin\theta_{(x,x'),(x,z')}\right)^2}{(e_y)^2} \right]^{-\frac{1}{2}} \tag{D.1}$$

where $\theta_{(x,x')}$ is the angle between x and x' (= dip angle of the bedding) and used to calculate $e_{x'}$. For the calculation of $e_{y'}$, $\theta_{(x,z')}$ is the angle between x and z' (= 90 – bedding). The length of the third axis does not change ($e_y = e_{y'} = 1$), because $y = y'$.
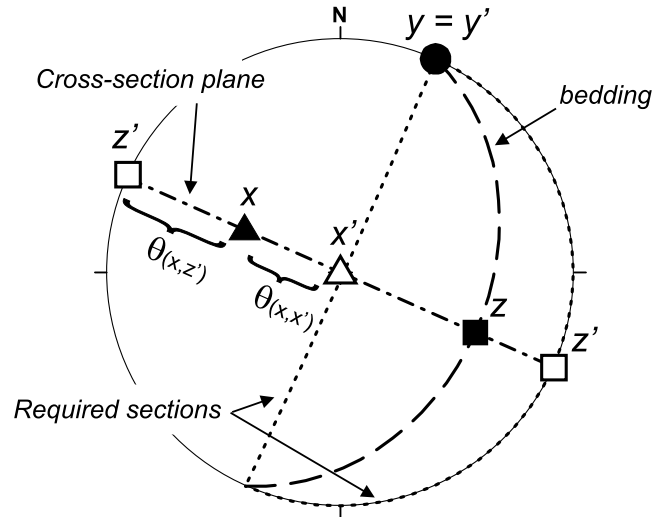
Figure D.1: Schmidt-net projection (lower hemisphere, equal area) to illustrate the projection of vertical and horizontal sections through a compaction ellipsoid. The projection procedure is described in the text. In this example (ke01) $e_x = 1.39$, $e_y = 1$, $e_z = 1$, the bedding plane is 114/37, $\theta'_{(x,x')} = 37$, $\theta'_{(x,z')} = 53$. The lengths of the projected principal axes are $e_{x'} = 1.20$ and $e_{y'} = 1.10$. In the required vertical section, the compaction ellipse is determined with the vertical dipping $e_{x'}$ and the horizontal e_y. The horizontal section is the plane containing y (strike = 24°) and z (strike = 114°), i.e. e_y and $e_{z'}$ respectively.

D.2   Decompaction

DE-COMPACTION: POROSITY LOSS AND INVERSE STRAIN ELLIPSOID

Sample	$\phi_0[\%]$	$k[MPa]$	$h[m]$	$\phi_{\text{depth}}[m]$	$\delta\phi_{\text{depth}}[\%]$	$e_{x(depth)}$	$e_{x'}$	$e_{z'}$
ke01	48.0	31.03	1200	20.1	27.9	1.39	1.20	1.10
ke03	48.0	31.03	100	44.6	3.4	1.04	-	-
ke04	48.0	31.03	2575	7.4	40.6	1.68	1.12	1.34
ke05	48.0	31.03	190	41.8	6.2	1.07	1.07	1.00
ke06	48.0	31.03	1400	17.3	30.7	1.44	-	-
ke07	48.0	31.03	850	25.9	22.1	1.28	-	-
ke08	48.0	31.03	190	41.8	6.2	1.07	-	-
ke09	48.0	31.03	520	32.9	15.1	1.18	-	-
ke13	48.0	31.03	330	37.8	10.2	1.11	1.00	1.11
ke15	48.0	31.03	630	30.4	17.6	1.21	1.03	1.17
ke20	48.0	31.03	100	44.6	3.4	1.04	-	-
ke23	48.0	31.03	1255	19.3	28.7	1.40	-	-
ke31	48.0	31.03	250	40.0	8.0	1.09	-	-
ke44	38.0	25.00	4295	0.8	37.2	1.85	-	-
ke45	38.0	25.00	3895	1.1	36.9	1.82	-	-

Table D.5: Calculation of the inverse strain ellipsoid from porosity depth graphs. $\phi_0[\%]$ is the average initial porosity of sandstones (48%) or siltstones (38%), k the compaction modulus, h the maximum burial depth, ϕ_{depth} the porosity at h, $\delta\phi_{\text{depth}}$ the difference between $\phi_0[\%]$ and ϕ_{depth}, $e_{X(depth)}$ the calculated length of the long axis (X) of the compaction ellipsoid (see section 5.4.1 for equations). $e_{x'}$ and $e_{z'}$ are the lengths of the two principal axes X and Z of the compaction ellipsoid in the horizontal and vertical sections. These were projected through the compaction ellipsoid for those samples where the measured thin sections are not parallel to the principal planes of the compaction ellipsoid. e_y is always = 1 because it does not change its orientation (see section 5.4.2 and App. D.1 for further explanation). The lengths of the principal axes of the inverse compaction ellipsoid for the samples with sections parallel to the principal planes (= no values for $e_{x'}$ and $e_{z'}$) of the inverse compaction ellipsoid are: $e_x(depth)$ (from column 7) and $e_y = e_z = 1$.

Table D.6: (next page) Results of the 2D decompaction. The first two columns are *dip direction* and *dip angle* of the 2D sections. R_s and ϕ_s are the results from the 2D strain analysis (X/Y and ϕ' from Fry [Table D.3] and R_s *from* χ^2 and χ^2 from R_f/ϕ' after Peach and Lisle [1979][Table D.4]), R_c and ϕ_c the inverse compaction ellipse, and R_{ts} and ϕ_{ts} the results of the decompaction calculated with 'Shear 3.0'. $\phi_{ts}rot$ is the direction of the long axis of the ellipses after rotation of the bedding back to the correct angle of the measured section (for the decompaction of the cross-section planes [samples with the suffix -3] the finite-strain ellipse was rotated until the bedding was vertical). Sections parallel to the XY plane of the inverse compaction ellipse were not affected by the decompaction (i.e. many samples with the suffix -1). In these cases, R_{ts} and ϕ_{ts} are directly the 2D results of the finite strain measurements (see Table D.3 and D.4). R_{ts} and ϕ_{ts} are the input for TRISEC to calculate the 3D tectonic-strain ellipsoids. Every ϕ are with respect to a horizontal reference, angles are anticlockwise positive.

DE-COMPACTION: 2D RESULTS

Sample	dip dir.	dip angle	R_s	ϕ_s	R_c	ϕ_c	R_{ts}	ϕ_{ts}	ϕ_{ts} rot.
ke01-1	114	1	1.00	16	1.11	0	**1.11**	−0.2	**−0.2**
ke01-2	114	89	1.30	13	1.38	0	**1.13**	34.9	**34.9**
ke01-3	24	89	1.20	-49	1.38	0	**1.42**	−15.6	**−68.6**
ke03-1	45	1	1.00	33	1.02	0	**1.02**	0.6	**0.6**
ke03-2	225	89	1.20	6	1.04	90	**1.15**	7.8	**7.8**
ke03-3	135	89	1.10	-80	1.04	0	**1.06**	−72.8	**−67.8**
ke04-1	238	1	1.20	10	1.35	0	**1.61**	4.1	**4.1**
ke04-2	58	89	1.10	13	1.19	90	**1.10**	77.8	**77.8**
ke04-3	328	89	1.10	42	1.69	0	**1.72**	5.1	**−29.1**
ke05-1	125	1	1.40	13	1.02	90	**1.38**	13.3	**13.3**
ke05-2	125	89	1.30	-22	1.06	0	**1.36**	−18.2	**−18.2**
ke05-3	35	89	1.20	-97	1.06	0	**1.13**	79.4	**−5.6**
ke06-1	308	52					**1.08**		**27.8**
ke06-2	128	38	1.30	25	1.44	90	**1.33**	67.5	**67.5**
ke06-3	38	89	1.30	63	1.45	0	**1.36**	22.1	**−15.9**
ke07-1	145	35					**1.22**		**23.6**
ke07-2	325	55	1.30	13	1.28	90	**1.12**	47.6	**47.6**
ke07-3	235	89	1.30	-42	1.29	0	**1.47**	−21.1	**33.9**
ke08-1	100	5					**1.19**		**23.4**
ke08-2	280	85	1.20	39	1.06	90	**1.20**	48.2	**48.2**
ke08-3	190	89	1.30	-72	1.06	0	**1.24**	−66.6	**18.4**
ke09-1	69	3					**1.17**		**89.7**
ke09-2	249	87	1.40	-7	1.19	90	**1.19**	−14.4	**−14.4**
ke09-3	339	89	1.50	76	1.18	0	**1.31**	66.7	**−20.3**
ke13-1	301	1	1.20	-21	1.10	0	**1.31**	−13.6	**−13.6**
ke13-2	121	89	1.20	57	1.02	90	**1.21**	60.5	**60.5**
ke13-3	211	89	1.10	6	1.11	0	**1.22**	2.5	**−3.5**
ke15-1	308	1	1.20	11	1.16	0	**1.38**	5.6	**5.6**
ke15-2	128	89	1.20	15	1.02	90	**1.18**	16.8	**16.8**
ke15-3	218	89	1.10	33	1.21	0	**1.28**	11.0	**−13.0**
ke20-1	240	19					**1.11**		**−42.2**
ke20-3	150	89	1.10	-42	1.04	90	**1.10**	−52.9	**−52.9**
ke20-2	60	71	1.10	85	1.04	0	**1.06**	81.4	**−79.6**
ke23-1	300	83					**1.12**		**8.0**
ke23-2	120	7	1.30	7	1.39	90	**1.11**	70.3	**70.3**
ke23-3	30	89	1.10	18	1.42	0	**1.54**	3.4	**−3.6**
ke31-1	278	20					**1.19**		**0.4**
ke31-2	98	70	1.20	-33	1.25	90	**1.25**	66.0	**66.0**
ke31-3	8	89	1.30	-60	1.09	0	**1.26**	−50.8	**19.2**
ke44-1	278	80					**1.09**		**6.4**
ke44-2	107	20	1.10	17	1.59	90	**1.47**	85.9	**85.9**
ke44-3	17	89	1.00	24	1.60	0	**1.60**	0.4	**10.4**
ke45-1	285	85					**1.24**		**60.2**
ke45-2	105	5	1.10	22	1.44	90	**1.35**	83.6	**83.6**
ke45-3	195	89	1.20	68	1.60	0	**1.44**	9.7	**−85.3**

FINITE STRAIN ELLIPSOIDS

Samples from the Eastern Altiplano

Sample	method	X_{norm}	Y_{norm}	Z_{norm}	X_{trend}	X_{length}	Y_{trend}	Y_{length}	Z_{trend}	Z_{length}	ν	ε_s	XY_{plane}
ke04	R_f/ϕ'	1.097	0.979	0.931	251/04	1.171	159/28	1.045	348/28	0.993	-0.381	0.138	168/29
ke05	*Fry*	1.271	0.917	0.858	17/17	1.578	286/04	1.139	182/72	1.066	-0.665	0.380	362/18
ke07	R_f/ϕ'	1.139	1.053	0.834	124/08	1.310	31/19	1.211	236/69	0.959	0.497	0.211	56/21
ke08	R_f/ϕ'	1.171	0.966	0.884	328/22	1.185	238/01	0.978	147/68	0.895	-0.369	0.233	327/22
ke09	*Fry*	1.164	1.108	0.776	323/09	1.199	57/24	1.141	213/64	0.799	0.756	0.297	33/26

Hanging walls of thrusts or steep fold limbs (Central Altiplano)

Sample	method	X_{norm}	Y_{norm}	Z_{norm}	X_{trend}	X_{length}	Y_{trend}	Y_{length}	Z_{trend}	Z_{length}	ν	ε_s	XY_{plane}
ke01	R_f/ϕ'	1.088	1.051	0.875	180/15	1.184	271/04	1.144	15/75	0.952	0.685	0.155	195/15
ke06	R_f/ϕ'	1.101	1.020	0.890	181/08	1.357	89/16	1.257	295/72	1.097	0.274	0.142	115/18
ke15	R_f/ϕ'	1.114	0.999	0.899	291/01	1.132	21/28	1.015	199/62	0.913	-0.015	0.153	19/28
ke44	R_f/ϕ'	1.094	1.069	0.855	70/16	1.024	339/03	0.986	238/74	0.956	-0.084	0.050	58/16
ke45	R_f/ϕ'	1.036	0.998	0.967	104/25	1.131	208/28	1.105	339/51	0.884	0.810	0.184	159/39

Minor deformation or post-tectonic (Central and Western Altiplano)

Sample	method	X_{norm}	Y_{norm}	Z_{norm}	X_{trend}	X_{length}	Y_{trend}	Y_{length}	Z_{trend}	Z_{length}	ν	ε_s	XY_{plane}
ke03	R_f/ϕ'	1.057	0.988	0.958	333/13	1.099	68/22	1.027	214/64	0.996	-0.377	0.083	34/26
ke13	*Fry*	1.122	1.024	0.870	92/19	1.139	335/53	1.039	194/30	0.883	0.276	0.170	14/60
ke20	*Fry*	1.080	1.010	0.917	350/58	1.118	120/22	1.045	219/22	0.949	0.181	0.111	39/68
ke23	R_f/ϕ'	1.065	0.995	0.944	194/20	1.241	6/70	1.160	103/03	1.100	-0.197	0.085	283/87
ke31	*Fry*	1.163	0.991	0.867	259/48	1.306	154/13	1.113	53/39	0.974	-0.092	0.215	53/51

Table D.7: Results from the calculation of the finite-strain ellipsoids. $X, Y, Z\ norm$ is the normalised length of the principal ellipsoid axes, $X, Y, Z\ trend$ the orientation (trend/plunge), $X, Y, Z\ length$ the calculated length from TRISEC (**not normalised**), ν Lode's parameter, and ε_s the strain intensity.

TECTONIC STRAIN ELLIPSOIDS

Samples from the Eastern Altiplano

Sample	method	X_{norm}	Y_{norm}	Z_{norm}	X_{trend}	X_{length}	Y_{trend}	Y_{length}	Z_{trend}	Z_{length}	ν	ε_s	XY_{plane}
ke04	R_f/ϕ'	1.485	0.852	0.791	56/27	1.784	193/56	1.023	315/20	0.950	−0.764	0.645	135/70
ke05	Fry	1.260	0.923	0.860	20/15	1.516	111/06	1.111	223/74	1.035	−0.630	0.363	43/16
ke07	R_f/ϕ'	1.190	1.002	0.839	327/26	1.490	73/30	1.255	204/48	1.050	0.019	0.246	24/42
ke08	R_f/ϕ'	1.189	0.949	0.887	328/28	1.223	59/01	0.976	151/62	0.912	−0.540	0.266	331/28
ke09	Fry	1.169	0.999	0.856	242/18	1.181	148/12	1.009	27/68	0.865	−0.008	0.221	207/22

Hanging walls of thrusts or steep fold limbs (Central Altiplano)

Sample	method	X_{norm}	Y_{norm}	Z_{norm}	X_{trend}	X_{length}	Y_{trend}	Y_{length}	Z_{trend}	Z_{length}	ν	ε_s	XY_{plane}
ke01	R_f/ϕ'	1.181	0.961	0.881	265/57	1.299	2/05	1.057	95/33	0.969	−0.412	0.249	275/57
ke06	R_f/ϕ'	1.251	0.932	0.857	330/01	1.351	239/37	1.007	61/53	0.926	−0.556	0.346	241/37
ke15	R_f/ϕ'	1.210	0.966	0.856	123/09	1.385	218/29	1.105	18/60	0.979	−0.306	0.279	198/30
ke44	R_f/ϕ'	1.166	1.038	0.826	30/02	1.797	120/01	1.599	241/88	1.273	0.323	0.230	61/02
ke45	R_f/ϕ'	1.200	1.008	0.827	217/17	1.195	308/04	1.003	52/73	0.823	0.062	0.259	232/17

Minor deformation or post-tectonic (Central and Western Altiplano)

Sample	method	X_{norm}	Y_{norm}	Z_{norm}	X_{trend}	X_{length}	Y_{trend}	Y_{length}	Z_{trend}	Z_{length}	ν	ε_s	XY_{plane}
ke03	R_f/ϕ'	1.051	1.019	0.934	342/04	1.061	251/18	1.0288	85/71	0.943	0.46	0.079	265/19
ke13	Fry	1.170	1.012	0.844	315/05	1.244	54/60	1.076	223/30	0.897	0.114	0.224	43/60
ke20	Fry	1.081	0.972	0.951	139/21	1.150	229/00	1.034	319/69	1.012	−0.661	0.124	139/21
ke23	R_f/ϕ'	1.208	0.941	0.880	306/09	1.557	212/22	1.213	56/66	1.135	−0.576	0.293	236/24
ke31	Fry	1.204	0.974	0.853	111/23	1.280	232/50	1.035	6/31	0.906	−0.233	0.269	186/59

Table D.8: Results from the calculation of the tectonic-strain ellipsoids after decompaction. $X, Y, Z \ norm$ is the normalised length of the principal ellipsoid axes, $X, Y, Z \ trend$ the orientation (trend/plunge), $X, Y, Z \ length$ the calculated length from TRISEC (**not normalised**), ν Lode's parameter, and ε_s the strain intensity.

LINE LENGTH AND THICKNESS CORRECTION DUE TO DUCTILE STRAIN

| | INPUT | | | | | | | OUTPUT | | | | | |
| | | | | XY-plane, angle | | P90, angle | | length correction in % ... | | | | correction of CSP | |
Sample	R_{P90}	R_{XY}	*dV*	*X,δ*	*X,hor*	*la,hor*	*la,bed*	‖δ *in XY*	*hor in XY*	*in P90* ‖ *bed*	*in P90* ⊥ *bed*	⊥ *CSP*	‖ *bed*
ke01	1.42	1.229	0	75	57	+57	−87	−0.35	+3.86	−16.15	+19.04	+3.72	−16.08
ke03	1.06	1.031	0	28	04	+13	+08	+3.12	+3.81	+1.25	−4.26	+1.69	+3.34
ke05	1.13	1.365	0	30	15	−01	−03	+13.88	+22.09	−2.21	−13.40	+19.86	−1.01
ke06	1.36	1.342	0	69	01	−18	+34	−4.68	+24.20	+5.14	−6.02	+21.92	+6.59
ke07	1.47	1.187	0	89	26	+26	−61	+1.43	+15.92	−12.39	+6.70	+3.81	−5.47
ke08	1.24	1.253	0	50	28	+18	−24	+3.86	+13.08	+3.44	−10.32	+12.75	+3.69
ke09	1.31	1.170	0	82	18	−16	−20	−1.08	+13.45	+10.49	−9.97	+12.15	+11.74
ke20	1.06	1.112	0	26	21	−01	+20	+6.37	+7.14	−1.06	−5.38	+2.09	+3.51
ke23	1.54	1.284	0	86	09	−10	+73	−2.10	+24.60	−16.49	+18.62	+22.35	−15.79
ke44	1.44	1.124	0	13	02	−01	+80	+21.06	+21.84	−23.71	+7.27	+21.58	−23.65
ke45	1.44	1.191	0	26	26	+10	+75	+20.89	+20.89	−23.22	+4.92	+20.21	−23.05

Table D.9: Calculation of the line length and thickness variation in cross-section plane and along strike based on the 3D strain analysis. R_{P90} is the axial ratio of the decompacted strain ellipse in the profile plane 90° to the fold axis (= *P90*, samples -3, see Table D.6) and R_{XY} the axial ratio from the tectonic-strain ellipsoid. *dV* is = 0 in case of no volume loss (assumed for all samples). *X,δ* is the angle between the long axis of the strain ellipsoid and the trend of the fold axis *δ* in the XY-plane of the strain ellipsoid, *X,hor* the angle between *X* and the horizontal, also in the XY-plane. *P90* is the plane of samples with the suffix -3 (this plane is generally close to the cross-section plane), *la,hor* is the angle between the long axis of the strain ellipsoid in the *P90*-plane and the horizontal, *la,bed* the angle between the long axis and the bedding (= *bed*). The output is the line-length correction in the XY-plane parallel to the fold axis ‖δ *in XY* and *horizontal in XY*. *in P90* ‖ *bed* is the horizontal line-length correction for the undeformed section and *in P90* ⊥ *bed* the corresponding thickness correction for each sample. The last two columns are the corrected values for the horizontal correction in and perpendicular to the cross-section plane. See text for further explanation.

Appendix E

Unsuccessful balanced cross-sections

A **Deformed**

San Cristóbal Block

Central Block

IPF

Undeformed

Central Block   San Cristóbal Block

IPF

B **Deformed**

Undeformed
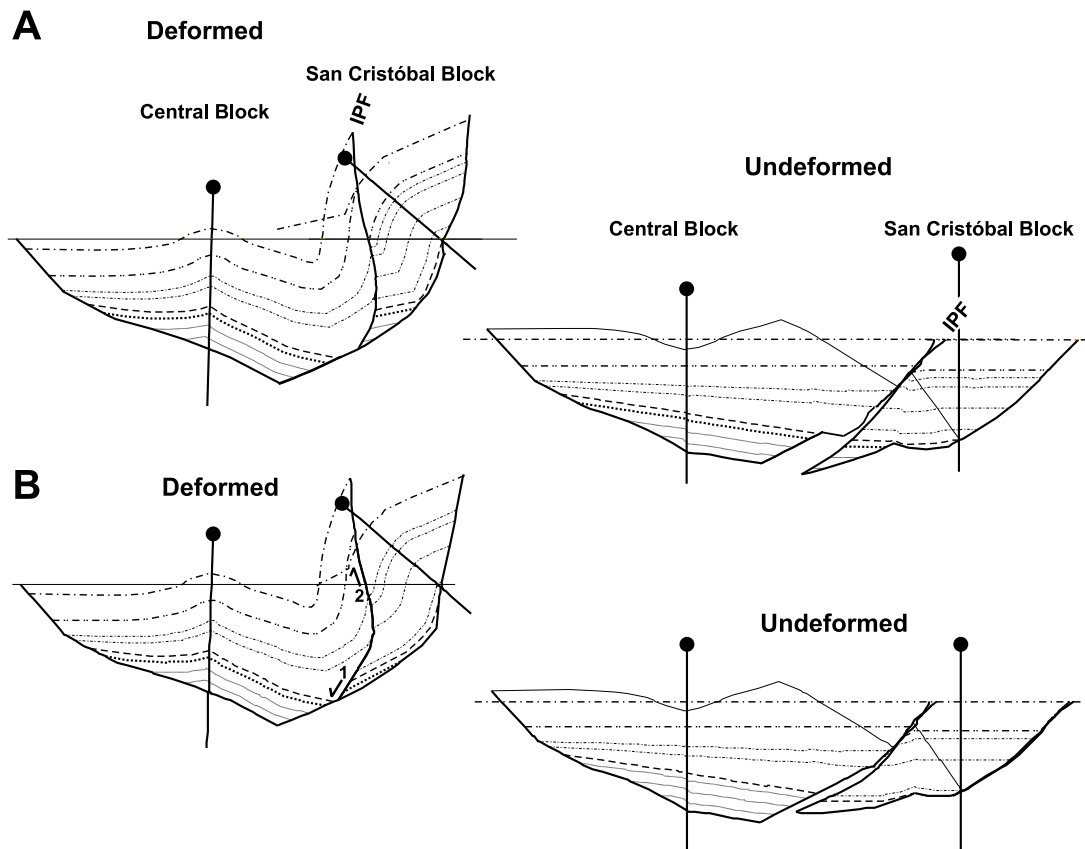
Figure E.1: Unsuccessful attempts to balance the lower portion of the Central and San Cristóbal Blocks. **A:** This geometry shows the result of higher cutoff angles in the San Cristobal Block than in the Central Block; it produces slightly incorrect fault geometries and a void occurs in the undeformed section. **B:** Curved stratigraphic traces of the San Cristobal Block (in contrast to those of A). After retro-deformation: both fault trace and stratigraphy east and west of the Intra-Potoco Fault fit. But there is a kinematically-impossible change along the Intra-Potoco Fault (IFP) from thrusting in the upper strata (arrow 2) to normal faulting in the lower portion (arrow 1) of the Central Block. Line signatures as in Fig. 9.7.
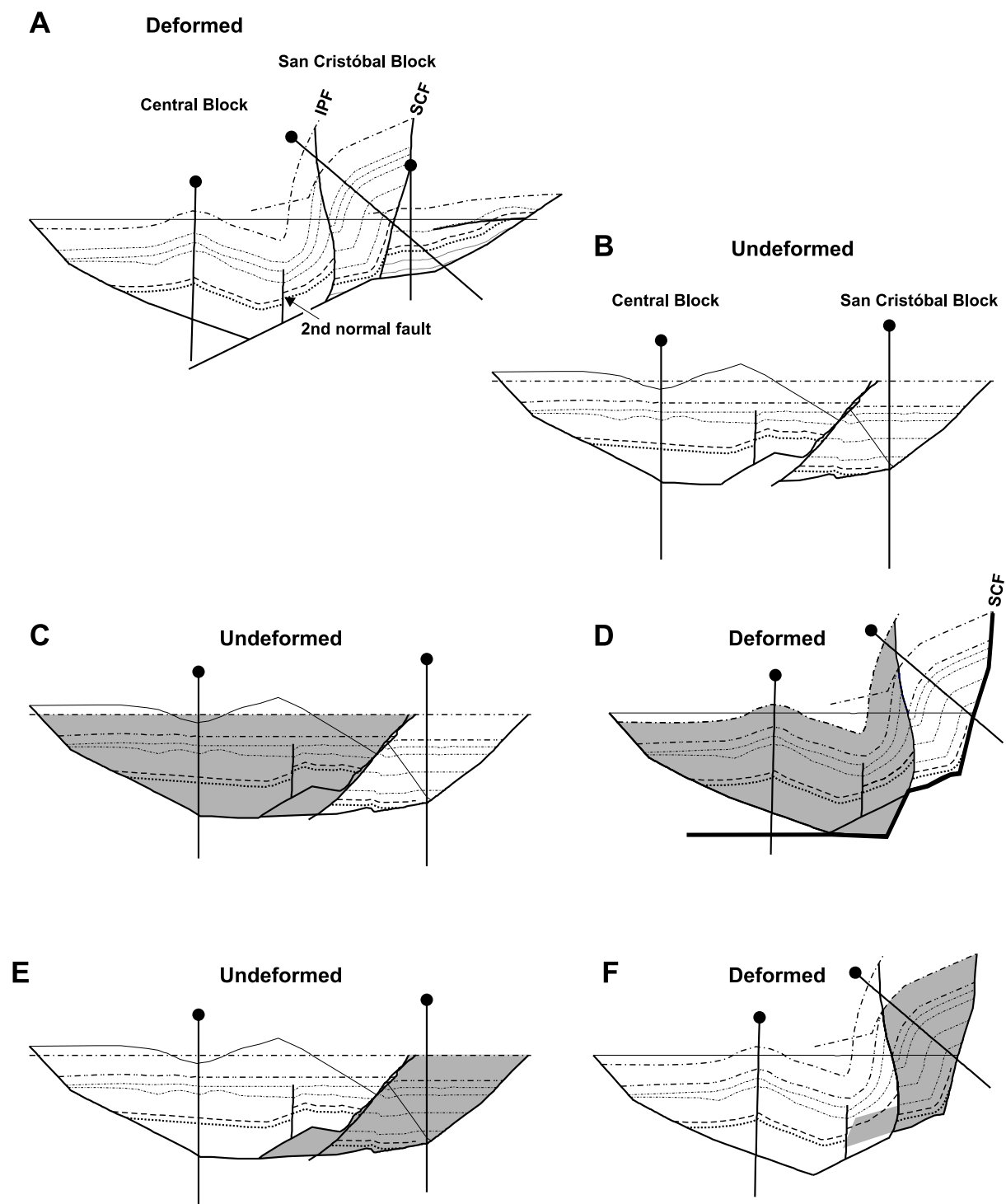
Figure E.2: Unsuccessful attempts to balance the lower portion of the Central and San Cristóbal Blocks (2nd). **A:** Introducing a second normal fault parallel to the San Cristobal Fault yields a consistent displacement geometry in the deformed state. **B:** The retro-deformation, however, also produces a void in the lower portion of the Central Block. There are two possibilities to close the void: **C, D:** either insertion of a series of ramps in the lower part of the San Cristobal Fault (bold line in D, geologically not very senseful) in the deformed state (if the void is part of the Central Block) or, **E, F:** adding the void to the San Cristobal component, which after retro-deformation leads to overlap of material in the Central Block.

Appendix F

Geological map and balanced cross-section

F.1 Geological map of the Southern Altiplano, scale 1:500000, modified from YPFB

A larger version of the map (1:250000) is available from the author: kelger@gfz-potsdam.de

F.2 Balanced cross-section (Eastern and Central Altiplano)

Ich danke...

... Herrn Prof. Dr. Onno Oncken, meinem Doktorvater, für seine Anregungen, seine Geduld, das immer offene Ohr für Fragen und die vielen fruchtbaren Diskussionen, die halfen diese Arbeit zu einem Ganzen zusammenzufügen.

... Herrn Prof. Dr. Christoph Heubeck, für Beratungen und wertvolle Hinweise zur Interpretation der seismischen Profile und für die Erstellung des Zweitgutachtens.

... meinem bolivianischen Koorperationspartner Yacimientos Petroliferos Fiscales Bolivianos (YPFB), insbesondere David Tufiño B. und Ramiro Suarez S., für die Bereitstellung der seismischen Profile, geologischer Karten und Berichte, und logistische Hilfe bei der Kooperation.

... Dr. Christoph Gaedicke für die Iniziierung des Projektes.

... vielen bolivianischen und chilenischen Freunden und Kollegen, die mit ihrer Zeit und ihrer Hilfe dazu beigetragen haben, die Geländeaufenthalte zu unvergessenen Erlebnissen zu machen: Ramiro Suárez Soruco (YPFB), Oscar Aranibar und Eloy Martínez (Chaco SA., Santa Cruz); Heriberto Salamanca und Renato Sanchez C. (UATF Potosí); Guillermo Chong, Hans Wilke, Luis Olmos (UCN Antofagasta); Sven Herlitz; Luís Baeza (Codelco), Hernán Castillo, Rene Ortiz und Daniel Ayala (meinen Mitstreitern im Gelände)

... Reinhard Rössling, Sohrab Tawackoli und Raúl Bascope (SERGEOMIN, La Paz), ohne deren Hilfe ich bereits an der chilenisch-bolivianischen Grenze gescheitert wäre und für vieles mehr. Ausserdem Dorothee Mertmann, Klaus J. Reutter, Ekkehard Scheuber, Harald Ege, Ralph Hinsch, Tim Vietor, Patricio Silva G., Patrick Gôni und Jörn Levenhagen für die Geländebegleitung und -betreuung.

... ganz besonders Dave Tanner, der mir nicht nur durch seine sehr didaktisch ausgerichteten Korrekturen den Spass am Englisch schreiben gebracht hat, sondern auch zu einer meiner wichtigsten Diskussionspartner war.

... insbesondere Tim Vietor, meinem langjährigen Zimmerpartner, dem ich die 14 effektivsten Geländetage verdanke und der mir immer bei kleineren und größeren Wehwehchen mit Rat, Tat und Diskussion zur Seite stand. Johannes Glodny für seine Hilfe und Motivation bei der Mineralseparation und der Interpretation der Datierungen. Charlotte Krawczyk für alles 'rund um die Seismik' und Jürgen Adam, und das nicht nur für die Kekse.

... zahlreichen Mitarbeitern des SFB 267 und des GFZ Potsdam, die mir halfen über den Tellerrand zu blicken, insbesondere Harald Ege, Kerstin Fiedler, Sven Egenhoff, Klaus J. Reutter, Jonas Kley, Uwe Meyer, Ekkehard Scheuber, Dorothee Mertmann, Ulrich Riller, Tim Vietor, Henri Brasse, David Hindle, Andreas Günther u.a. für die so wichtige 'Starthilfe' bei der Strainanalyse, Trond Ryberg, Patricio Silva G., Frank Schilling, George Hilley, Andrey Babeyko, Bertram Heinze, Norbert Ott und nicht zuletzt H.J. Götze und Sabine Schmidt für die Gravimetriekarte und Hilfe bei deren Interpretation.

... allen Mitarbeitern der Sektion 3.1 des GFZ, zuallererst unserer Sekretärin Frau Wolff, Gabi Arnold und Michael Köhler, für die Herstellung von Dünnschliffen, Juliane Herwig für ihre Hilfe bei der Mineralseparation, den Graphikern Manuela Dziggel und Andreas Hendrich, Herrn Herr, der 'Retter in der Not' bei Rechnerproblemen, Wolfgang Seiffert, der in Rekordzeit das Kalium an meinen Hornblenden bestimmte, Helmut Echtler, Ulrich Riller, Ralph Hinsch, Jo Lohrmann, Ralf Freitag, Klaus Pelz, Pia Victor, Wolfgang Kramer, Silvan Hoth, Matthias Rosenau, Andrea Hampel, Michael Haschke, Helga Kemnitz, Daniel Melnick, Katrin Huhn, Nina Kukowski, etc. ... 'meinen' Hiwis, Hendrik Müller, Rüdiger Wagner und Markus Wolff, ohne die ich heute noch Dünnschliffe für die Strainanalyse digitalisieren wuerde, oder Hornblenden picken, oder....

... P. Wessel und W.H.F. Smith (1998) für GMT und Donald E. Knuth for TeX

... und Fritz Echternacht, für alles ...

Geological map of the
Southern Altiplano
(67.68-66.28°W, 20.55-21.67°S)
(Bolivia)

compiled and modified after YPFB
Kirsten Elger
1:500000
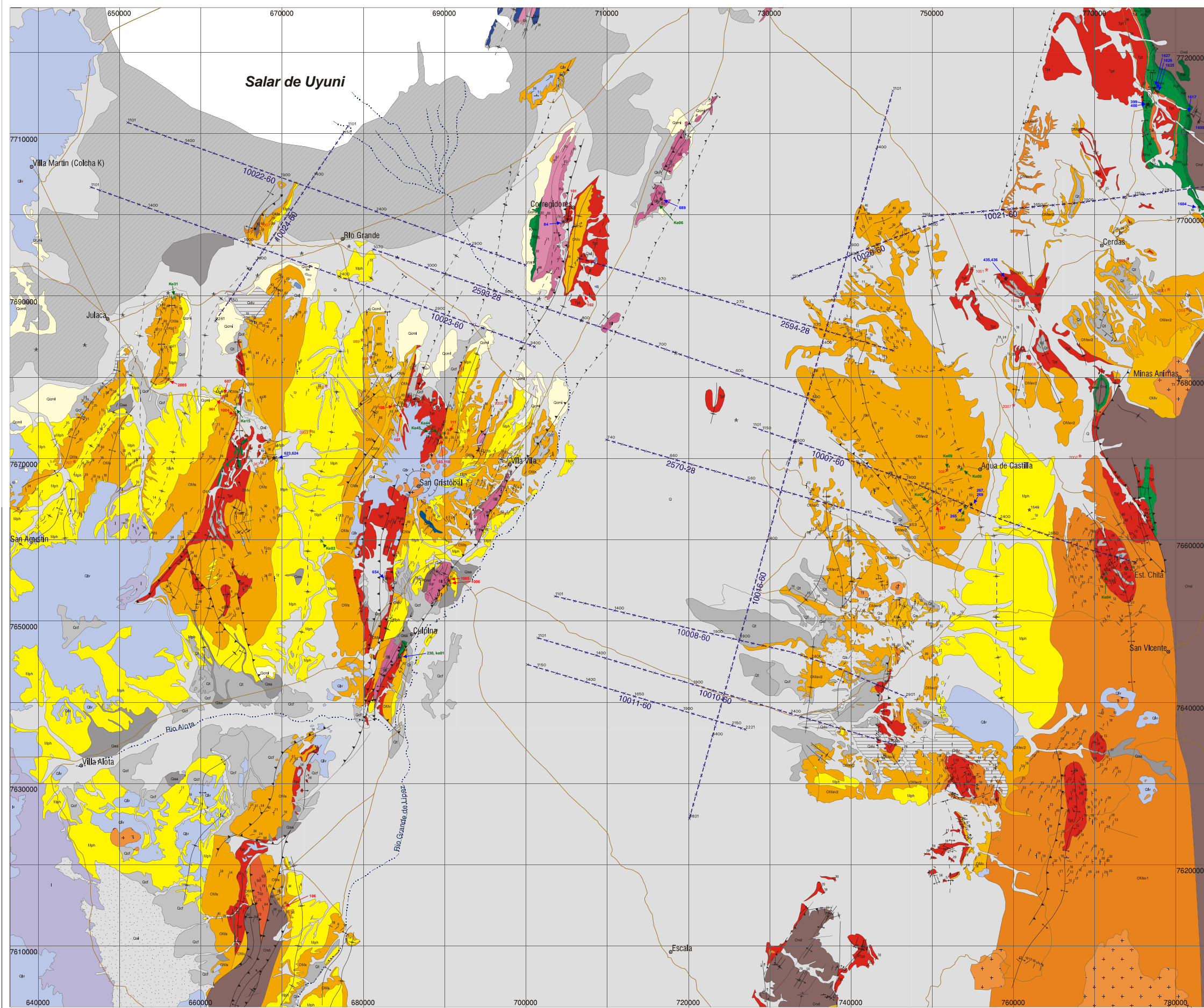
Projection: UTM, units: metres, datum: Provisorial South American 1956

Salar de Uyuni

Villa Martín (Colcha K)
Julaca
San Agustín
Villa Alota
Río Grande
Corregidora
Río Grande
Villa Vila
San Cristóbal
Colcha
Escala
Cerdas
Minas Antiñas
Agua de Castilla
Est. Chita
San Vicente
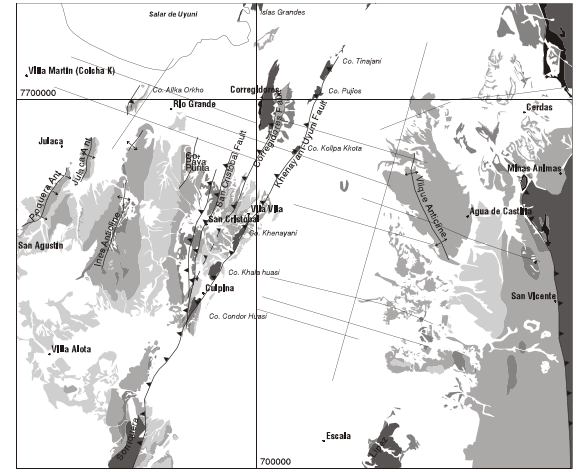
Legend:

- Quaternary, undiff. (Q)
- Salt lakes (Qe)
- Salt flats, fluvio-lacustrine deposits (Qes)
- Alluvial deposits (Qal, Qa)
- Alluvial fans (Qaa)
- Colluvial-fluviatil deposits (Qcf)
- Dunes (Qdu)
- Terrasses (Qt)
- Lacustrine limestone (Minchin) (Qcml)
- Lava flows (Qlv)
- Ignimbrites (Nqi)
- Miocene syntectonic sediments (Fm. Pikhaua)(Mph)
- Oligocene/ Miocene volcanics (Fm. San Vicente)(OMv)
- Oligocene/ Miocene sediments (Fm. San Vicente)(OMs, OMsv2)
- Oligocene/ Miocene conglomerates (Fm. San Vicente)(OMsv1)
- Eocenel Oligocene sediments (Fm. Potoco)(EOpt)
- Paleocene sediments (Fm. Cayara)(Tcy)
- Paleocene sediments (Fm. Santa Lucía)(Psl)
- Tertiary intrusives (Ti)
- U-Cretaceous sediments (Fm. El Molino)(Kmo)
- U-Cretaceous sediments (Fm. Chaunaca)(Kch)
- U-Cretaceous sediments (Fm. Aroifilla)(Kar)
- Devonian sediments (Fm. Vila Vila)(Dvv)

- Silurian sediments (Fm. Catavi)(Sc)
- Silurian sediments (Fm. Uncia)(Su)
- Silurian sediments (Fm. Llallagua)(Sll)
- Lower Silurian tillite (Fm. Cancañiri)(Scc)
- Ordovician, undiff. (O)

- Syncline
- Anticline
- Reverse fault
- Reverse fault, overturned
- Normal fault
- Oblique reverse fault
- Reverse fault, under Quaternary cover
- Sinistral strike-slip fault
- Dextral strike-slip fault
- Fault
- Lithological boundary
- Seismic profile (YPFB)(with number)
- Roads
- Rivers
- Bedding (with dip angle)
- Overturned bedding (with dip angle)
- Shot point of seismic profiles
- Shot point of the ANCORP'96 profile
- Town
- Locality of strain sample
- Locality of striated faults
- Locality of age sample

Ages of volcanic rocks

No.	Sample	Age	Mineral	Method
38	KE10-99	17.8 ± 0.5	Bio	K/Ar
287	KE06-99	18.2 ± 0.5	Bio	K/Ar
317	KE11-99	23.6 ± 0.6	Bio	K/Ar
317	KE12-99	24.2 ± 1.2	Fsp	K/Ar
319	KE28-00	20.9 ± 0.2	Bio	Ar/Ar
367	KE19-99	24.7 ± 0.6	Glas	K/Ar
607	KE01-00	15.8 ± 1.2	Bio	Ar/Ar
707	KE13-00	9.4 ± 0.3	Bio	Ar/Ar
919	KE24-00	17.1 ± 0.7	Bio	Ar/Ar
988	KE39-00	8.3 ± 1.2	Hbl	Ar/Ar
989	KE40-00	7.9 ± 0.2	Bio	Ar/Ar
998	KE41-00	29.3 ± 2.0	Hbl	Ar/Ar

Radiometric ages from Silva (in prep)

No.	Sample	Age	Mineral	Method
92	SR99-14	24.3 ± 1.2	WR	K/Ar
100	SR99-15	10.4 ± 0.3	Bio	K/Ar
101	SR99-10	11.0 ± 0.5	Hbl	K/Ar
102	SR99-06	11.4 ± 0.3	Bio	K/Ar
103	SR99-13	12.9 ± 0.3	Bio	K/Ar
104	SR99-01	14.7 ± 0.4	Bio	K/Ar

No.	Sample	Age	Mineral	Method
110	PS 99-17	13.7 ± 0.4	Bio	K/Ar
111	PS 99-26	11.0 ± 0.3	Bio	K/Ar
112	PS99-47	12.3 ± 0.4	Bio	K/Ar
1000	SB00-02	10.6 ± 0.3	Bio	K/Ar
1001	SB00-10	20.1 ± 0.5	Bio	K/Ar
1002	SB00-12	19.2 ± 0.5	Bio	K/Ar
1003	SB00-14	12.7 ± 0.4	Bio	K/Ar
1004	SB00-25	23.4 ± 1.1	Hbl	K/Ar
1004	SB00-31	18.0 ± 0.5	Bio,Epi	K/Ar
1005	SB00-33	10.8 ± 0.3	Bio	K/Ar
1006	SB00-40	9.2 ± 0.3	Bio	K/Ar
1007	SB00-44	22.5 ± 0.8	Bio	K/Ar
1008	DLP02-2000	16.1 ± 0.4	Bio	K/Ar
1009	CE 05-2000	3.0 ± 0.1	Bio	K/Ar
2000	SB00-7	9.4 ± 0.3	Bio	K/Ar
2001	SB00-15	35.2 ± 0.9	Bio	K/Ar
2002	SB00-17	7.6 ± 0.2	Bio	K/Ar
2003	SB00-41	9.4 ± 0.3	Bio	K/Ar
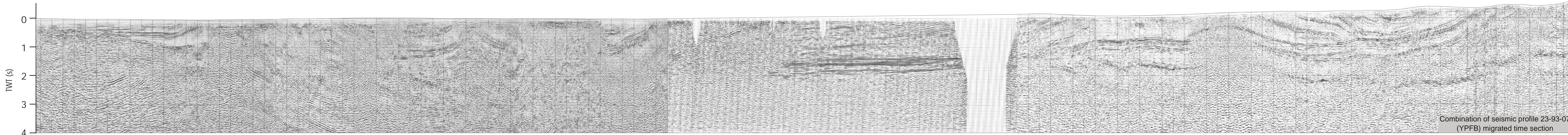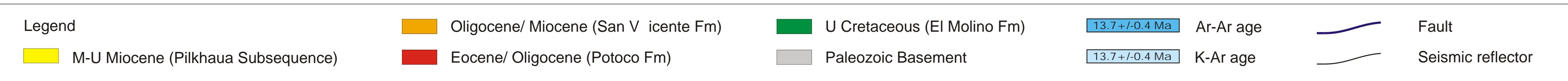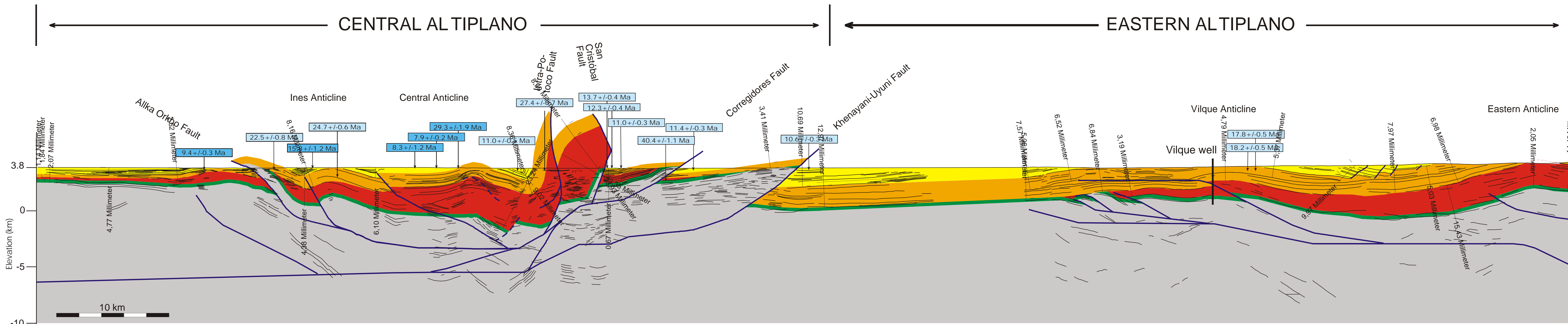
Appendix F2: Balanced Cross-Section of the Central and Eastern Altiplano (1:250000) - Main Cross-Section